NEW TOOLS FOR RAPID MASS SPECTROMETRIC SCREENING

A Dissertation
Presented to
The Academic Faculty

by

Stephen Zambrzycki

In Partial Fulfillment
of the Requirements for the Degree
Doctor of Philosophy in the
School of Chemistry and Biochemistry

Georgia Institute of Technology
August 2021

NEW TOOLS FOR RAPID MASS SPECTROMETRIC SCREENING

Approved by:

Dr. Facundo M. Fernández, Advisor
School of Chemistry and Biochemistry
Georgia Institute of Technology

Dr. Amanda Stockton
School of Chemistry and Biochemistry
Georgia Institute of Technology

Dr. Julia Kubanek
School of Chemistry and Biochemistry
Georgia Institute of Technology

Dr. Ronghu Wu
School of Chemistry and Biochemistry
Georgia Institute of Technology

Dr. Matthew Torres
School of Biology
Georgia Institute of Technology

Date Approved: July 22, 2021

You'll need coffee shops and sunsets and road trips. Airplanes and passports and new songs and old songs, but people more than anything else. You will need other people and you will need to be that other person to someone else, a living breathing screaming invitation to believe better things.

-Jamie Tworkowski; TO WRITE LOVE ON HER ARMS

ACKNOWLEDGEMENTS

I cannot thank the countless people along my journey through graduate school enough for the life changing experiences that have shaped me. This document you read now is all possible through the unending love and support from everyone to celebrate the good times and help overcome the bad. I am eternally grateful for all the opportunities granted to me during my career here at Georgia Tech. There are so many names to mention worthy of a movie style credits list, so I will attempt my best to summarize below.

I'd like to thank Dr. Facundo M. Fernández for his mentorship, patience, and perseverance. With Facundo's leadership, I was able to work on some of the coolest and most ambitious projects that I never would have imagined working at Tech. These opportunities allowed me to meet so many incredible people. I also want to thank Dr. Julia Kubanek and Dr. Ronghu Wu for allowing me to rotate in their labs when I first started. The rotations helped me begin to understand the research dynamics at a powerhouse like Georgia Tech. I am grateful for Dr. Kubanek, Dr. Wu, Dr. Matthew Torres, and Dr. Amanda Stockton for their guidance serving on my committee to make this thesis possible.

Before Georgia Tech was ever on my radar, the Department of Chemistry and Chemical Engineering at the University of New Haven (UNH) helped show me that these opportunities existed. I cannot thank Dr. Nancy Savage and Dr. Eddie Luzik enough for their endless support. They granted me the opportunity to work and do some of my first ever research projects. This is where I found my passion for chemical analysis tools that helped drive the work I do today. I am so incredibly thankful for all the folks at UNH I was

able to work with. I also cannot thank all the friends I have made at UNH to get me through undergrad. You planted the seed that got me started at Georgia Tech.

I want to give some of the biggest thanks to all the colleagues I have worked with in the Fernández lab. My first- and second-year mentors Dr. Matthew Bernier, Dr. Jay Forsythe, and Dr. Joel Keelor gave me so much support and advice when I first started at Tech. They are still such a help. I am so grateful for the opportunity to work with the lab's former alumni: Dr. Marcos Bouza, Dr. Chaevien Clendinen, David Donndelinger, Lauren Geben, Eric Gier, Dr. Molly Hopper, Dr. Danning Huang, Dr. Anyin Li, Dr. Li Li, Dr. Yafeng Li, Jazzlyn Murphy, Dr. Martin Paine, Dr. Eric Parker, Monica Tran, and Dr. Xiaoling Zang. Also big thanks to Dr. Danning Huang for the support during my last project and data review/thesis season which was one of the biggest hurdles in my career. Thank you to all the current members of the Fernández lab for your support in seeing me through the finish line: Carter Asef, Dmitry Leontyev, Dr. Xin Ma, Kristin Mckenna, Emily Phillips, Markace Rainey, Samyukta Sah, and Alexandria Van Grouw. Big thanks to all the folks who work in the mass spec cores for their advice and friendship: Dr. David Gaul, Sam Moore, Alexis Bennett, David Smalley, and Dr. David Bostwick. Thank you so much Shantel Floyd for helping me navigate the Georgia Tech bureaucracy when things came to a bind, projects would not be moving without you. Such an amazing group of folks to work with and I wish them all the best!!!

I am so grateful for all the collaborators I've met outside of the Fernández lab. The NSF/NASA Center for Chemical Evolution (CCE) was the first major research organization that I have worked with. So many amazing people to thank who I've met in the CCE including Dr. Christine Conwell, Christopher Parsons, and Dr. Rio Febrian to

name a few. The Aero-VaPI project would not be possible without the help from the CCE, Dr. Sandra Blair, and Dr. Nga Ng. Pyro-VaPI would not be possible without the support from Dr. James Bradshaw from Consolidated Nuclear Securities. One of the largest projects undertaken in my career was the evaluation of portable screening devices for poor quality medicines supported by the Asian Development Bank, Wellcome Trust, Infectious Diseases Data Observatory, and Worldwide Antimalarial Resistance Network. Completing this international collection of projects would not have been possible without help from: Dr. Celine Caillet, Dr. Serena Vickers, Dr. Paul Newton, Phonepasith Boupha, Kem Boutsamay, Vayouly Vidhamaly, Dr. Nantasit Luangasanatip, and Dr. Yoel Lubell. Finally, I want to thank the people at the NSF Center for Cell Manufacturing and Technology (CMaT) for introducing me to a brand new field of research I never expected to be in. I want to thank Priyanka Priyadarshani, Gilad Doron, Arina Nikitina, Dr. Melissa Kemp, and Dr. Johnna Temmenoff for all there help and patience with the ASPECT and MALDI imaging projects. I would also like to thank the incredible people I have worked with in CMaT's Student Leadership Council, especially Chaitanya Tondepu with whom we created the first student newsletter for the center. None of this thesis would have been possible without you.

Last and certainly not least, I would like to thank my friends and family for all their loving support. None of this would have been possible and enjoyable without you. I cannot thank my parents Dorota and Zbigniew Zambrzycki enough for their endless love and support to pursue my dreams. The best friends I have created in the 2015 incoming graduate class cohort in Georgia Tech's chemistry program, including all the friends I have met in the chemistry department through the Graduate Student Forum are irreplaceable. I want to

thank all the athletes at Big Peach Running Company's group runs and November Project workouts throughout the years for being a consistent source of stress relief and helping me embrace new physical challenges. Shout out to the Cyclodillas crew for so many fun adventures biking, camping, trail running, and marathon racing. So many names to list that it would take another thesis sized document, especially for everyone I met just along the way. You have all been such an important part in all my most beloved memories, as well as getting me through some of the toughest times too.

Thank you.

TABLE OF CONTENTS

ACKNOWLEDGEMENTS iv

LIST OF TABLES viii

LIST OF FIGURES ix

LIST OF SYMBOLS AND ABBREVIATIONS xviii

SUMMARY xxiv

CHAPTER 1. INTRODUCTION 1
1.1 Abstract 1
1.2 Principles of Ambient Plasma Ionization Mass Spectrometry 1
1.3 Principles of Ion Mobility Spectrometry 7
1.4 Current Quality Problems with Pharmaceuticals 11
1.5 References 13

PART 1. VACUUM ASSISTED PLASMA IONIZATION DEVELOPMENT 18

CHAPTER 2. AEROSOL VACUUM-ASSISSTED PLASMA IONIZATION (AERO-VAPI) COUPLED TO ION MOBILITY-MASS SPECTROMTRY 19
2.1 Abstract 19
2.2 Introduction 21
2.3 Experimental 22
2.3.1 Materials 22
2.3.2 Instrumentation 23
2.4 Results and Discussion 26
2.5 Conclusions 33
2.6 References 33

CHAPTER 3. PYROLYSIS VACUUM-ASSISTED PLASMA IONIZATION (PYRO-VAPI) ION MOBILITY-MASS SPECTROMETRY FOR INSOLUBLE POLYMER ANALYSIS 37
3.1 Abstract 37
3.2 Introduction 38
3.3 Experimental 39
3.3.1 Materials 39
3.3.2 Pyrolysis/Heating Unit 40
3.3.3 Instrumentation 40
3.4 Results and Discussion 43
3.5 Conclusions 50
3.6 References 50

PART 2. RAPID PHARMACEUTICAL QUALITY SCREENING 53

CHAPTER 4. LABORATORY EVALUATION OF TWELVE PORTABLE DEVICES FOR MEDICINE QUALITY SCREENING 54
4.1 Abstract 54
4.1.1 Background: 54
4.1.2 Methods and Findings: 54
4.1.3 Conclusions: 55
4.2 Introduction 55
4.3 Experimental 56
4.3.1 Devices: 56
4.3.2 Samples: 59
4.3.3 Data Analysis: 60
4.3.4 Statistical Analysis: 63
4.4 Results 64
4.4.1 Thin Layer Chromatography: Minilab 67
4.4.2 Single Use Devices: PAD and RDT 67
4.4.3 MIR Spectrometer: 4500a 68
4.4.4 NIR Spectrometers: Neospectra 2.5, NIR-S-G1, & MicroPHAZIR RX 69
4.4.5 Raman Spectrometers: Progeny and TruScan RM 72
4.4.6 Quantitative Instruments: C-Vue, PharmaChk, & QDa 75
4.4.7 Device Comparison 76
4.5 Discussion 79
4.6 References 85

CHAPTER 5. ACCELERATED SCREENING FOR THE PROTETCION AND EFFICACY OF CELL TREATEMTNS (ASPECT) VIA MALDI-MS 89
5.1 Abstract 89
5.2 Introduction 90
5.3 Experimental 93
5.4 Results and Discussion 101
5.5 Conclusions 108
5.6 References 109

CHAPTER 6. CONCLUSIONS AND OUTLOOK 113
6.1 Abstract 113
6.2 Major Accomplishments 113
6.2.1 Vacuum Assisted Plasma Ionization Development 113
6.2.2 Rapid Pharmaceutical Quality Screening 114
6.3 Impact and Future Direction 116
6.4 References 119

APPENDIX A. MICROPLASMA IONIZATION OF VOLATILE ORGANICS FOR IMPROVING AIR/WATER MONITORING SYSTEMS ON-BOARD THE INTERNATIONAL SPACE STATION 121
A.1 Abstract 121
A.2 Introduction 122
A.3 Experimental 124
A.3.1 Chemicals 124

A.3.2 MHCD Microplasmas 124
A.3.3 Direct Analysis in Real-Time 127
A.3.4 TOF MS Instrumentation 127
A.4 Results and Discussion 128
A.4.1 Optimization and Comparison to DART 128
A.4.2 Optimization and Comparison to DART 132
A.4.3 Power and Lifetime Characterization 139
A.5 Conclusion 142
A.6 References 143

APPENDIX B. A MULTI-PHASE EVALUATION OF PORTABLE SCREENING DEVICES TO ASSESS MEDICINES QUALITY FOR NATIONAL MEDICINES REGULATORY AUTHORITIES 147
B.1 Introduction 147
B.2 Literature Review 148
B.2.1 Background 148
B.2.2 Methods 148
B.2.3 Results 149
B.2.4 Conclusion 149
B.3 Field Evaluation 150
B.3.1 Background 150
B.3.2 Methodology/Principal findings 150
B.3.3 Conclusions/Significance 151
B.4 Cost Effectiveness 151
B.4.1 Background 151
B.4.2 Methods and findings 152
B.4.3 Conclusions: 153
B.5 Recommendations and Next Steps 153

APPENDIX C. ATMOSPHERIC PRESSURE DRIFT TUBE ION MOBILITY–ORBITRAP MASS SPECTROMETRY: INITIAL PERFORMANCE CHARACTERIZATION. 155
C.1 Abstract 155
C.2 Introduction 155
C.3 Experimental 159
C.3.1 Chemicals and Materials 159
C.3.2 Instrument and System Parameters 160
C.3.3 DTIMS Ion Gating Schemes 165
C.4 Results and Discussion 167
C.4.1 AP-DTIMS Basic Performance Optimization 167
C.4.2 DTIMS Gate Pulse Width Scan Step Functions 168
C.4.3 Effect of Orbitrap Automatic Gain Control and Injection Time 172
C.4.4 DTIMS-Orbitrap MS Applications 172
C.5 Conclusion 177
C.6 References 177

APPENDIX D. ROBOTIC SURFACE ANALYSIS MASS SPECTROMETRY (ROSA-MS) OF THREE-DIMENSIONAL OBJECTS. 181
D.1 Abstract 181
D.2 Introduction 182
D.3 Experimental 184
D.3.1 RoSA System 184
D.3.2 Mass Spectrometric Analysis 187
D.3.3 RoSA Data Processing and Fusion 190
D.4 Results and Discussion 191
D.4.1 Sampling Precision and Resolution 191
D.4.2 Characterization of OPSI Performance 193
D.4.3 Molecular Cartography RoSA-MS Applications 194
D.5 Conclusion 204
D.6 References 204

LIST OF TABLES

Table 4-1	List of instruments and devices evaluated, including their underlying technology and basic instrument specifications.	**58**
Table 4-2	Sensitivity and specificity to correctly determine quality of medicine samples for the 12 tested devices.	**66**
Table 4-3	Pair-wise sensitivity comparisons of the devices used to test 50 % and 80 % API samples outside their packaging. Sensitivities expressed as 95% CI, in grey. The p-value of the McNemar test (n=number of 0%/wrong API medicines assessed by both devices in the pair) is presented. The pairs for which a significant difference was observed are shown in orange, if any.	**78**
Table 5-1	Key sample preparation procedures, MALDI settings, and ASPECT script parameters.	**95**
Table C-1	Summary of key system parameters	**162**

LIST OF FIGURES

Figure 1-1 Diagram of how DART operates and protonates volatilized analytes in positive ion mode. Helium gas is fed through a glow discharge that creates metastable species. These metastables interact with the ambient atmosphere as they exit the DART source to create a variety of reactive ion species. One of the reactive ion species created are protonated water clusters that donate their proton when interacting with the gas-phase analyte [M]. **4**

Figure 1-2 Diagram of a standalone drift tube. As the Bradbury-Nielson ion gate opens and closes, the electric field gradient pushes a packet of ions through a reduced or ambient pressure drift cell. The ions collide with neutral gases in the drift cell. Ions with larger collisional cross sections collide with more drift gases and travel slower in the drift tube. As a result, ions are separated based on their collisional cross sections. At the end of the drift tube, the ion collides with a detector such as a Faraday plate. The change in time between the detection event and when the ion gate was opened is the ion's drift time. The drift time is correlated to the ion's collisional cross section. **9**

Figure 2-1 Cross-sectional view of the home-built Aero-VaPI ion source coupled to IM-MS via a VAPUR® interface that had its side vacuum port blocked, serving only as a mechanical adapter. **25**

Figure 2-2 Relative mass-weighted particle size distributions for (A) 2 mM methanolic solution of monocaprin and (B) 2 mM aqueous solution of decanoic acid. Aero-VaPI-MS signals for aerosol particles consisting of (C) monocaprin in (+)-mode; $[M - H_2O + H]^+$ monitored at m/z 229, from protonation-induced water loss (D) decanoic acid in (–)-mode; $[M - H]^-$ monitored at m/z 171 **28**

Figure 2-3 Negative ion mode of poly-L-malic acid (A) ESI IM-MS averaged mass spectrum, (B) ESI IM-MS ion mobility arrival time distribution, (C) Aero-VaPI IM-MS averaged mass spectrum and (D) Aero-VaPI IM-MS ion mobility arrival time distribution. Oligomer $[M-H]^-$ (solid circles) and $[M'-H]^-$ (open circles) signals are denoted by markers colored by the number of monomer units. The ion mobility arrival time distribution signals are colored similarly. (E) Poly-L-malic acid aerosol relative mass-weighted particle size distribution. Particles were generated from a 0.5 mM aqueous solution of poly-L-malic acid. **30**

Figure 2-4 Negative ion mode Aero-VaPI-IM-MS ion mobility arrival time distribution in the 1-2 ms time range for a poly-L-malic acid aerosol. Particles were generated from a 0.5 mM aqueous solution of poly-L-malic acid. Observed fragment and oxidized species ions are plotted by color and line style with m/z of each ion listed in the legend. Unidentified peaks are labeled as "UN". **32**

Figure 3-1 Diagram of the pyro-VaPI IM-MS platform (not to scale). The pyrolysis unit was placed in a fume hood together with the heating power supply unit to minimize fire hazards and to prevent fumes from the pyrolysis experiments from reaching the user. A PTFE tube extended from the pyrolysis unit to the VaPI ion source, which was directly connected to a Waters Synapt G2-S ion mobility-mass spectrometer via the IonSense VAPUR interface. **42**

Figure 3-2 Extracted arrival time distributions for various pyrolyzed nylon polymers matching the (A) cyclic monomer ions with *m/z* 114.09, 184.17, 198.19, 227.18, 269.22, 283.24, and 311.27 for nylon 6, nylon 11, nylon 12, nylon 6-6, nylon 6-9, nylon 6-10, and nylon 6-12, respectively; (B) cyclic dimer ions with *m/z* 227.18, 367.33, 395.36, 453.34, 537.44, 565.47,and 621.53 for nylon 6, nylon 11, nylon 12, nylon 6-6, nylon 6-9, nylon 6-10, and nylon 6-12, respectively; (C) cyclic trimer ions with *m/z* 340.26, 550.49, 592.54, and 679.51 for nylon 6, nylon 11, nylon 12, and nylon 6-6, respectively; and (D) cyclic tetramer ions with *m/z* 453.34 and 733.66 for nylon 6 and nylon 11, respectively. **44**

Figure 3-3 Pyro-VaPI analysis of nylon 6-6 (polyhexamethylene adipamide). (A) Extracted drift time for the cyclic dimer at m/z 453.36 showing potentially two different isomers/conformers of nylon 6-6. These species were fragmented in the transfer cell (post-mobility) at 13 eV collision energy. The MS/MS spectra for the fragmented cyclic dimer species at (B) 4.24 ms and (C) 4.67 ms peak are presented. M refers to a repeat unit of nylon 6-6 in the cyclic species. **46**

Figure 3-4 Investigation of pyro-VaPI ion abundances for nylon 6-6 (polyhexamethylene adipamide) at various time-points of a temperature gradient. (A) The cumulative arrival time distribution, the arrival time distribution between 2 and 4 minutes of the temperature gradient, and the arrival time distribution between 12 and 14 minutes of the gradient for the cyclic dimer ion extracted at m/z 453.36 showing two different species for nylon 6-6. (B) IM drift time vs. temperature gradient time for m/z 453.36. The intensity was log scaled. The minimum intensity threshold was set at 54 %. (C) Temperature profile of the shallow cup pyrolysis experiment measured with a thermocouple. **49**

Figure 4-1 Illustration of the basic processes for qualitative spectral comparison and quantitative analysis. (A) Process for reference library creation and spectral comparison analysis. From top to bottom: (i) spectra are collected from different batches of the same medicine and compiled into a mean spectrum representative of that medicine. (ii) This mean spectrum is used to build a "library" or database that serves as the comparator against which test samples are compared. (iii) Test samples are scanned and then (iv) the test sample spectra are overlaid with the reference spectrum for visual or computational comparison to determine a pass or fail. (B) Illustration of a basic quantitative experiment. From left to right and top to bottom. (i) A set of standard calibration samples with increasing API concentration is prepared along with a solution of the test sample that should fit in the concentration range of those standards. (ii) All solutions are then tested on the instrument and (iii) the data collected. (iv) The data obtained is then used to build a calibration curve via linear least-squares regression. Interpolation of the peak area of the questioned sample into this curve yields the estimated API concentration. **62**

Figure 4-2 Comparison of NIR spectra obtained for ofloxacin-containing simulated medicines. Spectra were collected for ofloxacin-containing simulated medicines using the (A) Neospectra 2.5, (B) NIR-S-G1, and (C) MicroPHAZIR RX spectrometers. The black trace is of a falsified simulated medicine tablet containing only starch. The blue trace is of a simulated good quality ofloxacin sample that contained starch as the bulk excipient. **71**

Figure 4-3 Comparison of Raman spectra obtained for Artesun artesunate powder. Raman spectra were collected with the (A) Progeny and (B) TruScan RM spectrometers for Artesun artesunate powder for injection. Spectra are provided for 1) a scan of the bottom of the Artesun glass vial containing no artesunate (blue trace), 2) a sample containing 60 mg of artesunate powder, scanned through the bottom of the glass vial (orange trace), and 3) the artesunate powder transferred to a polypropylene bag and compacted into a more localized area to enable more focused analysis (green trace) **74**

Figure 4-4 Intact vs. crushed ACA tablet analysis by Raman and NIR spectrometers. Spectral comparisons of a field collected sample of AMK 1000 mg (a co-formulation of amoxicillin and clavulanic acid) are shown with the (A) Progeny, (B) Truscan RM, (C) MicroPHAZIR RX, (D) NIR-S-G1, and (E) Neospectra 2.5 spectrometers. The spectra in blue are scans of an intact tablet of AMK 1000 mg. The spectra in black are scans of the powder from a crushed AMK 1000 mg tablet. **81**

Figure 4-5 Receiver operating characteristic (ROC) curves for substandard analysis with the spectrometers. ROC curves were created for the (A) 4500a, (B) MicroPHAZIR RX, (C) Progeny, and (D) TruScan RM spectrometers. ROC curves were based only on the results for simulated substandard and good quality medicines. Each legend identifies the threshold chosen for each point, with the one labelled "Stock" being the threshold used for the study. The stock thresholds for the MicroPHAZIR RX's correlation coefficient, Progeny's correlation coefficient, and TruScan RM's p-value were the default values set by the manufacturer. The 4500a stock threshold was selected for the study since that instrument did not output pass/fail results. **83**

Figure 5-1 To demonstrate the rapifleX's speed, the total ion current for each protein profiling experiment was plotted versus the overall time taken to process a fully spotted 384 ground steel target plate. Each peak represents the total ion current of a single spot on the target plate. The gaps in time between each target plate row are when the rapifleX is transitioning from one row to the next. Each row contains 24 spots. **97**

Figure 5-2 Diagram of the workflow in the second script in ASPECT. (A) After the .mzXML spectra have been imported into MATLAB, (B) the spectra are baselined corrected and normalized. (C) Then, the spectra are binned to reduce noise and the mass range is trimmed to isolate a specific region of interest. This spectral region of interest may be more biologically relevant than others. (D) The spectra from the questioned samples are then compared to a reference sample through CC testing. A CC score is output that measures the relative match in the spectral pattern between the questioned sample and the reference. A score of 0 is not a match and a score of 1 is a perfect match. The scores are compiled into two MALDI target plate maps. (E) The end user would receive a map indicating which samples passed or failed CC testing given the defined threshold for passing. (F) If the developer evaluating the assay uploads a file with the known samples' quality, the developer's view calls attention to which spots did not perform as expected. False negatives and false positives are highlighted by being large circles. The sensitivity and specificity of the assay is automatically calculated and output in the developer's view. In either the user or developer view, gradient colors can be displayed to visually estimate the CC score too. **100**

Figure 5-3 The mean unprocessed lipid profiling spectra (n=24) are plotted for (A) ethanol incubated cells and (B) untreated cells. Ethanol incubation shows a dramatic shift in the lipid profile. (C) After ASPECT data processing, the developer's view of the MALDI **102**

target plate map shows that all samples were correctly classified with a specificity and sensitivity of 1 (0.85 to 1, 95% CI). All untreated cells passed with CC scores >0.8 and all ethanol incubated cells failed with CC scores <0.5. No false positives or negatives were detected since all the spots on the target plate map were small circles (D) The ROC curve shows that the CC threshold can be set as low as 0.525 and still have a specificity and sensitivity of 1 to detect ethanol incubation via lipid profiling. Increasing the CC threshold beyond 0.8 increases the false positive rate.

Figure 5-4 The mean unprocessed protein profiling spectra (n=24) are plotted for (A) ethanol-incubated cells and (B) untreated cells. Only one feature from the untreated cells is extracted after ethanol incubation highlighted by the red box. (C) After ASPECT data processing, the developer's view of the MALDI target plate map shows a high sensitivity of 0.96 (0.78 to 0.99, 95% CI) with only one false negative at spot D19. The specificity is slightly reduced to 0.83 (0.62 to 0.95, 95% CI) due to 4 false positives at spots C7, C12, C13, and C23. (D) The ROC curve shows that setting the CC threshold below 0.85 causes the sensitivity of ASPECT towards ethanol incubation detection to decrease. Increasing the CC threshold beyond 0.85 increases the false positive rate. (E) The mean spectra for the false positive spots C7, C12, C13, and C23 are plotted. These false positives show poor acquisition likely correlated to poor sample preparations or the random sampling laser missing key spots with concentrated analytes. (F) The spectra for the false negative at spot D19 shows the limited difference between untreated vs. ethanol incubated cells for protein profiling. **104**

Figure 5-5 The mean unprocessed metabolite profiling spectra (n=24) are plotted for (A) ethanol incubated cells and (B) untreated cells. There are changes in the intensities between the untreated versus ethanol incubated cells; however, the features remain the same except for a peak or two. (C) After ASPECT data processing, the developer's view of the MALDI target plate map shows a high sensitivity of 1 (0.85 to 1, 95% CI) in row L, and a high specificity of 0.96 (0.79 to 0.99, 95% CI) in row K with only one misclassification at spot K23. (D) The ROC curve shows that setting the CC threshold below 0.95 causes the sensitivity of ASPECT towards ethanol incubation detection to plummet. Increasing the CC threshold beyond 0.95 increases the false positive rate for ethanol incubation detection. (E) The spectra for the false positive spot at K23 is plotted. The baseline noise for K23 may be the most contributing factor to the misclassification due to a high CC threshold. **107**

Figure A-1 Schematics and images of the metal-insulator-metal (MIM)-type micro-hollow cathode discharge (MHCD) microplasma ion source with (A) details of the components of the MHCD assembly, and (B) a side-view and front-view of the device showing the plasma discharge in operation using 0.3 L min^{-1} high purity nitrogen. **126**

Figure A-2 Mass spectra of select target analytes acquired using DART and microplasma ion sources with nitrogen at 2.2 L min^{-1} and 0.5 L min^{-1}, respectively. The left column (DART) and right column (MHCD) with (A) background spectra, (B) methanol, (C) ethanol (5% IPA), (D) pure isopropanol, and (E) acetone. Mass spectrometer parameters were selected to prevent activation in the transfer ion optics: orifice lens 1 at 10 V, ring lens at 6 V, orifice lens 2 at 2 V, bias at 29 V, pusher bias voltage at –0.28 V. **129**

Figure A-3 Microplasma mass spectra for select target analytes acquired using N_2, Ar, and He as the plasma gases at optimized flow rates of 1.0, 0.3, and 0.5 L min–1, respectively and currents of 0.050 mA for all three. Compounds shown include (A) methanol, (B) ethanol, (C) isopropanol, and (D) acetone and show the positions and relative intensities of the $[M + H]^+$ (black triangles), $[M + NH_4]^+$ (black stars), and $[2 M + H]^+$ (black circles). Operation parameters set to same low-activation settings as in Figure 2: orifice lens 1 at 10 V, ring lens at 6 V, orifice lens 2 at 2 V, bias at 29 V, pusher bias voltage at –0.28 V. Spectra are an average of three trials collected from one total ion chromatogram taken over multiple capillary introductions of the volatile sample. **134**

Figure A-4 Peak areas for the $[2M + H]^+$ species for (A) methanol, (B) ethanol, (C) isopropanol, and (D) acetone using argon gas (first - purple), helium gas (second - orange), and nitrogen gas (third - green) for microplasma (left) and DART (right) at a series flow rates (L min^{-1}). Flow rates for each gas were set to 0.05, 0.15, 0.3, 0.5, and 1.0 L min^{-1} for MHCD and 0.15, 0.3, 0.5, 1.0, 1.4, 1.8, and 2.2 L min^{-1} for DART. Error bars are derived from the standard deviation of three experiments. **138**

Figure A-5 Microplasma power consumption by plasma gas type at a constant flow rate of 0.100 L min^{-1} with nitrogen highlighted in green (diamonds), argon highlighted in purple (squares), and helium gas in orange (triangles). **141**

Figure C-1 Illustration of the AP-DTIMS-Orbitrap MS instrument configuration. **164**

Figure C-2 Illustration of the DTIMS dual-gate modes of operation for ion selection and filtering. The corresponding MS TIC traces for gate **166**

#2 operations using gated mode and scan mode IM-MS acquisition schemes are shown.

Figure C-3 (A) Faraday response for 4 ppm w/v citric acid in 80:20 methanol/water for increasing DTIMS gate #1 pulse widths. (B) MS signal for 10 ppm w/v citric acid for increasing DTIMS gate #2 pulse widths over a 2.5 ms scan window. The gate #1 pulse width was 100 µs and the scan step was 25 µs. (C) MS signal for 10 ppm w/v citric acid for increasing DTIMS gate #2 scan step ratios over a 2.5 ms scan window. Gate #1 and #2 pulse widths were set equal at 100 µs. The number of data points per peak is plotted with each curve trace. For (A-C), DTIMS operation potential was -7000 V, drift gas temperature was 200 ˚C, and drift gas flow rate and exhaust pump rate were 2.0 L min^{-1} and 0.5 L min^{-1}, respectively. **170**

Figure C-4 Scan mode averaged mass spectrum and Faraday response (inset) for 100 ppm w/v of mixture of [Ser-Asp-Gly-Arg-Gly] and [Gly-Arg-Gly-Asp-Ser] peptide sequence isomers in 50:50 acetonitrile/water with 0.1% formic acid (A). All ion fragmentation HCD of the separated peptide isomers using a normalized collision energy of 20 V, where individual $[M+2H]^+$ species were isolated by ion mobility before fragmentation (B and C). Asterisks (*) denote identified sidechain fragments of serine, aspartic acid, and arginine. (DTIMS operation potential: 10,000 V, drift gas temperature: 220 ˚C, drift gas flow rate: 3.0 L min^{-1}, exhaust pump rate: 1.5 L min^{-1}; gate #1 and #2 pulse width: 150 µs; scan step: 50 µs). **174**

Figure C-5 AP-DTIMS-Orbitrap MS analysis for 100 ppm solution (w/v in 50:50 methanol/water) of 3 saccharides: D-(+)-melibiose, D-(+)-melezitose, and D-(+)-raffinose. Panels show the extracted mass spectra for each mixture component (A), the corresponding Faraday response (B), a map of the chemical space with *m/z* plotted as a function of drift time (C), and the extracted MS total ion chronograms (D). (gate #1 & #2: 200 µs, scan step: 50 µs; AGC: 5.0E+06, IT: 1000 ms, Resolution: 35,000). **176**

Figure D-1 a) The robot and laboratory environment integrated into the Actin GUI. The digitized object surface contour following the laser scan was also included (shown in red). (B) Laser scan start and end waypoints being programmed in Actin-MS to define the length of the scan. (C) A bell pepper being scanned by the laser. A block of foam was placed on the actual workbench to define a safety buffer zone. The scanned object contour appears to be “floating” in GUI **185**

space because it was placed on this foam piece, which was not digitized.

Figure D-2 (A) During RoSA-MS analysis, the robot docks the needle probe into an open port sampling interface (OPSI). (B) Schematic of the needle probe docked in the OPSI. Pressure from the spring-loaded probe against the annulus tubing maintains a sealed junction. The solvent flow between the annulus and the center capillary dissolves the material on the needle tip. The sealed fluidics system delivers the solubilized sample to the mass spectrometer. **189**

Figure D-3 (A) To evaluate the precision of the robot controlled by Actin, a 0.125 mm OD needle was programed to pierce the same location on a piece of paper after a random 3-waypoint arm movement. (B) For the first twenty cycles of piercing, the needle went through the paper creating a single hole 200 μm in diameter. From these measurements, the estimated deviation was calculated to be in the order of 200 μm -125 μm =75 μm, for an overall precision of 75 μm/2=37.5 μm (~40 μm). Following this experiment, the RoSA system was restarted to test experiment-to-experiment positioning robustness. The system was programmed to pierce the same location as in the previous experiment for an additional 20 cycles. In this case, it was observed that the system showed a offset that created a new hole ~300 μm away from the original location. (C) Several objects scanned by the laser scanner, (D) the obtained point cloud data revealing the laser scanner's precision in the x, y, z directions. **192**

Figure D-4 (A) Digitized surface mesh for a coffee cup. The red dot indicates the selected sampling point. (B) Photo showing the needle probe contacting the sample surface. (C) Mass spectrum obtained for the material detached by the probe and injected into the OPSI. **196**

Figure D-5 (A) Genuine artemether/lumefantrine antimalarial combination medicine blister pack being laser scanned. The relative abundances for artemether (m/z = 321, 619) (B) and various sugar-like compounds (m/z = 203, 205, and 365) (C) are plotted on the mesh surface. (D) Falsified antimalarial combination medicine blister pack being laser scanned, (E) and (F) show intensities for artemether (m/z = 321, 619) and various sugar ions (m/z = 203, 205, and 365) ions. The corresponding survey mass spectra are shown in (G) and (H). **198**

Figure D-6 (A) A hand that was sprayed with DEET holding a football. (B) Several locations on this football were analyzed by RoSA-MS. The summed peak area (m/z 192 + 214) for DEET ions was converted to a pseudo color scale for the specific coordinates sampled. The **200**

dashed lines indicate the approximate boundary of the fingers when touching the football surface. (C) Full scan mass spectrum obtained from the coordinates where the thumb contacted the surface.

Figure D-7 (A) A spot plate following a dry down condensation reaction involving amino acids and hydroxy acids to form mixed amide/ester-linked oligomers, known as depsipeptides. The surface of the wells was analyzed by RoSA-MS to detect product formation. The dashed line in the inset indicates the sampled transect. (B) Seven independent surface points were probed, and the abundances of the g′GAg′ depsipeptide, one of the reaction products, mapped on the mesh representation of the surface. (g′, glycolic acid; G, glycine; A, alanine.) (C) Surface abundance for leucine, one of the starting reagents. (D) Surface abundance ratio between the g′GAg′ depsipeptide and leucine. **203**

LIST OF SYMBOLS AND ABBREVIATIONS

%	Percentage
°C	Degrees Celsius
µL	Microliter
µm	Micrometer
µs	Microsecond
3D	Three-dimensional
9AA	9-aminoacrdine
A	Ampere
AC	Alternating current
ACA	Amoxicillin clavulanic acid
ACN	Acetonitrile
ACT	Artemisinin-based combination therapies
AeroFAPA	Aerosol flowing atmospheric-pressure afterglow
Aero-VaPI	Aerosol vacuum-assisted plasma ionization
AGC	Automatic gain control
AIF	All ion fragmentation
AP	Atmospheric pressure
API	Active pharmaceutical ingredient
arb.	Arbitrary
ART	Artesunate
ASAP	Atmospheric solids analysis probe
SPECT	Acceleration Screening for the Protection and Efficacy of Cellular Therapies

AZITH	Azithromycin
CA	Clavulanic acid
CC	Correlation coefficient
CE	Capillary electrophoresis
Cells/mL	Cells per milliliter
CI	Confidence interval
cm	Centimeters
cm s^{-1}	Centimeters per second
cm^{-1}	Inverse centimeters
Da	Dalton
DART	Direct analysis in real time
DBD	Dielectric barrier discharge
DC	Direct current
DEET	N,N-diethyl-meta-toluamide
DESI	Desorption electrospray ionization
DHA	Dihydroartemisinin
DHB	2,5-dihydroxybenzoic acid
DTIMS	Drift tube ion mobility spectrometry
ECLS	Environmental control and life support
EIC	Extracted ion chronogram
EP	Evaluation pharmacy
ESI	Electrospray ionization
ETC	Electrothermal vaporization
eV	Electron volts
FAPA	Flowing atmospheric-pressure afterglow

FCM	Field collected medicines
FDA	Food and Drug Administration
FIGAERO	Filter inlet for gases and aerosols
FTIR	Fourier transform infrared
FWHM	Full width half max
GC	Gas chromatography
GMP	Good manufacturing practices
GMS	Greater Mekong sub-region
GUI	Graphical user interface
h	Hour
HCCA	α-Cyano-4-hydroxycinnamic acid
HCD	High-energy collision dissociation
HESI	Heated electrospray ionization
HRToF-CIMS	High-resolution time-of-flight chemical ionization-mass spectrometer
ICR	Ion cyclotron resonance
ID	Inner diameter
IM	Ion mobility
IM-MS	Ion mobility-mass spectrometry
in.	Inch
ISS	International Space Station
IT	Injection time
kHz	Kilohertz
kV	Kilovolts
L h^{-1}	Liter per hour
LAESI	Laser ablation-electrospray ionization

lbs in^{-1}	Pounds per inch
LC	Liquid chromatography
LESA	Liquid extraction surface analysis
LMJ-SSP	Liquid microjunction surface sampling probe
LTP	Low temperature plasma
m s^{-1}	Meters per second
m/z	Mass-to-charge ratio
mA	Milliampere
MALDESI	Matrix-assisted laser desorption electrospray ionization
MALDI	Matrix-assisted laser desorption ionization
mbar	Millibar
MeOH	Methanol
mg	Milligram
MHCD	Micro hollow cathode discharge
MIM	Metal-insulator-metal
MIR	Mid-infrared
mL min^{-1}	Milliliters per minute
mM	Millimolar
mm	Millimeter
MS	Mass spectrometry
ms	Milliseconds
MSC	Mesenchymal stromal cells
MSI	Mass spectrometry imaging
MΩ	Megaohms
n	Number

NCE	Normalized collision energy
ng	Nanogram
NIR	Near-infrared
nm	Nanometer
OD	Outer diameter
OFLO	Ofloxacin
OPSI	Open port sampling interface
P	Piperaquine
PAD	Paper analytical devices
PBS	Phosphate buffered solution
pg	Picogram
PMS	Post-market surveillance
ppb	Part-per-billion
ppm	Part-per-million
PRM	parallel reaction monitoring
PTFE	polytetrafluoroethylene
Py-GC-MS	Pyrolysis gas chromatography-mass spectrometry
pyro-VaPI	Pyrolysis vacuum-assisted plasma ionization
RDT	Rapid diagnostic tests
rf	Radio frequency
RIP	Reactive ion population
RMTF	Regional Malaria and Communicable Disease Trust Fund
ROC	Receiver operating characteristic
RoSA	Robotic surface analysis
Rp	Resolving power

s	Seconds
SF	Substandard or falsified
SIM	Simulated medicines
SIMS	Secondary ion mass spectrometry
SLM	Standard liters per minute
SM	Sulfamethoxazole
SSM	Sample set of medicines
SWEG	Spacecraft water exposure guideline
TFA	Trifluoroacetic acid
TM	Trimethoprim
TOF	Time-of-flight
TWIMS	Traveling wave ion mobility spectrometry
UPLC	Ultraperformance liquid chromatography
V	Volts
Vcm^{-1}	Volt per centimeter
VaPI	Vacuum assisted plasma ionization
VOA	Volatile organic analyzer
VUV	Vacuum ultraviolet
W	Watt
WHO	World Health Organization

SUMMARY

The development of new chemical analysis tools and the assessment of current technologies help explore new realms of chemistry and ensure the quality of chemical products. Mass spectrometry is a powerful analytical tool that measures the mass-to-charge ratio of ionized analytes that can explore and ensure the quality of various chemistries. In **Part 1** of this thesis, new tools were constructed for Vacuum-assisted Plasma Ionization (VaPI) for rapid ionization of analytes to measure aerosol chemistries and pyrolyzed polymers in real time. In **Part 2** of this thesis, portable mass spectrometry was evaluated for the rapid screening of small molecule pharmaceuticals. Matrix assisted laser desorption ionization (MALDI) mass spectrometry was also developed to rapidly assess the quality of cellular therapies.

Chapter 1 begins with introducing the major concepts behind ambient plasma ionization. The advantages and disadvantages of various plasma ionization sources are discussed. Many of the drawbacks found in these plasma ionizations sources include the loss of ions due to the fluid dynamics of the plasma stream. VaPI was developed to combat these fluid dynamic problems and later chapters in this thesis will build upon the plasma source for new applications. One of the major upgrades to the VaPI source was coupling it to an ion mobility mass spectrometer. The second part of **Chapter 1** introduces the fundamentals of ion mobility spectrometry. Ion mobility offers an orthogonal separation technique to mass spectrometry based upon an ion's collisional cross section that can help separate isomers. Finally, the third part of **Chapter 1** discusses the current challenges combating poor quality pharmaceuticals. The problems small molecule medicines

currently face and how they are applicable to new treatments such as cellular therapies are summarized.

In **Part 1** of this thesis, **Chapter 2** developed VaPI into a real time analysis tool for aerosol chemistries known as aero-VaPI. The aero-VaPI source was developed to analyze pre-biotic aerosol chemistries. The VaPI source was coupled to two key technologies. First, the VaPI source was coupled in parallel to a scanning mobility particle size analyzer to measure the diameters of aerosols key to understanding their underlying chemistries. Second, the VaPI source was built to connect to the ambient pressure interface of the Waters Synapt G2s, an ion mobility mass spectrometer. The main benefit of aero-VaPI over other commercial aerosol analyzers is the soft ionization source that allows for the analysis of intact analytes and the capability to separate intact isomers with different ion mobilities. The capabilities of aero-VaPI were demonstrated with lipids and aerosolized dry-down reactions to simulate pre-biotic chemistries. Simultaneous acquisition of the aerosol diameter, ion mobility, and m/z illustrates the breadth of chemical information that can be acquired in real time for pre-biotic aerosolized chemical reactions using aero-VaPI.

Chapter 3 details the construction of a pyrolysis device for VaPI (pyro-VaPI) used for the analysis of pyrolyzed polymers. Mechanistic insight into pyrolyzed polymers can lead to better identifications and property understandings for polymers. Other pyrolysis mass spectrometers on the market either harshly fragments the ions with electron ionization, have additional sample preparations steps, or do not have the capability to conduct ion mobility separations. A home-built pyrolysis device that could pyrolyze samples as high as 900°C was constructed and coupled to the VaPI-Synapt G2s platform. The ability to regulate the pyrolysis device's temperature controls the analyte's volatilities

which can be measured orthogonally to the ion mobility and m/z information collected by the Synapt G2s. Nylons were used to evaluate pyro-VaPI as it is a common well-studied polymer. Unique isobaric species of pyrolyzed nylons were discovered in the ion mobility region once a certain temperature was reached. The separated isobars were fragmented post-mobility to confirm the species were nylons. Each nylon isobaric ion mobility peak fragmented differently under the same collision energy suggesting different bond strengths. The combination of measurements in volatilities, collision cross section, and m/z show how new potential molecular interactions of pyrolyzed species can be discovered with pyro-VaPI.

Part 2 of this thesis begins with **Chapter 4** that evaluates 12 portable screening devices alongside each other for small molecule pharmaceutical screening in a controlled laboratory setting. Middle to low income nations with poor regulation face illicit or poorly manufactured pharmaceuticals. These poor quality pharmaceuticals can include medicines with no active pharmaceutical ingredient (API), the wrong API, or inadequate amounts of API. Portable screening tools can assist inspectors to find poor quality medicines; however, there is little literature for regulators comparing more than one device side by side. In this study, 12 devices ranging from a single use colorimetric assay, to Raman spectrometers, and to a portable mass spectrometer such as the Waters QDa were evaluated together. Each device tested as many simulated and field collected medicines as they were capable of. Advantages and disadvantages for each device were detailed including setup, required consumables, ease of use, and performance. Overall, all 12 devices could detect medicines with none or the wrong API. Medicines with the correct but reduced concentrations of API were more difficult to detect. Spectroscopy tools and single use disposable assays had low

sensitivities towards reduced API concentration medicines. Quantitative devices such as the QDa had higher sensitivities for reduced API concentration medicines, but reduced specificities. Although the QDa had one of the highest sensitivities in the study, further refinement of the consumables and instrument are required for resource limited field deployment.

Chapter 5 explores the use of MALDI for the rapid screening of cellular therapies. These cellular therapies such as stem cells are increasingly becoming popular as they offer revolutionary treatments in regenerative medicine. Due to their popularity, many of the poor quality problems that impact small molecule medicines are affecting cellular therapies such as poor quality or illicit products. Regulators need rapid screening tools for the pre- and post-market surveillance of cellular therapies. MALDI is already clinically approved to rapidly speciate bacteria. The high throughput capabilities, simple consumables, and simple protocols of MALDI are ideal as a rapid screening tool. To accelerate the MALDI pipeline towards cellular therapy screening, the Accelerated Screening for the Protection and Efficacy of Cellular Therapies (ASPECT) workflow was developed to rapidly process samples and receive an automated easy to read output for the end user. Custom scripts were written to rapidly extract and process the MALDI data. A MALDI target plate map at the end of the script would indicate to the end user which samples passed and failed. In a preliminary data set, untreated and ethanol incubated mesenchymal stromal cells were compared using lipid, metabolite, and lipid profiling. Overall, lipid profiling had the most sensitivity towards disruption of the cellular membrane through ethanol incubation. Although protein and metabolite profiling had less sensitivity toward ethanol incubated cells, ASPECT may be improved with better algorithms in the script.

Chapter 6 summarizes the conclusions drawn from the main chapters of this thesis work, with the impact and possible future work also discussed.

The **Appendices** describe various projects that were in parallel with this thesis work. **Appendix A** evaluates a microplasma ionization source for air and water monitoring on environments like the International Space Station (ISS). The power consumption, gas consumption, and ionization potential were compared between various gases and a commercial plasma ionization source. Overall, the microplasma source is very resource efficient compared to the commercial plasma source. Argon or nitrogen gas would have sufficient ionization potential and is renewable onboard the ISS compared to helium. **Appendix B** summarizes the collection of projects that evaluated screening devices for poor quality small molecule medicines. A literature review was conducted on 41 devices, of which 12 were selected for the laboratory phase described in **Chapter 4.** A selection of 6 devices from the laboratory phase were evaluated by pharmacy inspectors in Laos to determine their usability and required training. The devices in the field phase were then cost analyzed to estimate expenses compared to their overall effectiveness. Finally, an article summarized the lessons learnt and future steps for the research collection.

Appendix C evaluates coupling atmospheric drift tube ion mobility to an Orbitrap high resolution mass spectrometer. Various settings such as ion mobility gating schemes and Orbitrap parameters were assessed to achieve maximum mobility resolution and signal intensity. Isobaric peptides and sugar isomers were successfully resolved and confirmed through high-energy collision dissociation experiments. Finally, **Appendix D** describes the construction of a robotic sampling platform to acquire 3D data for mass spectrometry. The robot would probe a surface, record the location of the probe, move the probe to the

sampling interface of the mass spectrometer, and finally the mass spectrum of the adhered compounds on the probe would be recorded. 3D chemical maps were created for several samples, including a comparison between a genuine and falsified pack of anti-malarial medicines.

CHAPTER 1. INTRODUCTION

1.1 Abstract

The development of new chemical analysis tools and the assessment of current technologies can help rapidly explore new realms of chemistry and quickly ensure the quality of chemical products. This chapter is divided into three parts. The first part provides an overview of ambient plasma ionization mass spectrometry. Ambient plasma ionization directly ionizes samples without the need for complex solvents or matrices, a desired trait for rapid screening applications. The second part summarizes ion mobility, a tool in mass spectrometry that can help rapidly separate isomers in the gas phase on the millisecond time scale. Ion mobility provides valuable orthogonal collisional cross section data in mass spectrometry compared to measuring the *m/z* alone. Chapters 2 and 3 in this dissertation will combine ambient plasma ionization and ion mobility for mass spectrometry in aerosol and polymer analysis. The third part of this chapter introduces a brief overview of poor quality medicines. Since the dawn of modern medicine, pharmaceuticals have been falsified or poorly manufactured impacting the health of patients. Chapters 4 and 5 of this dissertation go in depth into the evaluation and development of tools for the rapid quality screening of small molecule pharmaceuticals and biopharmaceuticals.

1.2 Principles of Ambient Plasma Ionization Mass Spectrometry

In mass spectrometry, softly ionizing analytes is most desired. Soft ionization allows for the analysis of simplified spectra so additional experiments can be conducted on the intact precursor ions for further identification of the analyte. The two most widely used

sources for soft ionization include electrospray ionization (ESI) and matrix-assisted laser desorption ionization (MALDI) [1–3]. ESI, MALDI, and many of their derivatives require significant sample preparation or solvents. ESI requires the analytes to be dissolved in solution and MALDI requires samples to be mixed with a matrix and dried prior to ionization [4]. Ambient plasma ionization is a soft ionization technique with little to no sample preparation required that can also minimize solvent use.

The earliest publication using a plasma to softly ionize samples for ambient pressure mass spectrometry was in 2005 with the Direct Analysis in Real Time (DART) source [5]. DART operates similarly to many other ambient plasma ionization sources later developed (Figure 1-1). First, the plasma is generated within DART by flowing a gas such as helium through a direct current point to plane electrical discharge. Metastables of the gases are created as they interact with the electrical discharge. As these metastables exit the ion source, they interact with the ambient atmosphere to create a variety of reactive ion species. One of the most widely known reactive ion species in helium plasmas emerge from the Penning ionization of water in the ambient atmosphere to create protonated water clusters shown in the scheme below.

$$He^* + nH_2O \rightarrow He + (nH_2O)_{n-1}H^+ + OH^-$$

$$M + (nH_2O)_{n-1}H^+ \rightarrow [M+H]^+ + nH_2O$$

These protonated water clusters interact with and ionize the analyte before entering the mass spectrometer [6]. Other reactive ion species are created in helium plasmas as it interacts with the ambient atmosphere such as N_2^+, but to a lesser extent [7]. Changing the plasma gas from helium to nitrogen also creates some $[M+H]^+$ ions through nitrogen

metastable Penning ionization, but the generation of $[M+NH_4]^+$ through the scheme below is generally more prevalent [8].

$$N_2^*/N^* + NH_3 \rightarrow N_2/N + NH_3^+ + e^-$$

$$NH_3^+ + H_2O \rightarrow HO^- + NH_4^+$$

$$M + NH_4^+ \rightarrow [M + NH_4]^+$$

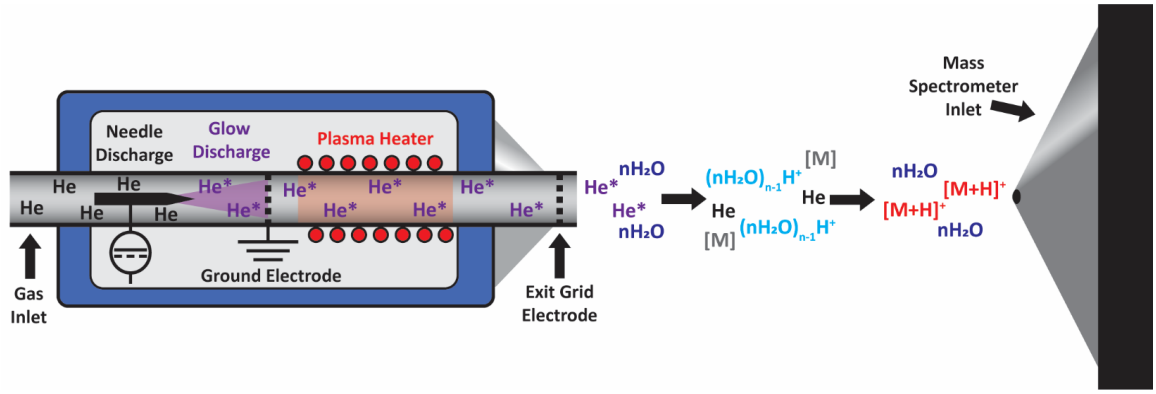

Figure 1-1 Diagram of how DART operates and protonates volatilized analytes in positive ion mode. Helium gas is fed through a glow discharge that creates metastable species. These metastables interact with the ambient atmosphere as they exit the DART source to create a variety of reactive ion species. One of the reactive ion species created are protonated water clusters that donate their proton when interacting with the gas-phase analyte [M].

One aspect of ambient plasma ionization that allows for minimal sample preparations is the ability to desorb analytes with the plasma. Gases and volatile chemicals can be immediately introduced in front of the plasma stream for ionization. Solid or less volatile samples introduced into the plasma stream can be desorbed through various means. Ion sources like DART can heat the plasma stream to further volatize the analytes on the surfaces with no need to extract or dilute the analyte [9]. Placing the sample on an external heater can help further vaporize or thermally desorb samples into DART's plasma stream [9–12]. Laser ablation has also been coupled to DART to ablate samples into the plasma stream without the need of a matrix layer compared to ambient pressure MALDI [13, 14].

DART is a widely used commercial ion source for ambient plasma ionization, but many others are available with different configurations. Dielectric barrier discharge (DBD) plasma ion sources operate using an alternating current to create the plasma. The first DBD source reported for mass spectrometry used a microscope slide with the sample mounted to the surface of the slide as the dielectric barrier between two electrodes [15]. The low temperature plasma (LTP) probe is an example of a DBD plasma source that acts as a plasma gun similarly to DART. The LTP probe can operate at significantly lower temperatures than DART, making it possible to analyze more thermally labile molecules [16]. LTP's construction is simple and small enough to be coupled to a backpack mass spectrometer [17]. DBD sources have also been configured to maximize the sensitivity for volatile samples by pulling the analytes into an enclosed junction with the plasma stream directly connected to the ambient pressure interface of the mass spectrometer [18]. Other variants of DBD ion sources also exist. The plasma-assisted desorption ionization source is a low temperature AC plasma probe without the use of a dielectric barrier [19]. If a

higher temperature and higher density plasma stream is required, microwave-induced plasma desorption/ionization is another DBD like source that can be utilized [20].

As widely used as the previously mentioned ambient plasma ionization sources are, high resource requirements and low sensitivity reduce rapid screening applications. For DART and similar sources, the fluid dynamics of a high-volume gas flow can push analytes away from the inlet of the mass spectrometer reducing sensitivity [21]. The high plasma gas volume can also overwhelm the vacuum on the ambient pressure interface of the mass spectrometer. Modifications to the ambient pressure interface of the mass spectrometer such as the VAPUR™ gas ion separator tube can help remove the excess plasma gas, but may inadvertently pull analytes away reducing sensitivity [22]. Wasting plasma gas that does not ionize analytes increase resource requirements and reduces the portability of plasma sources. Helium is the most widely used ambient plasma ionization gas due to its high ionization potential, but it is a scarce resource that further reduces portability [23].

Several efforts have been made to minimize the resource requirements for ambient plasma ionization to make them more appealing for rapid low resource screening applications. Switching from resource limited helium to more plentiful gases like pure nitrogen, pure argon, and doping gases like argon with hydrogen to boost ionization efficiency have been made [16, 24, 25]. To reduce electrical and gas consumption, miniaturizing the plasma source to the micron level diameter outlet with a micro hollow cathode discharge (MHCD) has been built [26]. To minimize the loss of analytes due to the fluid dynamic of the plasma stream, the vacuum assisted plasma ionization (VaPI) source was developed. VaPI is configured similarly to the previously mentioned DBD source optimized for volatile analysis [18]; however the VaPI has a much larger and more

modular sampling junction allowing for the coupling of other ablation techniques such as with a laser [27]. In this thesis, the capabilities and applications of VaPI will be further expanded for aerosol and polymer analysis when coupled to ion mobility in Chapters 2 & 3. The MHCD source will also be evaluated as a more resource efficient plasma ionization source for the International Space Station in Appendix A.

1.3 Principles of Ion Mobility Spectrometry

In mass spectrometry, separating different classes of analytes prior to the mass analyzer allows for the acquisition of multidimensional data. Gas chromatography (GC) and liquid chromatography (LC) are well established pre-ionization separation techniques. These chromatographic techniques separate analytes based on their affinity towards a stationary phase versus the gas or liquid mobile phase. Analytes with higher affinities towards the stationary phase remain longer and are detected in later mass spectral scans than analytes with low affinities. These elution times off the stationary phase are a second dimension to the analyte's mass-to-charge that may be critical for the detection of isomers that are inseparable in the mass analyzer alone. Although widely used, GC and LC require considerable consumables such as solvents and stationary phase columns or capillaries. Chromatography separations of a single sample can take on the order of minutes as well [28–30]. Although techniques like ultra-performance liquid chromatography have helped improve throughput, large consumable requirements are not ideal for rapid screening applications [31]. Capillary electrophoresis (CE) is an alternative pre-ionization separation technique that can be faster and simpler than GC and LC. CE separates analytes based on their size and charge through a buffer solution with an applied voltage. Larger analytes with fewer charges travel slower in CE than smaller and more charged species. Although

basic CE does not require a stationary phase, it still requires solvents and capillaries that need replacement [32, 33].

Ion mobility offers rapid post-ionization separation of analytes in a fraction of the time it takes for traditional chromatography or CE. The measure of the mobility of ions through the ambient atmosphere began as early as 1906 [34], with a drift tube similar to that of modern configurations being developed in 1928 [35]. The basic configuration for drift tube ion mobility as shown in Figure 1-2 has minimally changed. First, a packet of ions is injected into the entrance of the drift cell. An electric field suspends the ions in the central axis of the drift cell and drives them towards the end where the detector is located. The drift cell is held at ambient or low gas pressures. As the ions travel through the drift cell, the analytes collide with neutral gases. Ions with more collisions travel slower in the drift cell. Isomers can be separated if their molecular arrangement changes the surface area of the molecule. Larger surface area molecules measured in terms of a collisional cross section encounter more collisions than smaller molecules and travel slower in the drift tube. At the end of the drift cell, the separated analytes enter the detector [36].

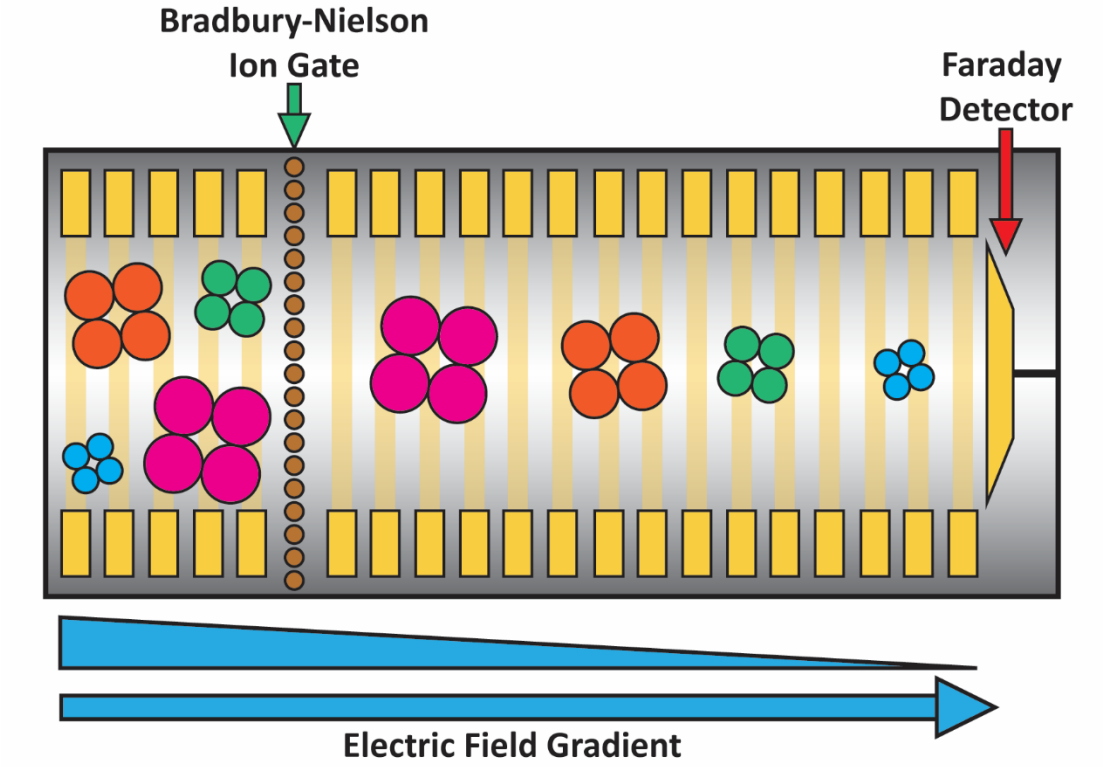

Figure 1-2 Diagram of a standalone drift tube. As the Bradbury-Nielson ion gate opens and closes, the electric field gradient pushes a packet of ions through a reduced or ambient pressure drift cell. The ions collide with neutral gases in the drift cell. Ions with larger collisional cross sections collide with more drift gases and travel slower in the drift tube. As a result, ions are separated based on their collisional cross sections. At the end of the drift tube, the ion collides with a detector such as a Faraday plate. The change in time between the detection event and when the ion gate was opened is the ion's drift time. The drift time is correlated to the ion's collisional cross section.

To best describe the factors that contribute to an analyte's ion mobility, one of the most widely used equations for a drift tube setup is the Mason-Schamp equation:

$$K = \frac{3}{16}\sqrt{\frac{2\pi}{\mu kT}}\frac{Q}{n\Omega}$$

In this equation: K is the analyte's ion mobility, μ is the reduced mass of the ion and neutral molecule mass, k is the Boltzmann constant, T is the gas temperature, Q is the charge, n is the density of drift gas molecules which is directly proportional to gas pressure, and Ω is the average collisional cross section. After an analyte's mobility is measured, the collisional cross section can be calculated from the known conditions of the drift tube and be an identifier for the molecule [37].

One of the simplest is a standalone drift tube described above with a Faraday plate as the detector (Figure 1-2). This standalone configuration is commonly used for portable explosives detection at security checkpoints such as airports [34]. Limited chemical information can be gathered with a standalone ion mobility spectrometer and analytes may be unresolved. Replacing the Faraday plate with a mass spectrometer can give orthogonal collisional cross section and mass to charge information about an analyte. The first reported ion mobility mass spectrometer was developed at Georgia Tech in 1962 by E.W. McDaniel [38]. Since then, many variants of ion mobility mass spectrometers have been developed and commercialized [39].

The Synapt series of mass spectrometers from Waters utilizes traveling wave ion mobility spectrometry (TWIMS) [40]. Unlike a traditional drift cell with a static electric field gradient, TWIMS pulses the voltages across the drift cell to create an electric field

wave from one end of the cell to the other. The ions are pushed by the electric field waves and collide with neutral gases in the reduced pressure drift cell. Smaller ions travel with the electric field wave better than larger ions that resists the wave's force. This separates isomers with different collisional cross sections before entering the time of flight mass analyzer. Although having TWIMS at the center of the mass spectrometer lowers the possible mobility resolution due to gas pressure limits set by the other high vacuum chambers of the instrument, this configuration offers many other capabilities. The addition of a quadrupole mass filter before the TWIMS drift cell allows for isolation of a single mass to charge feature for further investigation. The Synapt can also fragment ions before or after ion mobility separations. Pre-mobility fragmentation can help gather collisional cross section measurements about different fragments of the precursor ion. Post-mobility separations can help confirm if species with various drift times are arranged in different structures [41, 42].

The capabilities of a TWIMS mass spectrometer can help gather rich datasets for rapid sampling platforms. Due to the difficulty of pre-ionization separation for ambient plasma sources, the addition of ion mobility can help gather additional orthogonal collisional cross section data to distinguish isomers. With the added capabilities of fragmenting ions before or after the mobility region, higher confidence identifications can be achieved compared to a mass analyzer alone. In chapters 2 and 3 of this thesis, I show how by combining the capabilities of TWIMS with VaPI one can provide rapid and sensitive data collection to discover new potential chemistries.

1.4 Current Quality Problems with Pharmaceuticals

To maintain the safety and efficacy of pharmaceuticals, good manufacturing practices (GMP) dictate constant inspection of the ingredients and final product. GMP are empowered by thorough standardization and enforcement. Monographs established by agencies such as the United States Pharmacopeia ensure the accurate quality assessment of pharmaceuticals [43]. Enforcement agencies such as the Food and Drug Administration help police the market for poor quality medications created from poor GMP or illicit sales [44]. When the resources for these organizations are limited, patients face the chance of receiving poor quality medicines. These poor quality medicines can hurt patients by providing little to no treatment for their disease, creating distrust with the health system, and increasing anti-microbial resistance for anti-infectives with low active ingredient concentrations [45]. Low to middle income nations face the brunt of poor quality medicines due to the lack of resources available for standardized equipment and enforcement. Thirty percent of the world's medicine regulatory authorities have no drug regulation or a capacity that hardly functions. As a result, The World Health Organization estimates that 1 in 10 medicines is poor quality in low to middle income nations [46]. New portable and rapid screening tools are required to make GMP and market surveillance more feasible in resource-stricken nations.

Market surveillance is a key tool to prevent the sale of poor quality medicines to patients. Pharmacy inspections help ensure proper storage and distribution of medicines; however, simple paperwork and visual inspections of the medicines may miss various poor quality medicines. Substandard medicines may contain low active ingredient concentrations that the human eye alone cannot distinguish. Illicit manufacturers can replicate key complicated packaging designs such as holographic stickers to elude simple

visual inspections. Sugar pills with acetaminophen have been sold by illicit manufacturers to even elude the patients themselves into thinking they are getting treated for the disease [47]. To compliment visual pharmacy inspections, many tools including mass spectrometry have been developed to detect poor quality medicines. Chapters 4 and Appendix B of this thesis details a multiphase international project to test out various portable technologies, including portable mass spectrometry, to assess the quality of small molecule medicines such as anti-biotics and anti-malarials. Chapter 5 of this thesis explores using MALDI mass spectrometry for the rapid screening of poor quality cellular therapies, the next generation of pharmaceuticals.

1.5 References

1. Wong, S.F., Meng, C.K., Fenn, J.B.: Multiple charging in electrospray ionization of poly(ethylene glycols). J. Phys. Chem. 92, 546–550 (1988). https://doi.org/10.1021/j100313a058

2. Karas, M., Bachmann, D., Hillenkamp, F.: Influence of the Wavelength in High-Irradiance Ultraviolet Laser Desorption Mass Spectrometry of Organic Molecules. Anal. Chem. 57, 2935–2939 (1985). https://doi.org/10.1021/ac00291a042

3. Karas, M., Hillenkamp, F.: Laser Desorption Ionization of Proteins with Molecular Masses Exceeding 10 000 Daltons, https://pubs.acs.org/sharingguidelines, (1988)

4. El-Aneed, A., Cohen, A., Banoub, J.: Mass Spectrometry, Review of the Basics: Electrospray, MALDI, and Commonly Used Mass Analyzers. Appl. Spectrosc. Rev. 44, 210–230 (2009). https://doi.org/10.1080/05704920902717872

5. Cody, R.B., Laramée, J.A., Durst, H.D.: Versatile new ion source for the analysis of materials in open air under ambient conditions. Anal. Chem. 77, 2297–2302 (2005). https://doi.org/10.1021/ac050162j

6. Song, L., Gibson, S.C., Bhandari, D., Cook, K.D., Bartmess, J.E.: Ionization Mechanism of Positive-Ion Direct Analysis in Real Time: A Transient Microenvironment Concept. Anal. Chem. 81, 10080–10088 (2009). https://doi.org/10.1021/ac901122b

7. Chan, G.C.-Y., Shelley, J.T., Wiley, J.S., Engelhard, C., Jackson, A.U., Cooks, R.G., Hieftje, G.M.: Elucidation of Reaction Mechanisms Responsible for

Afterglow and Reagent-Ion Formation in the Low-Temperature Plasma Probe Ambient Ionization Source. Anal. Chem. 83, 3675–3686 (2011). https://doi.org/10.1021/ac103224x

8. Song, L., Chuah, W.C., Lu, X., Remsen, E., Bartmess, J.E.: Ionization Mechanism of Positive-Ion Nitrogen Direct Analysis in Real Time. J. Am. Soc. Mass Spectrom. 29, 640–650 (2018). https://doi.org/10.1007/s13361-017-1885-7

9. Forbes, T.P., Sisco, E., Staymates, M., Gillen, G.: DART-MS analysis of inorganic explosives using high temperature thermal desorption. Anal. Methods. 9, 4988–4996 (2017). https://doi.org/10.1039/c7ay00867h

10. Dwivedi, P., Gazda, D.B., Keelor, J.D., Limero, T.F., Wallace, W.T., Macatangay, A. V., Fernández, F.M.: Electro-thermal vaporization direct analysis in real time-mass spectrometry for water contaminant analysis during space missions. Anal. Chem. 85, 9898–9906 (2013). https://doi.org/10.1021/ac402365k

11. Sisco, E., Forbes, T.P., Staymates, M.E., Gillen, G.: Rapid analysis of trace drugs and metabolites using a thermal desorption DART-MS configuration. Anal. Methods. 8, 6494–6499 (2016). https://doi.org/10.1039/c6ay01851c

12. Marić, M., Marano, J., Cody, R.B., Bridge, C.: DART-MS: A New Analytical Technique for Forensic Paint Analysis. Anal. Chem. 90, 6877–6884 (2018). https://doi.org/10.1021/acs.analchem.8b01067

13. Fowble, K.L., Teramoto, K., Cody, R.B., Edwards, D., Guarrera, D., Musah, R.A.: Development of "Laser Ablation Direct Analysis in Real Time Imaging" Mass Spectrometry: Application to Spatial Distribution Mapping of Metabolites Along the Biosynthetic Cascade Leading to Synthesis of Atropine and Scopolamine in Plant Tissue. Anal. Chem. 89, 3421–3429 (2017). https://doi.org/10.1021/acs.analchem.6b04137

14. Fowble, K.L., Musah, R.A.: Simultaneous imaging of latent fingermarks and detection of analytes of forensic relevance by laser ablation direct analysis in real time imaging-mass spectrometry (LADI-MS). Forensic Chem. 15, (2019). https://doi.org/10.1016/j.forc.2019.100173

15. Na, N., Zhao, M., Zhang, S., Yang, C., Zhang, X.: Development of a Dielectric Barrier Discharge Ion Source for Ambient Mass Spectrometry. J. Am. Soc. Mass Spectrom. 18, 1859–1862 (2007). https://doi.org/10.1016/j.jasms.2007.07.027

16. Harper, J.D., Charipar, N.A., Mulligan, C.C., Zhang, X., Cooks, R.G., Ouyang, Z.: Low-Temperature Plasma Probe for Ambient Desorption Ionization. Anal. Chem. 80, 9097–9104 (2008). https://doi.org/10.1021/ac801641a

17. Hendricks, P.I., Dalgleish, J.K., Shelley, J.T., Kirleis, M.A., McNicholas, M.T., Li, L., Chen, T.C., Chen, C.H., Duncan, J.S., Boudreau, F., Noll, R.J., Denton, J.P., Roach, T.A., Ouyang, Z., Cooks, R.G.: Autonomous in situ analysis and real-time

chemical detection using a backpack miniature mass spectrometer: Concept, instrumentation development, and performance. Anal. Chem. 86, 2900–2908 (2014). https://doi.org/10.1021/ac403765x

18. Chen, L.C., Yu, Z., Furuya, H., Hashimoto, Y., Takekawa, K., Suzuki, H., Ariyada, O., Hiraoka, K.: Development of ambient sampling chemi/chemical ion source with dielectric barrier discharge. J. Mass Spectrom. 45, 861–869 (2010). https://doi.org/10.1002/jms.1772

19. Ratcliffe, L. V., Rutten, F.J.M., Barrett, D.A., Whitmore, T., Seymour, D., Greenwood, C., Aranda-Gonzalvo, Y., Robinson, S., McCoustra, M.: Surface analysis under ambient conditions using plasma-assisted desorption/ionization mass spectrometry. Anal. Chem. 79, 6094–6101 (2007). https://doi.org/10.1021/ac070109q

20. Zhan, X., Zhao, Z., Yuan, X., Wang, Q., Li, D., Xie, H., Li, X., Zhou, M., Duan, Y.: Microwave-induced plasma desorption/ionization source for ambient mass spectrometry. Anal. Chem. 85, 4512–4519 (2013). https://doi.org/10.1021/ac400296v

21. Harris, G.A., Fernández, F.M.: Simulations and Experimental Investigation of Atmospheric Transport in an Ambient Metastable-Induced Chemical Ionization Source. Anal. Chem. 81, 322–329 (2009). https://doi.org/10.1021/ac802117u

22. Zhou, M., McDonald, J.F., Fernández, F.M.: Optimization of a Direct Analysis in Real Time/Time-of-Flight Mass Spectrometry Method for Rapid Serum Metabolomic Fingerprinting. J. Am. Soc. Mass Spectrom. 21, 68–75 (2010). https://doi.org/10.1016/j.jasms.2009.09.004

23. Olafsdottir, A.H., Sverdrup, H.U.: Assessing the Past and Future Sustainability of Global Helium Resources, Extraction, Supply and Use, Using the Integrated Assessment Model WORLD7. Biophys. Econ. Sustain. 5, 3 (2020). https://doi.org/10.1007/s41247-020-00072-5

24. Chan, G.C.Y., Shelley, J.T., Jackson, A.U., Wiley, J.S., Engelhard, C., Cooks, R.G., Hieftje, G.M.: Spectroscopic plasma diagnostics on a low-temperature plasma probe for ambient mass spectrometry. J. Anal. At. Spectrom. 26, 1434–1444 (2011). https://doi.org/10.1039/c0ja00230e

25. Ellis, W.C., Lewis, C.R., Openshaw, A.P., Farnsworth, P.B.: The Effects of Added Hydrogen on Noble Gas Discharges Used as Ambient Desorption/Ionization Sources for Mass Spectrometry. J. Am. Soc. Mass Spectrom. 27, 1539–1549 (2016). https://doi.org/10.1007/s13361-016-1432-y

26. Symond, J.M., Galhena, A.S., Fernández, F.M., Orlando, T.M.: Microplasma discharge ionization source for ambient mass spectrometry. Anal. Chem. 82, 621–627 (2010). https://doi.org/10.1021/ac901964m

27. Keelor, J.D., Farnsworth, P.B., L. Weber, A., Abbott-Lyon, H., Fernández, F.M.: Multimodal Vacuum-Assisted Plasma Ion (VaPI) Source with Transmission Mode and Laser Ablation Sampling Capabilities. J. Am. Soc. Mass Spectrom. 27, 897–907 (2016). https://doi.org/10.1007/s13361-016-1354-8

28. Rose, B.A.: Gas chromatography and its analytical applications. A review, https://pubs.rsc.org/en/content/articlehtml/1959/an/an959840574b, (1959)

29. Dixon, P.F., Stoll, M.S., Lim, C.K.: High Pressure Liquid Chromatography in Clinical Chemistry: A Review. Ann. Clin. Biochem. 13, 409–432 (1976). https://doi.org/10.1177/000456327601300131

30. Eiceman, G.A., Gardea-Torresdey, J., Overton, E., Carney, K., Dorman, F.: Gas chromatography, https://pubs.acs.org/sharingguidelines, (2002)

31. Denoroy, L., Zimmer, L., Renaud, B., Parrot, S.: Ultra high performance liquid chromatography as a tool for the discovery and the analysis of biomarkers of diseases: A review, (2013)

32. Jorgenson, J.W., Lukacs, K.D.A.: Zone Electrophoresis in Open-Tubular Glass Capillaries. Anal. Chem. 53, 1298–1302 (1981). https://doi.org/10.1021/ac00231a037

33. Voeten, R.L.C., Ventouri, I.K., Haselberg, R., Somsen, G.W.: Capillary Electrophoresis: Trends and Recent Advances, /pmc/articles/PMC5994730/, (2018)

34. Ewing, R.G., Atkinson, D.A., Eiceman, G.A., Ewing, G.J.: A critical review of ion mobility spectrometry for the detection of explosives and explosive related compounds. Talanta. 54, 515–529 (2001). https://doi.org/10.1016/S0039-9140(00)00565-8

35. Tyndall, A.M., Starr, L.H.: The mobility of ions in air. Part IV.—Investigations by two new methods. Proc. R. Soc. London. Ser. A, Contain. Pap. a Math. Phys. Character. 121, 172–184 (1928). https://doi.org/10.1098/rspa.1928.0189

36. Cumeras, R., Figueras, E., Davis, C.E., Baumbach, J.I., Gràcia, I.: Review on Ion Mobility Spectrometry. Part 1: Current instrumentation, /pmc/articles/PMC4331213/, (2015)

37. Revercomb, H.E., Mason, E.A.: Theory of Plasma Chromatography/Gaseous Electrophoresis. A Review. Anal. Chem. 47, 970–983 (1975). https://doi.org/10.1021/ac60357a043

38. McDaniel, E.W., Martin, D.W., Barnes, W.S.: Drift tube-mass spectrometer for studies of low-energy ion-molecule reactions. Rev. Sci. Instrum. 33, 2–7 (1962). https://doi.org/10.1063/1.1717656

39. May, J.C., McLean, J.A.: Ion mobility-mass spectrometry: Time-dispersive

instrumentation, (2015)

40. Pringle, S.D., Giles, K., Wildgoose, J.L., Williams, J.P., Slade, S.E., Thalassinos, K., Bateman, R.H., Bowers, M.T., Scrivens, J.H.: An investigation of the mobility separation of some peptide and protein ions using a new hybrid quadrupole/travelling wave IMS/oa-ToF instrument. Int. J. Mass Spectrom. 261, 1–12 (2007). https://doi.org/10.1016/j.ijms.2006.07.021

41. Giles, K., Pringle, S.D., Worthington, K.R., Little, D., Wildgoose, J.L., Bateman, R.H.: Applications of a travelling wave-based radio-frequency-only stacked ring ion guide. Rapid Commun. Mass Spectrom. 18, 2401–2414 (2004). https://doi.org/10.1002/rcm.1641

42. Shvartsburg, A.A., Smith, R.D.: Fundamentals of traveling wave ion mobility spectrometry. Anal. Chem. 80, 9689–9699 (2008). https://doi.org/10.1021/ac8016295

43. Atouf, F., Venema, J.: Do Standards Matter? What is Their Value? J. Pharm. Sci. 109, 2387–2392 (2020). https://doi.org/10.1016/j.xphs.2020.04.017

44. Blackstone, E.A., Fuhr, J.P., Pociask, S.: The health and economic effects of counterfeit drugs. Am. Heal. Drug Benefits. 7, 216–224 (2014)

45. Newton, P.N., Green, M.D., Fernández, F.M.: Impact of poor-quality medicines in the "developing" world, (2010)

46. World Health Organization: Report of the Sixth Meeting of the Member State Mechanism on Substandard and Falsified Medical Products. , Geneva (2018)

47. Newton, P.N., Green, M.D., Fernández, F.M., Day, N.P., White, N.J.: Counterfeit anti-infective drugs, (2006)

PART 1. VACUUM ASSISTED PLASMA IONIZATION DEVELOPMENT

CHAPTER 2. AEROSOL VACUUM-ASSISSTED PLASMA IONIZATION (AERO-VAPI) COUPLED TO ION MOBILITY-MASS SPECTROMTRY

Adapted with permission from:

Blair, S.L., Ng, N.L., Zambrzycki, S.C., Li, A., Fernández, F.M.: Aerosol Vacuum-Assisted Plasma Ionization (Aero-VaPI) Coupled to Ion Mobility-Mass Spectrometry. J. Am. Soc. Mass Spectrom. 29, 635–639 (2018). https://doi.org/10.1007/s13361-017-1872z. Copyright 2018 American Chemical Society.

Blair S.L. optimized the aerosol generation and particle sizer. Zambrzycki S.C. built and optimized the VaPI source coupled to the mass spectrometer.

2.1 Abstract

We report on the real-time analysis of organic aerosol particles by Vacuum-assisted Plasma Ionization-Mass Spectrometry (Aero-VaPI-MS) using a home-built VaPI ion source coupled to a Synapt G2-S HDMS ion mobility-mass spectrometry (IM-MS) system. Standards of organic molecules of interest in prebiotic chemistry were used to generate aerosols. Monocaprin and decanoic acid aerosol particles were successfully detected in both the positive and negative ion modes, respectively. A complex aerosol mixture of different sizes of polymers of L-malic acid was also examined through ion mobility (IM) separations, resulting in the detection of polymers of up to eight monomeric units. This noncommercial plasma ion source is proposed as a low-cost alternative to other plasma ionization platforms used for aerosol analysis, and a higher-performance alternative to more traditional aerosol mass spectrometers. VaPI provides robust online ionization of

organics in aerosols without extensive ion activation, with the coupling to IM-MS providing higher peak capacity and excellent mass accuracy.

2.2 Introduction

Few mass spectrometry (MS) platforms are available for aerosol particle analysis that have both high temporal and high mass resolution [1]. Current online analysis methods suffer from limitations such as insufficient peak capacity, limited mass accuracy, unpredictable adduct formation, extensive ion activation, and slow response [2–8]. Developing soft aerosol ion sources that can be coupled to most high resolution mass spectrometers would thus enable more robust molecular identification of organics from aerosol particles, yielding more easily interpretable insights into aerosol chemistry mechanisms and composition.

One of the most commonly used mass spectrometers in the aerosol field is the high-resolution time-of-flight aerosol mass spectrometer (aerosol HR-ToF-AMS) [3]. It utilizes electron ionization, yielding complex fragment mass spectra absent of molecular ions, hindering the ability to easily track intact species [1]. Later, a Filter Inlet for Gases and AEROsols (FIGAERO) was developed and coupled to a high-resolution time-of-flight chemical ionization-mass spectrometer (aerosol HRToF-CIMS) [6], which relies on filter collection of particles followed by thermodesorption prior to ionization. Because of the finite filter collection time, aerosol particle measurements with the FIGAERO-HRToF-CIMS lack high temporal resolution, and are susceptible to on-filter reactions causing artifacts during sampling and measurement [9]. Ambient ionization techniques such as extractive electrospray ionization [8], direct analysis in real time (DART) [4], flowing atmospheric-pressure afterglow (FAPA) [2], and droplet assisted inlet ionization [5] have also been used for improving aerosol analysis. However, these MS techniques can still suffer from extraction efficiency limitations, ion suppression, incomplete aerosol sampling,

high background, or oxidation reactions. More recently, an aerosol flowing atmospheric-pressure afterglow (AeroFAPA) ion source was developed to detect organic compounds in aerosols [10]. Also, Zenobi et al. developed a dielectric barrier discharge plasma technique [11] used for studying offline-vaporized liquid or solid samples [12], and for real-time breath analysis [13]. Further enhancements to aerosol MS analysis have been achieved through the coupling of MS to ion mobility (IM), enabling the separation of isobaric species in aerosol mixtures [14].

In this work, we present a home-built Vacuum-assisted Plasma Ionization (VaPI) ion source for aerosols (Aero-VaPI) coupled to a Waters Synapt G2-S HDMS Ion Mobility-Mass Spectrometry (IM-MS) system. The Aero-VaPI ion source is an atmospheric pressure glow discharge plasma that is interconnected with the inlet of an IM-mass spectrometer. The vacuum pull from the mass spectrometer induces a Venturi effect at a sampling tee, enabling the capture and entrainment of the sample aerosol into the metastable atom population of the plasma before going into the mass spectrometer. This arrangement offers advantages such as a cost effective and simple assembly, efficient ionization, aerodynamic Venturi sample entrainment, and more straightforward molecular identification [15, 16]. The applicability of the Aero-VaPI-MS system to particle analysis in a prebiotic chemistry context is presented.

2.3 Experimental

2.3.1 Materials

Chemical standards of monocaprin (1-monodecanoylglycerol) and decanoic acid (each ≥99%) were purchased from Sigma Aldrich, and L-malic acid (99%) from Chem-

Impex International. Aerosol samples of monocaprin and decanoic acid were separately generated from aqueous and methanolic ~2 mM solutions with a TSI 3076 Constant Output Atomizer at 2 standard liters per minute (SLM) and measured with Aero-VaPI-MS in the positive and negative ion modes, respectively. Poly-L-malic acid was synthesized via heated dry-down reactions previously described by Forsythe et al. (2015) [17], without any purification. An L-malic acid-equivalent 0.50 mM solution of poly-L-malic acid was analyzed with ESI-IM-MS in the negative mode. A nebulizer (SLT8900H, Salter Labs® 8900 Series Small Volume Jet Nebulizer from Medline Inc.) was used to generate aerosols at 6 SLM of the same poly-L-malic acid solution and was measured with Aero-VaPI-IM-MS in the negative ion mode. The nebulizer offered an air jet of lower pressure (10 psi versus 34 psi of N2), producing a more stable signal for L-malic acid polymers during particle generation. Aerosols were not size-selected prior to mass spectrometry analysis.

2.3.2 Instrumentation

The Aero-VaPI ion source (Figure 2-1) consists of an enclosed system with an AC-powered point-to-plane glow discharge operating at near atmospheric pressure that intersects an aerosol sample stream suctioned by a Venturi sampling tee. Ions are transferred from the Venturi sampling tee into a Synapt G2-S HDMS (Waters, IMS-TOF) mass spectrometer. The power is supplied by a high voltage plasma generator with a sine waveform (T&C Power Conversion Inc.; Model AG 0201-HV, Rochester, NY) with a frequency adjustment of 6.68 and a rf adjustment of 1.34. The discharge frequency and voltage were 370 kHz at 2.9 kV peak to peak, respectively. The VaPI source is mounted on a VAPUR DART interface that had its vacuum port blocked, serving only as a mechanical support for the source, but not providing additional pumping. Analytes within

aerosol particles are desorbed by collisions with heated plasma gas within the sampling tee and chemically-ionized through proton transfer reactions with reactive ion species generated by the plasma. The He (UHP300 Airgas) flow, AC power, and temperature of the VaPI sampling tee were optimized to 0.40 SLM in order to maximize the metastable population without putting too much strain on the turbo pumps, 10.0 W forward and 0 W reverse applied to a tungsten needle, and 40 °C, to achieve thermal equilibrium while maintaining the lowest temperature possible to minimize fragmentation and potential z reactions, respectively. The electrode gap from the point of the tungsten tip to the inside of the grounded sampling tee (where the metal is first exposed) is 3 cm. Flows were measured with an Allicat Scientific mass flow meter (M-5SLPM-D, Tucson, AZ). The Venturi sampling tee was heated by heating tape (BriskHeat heating cord Model HTC451006) that was controlled by a temperature controller (BriskHeat; Model SDC120JF-A).

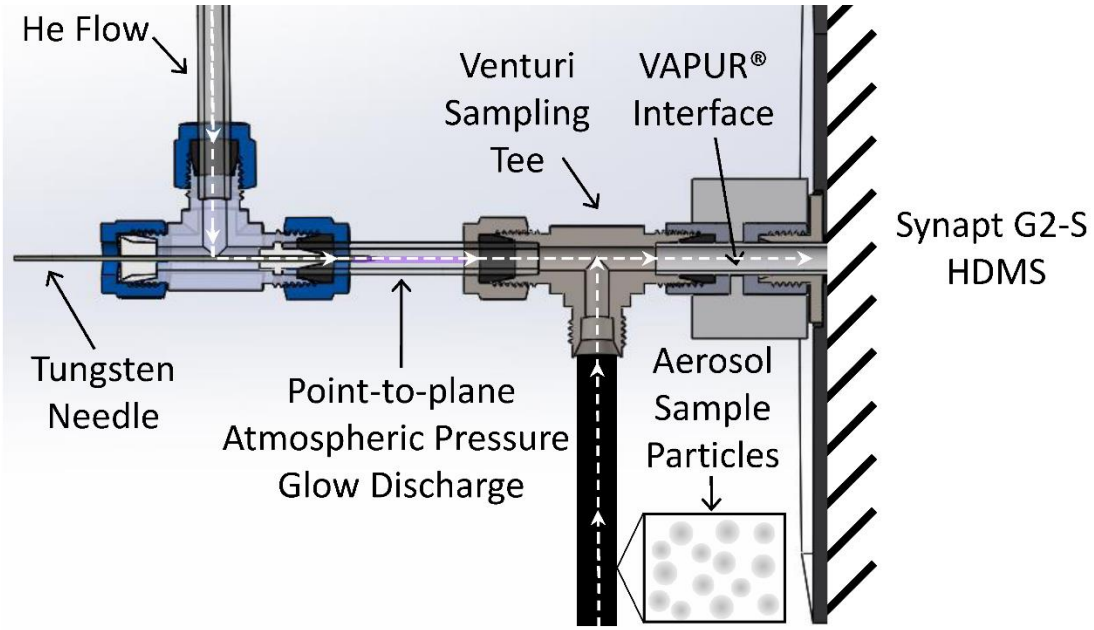

Figure 2-1 Cross-sectional view of the home-built Aero-VaPI ion source coupled to IM-MS via a VAPUR® interface that had its side vacuum port blocked, serving only as a mechanical adapter.

2.4 Results and Discussion

Our interest in aerosols stems from our research in the prebiotic de novo synthesis of proto-biopolymers in an origins of life scenario. It has been shown that aerosols can act as chemical reactors in the prebiotic formation of such polymeric species [18–21]. Dobson et al., for example, have proposed that by their ability to concentrate molecules, aerosols could have served as efficient prebiotic chemical reactors for the first protocelullar structures [19]. Condensation reactions are important in prebiotic chemistry, and include formation of lipids [18] and far-from-equilibrium polymers [22]. These reactions can be favored in aerosols, where water loss is driven by evaporation. Trainer et al. have hypothesized that organic species that have functionalities of interest to prebiotic chemistry are more likely to exist in the aerosol phase [23]. Previous studies have focused on amino acid or tholin formation [24, 25], but only few have investigated the molecular composition of products generated via aerosols [26].

As a first experiment, Aero-VaPI-MS was tested for aerosol composition determination in the positive and negative modes with monocaprin and decanoic acid aerosols (Figures 2-2 A & B), respectively. Bulk condensation reactions of glycerol and decanoic acid to form monocaprin have been studied by Apel and Deamer as a route for the production of a more evolved amphiphile leading to proto-cellular membranous structures [18]. In the positive mode monocaprin was detected as the $[M + H]^+$, as well as $[M - H_2O + H]^+$ resulting from protonation-induced water loss (Figure 2-2 C). The deprotonated ion of decanoic acid, $[M - H]^-$, was observed in the negative mode, as seen in Figure 2-2 D. In these experiments, the atomizer was sequentially turned on and off to verify that signal returned to baseline following introduction of the analyte. The rise time

of the signals for these aerosols was a function of the aerosol equilibration time in the tubing lines. It is expected that during application of this instrumentation to an aerosol reaction system, lines would be equilibrated at the start of the experiment and would continuously sample from the aerosol system, so no subsequent re-equilibration would be needed. It was observed that the signal dipped slightly below the original baseline following each injection event, likely due to a temporary pressure imbalance. Once the baseline was recovered, the next aerosol atomization event was triggered.

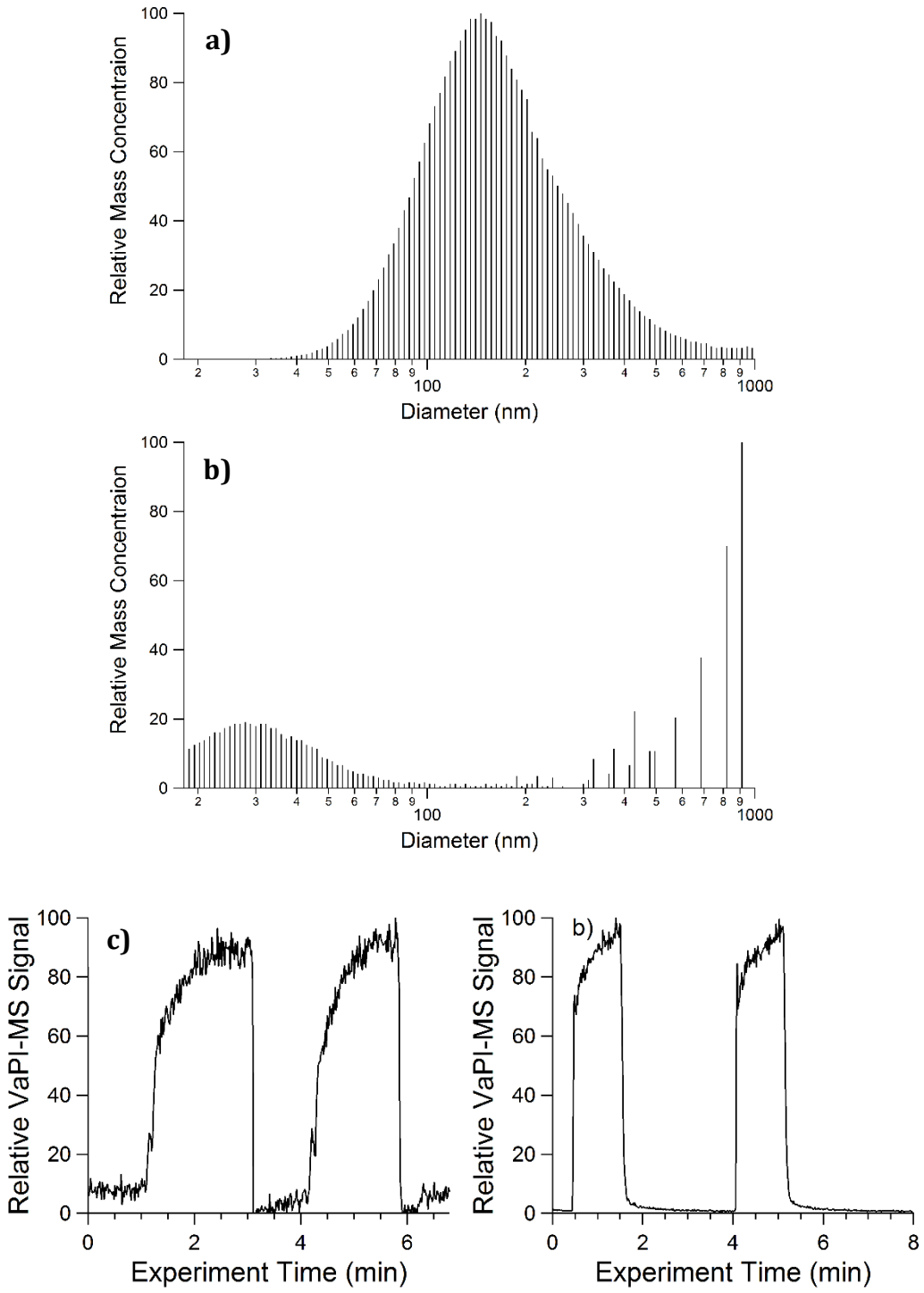

Figure 2-2 Relative mass-weighted particle size distributions for (A) 2 mM methanolic solution of monocaprin and (B) 2 mM aqueous solution of decanoic acid. Aero-VaPI-MS signals for aerosol particles consisting of (C) monocaprin in (+)-mode; $[M - H_2O + H]^+$ monitored at m/z 229, from protonation-induced water loss (D) decanoic acid in (–)-mode; $[M - H]^-$ monitored at m/z 171

Another molecule of interest in prebiotic chemistry is malic acid, being part of both the Calvin and citric acid cycles. Mamajanov et al. have studied the esterification of malic acid under wet/dry batch cycling conditions, proposing a ratcheting mechanism for the formation of far-from-equilibrium polymers [22]. Malic acid has also been proposed as an intermediate in the formation of proto-peptides [27]. Here, we used poly-L-malic acid aerosol as a test for Aero-VaPI-MS detection of products of prebiotic condensation polymerization reactions in aerosols. To this purpose, a solution of poly-L-malic acid was first analyzed by electrospray (ESI) IM-MS (Figure 2-3 A & B). All oligomers were well separated with IM and detected within a drift time of 8 ms. The average ESI IM-MS mass spectrum (Figure 2-3 A) showed [M – H]- ions for oligomers with chain lengths ranging from 1 to 8, together with their corresponding water loss ($\Delta m/z = 18$) species. The single water loss ion species, denoted as [M´ – H]-, contributed significantly to the total ion count, as seen in the ion mobility arrival time distribution (Figure 2-3 B). These neutral water losses are common in ESI-MS of acids, occurring by alcohol dehydration or cyclic anhydride formation between adjacent carboxyl groups [28].

Aero-VaPI-IM-MS spectral data for poly-L-malic acid aerosols (Figure 2-3 C & D) were very similar to that obtained by ESI IM-MS, with the interesting difference that the water loss signals were much less abundant than with ESI. It was necessary to multiply the [M´ – H]- ion signals by a factor of 10 in order to better observe their IM distribution (Figure 2-3 D).

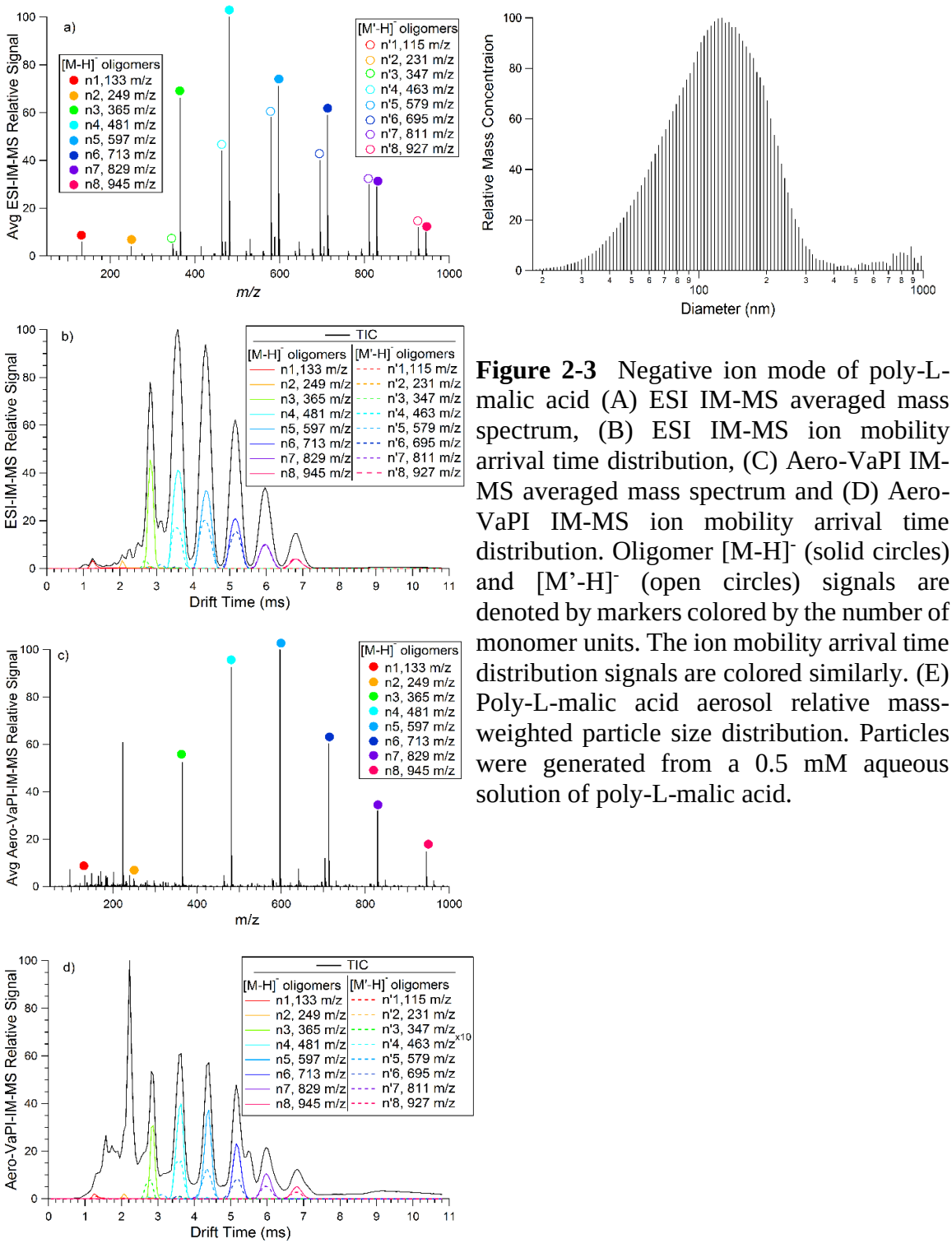

Figure 2-3 Negative ion mode of poly-L-malic acid (A) ESI IM-MS averaged mass spectrum, (B) ESI IM-MS ion mobility arrival time distribution, (C) Aero-VaPI IM-MS averaged mass spectrum and (D) Aero-VaPI IM-MS ion mobility arrival time distribution. Oligomer $[M-H]^-$ (solid circles) and $[M'-H]^-$ (open circles) signals are denoted by markers colored by the number of monomer units. The ion mobility arrival time distribution signals are colored similarly. (E) Poly-L-malic acid aerosol relative mass-weighted particle size distribution. Particles were generated from a 0.5 mM aqueous solution of poly-L-malic acid.

Oligomers did not represent the majority of the total ion signal in some drift time regions, such as the region between 1–2 ms and the shoulder at 5.5 ms. The first arrival time distribution region (1–2 ms) was broad and populated mostly by small ions such as water loss ions C4H1O3- and C4H3O4- at m/z 97 and 115, which may be dehydrated forms of malic acid such as maleic anhydride and maleic acid, respectively (Figure 2-4). Oxidized species possibly arising from these ions, such as C4H5O6-, C4H6O6-, C4H5O7-, and C4H7O8-, were also observed with corresponding m/z values of 149, 150, 165, and 183. The presence of these smaller ionic species suggests that oligomer ion-molecule reactions do occur within the Aero-VaPI source due to the higher reactivity of plasma sources relative to ESI [29]. VaPI plasma ionization is expected to have an abundance of high energy charge transfer species, as there is no grid electrode to filter them out from the plasma, as in DART [30]. Further experiments are required to investigate these and other phenomena related to ion generation mechanisms in VaPI.

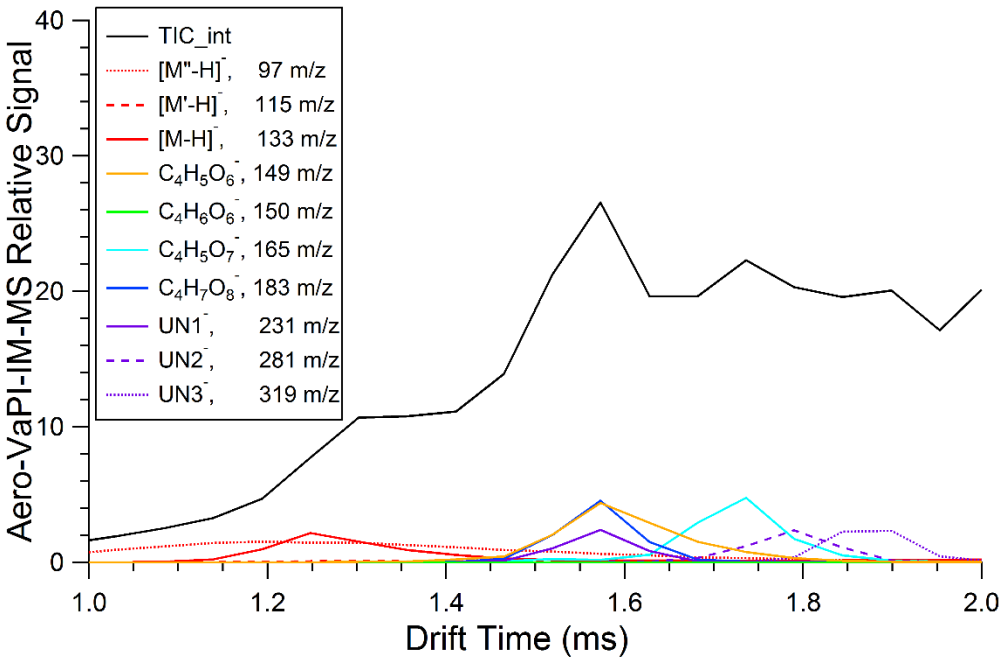

Figure 2-4 Negative ion mode Aero-VaPI-IM-MS ion mobility arrival time distribution in the 1-2 ms time range for a poly-L-malic acid aerosol. Particles were generated from a 0.5 mM aqueous solution of poly-L-malic acid. Observed fragment and oxidized species ions are plotted by color and line style with m/z of each ion listed in the legend. Unidentified peaks are labeled as "UN".

2.5 Conclusions

The Aero-VaPI ion source is cost effective, has minimal assembly, provides softer ionization than with standard aerosol mass spectrometers, and, when coupled to IM-MS, can rapidly separate species in aerosol mixtures for the molecular detection of organic analytes in particles. Although organics may undergo a small amount of activation in the VaPI source, no sample handling is required with the Aero-VaPI-MS system, avoiding solvent-dependent extraction efficiency limitations. Initial results suggest that this technique can be applied to monitor aerosol chemistry in real-time, including prebiotic condensation reactions. Future studies of new prebiotic aerosol chemistry with Aero-VaPI-MS are expected to provide insight into the mechanisms of de novo proto-biopolymer formation.

2.6 References

1. Glasius, M., Goldstein, A.H.: Recent Discoveries and Future Challenges in Atmospheric Organic Chemistry. Environ. Sci. Technol. 50, 2754–2764 (2016). https://doi.org/10.1021/acs.est.5b05105

2. Brüggemann, M., Karu, E., Hoffmann, T.: Critical assessment of ionization patterns and applications of ambient desorption/ionization mass spectrometry using FAPA-MS. J. Mass Spectrom. 51, 141–149 (2016). https://doi.org/10.1002/jms.3733

3. Peter F. DeCarlo, †,‡, Joel R. Kimmel, †, Achim Trimborn, ⊥, Megan J. Northway, ⊥, John T. Jayne, ⊥, Allison C. Aiken, †,§, Marc Gonin, ∥, Katrin Fuhrer, ∥, Thomas Horvath, ∥, Kenneth S. Docherty, †, Doug R. Worsnop, ⊥ and, Jose L. Jimenez*, †,§: Field-Deployable, High-Resolution, Time-of-Flight Aerosol Mass Spectrometer. (2006). https://doi.org/10.1021/AC061249N

4. Gross, J.H.: Direct analysis in real time—a critical review on DART-MS. Anal. Bioanal. Chem. 406, 63–80 (2014). https://doi.org/10.1007/s00216-013-7316-0

5. Horan, A.J., Apsokardu, M.J., Johnston, M. V.: Droplet Assisted Inlet Ionization for Online Analysis of Airborne Nanoparticles. Anal. Chem. 89, 1059–1062 (2017). https://doi.org/10.1021/acs.analchem.6b04718

6. Lopez-Hilfiker, F.D., Mohr, C., Ehn, M., Rubach, F., Kleist, E., Wildt, J., Mentel, T.F., Lutz, A., Hallquist, M., Worsnop, D., Thornton, J.A.: A novel method for online analysis of gas and particle composition: description and evaluation of a Filter Inlet for Gases and AEROsols (FIGAERO). Atmos. Meas. Tech. 7, 983–1001 (2014). https://doi.org/10.5194/amt-7-983-2014

7. Pratt, K.A., Prather, K.A.: Mass spectrometry of atmospheric aerosols-Recent developments and applications. Part II: On-line mass spectrometry techniques. Mass Spectrom. Rev. 31, 17–48 (2012). https://doi.org/10.1002/mas.20330

8. Swanson, K.D., Worth, A.L., Glish, G.L.: A coaxial extractive electrospray ionization source. Anal. Methods. 9, 4997–5002 (2017). https://doi.org/10.1039/C7AY00835J

9. Kristensen, K., Bilde, M., Aalto, P.P., Petäjä, T., Glasius, M.: Denuder/filter sampling of organic acids and organosulfates at urban and boreal forest sites: Gas/particle distribution and possible sampling artifacts. Atmos. Environ. 130, 36–53 (2016). https://doi.org/10.1016/J.ATMOSENV.2015.10.046

10. Brüggemann, M., Karu, E., Stelzer, T., Hoffmann, T.: Real-Time Analysis of Ambient Organic Aerosols Using Aerosol Flowing Atmospheric-Pressure Afterglow Mass Spectrometry (AeroFAPA-MS). Environ. Sci. Technol. 49, 5571–5578 (2015). https://doi.org/10.1021/es506186c

11. Wolf, J.-C., Gyr, L., Mirabelli, M.F., Schaer, M., Siegenthaler, P., Zenobi, R.: A Radical-Mediated Pathway for the Formation of [M + H]+ in Dielectric Barrier Discharge Ionization. J. Am. Soc. Mass Spectrom. 27, 1468–1475 (2016). https://doi.org/10.1007/s13361-016-1420-2

12. Mirabelli, M.F., Wolf, J.-C., Zenobi, R.: Atmospheric pressure soft ionization for gas chromatography with dielectric barrier discharge ionization-mass spectrometry (GC-DBDI-MS). Analyst. 142, 1909–1915 (2017). https://doi.org/10.1039/C7AN00245A

13. Bregy, L., Sinues, P.M.-L., Nudnova, M.M., Zenobi, R.: Real-time breath analysis with active capillary plasma ionization-ambient mass spectrometry. J. Breath Res. 8, 027102 (2014). https://doi.org/10.1088/1752-7155/8/2/027102

14. Krechmer, J.E., Groessl, M., Zhang, X., Junninen, H., Massoli, P., Lambe, A.T., Kimmel, J.R., Cubison, M.J., Graf, S., Lin, Y.-H., Budisulistiorini, S.H., Zhang, H., Surratt, J.D., Knochenmuss, R., Jayne, J.T., Worsnop, D.R., Jimenez, J.-L., Canagaratna, M.R.: Ion mobility spectrometry–mass spectrometry (IMS–MS) for on- and offline analysis of atmospheric gas and aerosol species. Atmos. Meas. Tech. 9, 3245–3262 (2016). https://doi.org/10.5194/amt-9-3245-2016

15. Forbes, T.P., Staymates, M.: Enhanced aerodynamic reach of vapor and aerosol sampling for real-time mass spectrometric detection using Venturi-assisted entrainment and ionization. Anal. Chim. Acta. 957, 20–28 (2017).

https://doi.org/10.1016/J.ACA.2016.12.037

16. Keelor, J.D., Farnsworth, P.B., L. Weber, A., Abbott-Lyon, H., Fernández, F.M.: Multimodal Vacuum-Assisted Plasma Ion (VaPI) Source with Transmission Mode and Laser Ablation Sampling Capabilities. J. Am. Soc. Mass Spectrom. 27, 897–907 (2016). https://doi.org/10.1007/s13361-016-1354-8

17. Forsythe, J.G., Petrov, A.S., Walker, C.A., Allen, S.J., Pellissier, J.S., Bush, M.F., Hud, N. V., Fernández, F.M.: Collision cross section calibrants for negative ion mode traveling wave ion mobility-mass spectrometry. Analyst. 140, 6853–6861 (2015). https://doi.org/10.1039/C5AN00946D

18. Apel, C.L., Deamer, D.W.: The Formation Of Glycerol Monodecanoate By A Dehydration Condensation Reaction: Increasing The Chemical Complexity Of Amphiphiles On The Early Earth. Orig. Life Evol. Biosph. 35, 323–332 (2005). https://doi.org/10.1007/s11084-005-2046-8

19. Dobson, C.M., Ellison, G.B., Tuck, A.F., Vaida, V.: Atmospheric aerosols as prebiotic chemical reactors. Proc. Natl. Acad. Sci. U. S. A. 97, 11864–8 (2000). https://doi.org/10.1073/pnas.200366897

20. Donaldson, D.J., Tervahattu, H., Tuck, A.F., Vaida, V.: Organic Aerosols and the Origin of Life: An Hypothesis. Orig. Life Evol. Biosph. 34, 57–67 (2004). https://doi.org/10.1023/B:ORIG.0000009828.40846.b3

21. Tuck, A.: The Role of Atmospheric Aerosols in the Origin Of Life. Surv. Geophys. 23, 379–409 (2002). https://doi.org/10.1023/A:1020123922767

22. Mamajanov, I., MacDonald, P.J., Ying, J., Duncanson, D.M., Dowdy, G.R., Walker, C.A., Engelhart, A.E., Fernández, F.M., Grover, M.A., Hud, N. V., Schork, F.J.: Ester Formation and Hydrolysis during Wet–Dry Cycles: Generation of Far-from-Equilibrium Polymers in a Model Prebiotic Reaction. Macromolecules. 47, 1334–1343 (2014). https://doi.org/10.1021/ma402256d

23. Trainer, M.G.: Atmospheric Prebiotic Chemistry and Organic Hazes. Curr. Org. Chem. 17, 1710–1723 (2013). https://doi.org/10.2174/13852728113179990078

24. Ruiz-Bermejo, M., Menor-Salván, C., Osuna-Esteban, S., Veintemillas-Verdaguer, S.: The Effects of Ferrous and other Ions on the Abiotic Formation of Biomolecules using Aqueous Aerosols and Spark Discharges. Orig. Life Evol. Biosph. 37, 507–521 (2007). https://doi.org/10.1007/s11084-007-9107-0

25. Ugelow, M.S., Zarzana, K.J., Day, D.A., Jimenez, J.L., Tolbert, M.A.: The optical and chemical properties of discharge generated organic haze using in-situ real-time techniques. Icarus. 294, 1–13 (2017). https://doi.org/10.1016/J.ICARUS.2017.04.028

26. Ruiz-Bermejo, M., Osuna-Esteban, S., Zorzano, M.-P.: Role of Ferrocyanides in the

Prebiotic Synthesis of α-Amino Acids. Orig. Life Evol. Biosph. 43, 191–206 (2013). https://doi.org/10.1007/s11084-013-9336-3

27. Forsythe, J.G., Yu, S.-S., Mamajanov, I., Grover, M.A., Krishnamurthy, R., Fernández, F.M., Hud, N. V.: Ester-Mediated Amide Bond Formation Driven by Wet-Dry Cycles: A Possible Path to Polypeptides on the Prebiotic Earth. Angew. Chemie Int. Ed. 54, 9871–9875 (2015). https://doi.org/10.1002/anie.201503792

28. Jerry A. Leenheer, *,†, Colleen E. Rostad, †, Paul M. Gates, †, Edward T. Furlong, † and, Ferrer‡, I.: Molecular Resolution and Fragmentation of Fulvic Acid by Electrospray Ionization/Multistage Tandem Mass Spectrometry. (2001). https://doi.org/10.1021/AC0012593

29. Harris, G.A., Hostetler, D.M., Hampton, C.Y., Fernández, F.M.: Comparison of the internal energy deposition of direct analysis in real time and electrospray ionization time-of-flight mass spectrometry. J. Am. Soc. Mass Spectrom. 21, 855–863 (2010). https://doi.org/10.1016/j.jasms.2010.01.019

30. Venter, A.R., Douglass, K.A., Shelley, J.T., Hasman, G., Honarvar, E.: Mechanisms of Real-Time, Proximal Sample Processing during Ambient Ionization Mass Spectrometry. Anal. Chem. 86, 233–249 (2014). https://doi.org/10.1021/ac4038569

CHAPTER 3. PYROLYSIS VACUUM-ASSISTED PLASMA IONIZATION (PYRO-VAPI) ION MOBILITY-MASS SPECTROMETRY FOR INSOLUBLE POLYMER ANALYSIS

Adapted with permission from:

Zambrzycki, S., Bernier, M., Bradshaw, J., Fernandez, F.: Pyrolysis Vacuum-Assisted Plasma Ionization Ion Mobility–Mass Spectrometry for Insoluble Polymer Analysis. J. Am. Soc. Mass Spectrom. 32, 1388–1392 (2021). https://doi.org/10.1021/jasms.1c00109

3.1 Abstract

This work describes a new thermal desorption/pyrolysis vacuum-assisted plasma ionization (pyro-VaPI) ion source coupled to ion mobility-mass spectrometry (IM-MS) for insoluble polymer analysis. Pyro-VaPI combines a pyrolysis device, soft ambient plasma ionization, IM, and MS into a single platform for polymer analysis with minimal sample preparation. Nylons, a widely used and well-studied thermoplastic, were chosen to evaluate pyro-VaPI performance. Six different nylon polymers were studied and characterized. With the application of IM-MS, two different isobars for the protonated cyclic dimers of 6-6, 6-9, 6-10, and 6-12 nylon and two isobars for the cyclic tetramer of nylon 6 were detected at 200 °C. These isobars were observed at different heating times, with the species drifting faster in the IM cell appearing several minutes after the slower drifting species. To the best of our knowledge, these isobaric dimers and tetramers have not been previously reported, indicating pyro-VaPI IM-MS is a useful tool for the structural characterization of heated or pyrolyzed polymers.

3.2 Introduction

Thermoplastics, such as nylons, play an integral role in many commonly used fibers, films and structural components due to their high strength and malleability when heated. Chemically-resistant thermoplastics offer enhanced durability in harsh conditions, but limited solubility can make their mass spectrometric analysis challenging. Correct identification of insoluble polymers, however, is critical for forensics investigations attempting to link evidence sources [1]. Mechanistic insights into thermal degradation of insoluble polymers can also be useful for developing new materials such as non-halogenated anti-flammable polymers [2].

Pyrolysis gas chromatography-mass spectrometry (Py-GC-MS) is well-established for characterizing insoluble polymers, as it does not require sample dissolution [3]. However, the use of electron ionization in Py-GC-MS produces complicated spectra, thus requiring GC separations and appropriate databases. The use of chemical ionization (CI) instead of EI somewhat simplifies mass spectra, and can even eliminate the need for GC [4, 5]. Electrospray ionization is softer than CI, but has been generally limited to contaminants or extractable dyes without breaking down polymers chemically [6, 7]. Matrix-assisted laser desorption ionization (MALDI) can analyze insoluble polymers without dissolution, but requires crushing the analyte together with the matrix in a highly homogeneous fashion [8, 9].

As alternatives to ESI and MALDI, a variety of ambient plasma ionization sources have been developed [10]. The atmospheric solids analysis probe (ASAP) is the most notable example for insoluble polymer analysis. In ASAP, a stream of heated nitrogen gas

is flowed over the sample to vaporize it into a corona discharge for atmospheric pressure CI [11], followed by MS or ion mobility mass spectrometry (IM-MS) analysis. Although many reports of polymer analysis with ASAP exist, they require the sample to be melted and re-solidified onto the probe, which may lead to unwanted changes [12–15]. The coupling of a thermal desorption cell such as in the ionRocket to direct analysis in real-time (DART) is an alternative to avoid the melting and re-solidifying steps required in ASAP [16, 17]. In this approach, the polymer sample is loaded into the ionRocket cup, the cup is heated, the analyte vapors merge with the DART plasma stream for ionization, and the ionized compounds are transported into the inlet of a mass spectrometer for analysis [18, 19]. Both ASAP and ionRocket/DART can conduct thermal gradient experiments that separate species with different volatilities.

In this communication, we describe a new platform that combines a home-built thermal desorption/pyrolysis unit with a vacuum-assisted plasma ionization ion source [20, 21], and IM-MS detection (Pyro-VaPI IM-MS). This technique offers a highly modular design that boosts sensitivity by enhanced sample plume entrainment compared to open air approaches such as DART. Pyro-VaPI enjoys the IM-MS capabilities of ASAP experiments and the simplicity of sample preparation of ionRocket/DART. Nylons were used to characterize pyro-VaPI performance as they are very common, well-studied insoluble polymers [22–26].

3.3 Experimental

3.3.1 Materials

Nylon polymers were sourced from the Nylon Polymer Kit (Cat# 2054) by Scientific Polymer Products Inc. (Ontario, NY). The following nylon polymers were tested: nylon 6 poly(caprolactam), nylon 6-6 poly(hexamethylene adipamide), nylon 6-9 poly(hexamethylene azelamide), nylon 6-10 poly(hexamethylene sebacamide), nylon 6-12 poly(hexamethylene dodecanediamide), nylon 11 poly(undecanoamide), and nylon 12 poly(laurolactam).

3.3.2 Pyrolysis/Heating Unit

A pyrolysis device that reached temperatures up to 900°C and currents of 5.5 A without failure was built. For polymer pyro-VaPI analysis, an intact single plastic pellet was placed into a stainless-steel cup, and the power supply was ramped to 200°C (2.5 A).

3.3.3 Instrumentation

A schematic of the pyro-VaPI IM-MS platform is shown in Figure 3-1. The VaPI system was coupled to a Waters Synapt G2-S IM-MS platform (Milford, MA). Manual controls were disabled for the traveling wave IM portion and the following parameters were utilized: wave height 40.0 V, wave velocity 650 m s^{-1}, gas flow 90.00 mL min^{-1}, and pressure 3.15 mbar. Briefly, a VaPI source was modified to connect to an IonSense VAPUR interface for Waters instruments (Saugus, MA) [21]. The gas used for sustaining the VaPI plasma was ultra-high purity helium from Airgas (Atlanta, GA). The He flow rate was set at 0.4 L min^{-1}, measured by an Alicat Scientific model M-5SLPM-D mass flow meter (Tucson, AZ). The plasma was created by a tungsten needle powered with a T&C Power Conversion Inc. model AG 0201-HV radio frequency high voltage generator (Rochester, NY). For plasma ignition, the radio frequency generator was set to a power of

10 W and frequency of 370 kHz, resulting in a peak to peak voltage of 2.9 kV. All samples were tested in positive ion mode in the 200 to 1200 *m/z* range. A polytetrafluoroethylene (PTFE) tube extended from the VaPI ion source and hovered at about 1 cm over the pyrolysis device cup, which was placed in a fume hood. This tube was cleaned with acetone after each experiment to avoid cross-talk between sample runs. The sampling tee connecting the VaPI plasma chamber with the sampling tube from the pyrolysis unit was held at 200 °C using a BriskHeat heating cord and controller, models HTC451006 and SDC120JF-A, respectively (Columbus, OH).

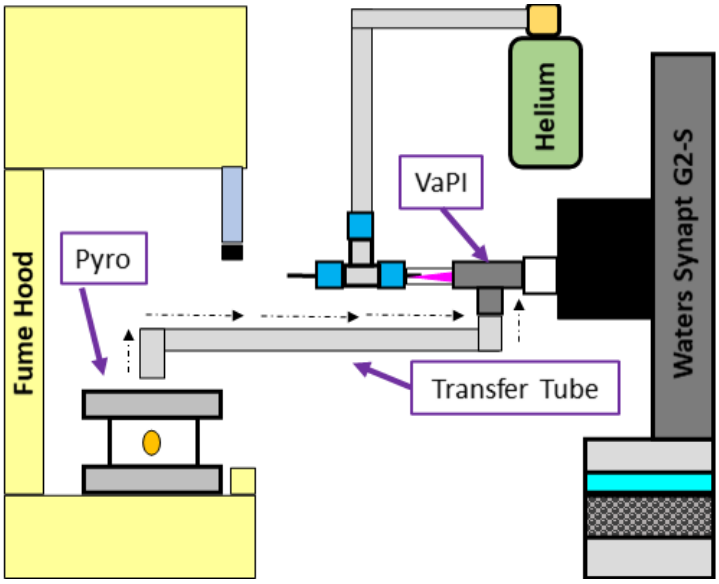

Figure 3-1 Diagram of the pyro-VaPI IM-MS platform (not to scale). The pyrolysis unit was placed in a fume hood together with the heating power supply unit to minimize fire hazards and to prevent fumes from the pyrolysis experiments from reaching the user. A PTFE tube extended from the pyrolysis unit to the VaPI ion source, which was directly connected to a Waters Synapt G2-S ion mobility-mass spectrometer via the IonSense VAPUR interface.

3.4 Results and Discussion

Pyro-VaPI IM-MS analysis of various common nylons showed ions with *m/z* corresponding to that of a cyclized monomer unit (Figure 3-2 A). Ions with *m/z* values corresponding to the cyclic ion resulting from two linked repeat units were also readily observed (Figure 3-2 B), with alternating polymers such as nylon 6-6, 6-9, 6-10, and 6-12 showing two isobaric species with different IM arrival times. Nylons 6, 6-6, 11, & 12, produced ions that matched the elemental formula of the cyclic trimers (Figures 3-2 C). Nylons 6 & 11 were the only nylons that yielded detectable gas phase species matching the cyclic tetramers, and two isobaric species of the cyclic tetramer of nylon 6 were also detected (Figures 3-2 D).

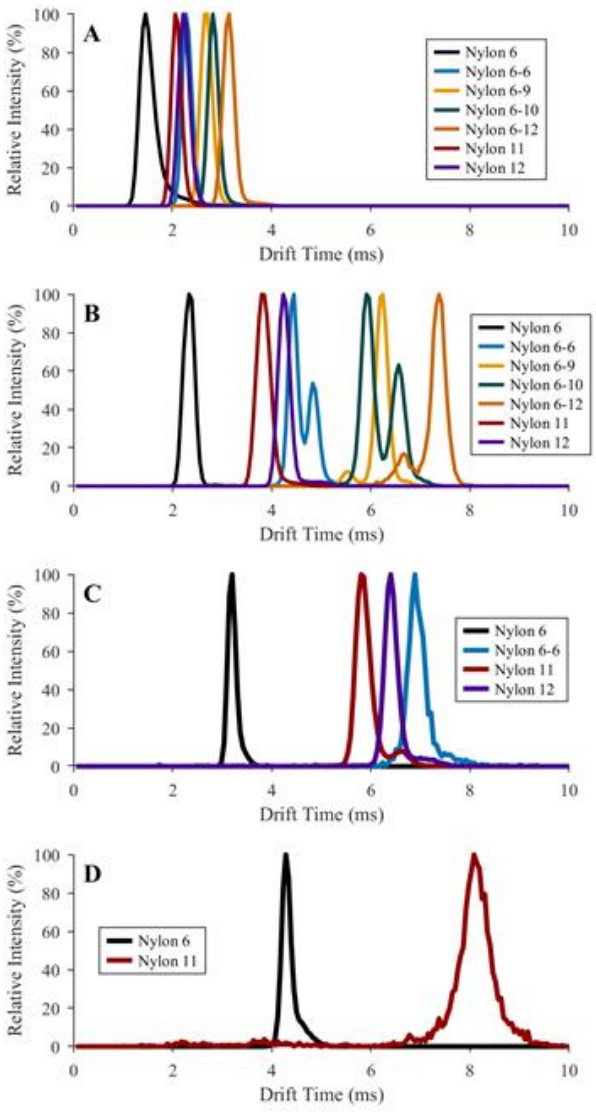

Figure 3-2 Extracted arrival time distributions for various pyrolyzed nylon polymers matching the (A) cyclic monomer ions with *m/z* 114.09, 184.17, 198.19, 227.18, 269.22, 283.24, and 311.27 for nylon 6, nylon 11, nylon 12, nylon 6-6, nylon 6-9, nylon 6-10, and nylon 6-12, respectively; (B) cyclic dimer ions with *m/z* 227.18, 367.33, 395.36, 453.34, 537.44, 565.47,and 621.53 for nylon 6, nylon 11, nylon 12, nylon 6-6, nylon 6-9, nylon 6-10, and nylon 6-12, respectively; (C) cyclic trimer ions with *m/z* 340.26, 550.49, 592.54, and 679.51 for nylon 6, nylon 11, nylon 12, and nylon 6-6, respectively; and (D) cyclic tetramer ions with *m/z* 453.34 and 733.66 for nylon 6 and nylon 11, respectively.

The identity of the two mobility-resolved cyclic species originating from the cyclic tetramer of nylon 6 and cyclic dimer of nylons 6-6, 6-9, 6-10, and 6-12 was confirmed by tandem MS experiments. The precursor ions for these species were mass selected in the IM-MS quadrupole mass analyzer, ion mobility-separated, and then fragmented post-mobility in the transfer cell. An example of results for these experiments is shown in Figures 3-3 for nylon 6-6, confirming that both mobility peaks observed resulted from repeat units of each respective nylon, as they readily fragmented into repeat unit species.

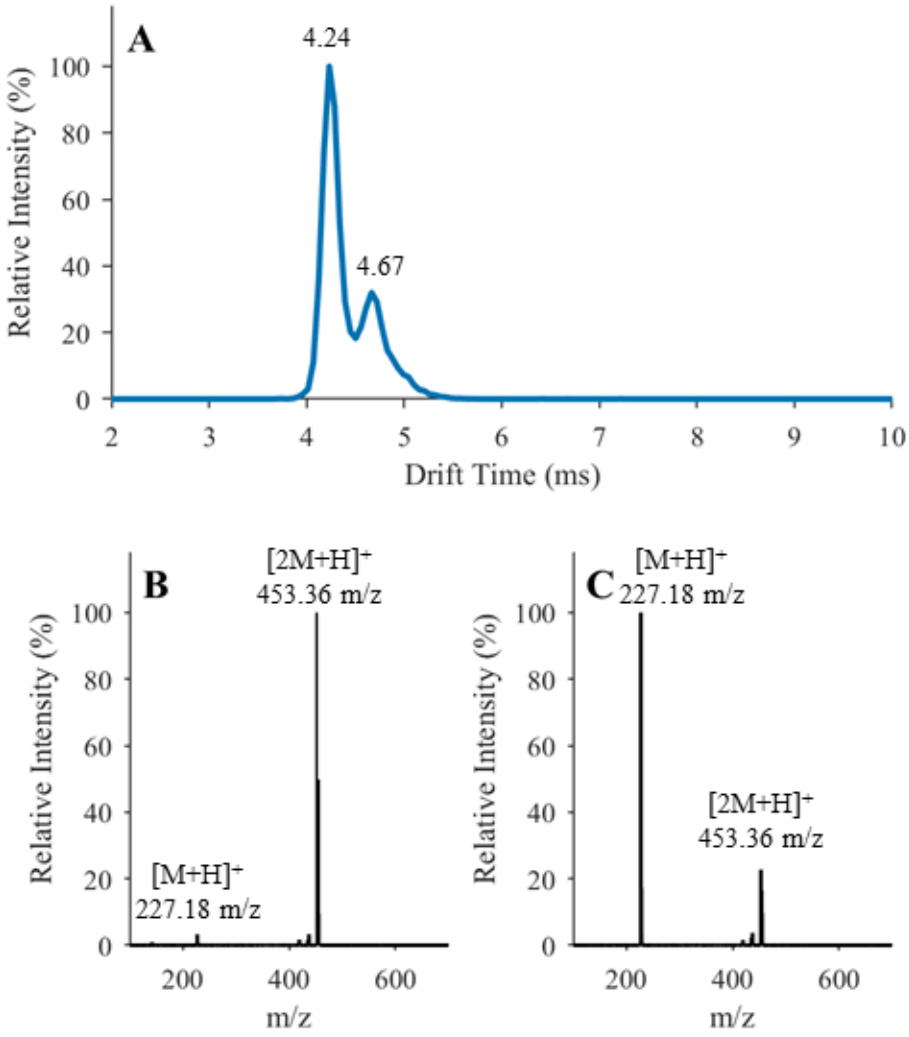

Figure 3-3 Pyro-VaPI analysis of nylon 6-6 (polyhexamethylene adipamide). (A) Extracted drift time for the cyclic dimer at m/z 453.36 showing potentially two different isomers/conformers of nylon 6-6. These species were fragmented in the transfer cell (post-mobility) at 13 eV collision energy. The MS/MS spectra for the fragmented cyclic dimer species at (B) 4.24 ms and (C) 4.67 ms peak are presented. M refers to a repeat unit of nylon 6-6 in the cyclic species.

In these experiments, we also observed that each of the two distinct IM features showed unique fragment ion abundances in their mobility-resolved MS/MS spectra. For the cyclic tetramer of nylon 6 and cyclic dimer of nylons 6-6, 6-9, 6-10, and 6-12, the shorter drift time species showed the highest abundance of the precursor ion. Conversely, the species with the longer drift time systematically showed the highest abundance for the smaller unit species upon fragmentation (Figures 3-3 B-C). The difference in drift time and fragmentation ion abundance in the two distinct IM features are likely due to the formation of different pyrolyzed nylons.

Examination of the IM arrival times for isobaric species of some of the investigated nylons showed that they were not resolvable in the ion mobility domain. For example, the cyclic species formed by a cyclic monomer of nylon 6-6 had a drift time of 2.28 ms (Figure 3-2 A). This species is isomeric with the cyclic dimer unit species of nylon 6 that had a drift time of 2.33 ms (Figure 3-2 B). A similar effect was observed between the cyclic dimer species of nylon 6-6 (4.34 ms, Figure 3-2 B) and the cyclic tetramer species of nylon 6 (4.23 ms, Figure 3-2 D). The lack of resolution between these species was disappointing but not completely unexpected due to the high structural similarity of the ions generated by pyrolysis, despite originating from different nylon polymers.

Next, it was investigated if the pyrolysis data contained any temperature-dependent trends in the arrival time distributions for nylons 6, 6-6, 6-9, 6-10, & 6-12. To this end, the experimental pyrolysis time, IM drift time, and feature abundance were plotted along various dimensions using DriftScope. Figure 3-4 shows some of the results of such analysis, indicating that the faster drifting species for nylon 6-6 did not appear until ~4 minutes into the pyrolysis process, which corresponded to a pyrolysis temperature 50 °C

hotter than for the slower drifting species. Similarly, faster drifting species were also detected for nylons 6, 6-9, 6-10, & 6-12 starting after ~4, ~4, ~2, and ~6 minutes into the pyrolysis process, respectively. This finding suggests that the faster-mobility species were not generated until the higher temperature was reached, or that they did not form until extended heating was applied to the sample. Sub-minute oscillations were seen in the DriftScope data in Figure 3-4 B. These oscillations are the likely result of the melted nylon bubbling during heating, releasing pyrolyzed nylon species after each bubble collapsed on the surface of the melted plastic. Overall, the multidimensional data presented in Figure 3-4 illustrates the power of combining information gathered from the thermal desorption/pyrolysis unit in real time with the ion mobility-mass spectral data collection. This generates a dataset with comprehensive chemical information that enables improved polymer characterization.

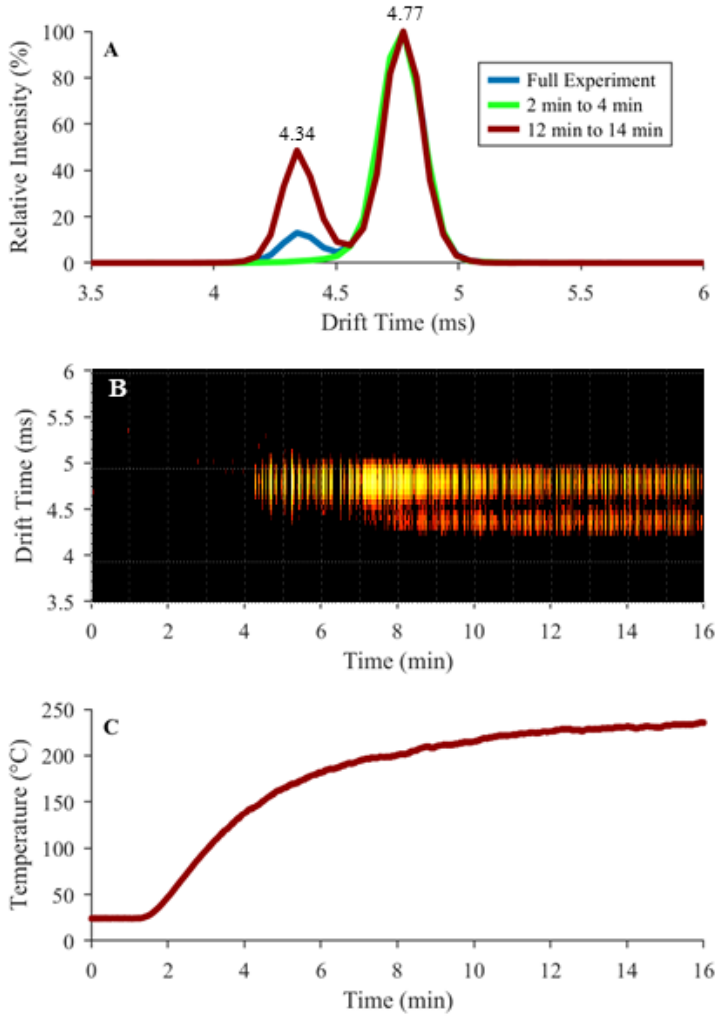

Figure 3-4 Investigation of pyro-VaPI ion abundances for nylon 6-6 (polyhexamethylene adipamide) at various time-points of a temperature gradient. (A) The cumulative arrival time distribution, the arrival time distribution between 2 and 4 minutes of the temperature gradient, and the arrival time distribution between 12 and 14 minutes of the gradient for the cyclic dimer ion extracted at m/z 453.36 showing two different species for nylon 6-6. (B) IM drift time vs. temperature gradient time for m/z 453.36. The intensity was log scaled. The minimum intensity threshold was set at 54 %. (C) Temperature profile of the shallow cup pyrolysis experiment measured with a thermocouple.

3.5 Conclusions

We have coupled a pyrolysis device to a VaPI ion source to combine the capabilities of thermal desorption/pyrolysis, soft ambient plasma ionization, ion mobility, and MS/MS into one platform. In addition, we have discovered unique isobaric species that nylons 6, 6-6, 6-9, 6-10, and 6-12 can release once a certain pyrolysis temperature is reached. With pyro-VaPI, improved identification and new potential mechanistic discoveries of pyrolyzed polymer molecular interactions can be achieved by combining the information gathered from volatilities, collisional cross sections, and *m/z* values.

3.6 References

1. Causin, V.: Polymers on the crime scene: How can analytical chemistry help to exploit the information from these mute witnesses? Anal. Methods. 2, 792–804 (2010). doi:10.1039/c0ay00115e

2. Ranganathan, T., Beaulieu, M., Zilberman, J., Smith, K.D., Westmoreland, P.R., Farris, R.J., Coughlin, E.B., Emrick, T.: Thermal degradation of deoxybenzoin polymers studied by pyrolysis-gas chromatography/mass spectrometry. Polym. Degrad. Stab. 93, 1059–1066 (2008). doi:10.1016/j.polymdegradstab.2008.03.021

3. Rial-Otero, R., Galesio, M., Capelo, J.-L., Simal-Gándara, J.: A Review of Synthetic Polymer Characterization by Pyrolysis–GC–MS. Chromatographia. 70, 339–348 (2009). doi:10.1365/s10337-009-1254-1

4. Shimizu, Y., Munson, B.: Pyrolysis/chemical ionization mass spectrometry of polymers. J. Polym. Sci. Polym. Chem. Ed. 17, 1991–2001 (1979). doi:10.1002/pol.1979.170170709

5. Qian, K., Killinger, W.E., Casey, M., Nicol, G.R.: Rapid Polymer Identification by In-Source Direct Pyrolysis Mass Spectrometry and Library Searching Techniques. Anal. Chem. 68, 1019–1027 (1996). doi:10.1021/ac951046r

6. Tran, J.C., Doucette, A.A.: Cyclic polyamide oligomers extracted from nylon 66 membrane filter disks as a source of contamination in liquid chromatography/mass spectrometry. J. Am. Soc. Mass Spectrom. 17, 652–656 (2006). doi:10.1016/j.jasms.2006.01.008

7. Tuinman, A.A., Lewis, L.A., Lewis, S.A.: Trace-Fiber Color Discrimination by

Electrospray Ionization Mass Spectrometry: A Tool for the Analysis of Dyes Extracted from Submillimeter Nylon Fibers. (2003). doi:10.1021/AC020618M

8. Skelton, R., Frédéric, D., Zenobi, R.: A MALDI Sample Preparation Method Suitable for Insoluble Polymers. (2000). doi:10.1021/AC991181U

9. Hanton, S.D., Parees, D.M.: Extending the solvent-free MALDI sample preparation method. J. Am. Soc. Mass Spectrom. 16, 90–93 (2005). doi:10.1016/J.JASMS.2004.09.019

10. Paine, M.R.L., Barker, P.J., Blanksby, S.J.: Ambient ionisation mass spectrometry for the characterisation of polymers and polymer additives: A review. Anal. Chim. Acta. 808, 70–82 (2014). doi:10.1016/J.ACA.2013.10.001

11. McEwen, C.N., McKay, R.G., Larsen, B.S.: Analysis of solids, liquids, and biological tissues using solids probe introduction at atmospheric pressure on commercial LC/MS instruments. Anal. Chem. 77, 7826–7831 (2005). doi:10.1021/ac051470k

12. Trimpin, S., Wijerathne, K., McEwen, C.N.: Rapid methods of polymer and polymer additives identification: Multi-sample solvent-free MALDI, pyrolysis at atmospheric pressure, and atmospheric solids analysis probe mass spectrometry. Anal. Chim. Acta. 654, 20–25 (2009). doi:10.1016/J.ACA.2009.06.050

13. Barrère, C., Maire, F., Afonso, C., Giusti, P.: Atmospheric Solid Analysis Probe–Ion Mobility Mass Spectrometry of Polypropylene. Anal. Chem. 84, 9349–9354 (2012). doi:10.1021/ac302109q

14. Barrère, C., Selmi, W., Hubert-Roux, M., Coupin, T., Assumani, B., Afonso, C., Giusti, P.: Rapid analysis of polyester and polyethylene blends by ion mobility-mass spectrometry. Polym. Chem. 5, 3576–3582 (2014). doi:10.1039/C4PY00164H

15. Farenc, M., Witt, M., Craven, K., Barrère-Mangote, C., Afonso, C., Giusti, P.: Characterization of Polyolefin Pyrolysis Species Produced Under Ambient Conditions by Fourier Transform Ion Cyclotron Resonance Mass Spectrometry and Ion Mobility-Mass Spectrometry. J. Am. Soc. Mass Spectrom. 28, 507–514 (2017). doi:10.1007/s13361-016-1572-0

16. Marić, M., Marano, J., Cody, R.B., Bridge, C.: DART-MS: A New Analytical Technique for Forensic Paint Analysis. Anal. Chem. 90, 6877–6884 (2018). doi:10.1021/acs.analchem.8b01067

17. Liang, J., Frazier, J., Benefield, V., Chong, N.S., Zhang, M.: Forensic Fiber Analysis by Thermal Desorption/Pyrolysis-Direct Analysis in Real Time-Mass Spectrometry. Anal. Chem. 92, 1925–1933 (2020). doi:10.1021/acs.analchem.9b04167

18. Cody, R.B., Fouquet, T.: "reverse Kendrick Mass Defect Analysis": Rotating Mass Defect Graphs to Determine Oligomer Compositions for Homopolymers. Anal.

Chem. 90, 12854–12860 (2018). doi:10.1021/acs.analchem.8b03413

19. Cody, R.B., Fouquet, T.N.J., Takei, C.: Thermal desorption and pyrolysis direct analysis in real time mass spectrometry for qualitative characterization of polymers and polymer additives. Rapid Commun. Mass Spectrom. 34, (2020). doi:10.1002/rcm.8687

20. Keelor, J.D., Farnsworth, P.B., L. Weber, A., Abbott-Lyon, H., Fernández, F.M.: Multimodal Vacuum-Assisted Plasma Ion (VaPI) Source with Transmission Mode and Laser Ablation Sampling Capabilities. J. Am. Soc. Mass Spectrom. 27, 897–907 (2016). doi:10.1007/s13361-016-1354-8

21. Blair, S.L., Ng, N.L., Zambrzycki, S.C., Li, A., Fernández, F.M.: Aerosol Vacuum-Assisted Plasma Ionization (Aero-VaPI) Coupled to Ion Mobility-Mass Spectrometry. J. Am. Soc. Mass Spectrom. 29, 635–639 (2018). doi:10.1007/s13361-017-1872-z

22. Goodman, I.: The thermal degradation of 66 nylon: Further studies on the pyrolysis of di-n-butyl adipamide. J. Polym. Sci. 17, 587–590 (1955). doi:10.1002/pol.1955.120178610

23. Ohtani, H., Nagaya, T., Sugimura, Y., Tsuge, S.: Studies on thermal degradation of aliphatic polyamides by pyrolysis-glass capillary chromatography. J. Anal. Appl. Pyrolysis. 4, 117–131 (1982). doi:10.1016/0165-2370(82)80003-X

24. Ballistreri, A., Garozzo, D., Giuffrida, M., Impallomeni, G., Montaudo, G.: Primary thermal decomposition processes in aliphatic polyamides. Polym. Degrad. Stab. 23, 25–41 (1989). doi:10.1016/0141-3910(89)90066-9

25. Lehrle, R.., Parsons, I.., Rollinson, M.: Thermal degradation mechanisms of nylon 6 deduced from kinetic studies by pyrolysis-g.c. Polym. Degrad. Stab. 67, 21–33 (2000). doi:10.1016/S0141-3910(99)00112-3

26. Abe, Y., Ackerman, L.K., Mutsuga, M., Sato, K., Begley, T.H.: Rapid identification of polyamides using direct analysis in real time mass spectrometry. Rapid Commun. Mass Spectrom. 34, (2020). doi:10.1002/rcm.8707

PART 2. RAPID PHARMACEUTICAL QUALITY SCREENING

CHAPTER 4. LABORATORY EVALUATION OF TWELVE PORTABLE DEVICES FOR MEDICINE QUALITY SCREENING

Adapted with permission from:

Zambrzycki, S., Caillet, C., Vickers, S., Bouza, M., Donndelinger, D.V., Geben, L.C., Bernier, M., Newton, P.N., Fernández, F.M. "Laboratory evaluation of twelve portable devices for medicine quality screening." PLOS Negl. Trop. Dis. Accepted April 2021.

4.1 Abstract

4.1.1 Background:

Post-market surveillance is a key regulatory function to prevent substandard and falsified (SF) medicines from being consumed by patients. Field deployable technologies offer the potential for rapid objective screening for SF medicines.

4.1.2 Methods and Findings:

We evaluated twelve devices: three near infrared spectrometers (MicroPHAZIR RX, NIR-S-G1, Neospectra 2.5), two Raman spectrometers (Progeny, TruScan RM), one mid-infrared spectrometer (4500a), one disposable colorimetric assay (Paper Analytical Devices, PAD), one disposable immunoassay (Rapid Diagnostic Test, RDT), one portable liquid chromatograph (C-Vue), one microfluidic system (PharmaChk), one mass spectrometer (QDa), and one thin layer chromatography kit (GPHF-Minilab). Each device was tested with a series of field collected medicines (FCM) along with simulated medicines

(SIM) formulated in a laboratory. The FCM and SIM ranged from samples with good quality active pharmaceutical ingredient (API) concentrations, reduced concentrations of API (80% and 50% of the API), no API, and the wrong API. All the devices had high sensitivities (91.5 to 100.0%) detecting medicines with no API or the wrong API. However, the sensitivities of each device towards samples with 50% and 80% API varied greatly, from 0% to 100%. The infrared and Raman spectrometers had variable sensitivities for detecting samples with 50% and 80% API (from 5.6% to 50.0%). The devices with the ability to quantitate API (C-Vue, PharmaChk, QDa) had sensitivities ranging from 91.7 % to 100 % to detect all poor quality samples. The specificity was lower for the quantitative C-Vue, PharmaChk, & QDa (50.0% to 91.7%) than for all the other devices in this study (95.5% to 100%).

4.1.3 Conclusions:

The twelve devices evaluated could detect medicines with the wrong or none of the APIs, consistent with falsified medicines, with high accuracy. However, API quantitation to detect formulations similar to those commonly found in substandards proved more difficult, requiring further technological innovation.

4.2 Introduction

Poor quality medicines are classified by the World Health Organization (WHO) as substandard or falsified (SF)[1]. Falsified medicines purport to be real, authorized medicines, but they ‘deliberately/fraudulently misrepresent their identity, composition or source'[1]. Falsified medicines are the result of criminal activity and usually have packaging that is a copy of a genuine product. They may contain the incorrect amount of

the correct active pharmaceutical ingredient (API), wrong API(s), or more commonly, no API at all. Substandard medicines are those authorized medical products 'that fail to meet either their quality standards or their specifications, or both' [1]. They negate the benefits of modern medicines, failed treatments, increased antimicrobial resistance, and distrust in the health system [2].

The recent expansion of the diversity of portable devices for medicine quality screening holds great hope for empowering inspectors in the field, making their work more cost-effective and actionable, improving MRA capacity, and protecting patients from the harms of SF medicines. However, significant knowledge gaps exist regarding the optimal choice of device, or combination of devices. These gaps impede decisions on how to best use these portable devices [3, 4].

We undertook a multi-phase collaborative project to evaluate diverse devices for SF medicine detection, producing key information required for deciding which of these technologies may be the most appropriate for field medicine quality screening. In this study we present the results for the evaluation of 12 portable screening technologies for distinguishing between genuine good quality, 50% and 80% API medicines (mimicking substandard medicines), and 0% and wrong API medicines (mimicking falsified products) under controlled laboratory conditions. We close with suggestions of which devices were prioritized for field testing, described in the third paper of the series.

4.3 Experimental

4.3.1 Devices:

Following a detailed literature review [5] and further discussions with experts, twelve devices were chosen for evaluation (Table 1). These included single-use Paper Analytical Devices (PAD), Rapid Diagnostic Tests (RDT), a portable liquid chromatograph, a single quadrupole benchtop mass spectrometer, the PharmaChk microfluidic device, an attenuated total reflectance mid-IR (MIR) spectrometer, three different near-infrared (NIR) spectrometers, two Raman spectrometers, and the Minilab thin layer chromatography kit.

These 12 devices were chosen to represent a variety of different technologies within the project's budget and time constraints. The ideal device should be portable, battery powered, durable, and require minimal training, consumables, sample preparation, and test the APIs included in this study. The two Raman spectrometers (TruScan RM and Progeny) were chosen for their different laser excitation sources. The infrared spectrometers (4500a, MicroPHAZIR RX, Neospectra 2.5, NIR-S-G1) were selected because they each had different testing modalities along with sampling in different infrared spectral ranges. The remaining devices were selected because they are representative of key technologies used in the screening of small molecule medicines.

Table 4-1 List of instruments and devices evaluated, including their underlying technology and basic instrument specifications.

Technology	***Device Name (Manufacturer)***	***Basic Instrument Specifications***	***APIs Tested***	***Market Status at the Time of this Study***
Colorimetric Assay	Paper Analytical Devices (PAD, Notre Dame University).	12 colorimetric chemical tests on a single-use paper card.	A, AZITH, P, OFLO, & SM	Under Development [6–8]
Lateral Flow Immunoassay	Rapid Diagnostic Tests, (RDT, China Agricultural University of Beijing and University of Pennsylvania).	Single-use disposable dipsticks, concentration specific.	Artemether, ART, & DHA	Under Development [9–11]
Liquid Chromatography	C-Vue (C-Vue).	Mercury lamp (≈254 nm) detector; Millipore Chromolith RP18e 25 x 4.6 mm column.	ACA, OFLO, & SMTM	Marketed [12]
Mass Spectrometry	QDa (Waters).	Selected ion monitoring mode per API; flow injection analysis.	All	Marketed [13]
Microfluidics	PharmaChk (Boston University).	Luminescence detection, 490 & 515 nm LED & filters.	ART	Under Development [14]
Mid-Infrared Spectroscopy	4500a FTIR Single Reflection† (Agilent)	Attenuated Total Reflectance. Spectral range: 2,500-15,384 nm.	All	Marketed [15]
Near-Infrared Spectroscopy	NeoSpectra 2.5* (Si-Ware).	Spectral range: 1,350-2,500 nm.	All	Marketed [16]
	MicroPHAZIR RX*† (Thermo Fisher Scientific).	Spectral range: 1,600-2,400 nm.	All	Marketed [17]
	NIR-S-G1*†° (Innospectra).	Spectral range: 900-1,700 nm.	All	Marketed [18, 19]
Raman Spectroscopy	Progeny*† (Rigaku).	Excitation Laser: 1,064 nm, Spectral range 200-2,500 cm^{-1}.	All	Marketed [20]
	TruScan RM*† (Thermo Fisher Scientific).	Excitation Laser: 785 nm, Spectral range 250-2,875 cm^{-1}.	All	Marketed [21]
Thin Layer Chromatography	Minilab‡ (Global Pharma Health Fund E.V.).	Detection by chemical staining and UV light exposure.	All	Marketed [22]

A: Amoxicillin; API, Active pharmaceutical ingredient; ART: Artesunate; AZITH: Azithromycin; CA: Clavulanic Acid; DHA: Dihydroartemisinin; FTIR: Fourier Transform Infrared, OLFO: Ofloxacin; P: Piperaquine; SM: Sulfamethoxazole; TM: Trimethoprim.

*Instrument/device could also scan samples through transparent packaging.

†Automatic spectral reference library comparison capabilities.

‡Only TLC portion of the Minilab was used in this study, but not the dissolution and weighing tests.

°Also referred to in this study as, "NIRscan", the beta version used in this study

4.3.2 Samples:

Antibiotic and antimalarial formulations represent a majority of the total number of SF medicines reported to the WHO Global Surveillance and Monitoring System between 2013-2017 [23]. Seven key antibiotics and antimalarials used in South-East Asia were chosen for device evaluation: AL=Artemether-Lumefantrine; ART=Artesunate; AZITH=Azithromycin; ACA= Amoxicillin-Clavulanic Acid; DHAP=Dihydroartemisinin-Piperaquine; OLFO=Ofloxacin; and SMTM=Sulfamethoxazole-Trimethoprim.

Field-collected medicines (FCM) and simulated medicines (SIM) were used to test the devices. FCM included good quality, falsified, and "look-alike" medicines. All FCM samples were tested with ultra-performance liquid chromatography (UPLC) or mass spectrometry (MS) to ensure quality. Good quality FCM were purchased from reliable wholesalers in the Greater Mekong Sub-Region or donated by manufacturers. Falsified FCM were collected during earlier studies (see [24] and references therein). Look-alike FCM were visually indistinguishable from genuine medicines, and contained APIs not evaluated in this study [25]. Five brands of FCM were sold in transparent packaging such as clear plastic blister packs or clear glass vials. Five devices tested claimed to be capable of performing nondestructive testing through transparent barriers (Table 1). Whenever feasible, FCM were also evaluated while sealed in their original packaging. Field-collected parenteral artesunate (Artesun) powder was removed from the vial and transferred to a plastic re-sealable bag for testing with Raman instruments because the powder was too dispersed in the original vial for one of the spectrometers to yield a stable signal and a consistent result. Device operators were not blinded to the identity of the samples being tested.

Most portable devices are only stated as able to check the presence/absence of the API or whole formulation spectra. Therefore, we did not examine dissolution rates, homogeneity of the API distribution within tablets, or tablet coating thicknesses. SIM were produced in the laboratory to mimic good quality, 80% and 50% API concentration tablets, mimicking substandard medicines, and no API and wrong API tablets, mimicking falsified medicines. All SIM were prepared as 100 mg 6 mm-diameter tablets, except for ART which was tested as a loose powder to simulate Artesun. ART, AZITH, OLFO, and SMTM powders (>98% purity) were purchased from TCI Chemical (Portland, OR). The simulated ACA, AL, and DHAP medicines, were produced from good quality FCM (AMK 1000 mg for ACA, Coartem for AL, and D-Artepp for DHAP) that were crushed, mixed, and re-pressed into SIM tablets. The excipients included cellulose, lactose, or starch as the bulking agents, and magnesium stearate as the lubricant, all sourced from Sigma Aldrich (St. Louis, MO). The only ingredient in FCM genuine artesunate intravenous vials was artesunate. Magnesium stearate was thus excluded from the ART SIM formulation to simulate a loose powder intravenous artesunate. To mimic 80% and 50% substandards, the excipients listed above were added to dilute the API. Acetaminophen was used as the wrong API for falsified SIM and was sourced from Sigma Aldrich (St. Louis, MO).

4.3.3 Data Analysis:

When testing medicine samples, devices generated results that were either qualitative or quantitative. Qualitative results were based upon pattern comparison between a known good quality medicine reference and the test medicine sample data. PAD chemically reacted with the medicine ingredients generating a color pattern, that was then visually compared to a reference photograph to determine the presence of an API. The

4500a, MicroPHAZIR RX, NIR-S-G1, Progeny, and TruScan RM spectrometers computationally compared experimentally-collected spectra to reference spectra of good quality medicines stored in the device's database. Each sample spectrum acquired was given a score by the device software resulting from the comparison with the good quality reference medicine spectrum. Such scores had to meet a given threshold to determine if a medicine passed (Figure 4-1 A). For the NIR-S-G1 spectrometer, reference samples were sent to the developer who prepared the reference libraries. The passing threshold values for the correlation coefficient or p-value testing initially set as default by the developer in the MicroPHAZIR RX, NIR-S-G1, Progeny, and TruScan RM spectrometers were utilized. These devices would directly tell the user 'pass' or 'fail', which were recorded. The pass threshold for the 4500a MIR spectrometer's correlation coefficient was set by us at >0.9 because the device would not output a direct pass/fail result, but rather give a list of matches with their associated correlation coefficients. The Neospectra 2.5 spectrometer did not include software to compare the experimentally-collected spectra to reference spectra. Therefore, experimental Neospectra 2.5 spectra were overlaid with reference spectra and visually compared by an analyst blinded to sample identity for determining the final pass/fail result.

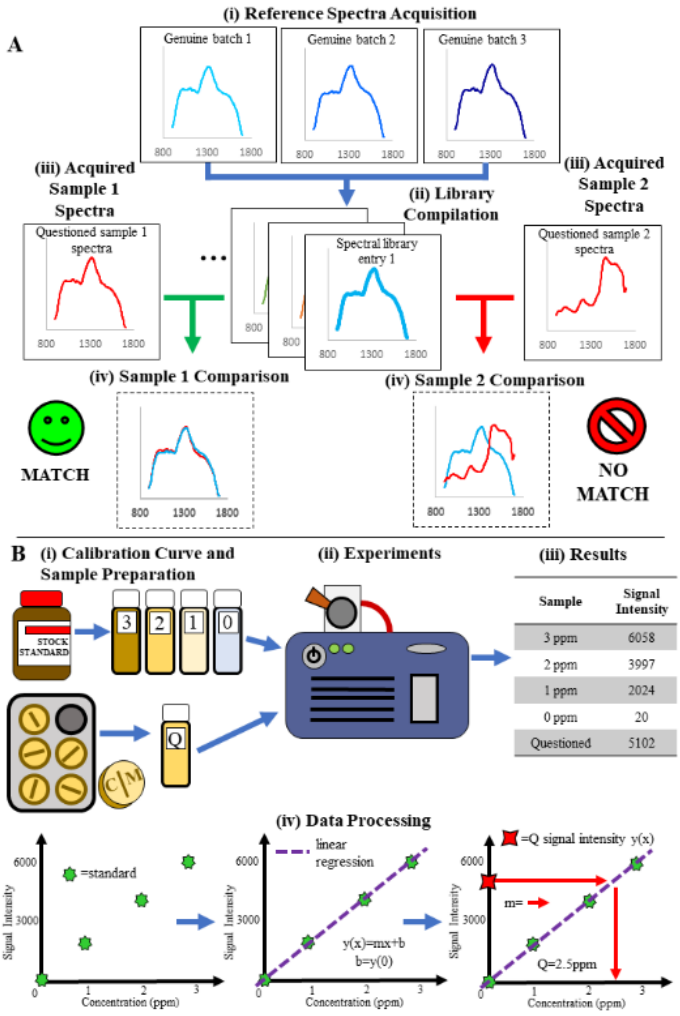

Figure 4-1 Illustration of the basic processes for qualitative spectral comparison and quantitative analysis. (A) Process for reference library creation and spectral comparison analysis. From top to bottom: (i) spectra are collected from different batches of the same medicine and compiled into a mean spectrum representative of that medicine. (ii) This mean spectrum is used to build a "library" or database that serves as the comparator against which test samples are compared. (iii) Test samples are scanned and then (iv) the test sample spectra are overlaid with the reference spectrum for visual or computational comparison to determine a pass or fail. (B) Illustration of a basic quantitative experiment. From left to right and top to bottom. (i) A set of standard calibration samples with increasing API concentration is prepared along with a solution of the test sample that should fit in the concentration range of those standards. (ii) All solutions are then tested on the instrument and (iii) the data collected. (iv) The data obtained is then used to build a calibration curve via linear least-squares regression. Interpolation of the peak area of the questioned sample into this curve yields the estimated API concentration.

To estimate the amount of API with quantitative instruments (C-Vue, PharmaChk and QDa) a calibration curve approach was used (Figure 4-1 B). After sample preparation and data acquisition with the instruments, the calculated API amount had to be within ± 10 % of the stated API amount for the sample to be classified as good quality, for both single and combination API medicines. We considered that medicines with %API outside the 90-110% range of the manufacturer's stated amount of API(s) were out of specification for any API included. For co-formulations, the entire medicine was deemed out of specification if at least one of the API was not within the 90-110% range.

Both the RDT and the Minilab-TLC are semi-quantitative devices. RDT rely on the color density of control and test lines to confirm the presence of an API at a specific concentration. The TLC portion of the Minilab kit relies on the size and migration distance of a spot that is formed by a small sample deposited on the TLC plate, compared to a good quality reference standard on the same plate.

When a sample failed the first test, we operated a 'best of three' system for overall sample classification (out of the three tests performed on the failing samples, the most frequently occurring of 'pass' or 'fail' would then be the overall sample classification), in the absence of devices manufacturer's guidelines. For the single-use RDT the failing samples were rerun only once due to a limited number of tests available. For the PAD, the failing samples were rerun once, as recommended by the developer. For both the RDT and PAD a third run was conducted when the first two test results were discordant, and the 2/3 majority result was retained.

4.3.4 Statistical Analysis:

The overall sample binary classification (‘pass’ or ‘fail’) was used to calculate the sensitivity and specificity for each instrument. Sensitivity was defined as the percentage of true positives over the total of true positives and false negatives, and specificity as the percentage of true negatives over the total of true negatives and false positives. A true positive was defined as the sample being poor quality with the device correctly giving a fail result. Sensitivity and specificity were expressed as percentages with their 95% confidence intervals (95% CI). The exact confidence interval was based on Jeffreys’ confidence interval formula [26]. Sensitivities and specificities were compared by device pairs using McNemar tests. Data analysis was carried out using Microsoft Excel 2013 and STATA 14.2. The level of significance was set at p=0.05 (two-sided).

To gauge whether the passing correlation coefficient or p-value threshold values initially set in the 4500a, MicroPHAZIR RX, Progeny, and TruScan RM spectrometers were optimal, receiver operating characteristic (ROC) curves were created. Only substandard and good quality SIM were used in the ROC curve analysis because these samples were shown to be the most challenging for the devices to distinguish. A variety of thresholds were tested to best visualize the curve and optimize the sensitivity and false positive rate (1-specificity). ROC curve analysis was also applied to the C-Vue, PharmaChk, and QDA, but the correlation coefficient or p-value thresholds were replaced with percent concentration thresholds.

4.4 Results

All devices showed 100% sensitivity to correctly identify tablets with 0% or wrong API after removal from their packaging, except for the NIR-S-G1 that showed a sensitivity

(95% CI) of 91.5% (79.6-97.6%,). Specificities of 100% were observed for most of the devices, except the C-Vue [60.0% (32.3-83.7%)], PharmaChk [50.0% (1.3-98.7%)], Progeny [95.5% (77.2-99.9%)] and the QDa [91.7% (73.0-99.0%)] (Table 2). The following subsections detail significant strengths and weaknesses observed for each during testing.

Table 4-2 Sensitivity and specificity to correctly determine quality of medicine samples for the 12 tested devices.

Devices	**0% API and wrong API samples**		**Genuine Good Quality**		**50% and 80% API samples**		**All poor quality samples**	
--------	**Sensitivity (95% CI)**	**n**	**Specificity (95% CI)**	**n**	**Sensitivity (95% CI)**	**n**	**Sensitivity (95% CI)**	**n**
*4500a FTIR**	100 (93.3-100)	53	100 (85.8-100)	24	28.6 (15.7-44.6)	42	68.4 (58.1-77.6)	95
C-Vue	100 (82.4-100)	19	60.0 (32.3-83.7)	15	100 (81.5-100)	18	100 (90.5-100)	37
*MicroPHAZIR RX**	100 (92.5-100)	47	100 (84.6-100)	22	50.0 (32.9-67.1)	36	78.3 (67.9-86.6)	83
Minilab	100 (93.3-100)	53	100 (85.8-100)	24	59.5 (43.3-74.4)	42	82.1 (72.9-89.2)	95
*Neospectra 2.5**	100 (92.5-100)	47	100 (84.6-100)	22	5.6 (0.7-18.7)	36	59.0 (47.7-69.7)	83
*NIR-S-G1**	91.5 (79.6-97.6)	47	100 (84.6-100)	22	30.6 (16.3-48.1)	36	65.1 (53.8-75.2)	83
PAD	100 (88.8-100)	31	100 (83.2-100)	20	0 (0-11.6)	30	50.8 (37.7-63.9)	61
PharmaChk	100 (54.1-100)	6	50.0 (1.3-98.7)	2	83.3 (35.9-99.6)	6	91.7 (61.5-99.8)	12
*Progeny**	100 (92.5-100)	47	95.5 (77.2-99.9)	22	16.7 (6.4-32.8)	36	63.9 (52.6-74.1)	83
QDa	100 (93.3-100)	53	91.7 (73.0-99.0)	24	100 (91.6-100)	42	100 (96.2-100)	95
RDT	100 (73.5-100)	12	100 (29.2-100)	3	16.7 (2.1-48.4)	12	58.3 (36.6-77.9)	24
*TruScan RM**	100 (92.5-100)	47	100 (84.6-100)	22	22.2 (10.1-39.2)	36	66.3 (55.1-76.3)	83

*With substantial and upfront work, optical spectrometers could theoretically perform API quantitation. Parameters could be adjusted for better analysis of medicines containing lower-than-stated amount of API(s). However, in this study, only default parameters provided by the manufacturer were used. It is believed, however, that potential enhancements in sensitivity and specificity could be made by optimizing threshold values and experimental settings for specific medicines.

4.4.1 Thin Layer Chromatography: Minilab

The Minilab TLC kit consisted of a hard-shell case containing all the chemical analysis equipment necessary to perform TLC experiments. It correctly characterized all good quality, no-API falsified, and wrong-API falsified FCM and SIM. Only 1 out of 21 of the SIM 50% API substandards were misidentified as good quality. A majority (16/21) of SIM 80% API substandards were misidentified as good quality as differences between the 100% and 80% reference spots on the TLC plates were difficult to distinguish visually. The Minilab is designed to detect samples with API below 80% API. The primary limitation identified was the higher requirements in terms of resources needed to conduct experiments, and the difficulties associated with visual interpretation of the results. Its primary strength was the wide variety of APIs covered and its detailed instructions.

4.4.2 Single Use Devices: PAD and RDT

The PAD are paper card colorimetric assays with 12 testing lanes. Test samples were applied by rubbing them onto the testing lanes. The bottom of the cards are placed in water, where they develop to generate a color pattern that confirms the presence (or not) of a given API. They correctly characterized all good quality, no-API falsified, and wrong-API falsified FCM and SIM. The PAD were not designed to detect substandard medicines containing lower API amounts than stated and all 50% and 80% API substandards samples were incorrectly classified as good quality. The primary limitation of PAD was that the colors were difficult to interpret for weakly colored reaction products. Their primary strengths were that the experiments required minimal effort and consumables.

RDT are lateral flow immunoassays that typically target a single API. They have the stated capability of distinguishing between substandard and falsified antimalarials. A subset of the RDT tested claimed to be able to detect artemether in artemether-lumefantrine co-formulated medicines. These RDT, however, were defective and not considered further. RDT specific for DHA and ART had a sensitivity of 16.7% in detecting substandards. RDT correctly characterized all the remaining good quality, no-API falsified, and wrong-API FCM and SIM. The primary limitations of RDT were the additional consumables required for their operation and the relatively extensive sample preparation needed compared to PAD. In a few cases it was difficult to read the RDT control lines on the cartridges due to inconsistent colors observed between RDT units. One advantage of RDT over PAD was their ability to detect some substandards.

4.4.3 MIR Spectrometer: 4500a

The 4500a is a MIR spectrometer that performs attenuated total reflection experiments on powdered samples. It is controlled through a computer or Windows-based smartphone. With a correlation coefficient threshold of >0.9 for pass/fail analysis, the 4500a MIR spectrometer correctly characterized all good quality, no-API falsified, and wrong-API falsified FCM and SIM. None of the 80% API substandard SIM were correctly classified as poor quality; however, over half (12/21) of the 50% API substandard SIM were correctly classified as poor quality. Primary weaknesses were its inability to test through transparent packaging because many plastics completely absorb MIR radiation, and the need to crush samples into powders. A major strength of the 4500a MIR spectrometer software was the step-by-step instructions provided to aid in correcting background, cleaning the unit, and labeling IR spectra.

4.4.4 NIR Spectrometers: Neospectra 2.5, NIR-S-G1, & MicroPHAZIR RX

The Neospectra 2.5 Fourier transform NIR detector module can be used to build a device that fits a user's custom needs. It correctly characterized all good quality, no-API falsified, and wrong-API falsified FCM and SIM. All the 80% API substandards and 16 out of 21 of the 50% API substandards were misidentified as good quality samples. The primary limitation was the inability to conduct automated spectral library matching. Although users can extract the raw spectra using third-party library comparison tools, this feature was not evaluated as it was outside the study scope. Its modularity was its primary strength, allowing to configure the system for sampling both solids and liquids. Its detector had the widest NIR wavelength range in this study, allowing for more spectral information to be collected.

The NIR-S-G1 NIR spectrometer is controlled by a smartphone via Bluetooth. Although this instrument correctly characterized all good quality medicines, it had difficulties in the analysis of the OFLO SIM. The no-API falsified, 50% substandard, and 80% substandard OFLO SIM were all incorrectly deemed as being good quality. This may have been because the limited device spectral range (Figure 4-2) did not reveal a sufficiently large number of significant features when comparing against the reference library entry. The library processing software was not able to detect the relatively small spectral differences observed in the ~1500 nm region (Figure 4-2 B). Since this device was able to correctly determine that the wrong-API OFLO medicines were poor quality, the API itself may have had limited NIR spectral features distinguishable from the excipients. Additionally, one falsified SIM sample containing only starch was misidentified as good quality DHAP. The simulated DHAP sample used D-Artepp as the source of API. It is

possible that if D-Artepp contained starch, this excipient may have contributed to the misclassification. Cellulose and lactose-containing falsified tablets were correctly characterized as poor quality DHAP. All other falsified samples were correctly identified. Four out of 21 (19%) of the 80% API substandards, and 10 out of 21 (48%) of the 50% API substandards were correctly identified as poor quality. The limited spectral range and limited chain-of-custody capabilities, which included the inability to record tested sample information in the software at the time of testing, were key limitations. The primary strengths were the user interface simplicity and that the NIR-S-G1 was the most portable spectrometer tested.

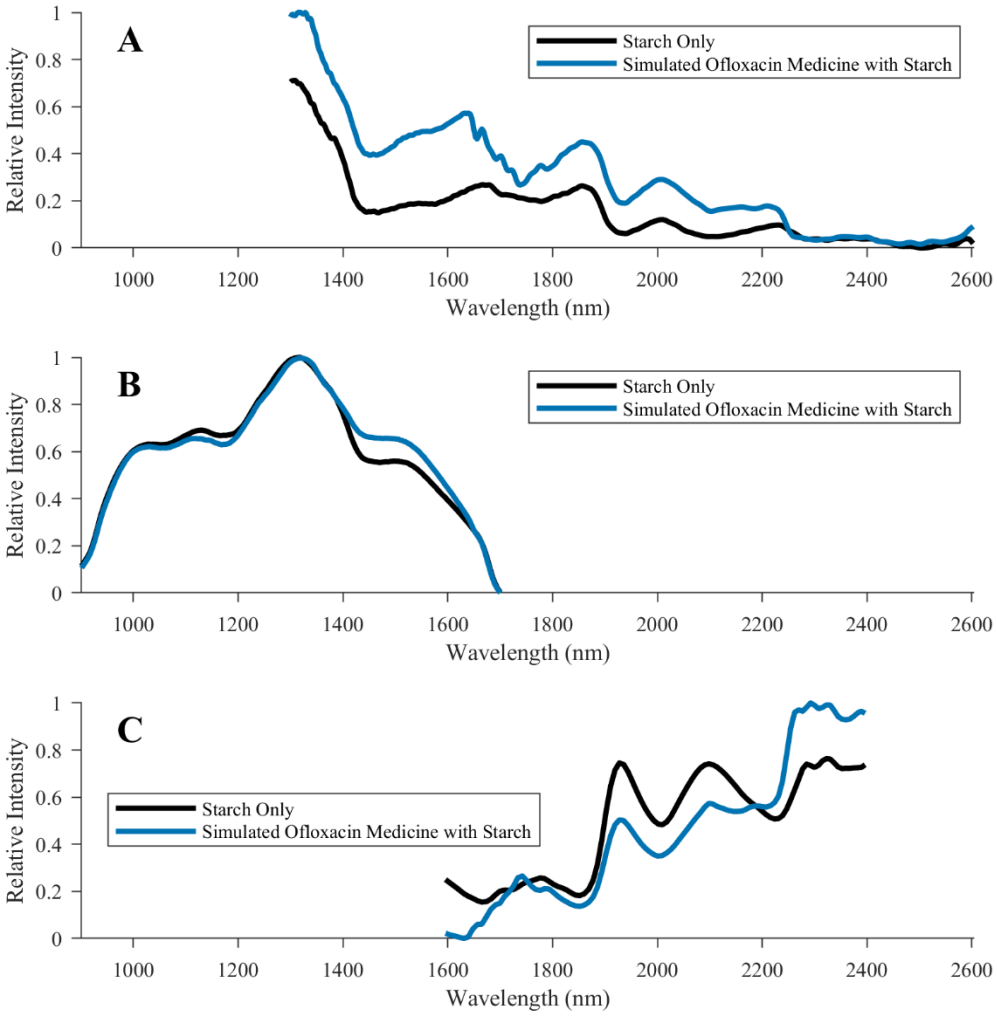

Figure 4-2 Comparison of NIR spectra obtained for ofloxacin-containing simulated medicines. Spectra were collected for ofloxacin-containing simulated medicines using the (A) Neospectra 2.5, (B) NIR-S-G1, and (C) MicroPHAZIR RX spectrometers. The black trace is of a falsified simulated medicine tablet containing only starch. The blue trace is of a simulated good quality ofloxacin sample that contained starch as the bulk excipient.

The MicroPHAZIR RX handheld NIR spectrometer contains the instrument and user interface in one module. It correctly characterized all good quality, 50% API substandard, no-API falsified, and wrong-API falsified FCM and SIM. Only 1 of the 21 (4.8%) 80% API SIM substandards was correctly classified as poor quality. The primary limitation of the MicroPHAZIR RX were the instrument's bulkiness and advanced skills necessary to process the spectra to generate reference libraries, but it had an easy-to-use interface.

4.4.5 Raman Spectrometers: Progeny and TruScan RM

The Progeny is a handheld Raman spectrometer with a 1064 nm excitation laser, resulting in lower fluorescence than shorter wavelength lasers. It correctly characterized all the no-API falsified and wrong-API falsified FCM and SIM. All good quality samples were correctly characterized, except the FCM Augmentin (ACA), which was incorrectly determined as being Roxythroxyl (roxithromycin). The outer tablet coating of Augmentin may have been chemically similar to that of Roxythroxyl, a spectrum stored in the master Progeny reference library. None of the 80% SIM substandards and only 7 out of 21 (33%) of the 50% SIM substandards were correctly characterized as poor quality. The Progeny spectrometer was heavier than other units (1.6 kg) and risked burning samples with the laser if the instrument's focal length was not properly set-up. The primary strengths were its simple to use touch screen interface, and the lack of fluorescence signals that could overwhelm the detector.

The TruScan RM is a handheld Raman spectrometer with a 756 nm excitation laser that correctly classified all the good quality, no-API falsified, and wrong-API falsified

medicines in the FCM and SIM collections. The device only correctly classified 3 out of 21 (14%) SIM 80% API, all three being DHAP samples. Seven out of 21 (33%) SIM 50 % API substandard were correctly classified. Limitations included the need for significant computer knowledge (e.g. setting up IP addresses, firewalls) to correctly complete the initial setup with the master computer and the excitation laser that caused significant fluorescence for ACA FCM and SIM samples when compared to the other non-destructive spectrometers tested. Sampling Artesun through the original sample glass vial yielded spectra that were indistinguishable from those of an empty glass vial, whereas this issue was not observed with the Progeny (Figure 4-3). The primary strengths of the TruScan RM were its relatively lower weight and bulkiness when compared with the Progeny and its ease of use.

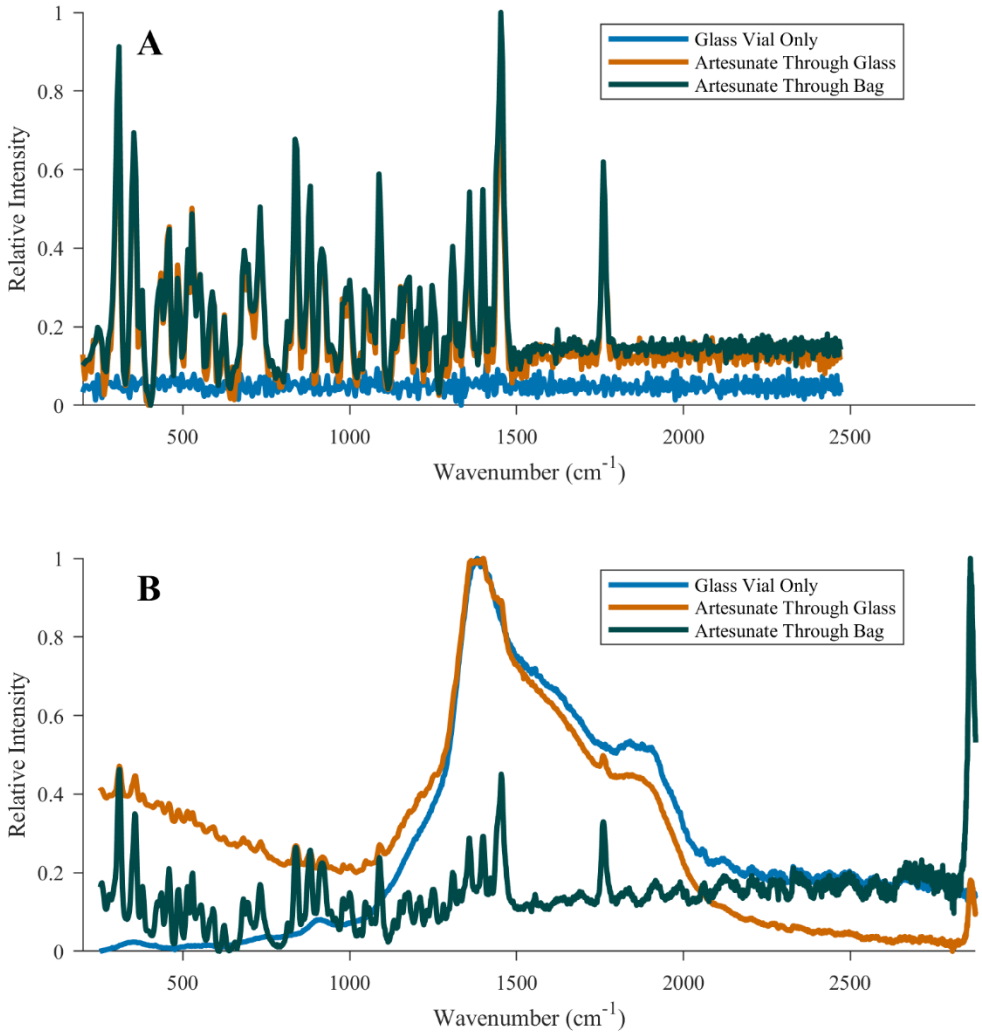

Figure 4-3 Comparison of Raman spectra obtained for Artesun artesunate powder. Raman spectra were collected with the (A) Progeny and (B) TruScan RM spectrometers for Artesun artesunate powder for injection. Spectra are provided for 1) a scan of the bottom of the Artesun glass vial containing no artesunate (blue trace), 2) a sample containing 60 mg of artesunate powder, scanned through the bottom of the glass vial (orange trace), and 3) the artesunate powder transferred to a polypropylene bag and compacted into a more localized area to enable more focused analysis (green trace).

4.4.6 Quantitative Instruments: C-Vue, PharmaChk, & QDa

The C-Vue is a portable lightweight tabletop liquid chromatograph equipped with a manual syringe pump, a manual injector, a reverse-phase column, two detectors, and a control laptop. It was able to correctly characterize all the 80% API substandard, 50% API substandard, no-API, and wrong-API OFLO, SMTM, and ACA. The C-Vue specificity was one of the lowest in this study (60% good quality FCM and SIM misidentified as poor quality), potentially due to matrix effects from the excipients that were not used in the preparation of the calibration solutions. The lowest specificity was observed for medicines formulated with more than one API (0% and 40% for ACA and SMTM, respectively), but none of the single API good quality OFLO FCM and SIM were misclassified. Two notable limitations are its inability to detect artemisinin derivatives with the setup tested and the significant effort required to continuously ensure that the pump was pressurized by hand. Newer versions of this instrument include an upgraded mobile phase electric pump that simplifies operation. Its primary strength was the simplicity of its design, making it easy to transport, repair, or modify in the field.

The PharmaChk is a portable microfluidic system that uses luminol-based chemiluminescence detection, contained inside a hard-shell case. The system can automatically calibrate itself and assay samples in a single experiment. It was able to correctly characterize all the 50% API substandard, no-API falsified, and wrong-API falsified ART SIM. One of the three 80% API substandards was misclassified as good quality. The FCM good quality ART was correctly classified, while the SIM 100% ART sample was incorrectly classified in two trials as poor quality, with yields of 51.6 mg (86%) and 53.75 mg (89.5%) of the stated 60 mg amount. Its primary limitations were that the

prototype used could only test for ART and the reagents degraded within a few hours after being prepared. Its primary strengths were the automation of all API concentration calculations in the embedded computer system, the capability of simultaneously infusing reagent and samples, and the clear step by step instructions.

The QDa is a benchtop single quadrupole mass spectrometer with an electrospray ion source. All the 80% API substandards, 50% API substandards, no-API falsified, and wrong-API falsified medicines were correctly classified. Two good quality FCM were misclassified as poor quality, likely due to incomplete API extraction. Limitations of the QDa were that it required significantly more extensive sample preparation than the C-Vue or the PharmaChk because it required several dilutions for the tested sample for the extracts to fall within the linear range of the instrument and not overwhelm the detector. The requirements for additional consumables such as compressed nitrogen gas, and the higher mechanical complexity of the instrument could make portability and serviceability challenging. Its primary strength was its quantitative capabilities for a wide range of APIs, and the high sample throughput once sample preparation was complete.

4.4.7 Device Comparison

Pair-wise comparisons of the sensitivities showed that no device had statistically significantly lower or higher sensitivities to correctly identify 0% and wrong API samples than any other device.

Specificity of the C-Vue was significantly lower than that of all other devices except the Progeny ($p=0.0625$) and the QDa ($p=0.1250$). The performances of the PharmaChk and RDT could not be compared with the C-Vue as this device was limited to

test ACA, OFLO and SMTM in the present study. Because only a few genuine medicine samples were available for specificity calculations, the interpretation of statistical comparisons is limited.

The C-Vue and QDa performed better to correctly identify 50% and 80% API samples than other devices they could be compared to, except the PharmaChk ($p<0.05$) (Table 3); the Minilab showed higher sensitivity than other devices, except the C-Vue, QDa, PharmaChk and MicroPHAZIR RX ($p<0.05$). The MicroPHAZIR RX showed higher sensitivity than other spectrometers ($p<0.05$) to correctly identify 50% and 80% API samples except the NIR-S-G1 ($p=0.0923$); the Neospectra 2.5 had lower sensitivity than other spectrometers ($p<0.05$) except the Progeny ($p=0.2188$). The PAD showed significantly lower sensitivity to correctly identify 50% and 80% API samples than the other devices except the RDT ($p=1.0$) and the Neospectra 2.5 ($p=0.50$) but the number of samples for comparisons was limited.

Table 4-3 Pair-wise sensitivity comparisons of the devices used to test 50 % and 80 % API samples outside their packaging. Sensitivities expressed as 95% CI, in grey. The p-value of the McNemar test (n=number of 0%/wrong API medicines assessed by both devices in the pair) is presented. The pairs for which a significant difference was observed are shown in orange, if any.

	4500a FTIR	**C-Vue**	**MicroPHAZIR RX**	**Minilab**	**Neospectra 2.5**	**NIR-S-G1**	**PADs**	**PharmaChk**	**Progeny**	**QDa**	**TruScan RM**	**RDT**
4500a FTIR	28.6 (15.7-44.6)											
C-Vue	**0.0005 (n=18)**	100 (81.5-100)										
MicroPHAZIR RX	**0.0078 (n=36)**	**0.0039 (n=18)**	50.0 (32.9-67.1)									
Minilab	**0.0002 (n=42)**	**0.0156 (n=18)**	0.6250 (n=36)	59.5 (43.3-74.4)								
Neospectra 2.5	**0.0215 (n=36)**	**<0.0001 (n=18)**	**<0.0001 (n=36)**	**<0.0001 (n=36)**	5.6 (0.7-18.7)							
NIR-S-G1	1 (n=36)	**0.0010 (n=18)**	0.0923 (n=36)	**0.0352 (n=36)**	**0.0117 (n=36)**	30.6 (16.3-48.1)						
PADs	**0.0078 (n=30)**	**<0.0001 (n=18)**	**0.0001 (n=30)**	**<0.0001 (n=30)**	0.5000 (n=30)	**0.0039 (n=30)**	0 (0-11.6)					
PharmaChk	0.2500 (n=6)	N/A	N/A	1 (n=6)	N/A	N/A	N/A	83.3 (35.9-99.6)				
Progeny	0.3438 (n=36)	**0.0001 (n=18)**	**0.0005 (n=36)**	**0.0001 (n=36)**	0.2188 (n=36)	0.1797 (n=36)	**0.0313 (n=30)**	N/A	16.7 (6.4-32.8)			
QDa	**<0.0001 (n=36)**	1 (n=18)	**<0.0001 (n=36)**	**<0.0001 (n=42)**	**<0.0001 (n=36)**	**<0.0001 (n=36)**	**<0.0001 (n=30)**	1 (n=6)	**<0.0001 (n=36)**	100 (91.6-100)		
TruScan RM	0.8036 (n=36)	**<0.0001 (n=18)**	**0.0213 (n=36)**	**0.0118 (n=36)**	**0.0313 (n=36)**	0.6072 (n=36)	**0.0078 (n=30)**	N/A	0.7539 (n=36)	**<0.0001 (n=36)**	22.2 (10.1-39.2)	
RDT	0.6250 (n=12)	N/A	0.2500 (n=6)	**0.0313 (n=12)**	0.5000 (n=6)	0.5000 (n=6)	1 (n=6)	0.25 (n=6)	1 (n=6)	**0.0020 (n=12)**	0.0625 (n=6)	16.7 (2.1-48.4)

4.5 Discussion

These results suggest that all tested devices are well-suited for detecting no API and wrong API medicines, these being common falsified medicines chemical compositions. Although detecting falsified medicines is of great public health importance, the co-detection of substandard medicines is also essential, especially as these will lead to cryptic therapeutic failure and engender antimicrobial resistance. Much needed technological improvements, as revealed by this study, are the ability to quantitate APIs *via* Raman/IR spectrometers or disposable devices, and improvement of the specificity of some of the quantitative devices. Although all substandards were successfully detected with quantitative devices, except two ART samples with the PharmaChk, their less-than-optimal specificity is of concern. Reduced specificities increase the number of confirmatory testing required in quality control laboratories, resulting in increasing cost and loss of time and resources. Quarantine or withdrawal of the samples failing the screening technologies from the market due to device limitations can also negatively impact manufacturers, pharmacies, and ultimately patients.

Many FCM tablets tested had coatings that made sampling of the tablet bulk difficult by spectroscopic techniques. To illustrate this point, the spectrometers (except the 4500a FTIR that cannot scan intact tablets) were used to sample AMK 1000 mg (ACA) tablets, both intact and crushed (Figure 4-4). The spectral fingerprint of the outer coating of intact tablets, depending on coating composition and thickness, may be insufficient to derive the quality of the medicine itself as a whole. Reference library creation could also be affected if the operator sampled the coating but attempted to match the spectrum to that

of a crushed tablet. We were unable to find evidence on the consequences of different coatings and their thickness on spectra [5].

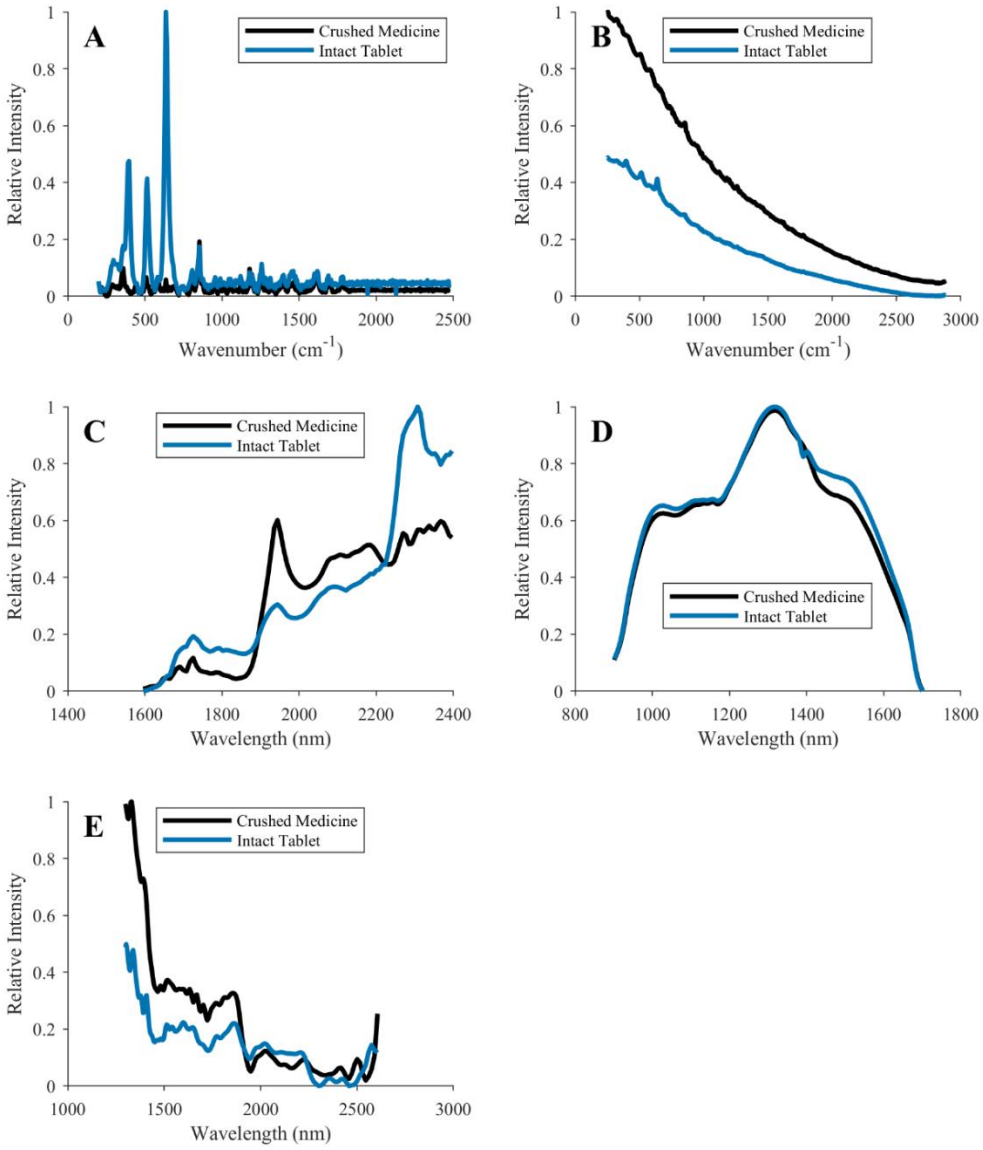

Figure 4-4 Intact vs. crushed ACA tablet analysis by Raman and NIR spectrometers. Spectral comparisons of a field collected sample of AMK 1000 mg (a co-formulation of amoxicillin and clavulanic acid) are shown with the (A) Progeny, (B) Truscan RM, (C) MicroPHAZIR RX, (D) NIR-S-G1, and (E) Neospectra 2.5 spectrometers. The spectra in blue are scans of an intact tablet of AMK 1000 mg. The spectra in black are scans of the powder from a crushed AMK 1000 mg tablet.

Optimization of the spectrometers' software's pass/fail threshold values in performing database matching could boost the instruments' sensitivities and specificities. The ROC curves constructed in Figure 4-5 for SIM with the 4500a, MicroPHAZIR RX, Progeny, and TruScan RM spectrometers show that setting a higher threshold improve devices sensitivities, but at the cost of reduced specificity. The quantitative devices' precision could also be optimized by adjusting the concentration threshold used for pass/fail decisions. Lowering the pass threshold concentrations for the quantitative devices (C-Vue, PharmaChk, & QDa) improves their specificities, but at the cost of reduced sensitivity. Therefore, the pass/fail threshold values for these instruments must be balanced to optimize the reliability of medicine quality classification. In most circumstances public health risks suggest that optimizing sensitivity for detecting SF medicines will be more important than specificity.

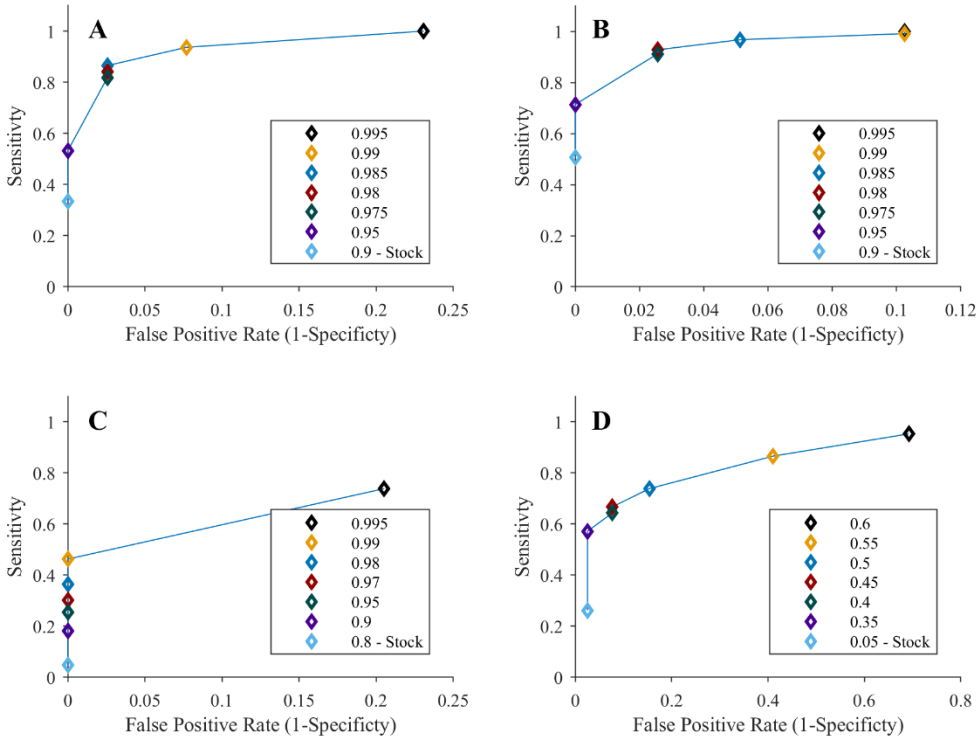

Figure 4-5 Receiver operating characteristic (ROC) curves for substandard analysis with the spectrometers. ROC curves were created for the (A) 4500a, (B) MicroPHAZIR RX, (C) Progeny, and (D) TruScan RM spectrometers. ROC curves were based only on the results for simulated substandard and good quality medicines. Each legend identifies the threshold chosen for each point, with the one labelled "Stock" being the threshold used for the study. The stock thresholds for the MicroPHAZIR RX's correlation coefficient, Progeny's correlation coefficient, and TruScan RM's p-value were the default values set by the manufacturer. The 4500a stock threshold was selected for the study since that instrument did not output pass/fail results.

Limitations of our study include: the limited number of APIs tested; difficulties with reference libraries creation for spectrometers; the limited comparability of reference libraries due to the variability of spectrometers; the investigators not being blinded to sample identity; the limited optimization of the devices to allow API quantitation; and the low power to compare sensitivities and specificities between devices.

With additional development and optimization, many of these devices may be able to perform both quantitative and qualitative analysis. For example, methods could be developed for spectrometers to perform quantitative analyses by selecting a spectral feature correlated to a specific chemical bond in an API, or by monitoring changes in the entire spectrum and correlate those to the differences in API concentration. A key obstacle to portable spectrometer quantitation would be instrument calibration per brand because they analyze the entire formulation that will vary between different excipient recipes. To ensure a reliable calibration at a variety of different API concentrations, the calibrants should be chemically similar to the medicine of interest due to potential matrix effects. The QDa mass spectrometer could be adapted for qualitative analysis by allowing the instrument to record the entire mass spectrum to analyze as many ingredients in the formulation as possible. However, analyzing a wider mass range risks less accurate quantitation compared to single ion monitoring used in this study.

Which device is optimal for different positions within the medicine distribution system will depend on the question being asked. For example, what type of medicine or API is tested, whether qualitative or quantitative assays are required, and what human and financial capacity is available. The Minilab, PAD, and RDT require minimal training and infrastructure to implement in the field rapidly. However, the PAD and RDT are limited

due to narrow range of detected API. The spectrometers have the advantages of being non-destructive (except the 4500a MIR spectrometer) and can analyze a broader API diversity. The spectrometers suffer from issues with tablet coatings, the spectral range of the NIR-S-G1 spectrometer, and fluorescence issues with the TruScan RM can reduce accuracy for some medicines. The smartphone simplicity with the NIR-S-G1 is highly desirable. With the increasing global prevalence of smartphone technology, connectivity using cell phone networks, and Wi-Fi to constantly update reference libraries, software, and back-up data could ensure these devices are performing to the best of their ability with rapid access to troubleshooting [27]. The simplicity of the C-Vue liquid chromatographer, the automation of the PharmaChk microfluidic system, and the sample variety and accuracy for the QDa mass spectrometer are all desirable traits for an optimal portable confirmatory instrument.

The following devices were selected for field testing described in the field evaluation in Laos - third paper of the PLOS NTD's collection: 4500a, Minilab, MicroPHAZIR RX, NIR-S-G1, PAD, Progeny, and TruScan RM. The main reasons were their ease of use, ease of training, portability, minimal consumables, and ease of export. The RDT were selected as field-suitable but could not be included in the field evaluation because not enough tests were available. The quantitative devices were not selected because of the consumables and training requirements. In addition, the QDa had high mechanical complexity, making export and setup difficult. The quantitative devices are highly capable, but the consumables and mechanical complexity make transport difficult and the devices would be more appropriate for a laboratory.

4.6 References

1. World Health Organization: A study on the public health and socioeconomic impact of substandard and falsified medical products. World Health Organization, Geneva (2017)

2. Nayyar, G.M.L., Attaran, A., Clark, J.P., Culzoni, M.J., Fernandez, F.M., Herrington, J.E., Kendall, M., Newton, P.N., Breman, J.G.: Responding to the pandemic of falsified medicines. Am. J. Trop. Med. Hyg. 92, 113–8 (2015). doi:10.4269/ajtmh.14-0393

3. Vickers, S., Bernier, M., Zambrzycki, S., Fernandez, F.M., Newton, P.N., Caillet, C.: Field detection devices for screening the quality of medicines: a systematic review. BMJ Glob. Heal. 3, e000725 (2018). doi:10.1136/bmjgh-2018-000725

4. Roth, L., Nalim, A., Turesson, B., Krech, L.: Global landscape assessment of screening technologies for medicine quality assurance: stakeholder perceptions and practices from ten countries. Global. Health. 14, 43 (2018). doi:10.1186/s12992-018-0360-y

5. Vickers, S., Bernier, M., Zambrzycki, S., Fernandez, F.M., Newton, P.N., Caillet, C.: Field detection devices for screening the quality of medicines: a systematic review. BMJ Glob. Heal. 3, e000725 (2018). doi:10.1136/bmjgh-2018-000725

6. Weaver, A.A., Reiser, H., Barstis, T., Benvenuti, M., Ghosh, D., Hunckler, M., Joy, B., Koenig, L., Raddell, K., Lieberman, M.: Paper Analytical Devices for Fast Field Screening of Beta Lactam Antibiotics and Antituberculosis Pharmaceuticals. Anal. Chem. 85, 6453–6460 (2013). doi:10.1021/ac400989p

7. Weaver, A.A., Lieberman, M.: Paper Test Cards for Presumptive Testing of Very Low Quality Antimalarial Medications. Am. J. Trop. Med. Hyg. 92, 17–23 (2015). doi:10.4269/ajtmh.14-0384

8. University of Notre Dame: Paper Analytical Device Project, https://padproject.nd.edu/

9. He, L., Nan, T., Cui, Y., Guo, S., Zhang, W., Zhang, R., Tan, G., Wang, B., Cui, L.: Development of a colloidal gold-based lateral flow dipstick immunoassay for rapid qualitative and semi-quantitative analysis of artesunate and dihydroartemisinin. Malar. J. 13, 127 (2014). doi:10.1186/1475-2875-13-127

10. Guo, S., Zhang, W., He, L., Tan, G., Min, M., Kyaw, M.P., Wang, B., Cui, L.: Rapid evaluation of artesunate quality with a specific monoclonal antibody-based lateral flow dipstick. Anal. Bioanal. Chem. 408, 6003–6008 (2016). doi:10.1007/s00216-016-9363-9

11. Guo, S., He, L., Tisch, D.J., Kazura, J., Mharakurwa, S., Mahanta, J., Herrera, S., Wang, B., Cui, L.: Pilot testing of dipsticks as point-of-care assays for rapid diagnosis of poor-quality artemisinin drugs in endemic settings. Trop. Med. Health. 44, 15 (2016). doi:10.1186/s41182-016-0015-8

12. C-Vue Chromatography, http://www.cvuechromatography.com/

13. Waters: ACQUITY QDa Mass Detector for Chromatographic Analysis, https://www.waters.com/waters/en_US/ACQUITY-QDa-Mass-Detector-for-Chromatographic-Analysis/nav.htm?cid=134761404&locale=en_US

14. Desai, D., Zaman, M.H.: Continuous flow microfluidic solution for quantitative analysis of active pharmaceutical ingredient content and kinetic release †. (2015). doi:10.1039/c4ay02884h

15. Agilent: 4500 Series Portable FTIR, https://www.agilent.com/en/products/ftir/ftir-compact-portable-systems/4500-series-portable-ftir

16. Si-Ware Systems: NeoSpectra-Module, https://www.neospectra.com/our-offerings/neospectra-module/

17. ThermoFisher Scientific: microPHAZIR™ RX Analyzer, https://www.thermofisher.com/order/catalog/product/MICROPHAZIRRX

18. Wilson, B.K., Kaur, H., Allan, E.L., Lozama, A., Bell, D.: A New Handheld Device for the Detection of Falsified Medicines: Demonstration on Falsified Artemisinin-Based Therapies from the Field. Am. J. Trop. Med. Hyg. 96, 1117–1123 (2017). doi:10.4269/ajtmh.16-0904

19. InnoSpectra Corporation, http://www.inno-spectra.com/en/product

20. Rigaku: Advanced handheld Raman spectrometer, https://www.rigaku.com/en/progeny

21. ThermoFisher Scientific: TruScan™ RM Handheld Raman Analyzer, https://www.thermofisher.com/order/catalog/product/TRUSCANRM

22. Global Pharma Health Fund: The GPHF-Minilab™ - Protection Against Counterfeit Medicines, https://www.gphf.org/en/minilab/index.htm

23. World Health Organization: Report of the Sixth Meeting of the Member State Mechanism on Substandard and Falsified Medical Products. , Geneva (2018)

24. Bernier, M.C., Li, F., Musselman, B., Newton, P.N., Fernández, F.M.: Fingerprinting of falsified artemisinin combination therapies via direct analysis in real time coupled to a compact single quadrupole mass spectrometer. Anal. Methods. 8, 6616–6624 (2016). doi:10.1039/C6AY01418F

25. Caillet, C., Sichanh, C., Assemat, G., Malet-Martino, M., Sommet, A., Bagheri, H., Sengxeu, N., Mongkhonmath, N., Mayxay, M., Syhakhang, L., Lapeyre-Mestre, M., Newton, P.N., Roussin, A.: Role of Medicines of Unknown Identity in Adverse Drug Reaction-Related Hospitalizations in Developing Countries: Evidence from a Cross-Sectional Study in a Teaching Hospital in the Lao People's Democratic

Republic. Drug Saf. 40, 809–821 (2017). doi:10.1007/s40264-017-0544-z

26. Brown, L.D., Cai, T.T., DasGupta, A.: Interval Estimation for a Binomial Proportion, (2001)

27. Taylor, K., Silver, L.: Smartphone Ownership Is Growing Rapidly Around the World, but Not Always Equally, https://www.pewglobal.org/2019/02/05/smartphone-ownership-is-growing-rapidly-around-the-world-but-not-always-equally/

CHAPTER 5. ACCELERATED SCREENING FOR THE PROTECTION AND EFFICACY OF CELL TREATMENTS (ASPECT) VIA MALDI-MS

5.1 Abstract

Cellular therapies offer the potential for revolutionary treatments for patients. Due to their high demand, illicit manufacturers are capitalizing on expensive and low availability cellular therapies by creating poor quality and falsified products. Regulatory agencies need rapid and simple tools for pre- and post-market surveillance of cellular therapies. Many quality control tools exist for cellular therapy screening such as microscopy, immunoassays, genotyping, and flow cytometry; however, these tools can be low throughput and have complex consumables. The Accelerated Screening for the Protection and Efficacy of Cellular Therapies (ASPECT) workflow was developed to rapidly screen the quality of cellular therapies using matrix assisted laser desorption ionization (MALDI) mass spectrometry. MALDI has been extensively used in the clinic to rapidly speciate bacteria with minimal simple consumables and the spectral libraries can be easily updated to include more species. The ASPECT workflow includes scripts to automatically analyze the raw data by comparing spectra using correlation coefficient testing with little user input and easy to read results. In this preliminary study, untreated mesenchymal stromal cells (MSC) were compared with ethanol incubated MSC to simulate egregious manufacturing. Lipid, protein, and metabolite profiling were evaluated to distinguish untreated and ethanol incubated cells. Lipid profiling proved to be effective at detecting ethanol's disruption of the cellular membrane. Although protein and metabolite profiling could distinguish

untreated and ethanol incubated cells, few spectral features distinguished the two conditions causing a few false positives and negatives. This preliminary data shows ASPECT's potential as a high throughput tool that uses simple consumables for screening cellular therapies.

5.2 Introduction

New emerging cellular therapies such as stem cells offer the potential for revolutionary treatments for patients in regenerative medicine and chronic disease [1–3]. The market for cellular therapies is rapidly expanding. From 2001 to 2019, an average of 2.5 cellular therapy medical products were approved each year worldwide by regulatory agencies [4]. Such high demands for these revolutionary medical products can cause an influx of poor quality and unregulated cells to enter the market. For example, traditional small molecule pharmaceuticals that have been on the market for decades continue to face quality concerns with illicit and poor manufacturing. The World Health Organization estimates that 1 in 10 medicines in low to middle income nations are deemed poor quality due to inadequate manufacturing practices, environmental degradation, or criminal falsification [5]. Poor quality small molecule pharmaceuticals such as antibiotics and antimalarials can prevent patients' treatment, cause microbial resistance to anti-infectives, and increase distrust in the health system [6].

Cellular therapies are currently suffering from similar quality problems as traditional small molecule pharmaceuticals. Unlicensed and illegitimate stem cell providers have been reported throughout the United States and worldwide [7, 8]. For example, a stem cell clinic in the United States has been charged with the sale of adulterated

and misbranded cellular therapies that were not approved by the Food and Drug Administration (FDA) [9]. Stem cell tourism in unregulated markets is expanding as patients seek cellular therapies that are cheaper or not available elsewhere [10]. There are many reports of complications from poor quality stem cells. A survey of academic neurologists regarding complications their patients suffered from stem cell tourist clinics include: stroke, infections, sepsis, death, and many others [11]. Multi-organ failure and death from an unapproved stem cell tourism therapy has been reported in detail as well [12]. Another quality problem with stem cells includes bacterial contamination of an approved cellular product reported by the U.S. Centers for Disease Control [13]. Illicit manufacturers capitalize on patients' vulnerabilities such as with the COVID-19 pandemic. The pandemic caused an influx of falsified medical products on the market including chloroquine, a purported COVID-19 treatment [14, 15]. This includes a Missouri state lawmaker selling amnionic fluid as an alleged stem cell treatment for COVID-19 [16].

To elude regulatory authorities, poor quality and falsified cellular therapies will become more difficult to detect. As an example in small molecule pharmaceuticals, illicit manufacturers have been known to falsify anti-malarials by: replicating the shape and color of genuine good quality tablets, imitating the original medicine's packaging, adding a non-therapeutic amount of active ingredient to pass rudimentary chemical tests, and copy the complex holographic stickers on the packaging used to confirm the authenticity of the medicine. Acetaminophen has also been added to falsified anti-malarials without the correct active ingredient to elude patients into thinking they are being treated [17]. Regulatory agencies will need various powerful tools for the pre- and post-market surveillance of cellular therapies to combat poor or illicit manufacturing.

There are many tools used to characterize cellular therapies for quality control [18–20]. Flow cytometry offers a highly sensitive and multiplexed technique for rapid quantitation of cellular targets [21]. Characterizing cells through genotyping can help speciate cells and monitor mutations in cell lines [22]. Microscopy is a versatile tool for stem cell quality control to monitor cells through label and label-free techniques [23]. The advent of mobile phone based microscopy can help create a field deployable tool for stem cell clinic inspections [24]. Immunoassays can be used to identify key cellular markers. Immunoassays can be combined with flow cytometry to improve speed or microscopy for the imaging of key cellular targets [25]. Although these technologies are widely used in stem cell quality control, some tools are low throughput, many of these tools can only analyze a few targets or features without major consumable changes, and many require complex consumables such as antibodies or enzymes for specific markers.

In this article, we show the first set of results regarding the use of matrix assisted laser desorption ionization (MALDI) mass spectrometry for the high throughput quality screening of cellular therapies. Regulators need a high throughput screening tool that can be easily updated with minimal consumables to detect illicit or poor quality cellular therapies. In microbiology, bacterial speciation using mass spectrometry was first demonstrated in 1975 [26], with MALDI biotyping being developed for rapid bacterial speciation in 1994 through protein profiling [27]. MALDI biotyping has been commercialized and is now an FDA approved method to speciate a wide variety of bacteria in the clinic [28–30]. The main advantage of MALDI biotyping is the ability to speciate a wide variety of bacteria with the same simple MALDI matrix and solvents. New bacteria can be easily added to the biotyping database by simply updating the spectral library

without the need to change the consumables and protocols. MALDI is entering the cellular therapy world as it has been used to profile embryonic stem cell differentiation [31]. To accelerate MALDI as an easy to use screening tool for cellular therapies, we have developed the Accelerated Screening for the Protection and Efficacy of Cell Technologies (ASPECT) workflow to swiftly process samples. At the end of the MALDI experiments and with minimal user input, the results are processed automatically and output in an easy to read format. Protein profiling traditionally used for MALDI biotyping, metabolite profiling, and lipid profiling were explored with ASPECT. Preliminary data was acquired comparing ethanol incubated versus untreated cells to evaluate ASPECT.

5.3 Experimental

Mesenchymal stromal cells (MSC) from RoosterBio (lot 182, 26 y.o. female; Frederick, MD) were utilized. Cells were expanded in a culture flask with culture media containing low-glucose Dulbecco's modified eagle medium, 10 % fetal bovine serum, and 1x antibiotic/antimycotic. The cell expansion was incubated at 37 °C with 5% CO_2. After incubation, the media was removed and cells were dislodged using trypLE solution. The cells were pelleted at 300 g for 5 minutes and resuspended in fresh media. An aliquot of cells was removed, stained with trypan blue, and the cell count measured with a hemocytometer. After counting, the stock of unstained cells was diluted with fresh media to $2.0*10^6$ cells/mL for testing. To simulate the detection of unaffected cells versus egregious poor manufacturing, half the MSC were untreated and the other half were incubated in ethanol for 15 minutes. After treatment, the cells were pelleted, supernatant media or ethanol removed, the pellet was resuspended in phosphate buffered solution (PBS), and frozen at -80°C until MALDI experiments.

All chemicals required for MALDI experiments were purchased from Sigma-Aldrich (St. Louis, MO) at their highest purity available, unless noted otherwise. Dried droplet sample preparation chemicals and MALDI matrices were developed from previously reported protocols. Bruker's (Billerica, MA) Bacterial Test Standard MALDI preparations method utilizing the matrix α-cyano-4-hydroxycinnamic acid was used for protein profiling [32]. The method using the matrix 9-aminoacridine from Edwards et al. was used for metabolite profiling [33]. Our lipid profiling method was developed using the matrix 2,5-dihydroxybenzoic acid with modification from Bruker's Guide to MALDI Sample Preparation [34]. Details for MALDI dried droplet sample preparation for each profiling method are given in detail in the first third of Table 5-1.

Table 5-1 Key sample preparation procedures, MALDI settings, and ASPECT script parameters.

Sample Preparation

Profiling Method	Protein	Metabolite	Lipid
MALDI Matrix	α-Cyano-4-hydroxycinnamic acid (HCCA)	9-aminoacidine (9AA)	2,5-Dihydroxybenzoic acid (DHB)
MALDI Matrix Solvent (v/v)	50.0 % ACN 47.5 % H_2O 2.5 % TFA	Acetone	90.0 % ACN 10.0 % H_2O 0.1 % TFA
Concentration of MALDI Matrix in Matrix Solvent	10 mg/mL*	9 mg/mL	20 mg/mL
Sample Solvent (v/v)	50.0 % ACN 47.5 % H_2O 2.5 % TFA	50 % MeOH 50 % H_2O	90.0 % ACN 10.0 % H_2O 0.1 % TFA
Volume of Matrix/Sample spotted onto target plate	1.0 µL	0.7 µL	0.7 µL
Spotting Protocol	Spot sample solution onto target plate and dry. Spot matrix solution on top of dried sample and dry.	Mix sample solution and matrix solution 1:1. Spot mixture onto target plate and dry.	Mix sample solution and matrix solution 1:1. Spot mixture onto target plate and dry.

MALDI Settings

Profiling Method	Protein	Metabolite	Lipid
Mode	Positive	Negative	Positive
Mass Range	2200 to 20000	170 to 2000 m/z	300 to 2000 m/z
Laser Shots	1000	5000	5000
Laser (Application – Smartbeam – Scan Range)	M5 Thin Layer – M5 – 50 µm	Custom – Single – 50 µm	Custom – Single – 50 µm
Shots at Raster Spot	50	10	10
Walk on Spot	Enabled	Enabled	Enabled
Movement on Sample Spot	Random – Partial Sample	Random – Complete Sample	Random – Complete Sample
Sample Rate	1.25 GS/s	5.00 GS/s	2.50 GS/s

ASPECT Script Settings

Profiling Method	Protein	Metabolite	Lipid
Mass Range Trim	2250 to 9000 m/z	400 to 670 m/z	650 to 870 m/z
Data Size Reduction	1.25x	2.00x	1.25x
Bin Size	25	25	25
Normalization	Total Ion Current (TIC)	Total Ion Current (TIC)	Total Ion Current (TIC)
Correlation Coefficient Threshold	0.85	0.95	0.8

ACN = acetonitrile; MeOH = methanol; TFA = trifluoroacetic acid

*Solution is supersaturated after sonication. Centrifuge the solution and spot the supernatant.

The prepared frozen cells were thawed at room temperature, pelleted, and the PBS supernatant was replaced in equal volume with the appropriate sample solvent necessary. All samples were spotted onto a Bruker ground steel MALDI target plate (Part# 8074115). In this preliminary data set, 4 spots were prepared with untreated cells and used as the reference sample for correlation coefficient (CC) testing for each profiling method. These 4 reference spots were not considered in sensitivity or specificity calculations on the MALDI target plate map. On the same target plate, 24 spots were created from the untreated cells and 24 spots were dispensed for the ethanol incubated samples for each profiling method. Other spots on the target plate included blanks and external mass accuracy calibrants. External mass accuracy calibration for protein profiling was conducted with the Bruker Protein Calibration Standard 1. Metabolite and lipid profiling external mass accuracy calibration was conducted with poly-alanine as detailed by Gruendling et al. [35].

The Bruker rapifleX MALDI Tissuetyper was utilized for all experiments. Each profiling method had their own unique mass spectrometry settings as defined in the second third of Table 5-1. The rapifleX's speed processing spots for MALDI is desirable for high throughput screening applications. To demonstrate the rapifleX's speed, Figure 5-2 plots the time to process a fully spotted 384 ground steel target plate with protein profiling in less than 40 minutes.

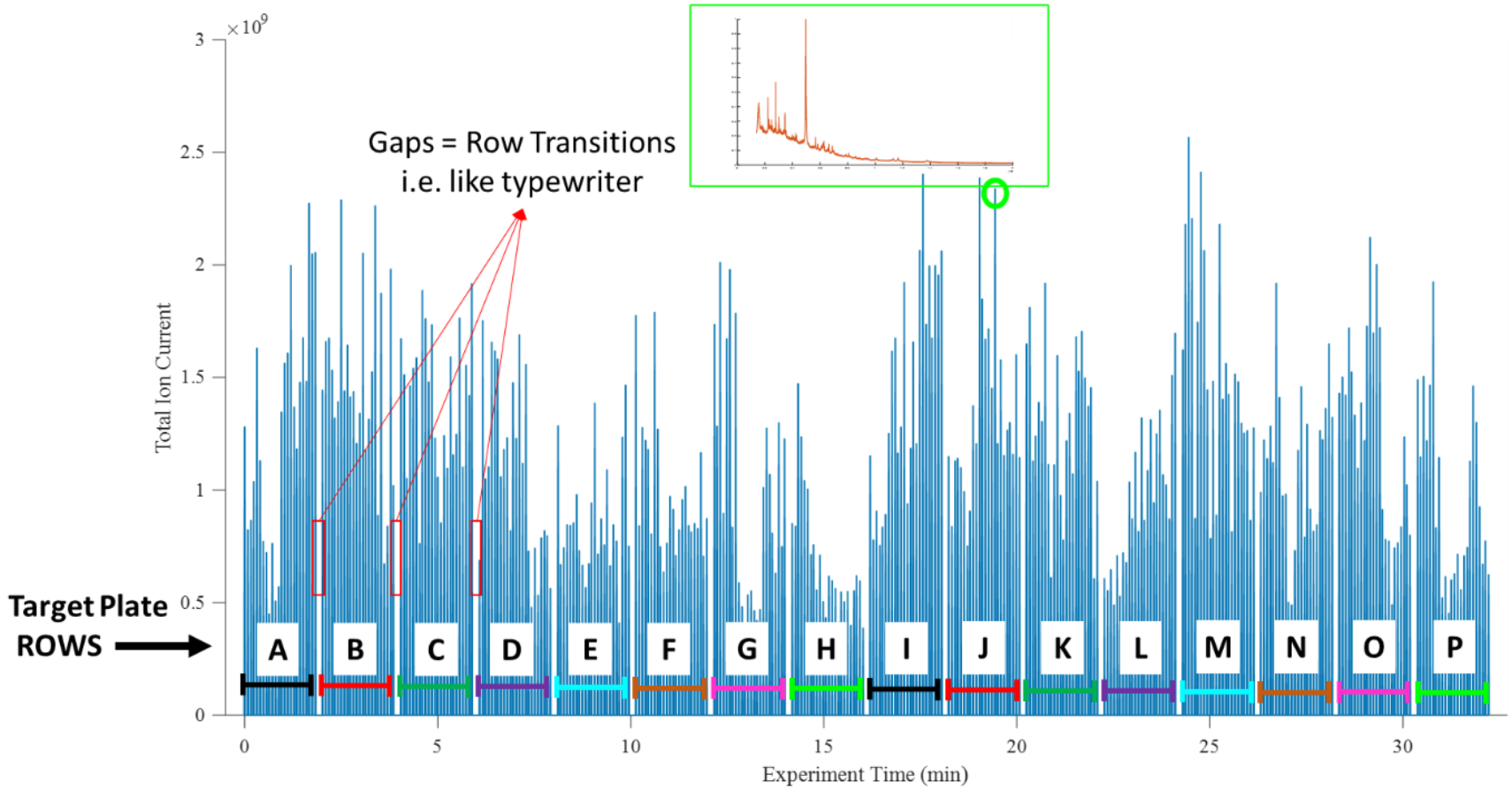

Figure 5-1 To demonstrate the rapifleX's speed, the total ion current for each protein profiling experiment was plotted versus the overall time taken to process a fully spotted 384 ground steel target plate. Each peak represents the total ion current of a single spot on the target plate. The gaps in time between each target plate row are when the rapifleX is transitioning from one row to the next. Each row contains 24 spots.

Two scripts were written for ASPECT. The first script rapidly converts an entire folder of Bruker's raw spectra file into the common .mzXML file format for data processing. After MALDI experiments were complete, FID files were created for the raw spectra collected using Bruker's flex Data Converter software. Then, a custom Python 3.7.3 script was written to automatically take an entire folder of spectra with the FID files and convert them to .mxXML files for later processing.

The second script processes the .mzXML files for data analysis and was written in MathWorks's (Natick, MA) MATLAB R2020b and outlined in Figure 5-2. Briefly, spectra are first baseline corrected and normalized. Second, the number of data points are reduced through binning to minimize noise. Then, the mass range can be trimmed to isolate a key spectral region of interest, especially those that are biologically relevant. Third, the questioned sample's spectra are then compared to a reference sample's spectra through CC testing. CC testing is a rapid to perform calculation to compare a questioned sample against a reference sample's spectral pattern. If the calculated CC score is greater than an established threshold, the questioned sample passes the test and is considered similar to the reference sample. Finally, a map of the MALDI target plate is created showing which samples passed and which ones failed. To assess the sensitivity and specificity of ASPECT, the developer can input a file with the known quality of the cells. The target plate map plots which samples are true positives, true negatives, false positives, and false negatives. In the field of poor quality medicine screening: a true positive indicates a poor quality sample was correctly identified. A true negative defines a good quality medicine was correctly identified. A false positive indicates a good quality sample was incorrectly identified as poor quality. Finally, a false negative defines a poor quality medicine that was incorrectly

identified as good quality. The sensitivity and specificity are automatically calculated and noted on the bottom of the target plate map. Sensitivity is the ratio of true positives over the sum of true positives and false negatives. Specificity is the ratio of true negatives over the sum of true negatives and false positives. Receiver operating characteristics (ROC) curves are automatically calculated and plotted to best find the appropriate CC threshold for the assay. Key parameters for the ASPECT data processing script are listed in the third section of Table 5-1.

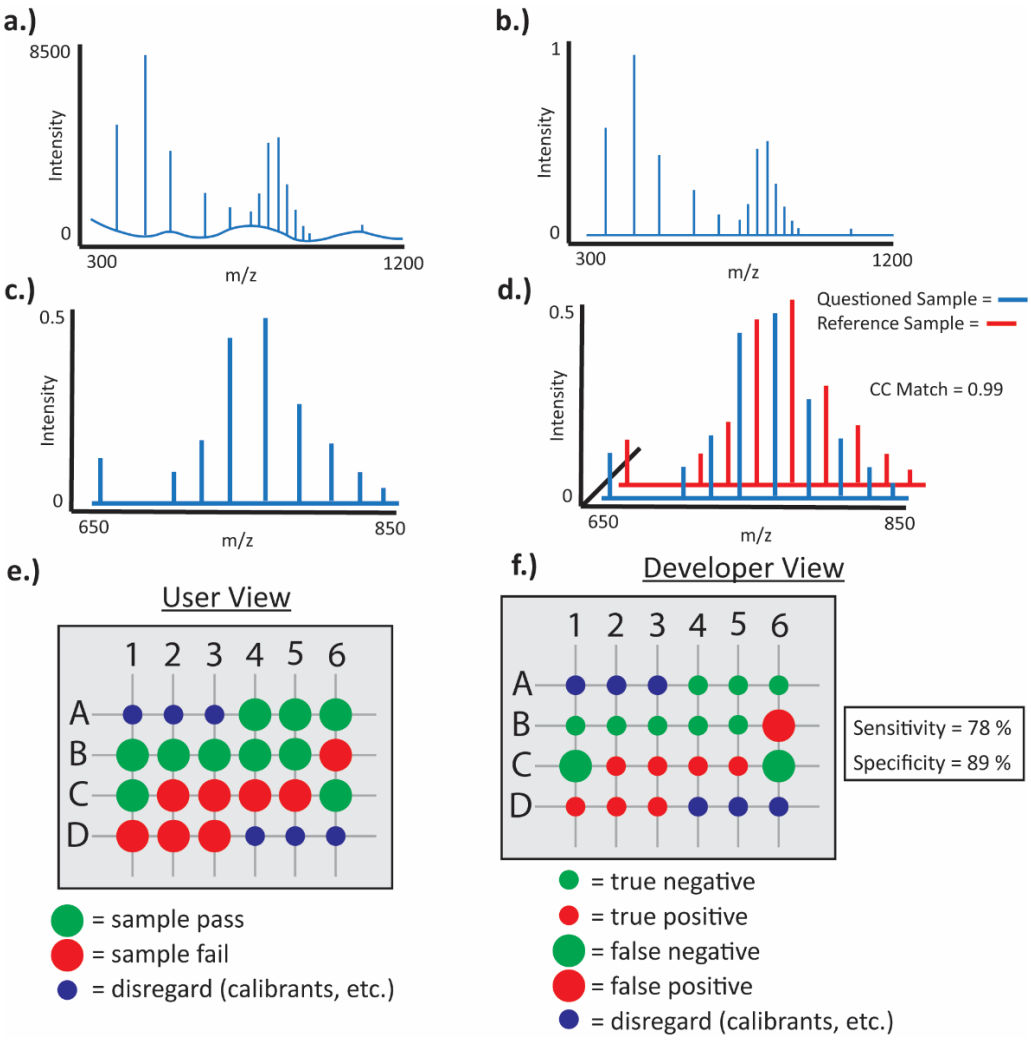

Figure 5-2 Diagram of the workflow in the second script in ASPECT. (A) After the .mzXML spectra have been imported into MATLAB, (B) the spectra are baselined corrected and normalized. (C) Then, the spectra are binned to reduce noise and the mass range is trimmed to isolate a specific region of interest. This spectral region of interest may be more biologically relevant than others. (D) The spectra from the questioned samples are then compared to a reference sample through CC testing. A CC score is output that measures the relative match in the spectral pattern between the questioned sample and the reference. A score of 0 is not a match and a score of 1 is a perfect match. The scores are compiled into two MALDI target plate maps. (E) The end user would receive a map indicating which samples passed or failed CC testing given the defined threshold for passing. (F) If the developer evaluating the assay uploads a file with the known samples' quality, the developer's view calls attention to which spots did not perform as expected. False negatives and false positives are highlighted by being large circles. The sensitivity and specificity of the assay is automatically calculated and output in the developer's view. In either the user or developer view, gradient colors can be displayed to visually estimate the CC score too.

5.4 Results and Discussion

Ethanol incubation disrupts cellular membranes by solubilizing lipids [36]. As seen in the mean lipid profiling spectra in Figures 5-3A & B, there is significant change in the profile of phospholipids from untreated to ethanol-incubated cells. After importing the data into the ASPECT processing script, CC testing correctly classified both the untreated and ethanol incubated cells as seen in the developer's MALDI target plate map in Figure 5-3C. All untreated cell spots in row G were classified as true negatives since they differed little from the reference samples. All ethanol incubated cell spots in row H were classified as true positives because of the distinct change in the spectra from untreated to ethanol incubated cells. The corresponding ROC curve to establish the CC threshold for lipid profiling is in Figure 5-3D. Although a threshold of 0.8 was set for the experiment, the ethanol incubated cells could be distinguished with a threshold as low as 0.525 on the ROC curve to still achieve maximum sensitivity and specificity. The orange and yellow small spots in row H show that the ethanol incubated cells' CC scores do not go beyond 0.5, suggesting a poor match with the untreated reference cells. The disruption and extraction of the cellular membrane lipids with ethanol caused a dramatic change in the lipid profile that could easily be detected by CC testing.

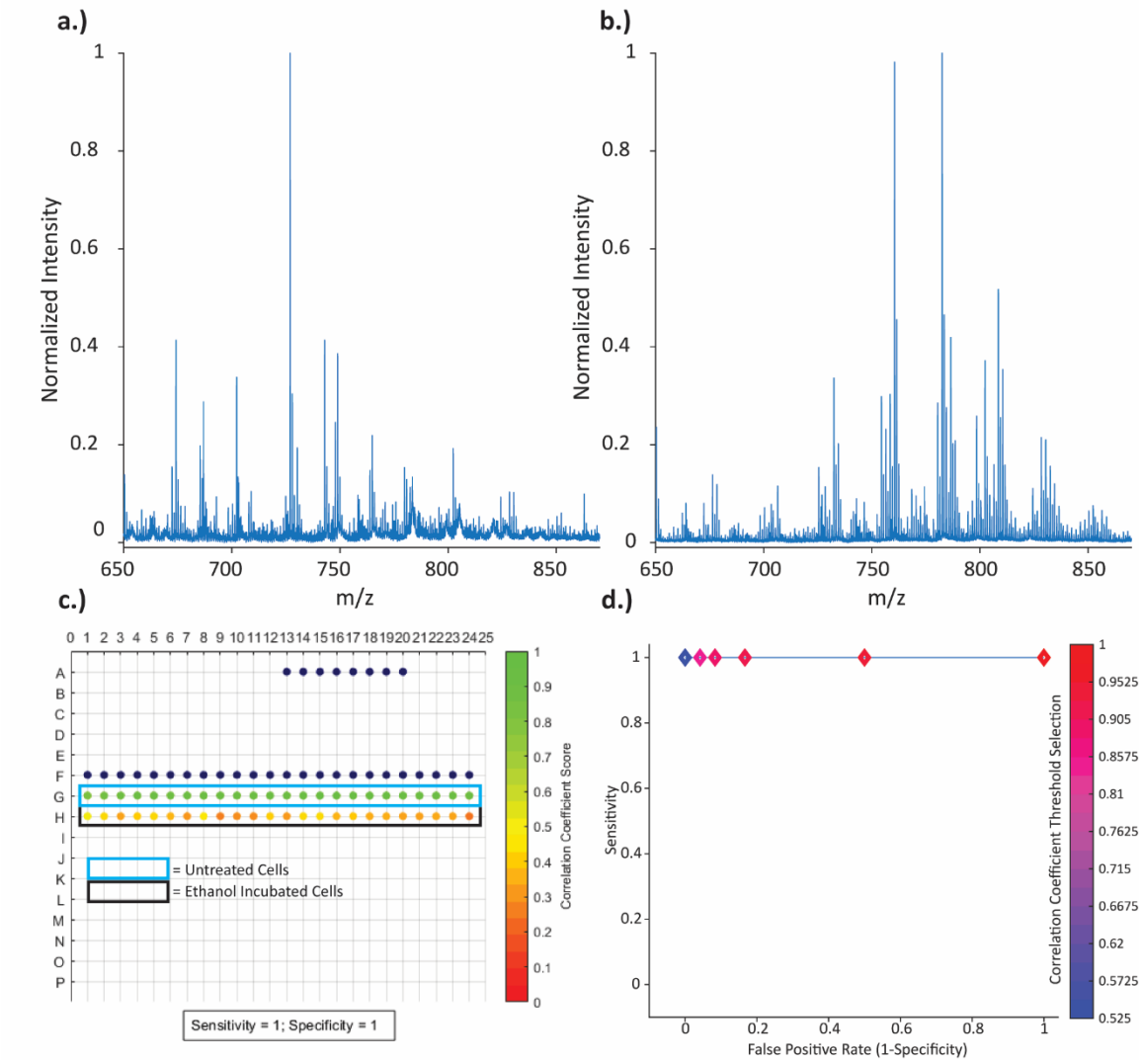

Figure 5-3 The mean unprocessed lipid profiling spectra (n=24) are plotted for (A) ethanol incubated cells and (B) untreated cells. Ethanol incubation shows a dramatic shift in the lipid profile. (C) After ASPECT data processing, the developer's view of the MALDI target plate map shows that all samples were correctly classified with a specificity and sensitivity of 1 (0.85 to 1, 95% CI). All untreated cells passed with CC scores >0.8 and all ethanol incubated cells failed with CC scores <0.5. No false positives or negatives were detected since all the spots on the target plate map were small circles (D) The ROC curve shows that the CC threshold can be set as low as 0.525 and still have a specificity and sensitivity of 1 to detect ethanol incubation via lipid profiling. Increasing the CC threshold beyond 0.8 increases the false positive rate.

Protein profiling is the primary method to speciate bacteria using MALDI biotyping [28–30]. After ethanol incubation, only one feature was extracted as highlighted by the red box in Figures 5-4A and B. CC testing can distinguish the difference with only one feature missing as seen in ASPECT's developer's view of the MALDI target plate map in Figure 5-4C. In row C, 20 true negatives (0.83 specificity; 0.62 to 0.95, 95% CI) and in row D, 23 true positives (0.96 sensitivity; 0.78 to 0.99, 95% CI) were measured. Establishing the appropriate CC threshold is critical to achieve these high sensitivities and specificities. As shown in Figure 5-4D, setting a CC threshold <0.85 causes the sensitivity of the assay to lower significantly. Setting the CC threshold >0.85 increases the false positive rate of this assay. The four false positive spots at C7, C12, C13, and C23 in the MALDI target plate map are the likely cause of poor spotting or the random sampling of the laser missing key areas with concentrated analyte or matrix on the dried droplet (Figure 5-4E). The false negative on spot D19 demonstrates how closely aligned the spectra are between the untreated and ethanol incubated cells (Figure 5-4F).

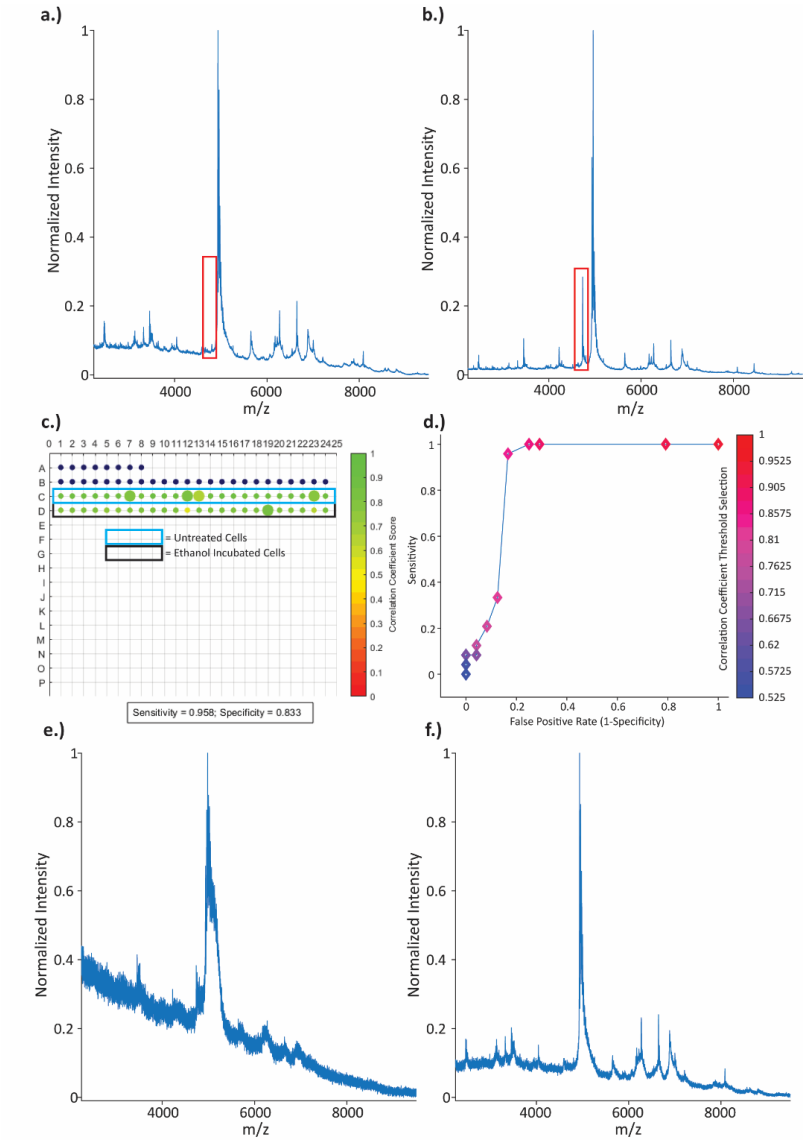

Figure 5-4 The mean unprocessed protein profiling spectra (n=24) are plotted for (A) ethanol-incubated cells and (B) untreated cells. Only one feature from the untreated cells is extracted after ethanol incubation highlighted by the red box. (C) After ASPECT data processing, the developer's view of the MALDI target plate map shows a high sensitivity of 0.96 (0.78 to 0.99, 95% CI) with only one false negative at spot D19. The specificity is slightly reduced to 0.83 (0.62 to 0.95, 95% CI) due to 4 false positives at spots C7, C12, C13, and C23. (D) The ROC curve shows that setting the CC threshold below 0.85 causes the sensitivity of ASPECT towards ethanol incubation detection to decrease. Increasing the CC threshold beyond 0.85 increases the false positive rate. (E) The mean spectra for the false positive spots C7, C12, C13, and C23 are plotted. These false positives show poor acquisition likely correlated to poor sample preparations or the random sampling laser missing key spots with concentrated analytes. (F) The spectra for the false negative at spot D19 shows the limited difference between untreated vs. ethanol incubated cells for protein profiling.

The large change in sensitivity and specificity in the ROC curve for protein profiling is caused by how close the CC scores are between untreated (row C) and ethanol incubated cells (row D) as seen by their green color (Figure 5-4C). Ethanol incubation likely killed the cells quicker than the proteome could react to cause a major change in the protein profile mass spectra. Since this preliminary data set is created with a single donor and batch of MSC, the proteome is not different enough after an ethanol incubation alone. Heap et al. shows the effectiveness of MALDI protein profiling for the phenotyping of differentiated mouse embryonic stem cells [31]. Cell differentiation significantly changes the proteome to modify the function of the cell. Protein profiling would likely be an excellent screening method if illicit manufacturers sell the patient the wrong or none of the stem cells. If the cells die too rapidly for the proteome to respond, protein profiling may not be optimal.

Metabolite profiling was evaluated as many of the analytes in the article by Edwards et al. have well defined metabolic pathways [33]. Ethanol incubation caused a change in intensities for many of the features compared to the untreated cells as shown in Figures 5-5A & B. Although the intensities changed likely due to ethanol extraction, there is no significant change in new features appearing or disappearing after ethanol incubation compared to lipid profiling. As shown in Figure 5-5C, ASPECT achieved 24 true positives in row L (1.00 sensitivity; 0.85 to 1, 95% CI) and 23 true negatives in row K (0.96 specificity; 0.79 to 0.99, 95% CI). A CC threshold of 0.95 was necessary to achieve the high sensitivities and specificities. Any other CC threshold above or below 0.95 would have drastically decreased the sensitivity or specificity as shown in the ROC curve in Figure 5-5D. Based on the spectra plotted in Figure 5-5E, the false positive spot K23 was

likely caused by some baseline noise where the laser may have shot less concentrated areas of the sample spot.

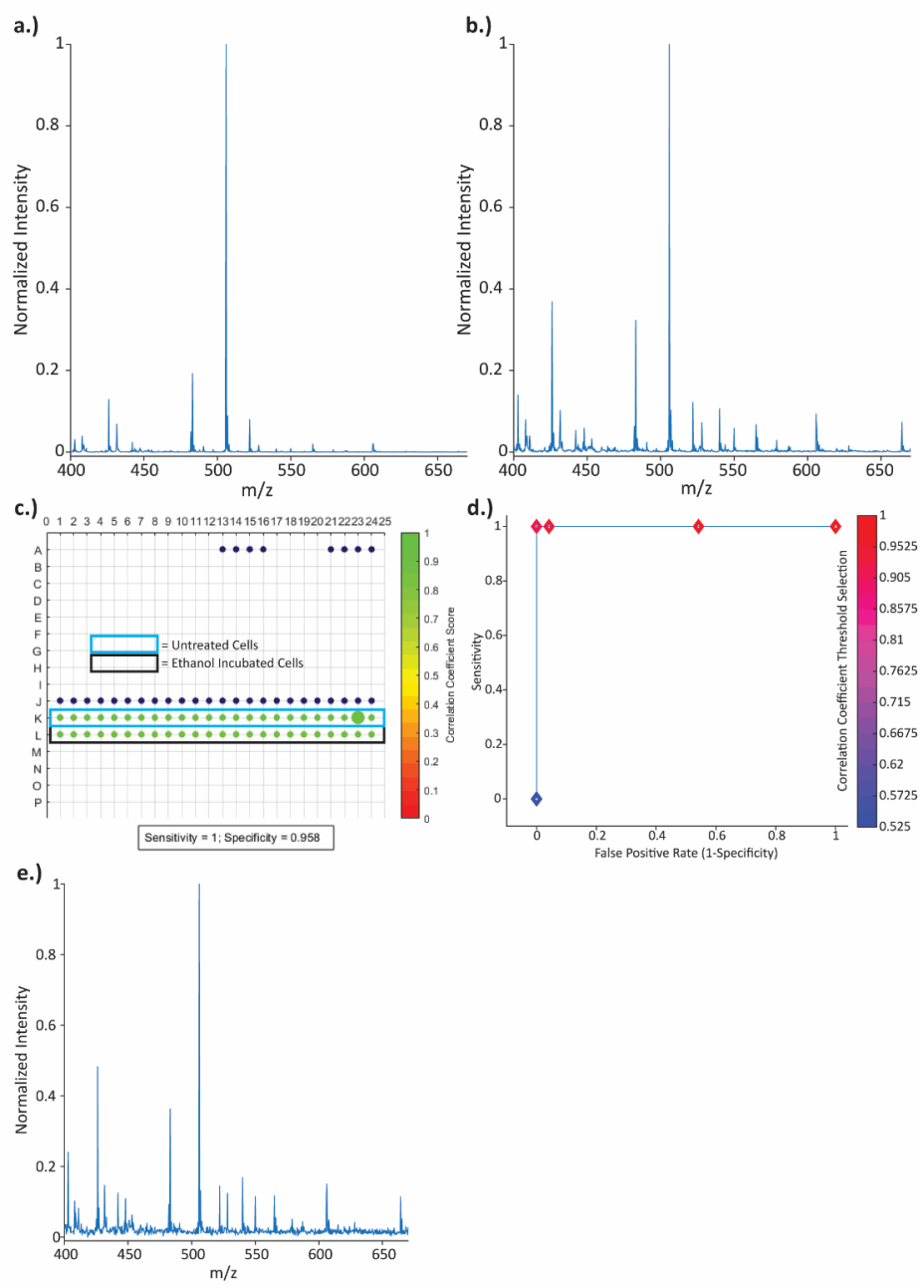

Figure 5-5 The mean unprocessed metabolite profiling spectra (n=24) are plotted for (A) ethanol incubated cells and (B) untreated cells. There are changes in the intensities between the untreated versus ethanol incubated cells; however, the features remain the same except for a peak or two. (C) After ASPECT data processing, the developer's view of the MALDI target plate map shows a high sensitivity of 1 (0.85 to 1, 95% CI) in row L, and a high specificity of 0.96 (0.79 to 0.99, 95% CI) in row K with only one misclassification at spot K23. (D) The ROC curve shows that setting the CC threshold below 0.95 causes the sensitivity of ASPECT towards ethanol incubation detection to plummet. Increasing the CC threshold beyond 0.95 increases the false positive rate for ethanol incubation detection. (E) The spectra for the false positive spot at K23 is plotted. The baseline noise for K23 may be the most contributing factor to the misclassification due to a high CC threshold.

The high CC threshold of 0.95 for metabolite profiling is necessary to distinguish ethanol incubated from untreated cells because so few new peaks appear or disappear after ethanol incubation compared with lipid profiling. As mentioned previously with protein profiling, the metabolome likely had little time to change drastically as the lipid cell membrane was immediately disrupted by ethanol incubation. The abundance differences can be attributed to potential extraction of some of the metabolites in the ethanol after the cell membrane was disrupted. Metabolite profiling maybe more sensitive to less intensive changes to the cell environment that do not immediately kill the cell. For example, culture conditions such as monolayer or aggregate expansion can change the metabolome of MSC [37].

5.5 Conclusions

This preliminary data showcases the potential of ASPECT as a rapid screening tool for cellular therapies. Disrupting the cellular membrane with ethanol was easily detected using lipid profiling. Although protein and metabolite profiling were able to distinguish between untreated and ethanol incubated cells, the few differential features between the two conditions can cause false positives and false negatives due to similar CC scores. To improve ASPECT's script such as in protein and metabolite profiling, other algorithms beyond CC testing may be necessary to better distinguish spectra with so few different features. It is likely ASPECT can be used to explore other kinds of quality issues commonly found in cellular therapies. Examples include detecting batches of cells with bacterial or other chemical contamination, evaluating different culture or storage conditions, and exploring if ASPECT can be sensitive enough to detect different donors or cell passage numbers. This preliminary study sets the basis for ASPECT being a method with simple

consumables that is high throughput and can be easily updated for the pass-fail screening of cellular therapies.

5.6 References

1. Mahla, R.S.: Stem cells applications in regenerative medicine and disease therapeutics. Int. J. Cell Biol. 2016, (2016). https://doi.org/10.1155/2016/6940283

2. Zakrzewski, W., Dobrzyński, M., Szymonowicz, M., Rybak, Z.: Stem cells: Past, present, and future. Stem Cell Res. Ther. 10, 1–22 (2019). https://doi.org/10.1186/s13287-019-1165-5

3. Aly, R.M.: Current state of stem cell-based therapies: An overview. Stem Cell Investig. 7, (2020). https://doi.org/10.21037/sci-2020-001

4. Ramezankhani, R., Torabi, S., Minaei, N., Madani, H., Rezaeiani, S., Hassani, S.N., Gee, A.P., Dominici, M., Silva, D.N., Baharvand, H., Hajizadeh-Saffar, E.: Two Decades of Global Progress in Authorized Advanced Therapy Medicinal Products: An Emerging Revolution in Therapeutic Strategies. Front. Cell Dev. Biol. 8, 1358 (2020). https://doi.org/10.3389/fcell.2020.547653

5. World Health Organization: A study on the public health and socioeconomic impact of substandard and falsified medical products. World Health Organization, Geneva (2017)

6. Newton, P.N., Green, M.D., Fernández, F.M.: Impact of poor-quality medicines in the "developing" world, (2010)

7. Taylor-Weiner, H., Graff Zivin, J.: Medicine's Wild West — Unlicensed Stem-Cell Clinics in the United States. N. Engl. J. Med. 373, 985–987 (2015). https://doi.org/10.1056/nejmp1504560

8. Murray, I.R., Chahla, J., Frank, R.M., Piuzzi, N.S., Mandelbaum, B.R., Dragoo, J.L.: Rogue stem cell clinics. Bone Jt. J. 102 B, 148–154 (2020). https://doi.org/10.1302/0301-620X.102B2.BJJ-2019-1104.R1

9. United States District Court, S.D.F.: UNITED STATES of America, Plaintiff, v. US STEM CELL CLINIC, LLC, et al.…. (2019)

10. Master, Z., Resnik, D.B.: Stem-cell tourism and scientific responsibility. Stem-cell researchers are in a unique position to curb the problem of stem-cell tourism. EMBO Rep. 12, 992–995 (2011). https://doi.org/10.1038/embor.2011.156

11. Julian, K., Yuhasz, N., Rai, W., Salerno, J.A., Imitola, J.: Complications from "Stem Cell Tourism" in Neurology. Ann. Neurol. 88, 661–668 (2020).

https://doi.org/10.1002/ana.25842

12. Večerić-Haler, Ž., Borštnar, Š., Luzar, B., Jerše, M., Kojc, N.: Multiorgan failure with fatal outcome after stem cell tourism. Eur. J. Med. Res. 26, 1–5 (2021). https://doi.org/10.1186/s40001-020-00477-4

13. Centers for Disease Control and Prevention: Contaminated Stem Cell Products - Bacterial infections after use of stem cell products, https://www.cdc.gov/hai/outbreaks/stem-cell-products.html, (2019)

14. Tesfaye, W., Abrha, S., Sinnollareddy, M., Arnold, B., Brown, A., Matthew, C., Oguoma, V.M., Peterson, G.M., Thomas, J.: How do we combat bogus medicines in the age of the COVID-19 pandemic? Am. J. Trop. Med. Hyg. 103, 1360–1363 (2020). https://doi.org/10.4269/ajtmh.20-0903

15. Gnegel, G., Hauk, C., Neci, R., Mutombo, G., Nyaah, F., Wistuba, D., Häfele-Abah, C., Heide, L.: Identification of falsified chloroquine tablets in Africa at the time of the COVID-19 pandemic. Am. J. Trop. Med. Hyg. 103, 73–76 (2020). https://doi.org/10.4269/ajtmh.20-0363

16. More Charges Against State Lawmaker for $900,000 COVID-19 Fraud Scheme at Springfield Health Care Charity | USAO-WDMO | Department of Justice, https://www.justice.gov/usao-wdmo/pr/more-charges-against-state-lawmaker-900000-covid-19-fraud-scheme-springfield-health

17. Newton, P.N., Green, M.D., Fernández, F.M., Day, N.P., White, N.J.: Counterfeit anti-infective drugs, (2006)

18. Sullivan, S., Stacey, G.N., Akazawa, C., Aoyama, N., Baptista, R., Bedford, P., Bennaceur Griscelli, A., Chandra, A., Elwood, N., Girard, M., Kawamata, S., Hanatani, T., Latsis, T., Lin, S., Ludwig, T.E., Malygina, T., Mack, A., Mountford, J.C., Noggle, S., Pereira, L. V, Price, J., Sheldon, M., Srivastava, A., Stachelscheid, H., Velayudhan, S.R., Ward, N.J., Turner, M.L., Barry, J., Song, J.: Quality control guidelines for clinical-grade human induced pluripotent stem cell lines. Regen. Med. 13, (2018). https://doi.org/10.2217/rme-2018-0095

19. Jossen, V., van den Bos, C., Eibl, R., Eibl, D.: Manufacturing human mesenchymal stem cells at clinical scale: process and regulatory challenges. Appl. Microbiol. Biotechnol. 102, 3981–3994 (2018). https://doi.org/10.1007/s00253-018-8912-x

20. Mizukami, A., Swiech, K.: Mesenchymal stromal cells: From discovery to manufacturing and commercialization. Stem Cells Int. 2018, (2018). https://doi.org/10.1155/2018/4083921

21. Donnenberg, V.S., Ulrich, H., Tárnok, A.: Cytometry in stem cell research and therapy. Cytom. Part A. 83 A, 1–4 (2013). https://doi.org/10.1002/cyto.a.22243

22. Jo, H.Y., Han, H.W., Jung, I., Ju, J.H., Park, S.J., Moon, S., Geum, D., Kim, H.,

Park, H.J., Kim, S., Stacey, G.N., Koo, S.K., Park, M.H., Kim, J.H.: Development of genetic quality tests for good manufacturing practice-compliant induced pluripotent stem cells and their derivatives. Sci. Rep. 10, 1–15 (2020). https://doi.org/10.1038/s41598-020-60466-9

23. Leahy, M., Thompson, K., Zafar, H., Alexandrov, S., Foley, M., O'Flatharta, C., Dockery, P.: Functional imaging for regenerative medicine. Stem Cell Res. Ther. 7, 1–13 (2016). https://doi.org/10.1186/s13287-016-0315-2

24. Rajchgot, J., Coulibaly, J.T., Keiser, J., Utzinger, J., Lo, N.C., Mondry, M.K., Andrews, J.R., Bogoch, I.I.: Mobile-phone and handheld microscopy for neglected tropical diseases. PLoS Negl. Trop. Dis. 11, e0005550 (2017). https://doi.org/10.1371/journal.pntd.0005550

25. Lin, C.S., Xin, Z.C., Dai, J., Lue, T.F.: Commonly used mesenchymal stem cell markers and tracking labels: Limitations and challenges, /pmc/articles/PMC3839663/, (2013)

26. Anhalt, J.P., Fenselau, C.: Identification of Bacteria using Mass Spectrometry. Anal. Chem. 47, 219–225 (1975). https://doi.org/10.1021/ac60352a007

27. Claydon, M.A., Davey, S.N., Edwards-Jones, V., Gordon, D.B.: The Rapid Identification of Intact Microorganisms Using Mass Spectrometry. Nat. Biotechnol. 14, 1584–1586 (1996). https://doi.org/10.1038/nbt1196-1584

28. DeMarco, M.L., Ford, B.A.: Beyond Identification: Emerging and Future Uses for MALDI-TOF Mass Spectrometry in the Clinical Microbiology Laboratory. Clin. Lab. Med. 33, 611–628 (2013). https://doi.org/10.1016/J.CLL.2013.03.013

29. Dudley, E.: MALDI profiling and applications in medicine. In: Advances in Experimental Medicine and Biology. pp. 33–58. Springer, Cham (2014)

30. Kostrzewa, M.: Application of the MALDI Biotyper to clinical microbiology: progress and potential. Expert Rev. Proteomics. 15, 193–202 (2018). https://doi.org/10.1080/14789450.2018.1438193

31. Heap, R.E., Segarra-Fas, A., Blain, A.P., Findlay, G.M., Trost, M.: Profiling embryonic stem cell differentiation by MALDI TOF mass spectrometry: Development of a reproducible and robust sample preparation workflow. Analyst. 144, 6371–6381 (2019). https://doi.org/10.1039/c9an00771g

32. Bruker Daltonix GmbH: Bruker Bacterial Test Standard - Instructions for Use. (2012)

33. Edwards, J.L., Kennedy, R.T.: Metabolomic analysis of eukaryotic tissue and prokaryotes using negative mode MALDI time-of-flight mass spectrometry. Anal. Chem. 77, 2201–2209 (2005). https://doi.org/10.1021/ac048323r

34. Bruker Daltonix GmbH: Bruker Guide to MALDI Sample Preparation. (2012)

35. Gruendling, T., Sauerland, V., Barahona, C., Herz, C., Nitsch, U.: Polyalanine - A practical polypeptide mass calibration standard for matrix-assisted laser desorption/ionization mass spectrometry and tandem mass spectrometry in positive and negative mode. Rapid Commun. Mass Spectrom. 30, 681–683 (2016). https://doi.org/10.1002/rcm.7492

36. Gurtovenko, A.A., Anwar, J.: Interaction of ethanol with biological membranes: The formation of non-bilayer structures within the membrane interior and their significance. J. Phys. Chem. B. 113, 1983–1992 (2009). https://doi.org/10.1021/jp808041z

37. Doron, G., Klontzas, M.E., Mantalaris, A., Guldberg, R.E., Temenoff, J.S.: Multiomics characterization of mesenchymal stromal cells cultured in monolayer and as aggregates. Biotechnol. Bioeng. 117, 1761–1778 (2020). https://doi.org/10.1002/bit.27317

CHAPTER 6. CONCLUSIONS AND OUTLOOK

6.1 Abstract

This chapter summarizes the conclusions drawn from each major project in this thesis. A summary for the major accomplishments constructing new tools using vacuum assisted plasma ionization (VaPI) are discussed. The impact of the multiphase project evaluating the available tools on the market, performance, cost, and field usability of several screening devices for small molecule pharmaceuticals is examined. The initial development of matrix assisted laser desorption ionization (MALDI) mass spectrometry for cellular therapy screening is assessed. Future work for each major project is also discussed.

6.2 Major Accomplishments

6.2.1 Vacuum Assisted Plasma Ionization Development

Chapter 2 describes the development of the aerosol vacuum assisted plasma ionization (Aero-VaPI) source coupled to the Waters Synapt G2s mass spectrometer. The Aero-VaPI source combines three key technologies. First, a scanning mobility particle sizer is coupled in parallel to measure the diameters of the aerosols tested. Second, VaPI boosts sensitivity by entraining the analytes into the plasma stream that is directly coupled to the ambient pressure interface of the mass spectrometer to minimize fluid dynamic losses of the ions. Robust online ionization can be conducted with VaPI and without extensive ion activation. Third and after VaPI ionization, the ion mobility mass spectrometer (IM-MS) in the Synapt captures orthogonal ion mobility and mass to charge information to separate

complex isomers that could be formed in aerosols. IM-MS provides higher peak capacity, good mass accuracy, and the additional capabilities of MS/MS can help identify features of interest. This new tool gathers simultaneous particle size, ion mobility, and *m/z* information in real time without fragmentation of the organic analytes in the ionization source. With this information, Aero-VaPI can lead to more in depth understanding about the complex chemistry inside of aerosols. Future studies of new prebiotic aerosol chemistries with Aero-VaPI-MS can provide insight into the mechanisms of biopolymer formation in these environments.

Chapter 3 details the construction of pyrolysis VaPI (pyro-VaPI) as a tool to analyze insoluble polymers such as nylons. The pyrolysis device was built in house that could reach temperatures of up to 900°C. The pyrolysis unit could controllably heat the sample impacting the pyrolyzed species' volatility. After soft ionization of the pyrolyzed analytes with VaPI, ion mobility and *m/z* data for the pyrolyzed analytes can be gathered in real time. With these capabilities, unique isobaric species for nylons 6, 6-6, 6-9, 6-10, and 6-12 were discovered through ion mobility separations once a certain pyrolysis temperature was reached. The added MS/MS capabilities of the Synapt allowed for confirmation that the separated isobars in the mobility region were their respective nylons. Both isobaric species of the same nylon fragmented differently under the same collision energy, suggesting different arrangements that impact the bond strength. This nylon data set shows how new potential mechanistic discoveries of pyrolyzed polymer molecular interactions can be achieved by combining the information gathered from the pyrolysis device temperature, collisional cross sections, and *m/z* values through pyro-VaPI.

6.2.2 Rapid Pharmaceutical Quality Screening

Chapter 4 evaluated twelve different portable tools for the post-market surveillance of small molecule pharmaceuticals in a laboratory setting. These twelve devices ranged from a simple single-use disposable colorimetric assay to a complex portable mass spectrometer. This overall study guides regulators about the advantages and disadvantages of each device from set-up to testing. This includes a performance evaluation in detecting poor quality medicines that included simulated and genuine field collected samples. Overall, all the devices could detect falsified medicines that contain none or the wrong active ingredient. Substandard detection with reduced active ingredient concentrations varied the most for all the devices evaluated. The quantitative devices such as the mass spectrometer had high sensitivities toward detecting reduced active ingredient concentrations; however, their specificity suffered when using pharmacopeial thresholds for passing tests. The laboratory phase in Chapter 4 is part of a multi-phase project outlined in Appendix B. As one of the largest studies for field deployable poor quality medicine detection devices, regulators will have 5 key publications to reference when deciding which devices to purchase. First, regulators will have a detailed review of the literature to see all the potential devices on the market. Second, a detailed performance evaluation was conducted in the laboratory for 12 devices covering the broadest array of technologies selected from the literature review. Third, devices deemed field suitable from the lab phase are evaluated in a simulated pharmacy by inspectors to assess their usability and note common problems. Fourth, a cost analysis is conducted for the tools deemed field deployable. Finally, the fifth article details lessons learnt from the project and recommendations for future study.

Chapter 5 explores the use of MALDI mass spectrometry as a new tool for the rapid quality screening of cellular therapies. The Accelerated Screening for the Protection and Efficacy of Cellular Therapies (ASPECT) workflow was developed to rapidly process cells with minimal user input. Lipid profiling, metabolite profiling, and protein profiling MALDI matrix protocols and mass spectrometer settings were established. Two custom scripts were written to rapidly process data with minimal user input. The first script rapidly extracts the instrument's proprietary data file format and converts it to the common format .mxXML. After conversion, the second script automatically processes the data with little user input and output's a MALDI target map with samples that passed or failed. The preliminary data set compared untreated versus ethanol incubated mesenchymal stromal cells to simulate normal versus egregiously manufactured cells. Lipid profiling was the most sensitive method towards detecting the disruption of the lipid membrane through ethanol incubation than protein or metabolite profiling. This preliminary data set demonstrates the underlying workflow for ASPECT that can be used to explore a wider array of samples and where room for improvement lies. ASPECT begins the conversation of developing tools like MALDI to combat the illicit manufacturing of poor quality cellular therapies on the market.

6.3 Impact and Future Direction

This thesis work has built and evaluated various mass spectrometric tools that can be used for a wide variety of applications. New tool development such as with VaPI can help explore new realms of chemistry inaccessible before. The modularity of the VaPI source allows for rapid adoptability for various applications. The coupling of VaPI to ion mobility mass spectrometry adds additional peak capacity to a technique previously limited to *m/z*

data alone. In the case of Aero-VaPI, there is a whole world of prebiotic chemistry to explore in aerosols as micro reaction vessels [1]. The field of aerosol chemistry is wide and Aero-VaPI can provide a new toolset for the identification of polymers in atmospheric organic aerosols [2].

Pyro-VaPI has many avenues of research to explore. Explaining the nylon isobaric species with different fragmentation patterns may be an interesting data set to model. Pyrolyzed polyolefins have been characterized through ion mobility mass spectrometry before; however, two isobaric species in the mobility region from the same chain length polymer have not been seen yet to the best of our knowledge [3]. Modeling of polymer pyrolysis products have been reported before, but the two isobaric species of the nylons in the mobility region have yet to be explained [4, 5]. Various other polymers can be explored to see if isobaric species as seen in nylon exist. Due to VaPI's modularity, it may be possible to combine Pyro-VaPI and Aero-VaPI into a single source known as Pyro-Aero-VaPI as aerosol characterization of pyrolysis products is a field of study [6, 7]. VaPI offers a highly adaptable tool and with the power of coupling the source to ion mobility mass spectrometry, new areas of chemistry can be explored.

The laboratory phase of the portable screening device project for small molecule pharmaceuticals evaluated 12 out of the 41 tools found in the literature review. There are many other devices to evaluate alongside each other to measure their performance, cost, and usability in the field. For example, there are many other portable mass spectrometers on the market other than the QDa. These portable mass spectrometers have various sampling and ionization platforms that maybe easier and cheaper to utilize than the QDa's flow injection analysis through electrospray ionization [8]. The QDa was the most powerful

platform within Chapter 4 at detecting substandard medicines with reduced active ingredient concentrations. However, the consumables and mechanical complexity make the QDa less attractive to deploy in the field compared to more robust handheld Raman or infrared spectrometers with little to no consumables required. These other portable mass spectrometers could be evaluated together to assess the most cost-effective, simple to use, and highest performance tool for the detection of poor quality medicines. Along with the United States Pharmacopeia's efforts through their technology review program, there is a great need to standardize the way these portable screening tools are evaluated with so many different devices on the market [9]. Further insight into public health policy regarding portable screening devices is necessary to keep pace with the technological advances and to be as efficient as possible combating poor quality medicines [10, 11].

The preliminary data from ASPECT along with the work by Heap et al. shows that MALDI can be a valuable tool for combating poor quality cellular therapies [12]. There are many avenues to evaluate and improve the ASPECT workflow. Assessing and expanding the capabilities of ASPECT can include: detecting bacterially- or chemically-contaminated cells, monitoring growing or storage conditions, or evaluating donor, lot number, and passage number variation. Evaluating the biological reproducibility of cellular therapies in MALDI experiments would be critical to establishing biotyping databases such as those used for bacteria. The scripts for ASPECT can also be further optimized. Although correlation coefficient testing is a quick and easy calculation, there are likely other more powerful algorithms that could be utilized to detect poor quality cellular therapies. Homogenizing the coding language and developing a graphical user interface for ASPECT data processing would make adoption in the field easier. Many of the same difficulties

described previously with screening devices for small molecule pharmaceuticals also applies to cellular therapy screening tools.

6.4 References

1. Tran, Q.P., Adam, Z.R., Fahrenbach, A.C.: Prebiotic reaction networks in water. Life. 10, 1–29 (2020). https://doi.org/10.3390/life10120352

2. Kalberer, M., Paulsen, D., Sax, M., Steinbacher, M., Dommen, J., Prevot, A.S.H., Fisseha, R., Weingartner, E., Frankevich, V., Zenobi, R., Baltensperger, U.: Identification of Polymers as Major Components of Atmospheric Organic Aerosols. Science (80-.). 303, 1659–1662 (2004). https://doi.org/10.1126/science.1092185

3. Farenc, M., Witt, M., Craven, K., Barrère-Mangote, C., Afonso, C., Giusti, P.: Characterization of Polyolefin Pyrolysis Species Produced Under Ambient Conditions by Fourier Transform Ion Cyclotron Resonance Mass Spectrometry and Ion Mobility-Mass Spectrometry. J. Am. Soc. Mass Spectrom. 28, 507–514 (2017). https://doi.org/10.1007/s13361-016-1572-0

4. Kruse, T.M., Wong, H.W., Broadbelt, L.J.: Mechanistic modeling of polymer pyrolysis: Polypropylene. Macromolecules. 36, 9594–9607 (2003). https://doi.org/10.1021/ma030322y

5. Hujuri, U., Ghoshal, A.K., Gumma, S.: Modeling pyrolysis kinetics of plastic mixtures. Polym. Degrad. Stab. 93, 1832–1837 (2008). https://doi.org/10.1016/j.polymdegradstab.2008.07.006

6. Iisa, K., Johansson, A.C., Pettersson, E., French, R.J., Orton, K.A., Wiinikka, H.: Chemical and physical characterization of aerosols from fast pyrolysis of biomass. J. Anal. Appl. Pyrolysis. 142, 104606 (2019). https://doi.org/10.1016/j.jaap.2019.04.022

7. Chen, W.H., Du, S.W., Yang, H.H., Wu, J.S.: Formation characteristics of aerosol particles from pulverized coal pyrolysis in high-temperature environments. J. Air Waste Manag. Assoc. 58, 702–710 (2008). https://doi.org/10.3155/1047-3289.58.5.702

8. Snyder, D.T., Pulliam, C.J., Ouyang, Z., Cooks, R.G.: Miniature and Fieldable Mass Spectrometers: Recent Advances. Anal. Chem. 88, 2–29 (2016). https://doi.org/10.1021/acs.analchem.5b03070

9. Technology Review Program | USP, https://www.usp.org/global-public-health/technology-review-program

10. Hamilton, W.L., Doyle, C., Halliwell-Ewen, M., Lambert, G.: Public health

interventions to protect against falsified medicines: A systematic review of international, national and local policies, https://academic.oup.com/heapol/article/31/10/1448/2567085, (2016)

11. Newton, P.N., Amin, A.A., Bird, C., Passmore, P., Dukes, G., Tomson, G., Simons, B., Bate, R., Guerin, P.J., White, N.J.: The primacy of public health considerations in defining poor quality medicines. PLoS Med. 8, (2011). https://doi.org/10.1371/journal.pmed.1001139

12. Heap, R.E., Segarra-Fas, A., Blain, A.P., Findlay, G.M., Trost, M.: Profiling embryonic stem cell differentiation by MALDI TOF mass spectrometry: Development of a reproducible and robust sample preparation workflow. Analyst. 144, 6371–6381 (2019). https://doi.org/10.1039/c9an00771g

APPENDIX A. MICROPLASMA IONIZATION OF VOLATILE ORGANICS FOR IMPROVING AIR/WATER MONITORING SYSTEMS ON-BOARD THE INTERNATIONAL SPACE STATION

Adapted with permission from:

Bernier, M.C., Alberici, R.M., Keelor, J.D., Dwivedi, P., Zambrzycki, S.C., Wallace, W.T., Gazda, D.B., Limero, T.F., Symonds, J.M., Orlando, T.M., Macatangay, A., Fernández, F.M.: Microplasma Ionization of Volatile Organics for Improving Air/Water Monitoring Systems On-Board the International Space Station. J. Am. Soc. Mass Spectrom. 27, 1203–1210 (2016). https://doi.org/10.1007/s13361-016-1388-y

Bernier, M.C., Alberici, R.M. and Keelor, J.D. constructed and tested the microplasma source. Dwivedi, P. and Zambrzycki, S.C. conducted experiments with the microplasma and DART sources.

A.1 Abstract

Low molecular weight polar organics are commonly observed in spacecraft environments. Increasing concentrations of one or more of these contaminants can negatively impact Environmental Control and Life Support (ECLS) systems and/or the health of crew members, posing potential risks to the success of manned space missions. Ambient plasma ionization mass spectrometry (MS) is finding effective use as part of the analytical methodologies being tested for next-generation space module environmental

analysis. However, ambient ionization methods employing atmospheric plasmas typically require relatively high operation voltages and power, thus limiting their applicability in combination with fieldable mass spectrometers. In this work, we investigate the use of a low power microplasma device in the microhollow cathode discharge (MHCD) configuration for the analysis of polar organics encountered in space missions. A metal-insulator-metal (MIM) structure with molybdenum foil disc electrodes and a mica insulator was used to form a 300 μm diameter plasma discharge cavity. We demonstrate the application of these MIM microplasmas as part of a versatile miniature ion source for the analysis of typical volatile contaminants found in the International Space Station (ISS) environment, highlighting their advantages as low cost and simple analytical devices.

A.2 Introduction

Current in-flight air monitoring systems provide the necessary information to accurately assess air quality in the International Space Station (ISS), but the information available regarding water quality is still limited. Cabin air monitors in the ISS have typically used gas chromatography, ion and differential mobility spectrometry, and mass spectrometry (MS) to monitor part-per-million (ppm) levels of air contaminants [1–4]. For water samples, electrochemistry and colorimetric solid-phase extraction/reflectance spectroscopy are used to determine total organic carbon and biocide concentrations, respectively [5, 6]. These on-board technologies, however, lack specificity or only focus on a narrow class of analytes, and are not implemented in a fashion that enables simultaneous air and water quality assessment. Therefore, the current environmental monitoring strategy still relies on ground analysis of returned water samples for obtaining more comprehensive chemical information. This limitation, if not addressed, could

seriously limit the scope of future space exploration missions beyond low-Earth orbit. To address these shortcomings, more advanced in-flight air and water chemical analyzers are needed to reduce crew time, provide real-time data to manage nominal and off-nominal scenarios, and help assure mission success.

Recent work by our team demonstrated a new electrothermal vaporization (ETV) sample introduction device coupled to a direct analysis in real-time (DART) ambient plasma ion source and a high-resolution time-of-flight mass spectrometer for identifying and quantifying a variety of volatile organic compounds of importance to the ISS environment [7]. The next logical step in the design of a combined air/water analyzer is the miniaturization of the plasma ion source itself by using a microplasma system, with the goal of reducing overall instrument size, required gas flow rates, and electrical power consumption.

Microplasmas are sub-millimeter scale non-equilibrium electrical discharges [8] that operate with unique geometries [9], and serve as effective sources for emission spectroscopy [10, 11], chemical ionization MS [12], and vacuum ultraviolet (VUV) photoionization MS [13]. Steady growth in the development of microplasmas and other low power plasma for analytical chemistry applications has been seen in the recent literature [14, 15], the driving force being the potential for developing small, low power devices with reduced operational cost and increased fieldability [16, 17], with many focused on coupling to portable low resource MS instrumentation [18–20]. Microplasma-based miniature ion sources operated under ambient sampling/ionization conditions have the additional advantages of high sample throughput and simplicity, enabling direct analysis with little or no sample preparation [21, 22].

Here, we report on the performance of a microhollow cathode discharge (MHCD) microplasma-based ion source for the mass spectrometric analysis of a series of organic analytes of relevance to the ISS environment. The performance of the MHCD is compared with a commercial DART ion source. To the best of our knowledge, this is the first attempt to use MHCD microplasmas for the ionization of analytes of environmental importance in space exploration.

A.3 Experimental

A.3.1 Chemicals

The target compounds were selected to include those representative of low-molecular-weight polar organics that are routinely detected in the ISS atmosphere and water. Analytes tested included methanol, ethanol, isopropanol, acetone, methyl ethyl ketone, and ethyl acetate. These were purchased from Fisher Scientific Inc. (Pittsburgh, PA, USA) and Sigma Aldrich (St. Louis, MO, USA) and used as received (>98% purity) without further purification. Gases used with both the MHCD and DART ion sources included industrial grade nitrogen (99.995%), ultrahigh purity helium (99.999%), and ultrahigh purity argon (99.999%) obtained from Airgas (Atlanta, GA, USA).

A.3.2 MHCD Microplasmas

The prototype microplasma ion source design and construction are shown in Figure A-1. The device's core consists of two conductive molybdenum foil discs (diameter = 8 mm, thickness = 100 μm) and an insulating mica disc (diameter = 10 mm, thickness = 100 μm) in a metal-insulator-metal (MIM) configuration. The cylindrical micro-discharge

cavity between the planar electrodes was fabricated by laser etching a 300 μm diameter hole through the center of the three discs [(16)]. The discs were aligned and mounted in an aluminum and PEEK screw-capsule housing containing a gas feed line and electrical contacts connected to a PS350/5000 V–25 W high voltage supply (Stanford Research Systems, Inc., Sunnyvale, CA, USA). In DC mode, a continuous potential bias in the range of +600–2400 V was applied to the front Mo electrode. The electrode was connected in series with a set of resistors totaling 20 MΩ and resulting in a current of 30–120 μA for an estimated discharge power of approximately 0.1 W using nitrogen gas (0.100–1.0 L min^{-1}). Helium and argon were also used as source gases at comparable currents and flow rates to investigate the operational parameters for optimal ionization efficiency and conservative gas flow. The distance between the MHCD microplasma and the mass spectrometer inlet was optimized to 4 mm, where the population of reactant ions consisting mostly of water clusters ranging from $[H_2O + H]^+$ to $[(H_2O)_4 + H]^+$ were observed at their maximum intensities.

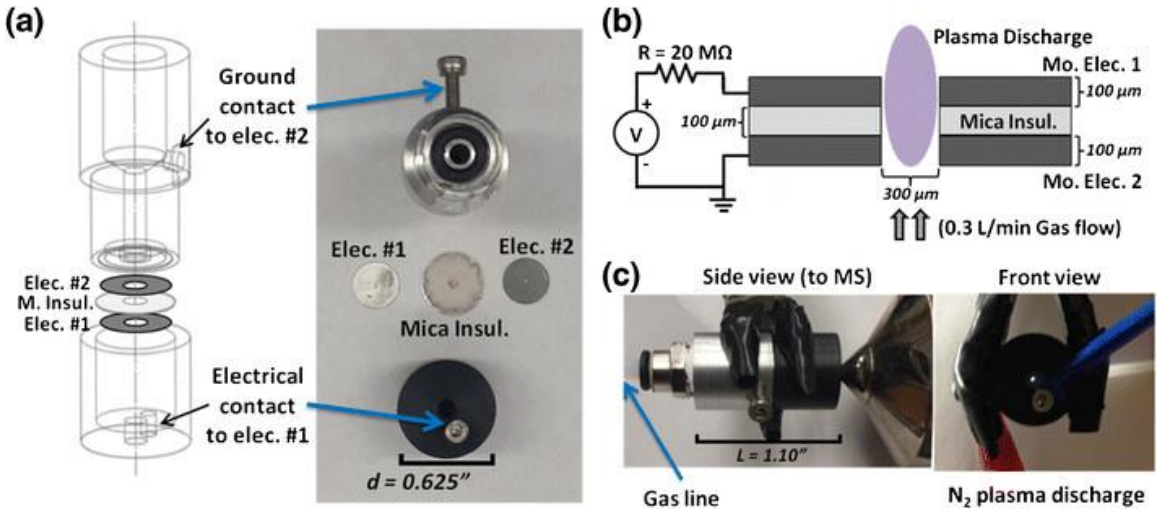

Figure A-1 Schematics and images of the metal-insulator-metal (MIM)-type micro-hollow cathode discharge (MHCD) microplasma ion source with (A) details of the components of the MHCD assembly, and (B) a side-view and front-view of the device showing the plasma discharge in operation using 0.3 L min^{-1} high purity nitrogen.

A.3.3 Direct Analysis in Real-Time

A detailed description of the commercial DART-SVP ion source (IonSense Inc., Saugus, MA, USA) is available elsewhere [23]. Briefly, this ion source consists of a point electrode spaced ≤1 mm from a grounded disc electrode. A negative DC potential bias of several kV is applied to the point electrode. The effective discharge potentials vary depending on source gas type, and were measured using a high voltage probe (Fluke 179 True RMS multimeter) to be approximately –400 V for helium and argon, and –1850 V for nitrogen. Undesired background ions were filtered from the post-discharge plasma gas stream by a molybdenum grid electrode (+200 V) positioned at the exit nozzle, ensuring that metastable species expelled into the ambient ionization region were the primary reactants. The DART source ceramic heater was left powered off for an accurate performance comparison with the MHCD microplasma source, based purely on plasma characteristics and operating at ambient temperature. The DART exit nozzle was optimized at a position 5–8 mm away and centered on axis with the mass spectrometer inlet. DART gas flow rates were adjusted from 0.15 L min^{-1} to 2 L min^{-1} to evaluate ionization efficiency under typical DART settings and settings comparable to those used for the MHCD microplasma ion source.

A.3.4 TOF MS Instrumentation

Both the DART and MHCD ion sources were coupled to an orthogonal time-of-flight (TOF) mass spectrometer (JEOL AccuTOF, Tokyo, Japan). The mass spectrometer was operated in positive ion mode. Typical ion optics conditions were as follows: orifice lens 1 set to 10 V, ring lens at 6 V, and orifice lens 2 at 2 V with the desolvation temperature

set to 100 °C. The ion guide reference voltage was set at –29 V and the pusher bias voltage was –0.28 V. Data was acquired using the JEOL Mass Center software in the 10–300 m/z range. The AccuTOF mass spectrometer provided a mass resolution ranging between 1700 and 4100 (FWHM) across the 18–121 Da range, corresponding to the target analytes.

A.4 Results and Discussion

A.4.1 Optimization and Comparison to DART

The ability of the compact, miniaturized MHCD microplasma to ionize low-molecular-weight organic volatiles and to match the performance of a commercial DART-SVP ion source was first evaluated. The DART heater was left disabled during these experiments, as enhanced thermal desorption was unnecessary due to the high vapor pressures of the target analytes. Furthermore, the addition of an independent resistive element would contribute unfavorably to material/power requirements aboard the ISS. The microplasma ion source position and operational parameters were adjusted for maximum intensity of plasma-derived reactant ions. Figure A-2 A shows results for both the DART (left) and MHCD (right) ion sources, operated with ambient temperature nitrogen as the plasma working gas at optimized gas flow rates of 2.2 L min^{-1} and 0.50 L min^{-1}, respectively. The background spectra for the microplasma showed a positive mode reactive ion population (RIP) consisting of several protonated water clusters $(H_2O)nH^+$, with the n = 2 (m/z = 37) protonated water dimer dominating the spectrum, and clusters observed up to n = 4 (m/z = 73). This reactant ion background was very similar to the RIP distribution observed for the DART ion source, which only lacked the $[(H_2O)_4H]^+$ species.

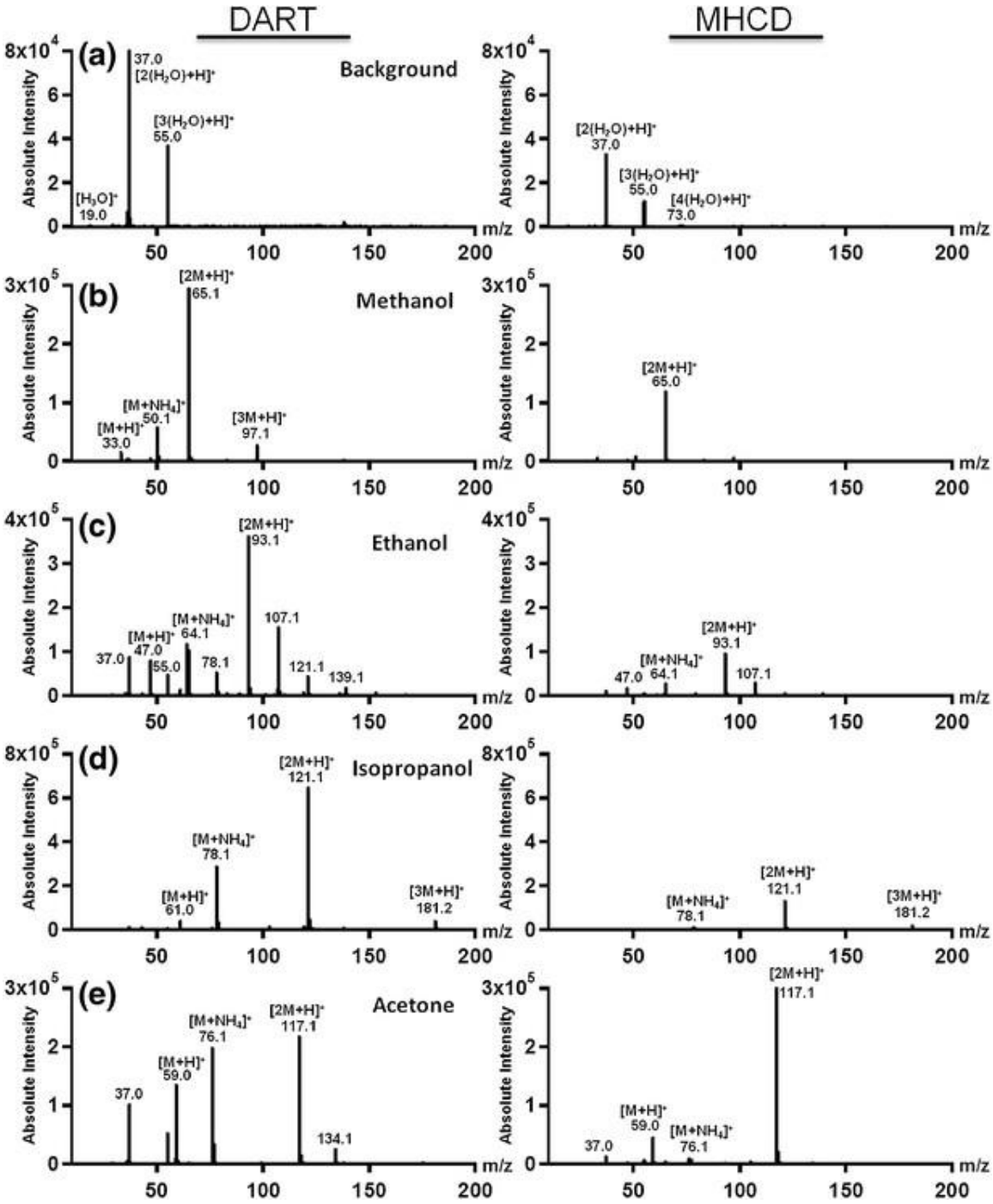

Figure A-2 Mass spectra of select target analytes acquired using DART and microplasma ion sources with nitrogen at 2.2 L min^{-1} and 0.5 L min^{-1}, respectively. The left column (DART) and right column (MHCD) with (A) background spectra, (B) methanol, (C) ethanol (5% IPA), (D) pure isopropanol, and (E) acetone. Mass spectrometer parameters were selected to prevent activation in the transfer ion optics: orifice lens 1 at 10 V, ring lens at 6 V, orifice lens 2 at 2 V, bias at 29 V, pusher bias voltage at –0.28 V.

Qualitative analysis of each of the four volatiles tested (Figure A-2 B&E) was conducted by coating the end of a borosilicate glass melting point capillary with neat sample solutions of each and holding the capillary probe approximately 2 mm away from the ion source gas outlet. Experimental variability originating from sample capillary positioning and the amount of solution deposited on the probe was mitigated by averaging peak areas from repeated measurements. All target compounds were observed mainly as their protonated monomer $[M + H]^+$ and dimer $[2M + H]^+$ ions, with the dimer ions in a majority of cases dominating the spectra. Some additional $[M+ NH_4]^+$ analyte species were also observed, but in lower abundances than protonated species. The detection of mostly clustered ions is attributed to the low inlet orifice potentials used, the neat solution concentrations sampled, and the unheated nitrogen ion source gas. Overall, the total ion signal intensity was lower for all analytes using the MHCD (approximately 35% of the DART signal on average), but the identities and relative ratios of ionic species for methanol, ethanol, or isopropanol did not change significantly between spectra for either ion source. For methanol, $[M + H]^+$ ions at m/z = 33, $[M + NH4]^+$ ions at m/z = 50, $[2M + H]^+$ ions at m/z = 65, and $[3M + H]^+$ ions at m/z = 97 were observed for both DART (Figure A-2 B left) and MHCD (Figure A-2 B right). Likewise, each ethanol spectrum presented $[2M + H]^+$ ions at m/z = 93, $[M + NH_4]^+$ ions at m/z = 64, $[M + H]^+$ ions at m/z = 47, and $[3M + H]^+$ ions at m/z = 139, in descending order of intensity. The only prominent exception to the observed matching ion distributions between DART and MHCD spectra was for acetone, where the $[M + NH4]^+$ signal equated to ~90% of the $[2M + H]^+$ signal for DART, but only 5% of the $[2M + H]^+$ abundance for the MHCD. It is not at all surprising that among these four simple volatile organic compounds, acetone showed the

greatest variability between the two ion sources, given the DART's and MHCD's drastically different flow rates and fluid dynamics. Of all analytes, acetone has the highest vapor pressure at 0.53 atm [24], whereas methanol, ethanol, and isopropanol possess vapor pressures of 0.07, 0.15, and 0.13 atm, respectively [24]. Likewise, the nature of the functional groups in each case (alcohol versus ketone) may offer very distinct stabilization of NH4+ adducts and different protonation sites, which would clearly have an influence on the relative spectral abundances. Such behavior could be useful in deciphering volatiles based on their fingerprint spectra (i.e., $[M + H]^+$ versus $[M + NH_4]^+$ versus $[2M + H]^+$) when low resolution mass analyzers are employed. The differences in sensitivity between the MHCD and DART ion sources seen in Figure A-2 are a consequence of differences in parameters such as gas flow rate and plasma current. The higher predicted gas velocity through the reduced dimensions of the MHCD disc electrode (i.d. = 300 μm) could also be a factor affecting ion transport under these conditions. The plasma generation conditions for each ionization source may also play a role in terms of differences in metastable abundances. However, the DART plasma operates in the corona-to-glow transition mode [25, 26], which is relatively similar to the MHCD glow mode, so in the absence of direct spectroscopic measurements, a solid conclusion cannot be drawn. Nevertheless, it appears that the limited scale and lower current of the MHCD are the primary reasons for a lower ion signal compared to the DART source, at least when the comparison is performed under gas flow regimes where DART is typically operated [26, 27].

To fully implement a system utilizing MHCD into the ISS, the ionization source must be characterized for limits of detection and ability for quantitation. Using the same capillary introduction system and using nitrogen plasma gas at a flow rate of 0.100 L min^-

[1], estimated LODs were defined as the minimum amount of material on the borosilicate capillary placed between the MHCD source and MS inlet that could be detected with high confidence. The values were found to be 3000 pmol (100 ppm) for methanol, 2000 pmol (100 ppm) for ethanol, 170 pmol (10 ppm) for isopropanol, and 430 pmol (25 ppm) for acetone. For MEK and ethyl acetate, LODs of 350 and 110 pmol (25 and 10 ppm) were achieved, respectively. These two compounds compare very well to previous work using our ETV source, which achieved quantitative limits of detection of 194 pmol for MEK and 2000 pmol for ethyl acetate injected into the sampling system [7]. For the three organic compounds with Spacecraft Water Exposure Guideline (SWEG) values, methanol, acetone, and MEK, 100-day allowable exposures were found to be 40, 150, and 54 ppm, respectively [28, 29]. While the methanol detection limit is 2.5 times higher with the current MHCD set-up than SWEG values, we believe much of the sample is being lost when placing the borosilicate capillary in an open pathway between the source and MS inlet. MEK and acetone detection limits, however, were lower than the recommended values stated in the exposure guidelines. Using a modified introduction method where sample loss is minimized through more efficient ion/neutral collection, focusing, and mixing of the plasma gas, LODs could be lowered dramatically enabling quantitation, as previously demonstrated using the ETV set-up coupled to DART [7].

A.4.2 Optimization and Comparison to DART

To fully qualify the viability of using MHCD microplasma devices as practical environmental sensing components aboard the ISS, it is critical that the operational parameter space be fully explored, including gas type and flow rate. Although nitrogen is an abundant and cost-effective option for sustaining MHCD plasmas, the power

requirements for stable plasma operation are still substantially larger than those needed for helium or argon-sustained discharges, even with the miniature cavity dimensions used. Figure A-3 showcases spectral differences observed for several analytes when operating the MHCD ion source with nitrogen, argon, or helium. Spectra of methanol (Figure A-3 A), ethanol (Figure A-3 B), isopropanol (Figure A-3 C), and acetone (Figure A-3 D) were acquired with low energy transfer ion optics settings in order to preserve the nature of the ion population without the influence of in-source declustering. Throughout these experiments, the plasma DC potential was held at a value necessary to achieve a plasma current of 0.050 mA regardless of the gas used, ensuring similar power consumption for each.

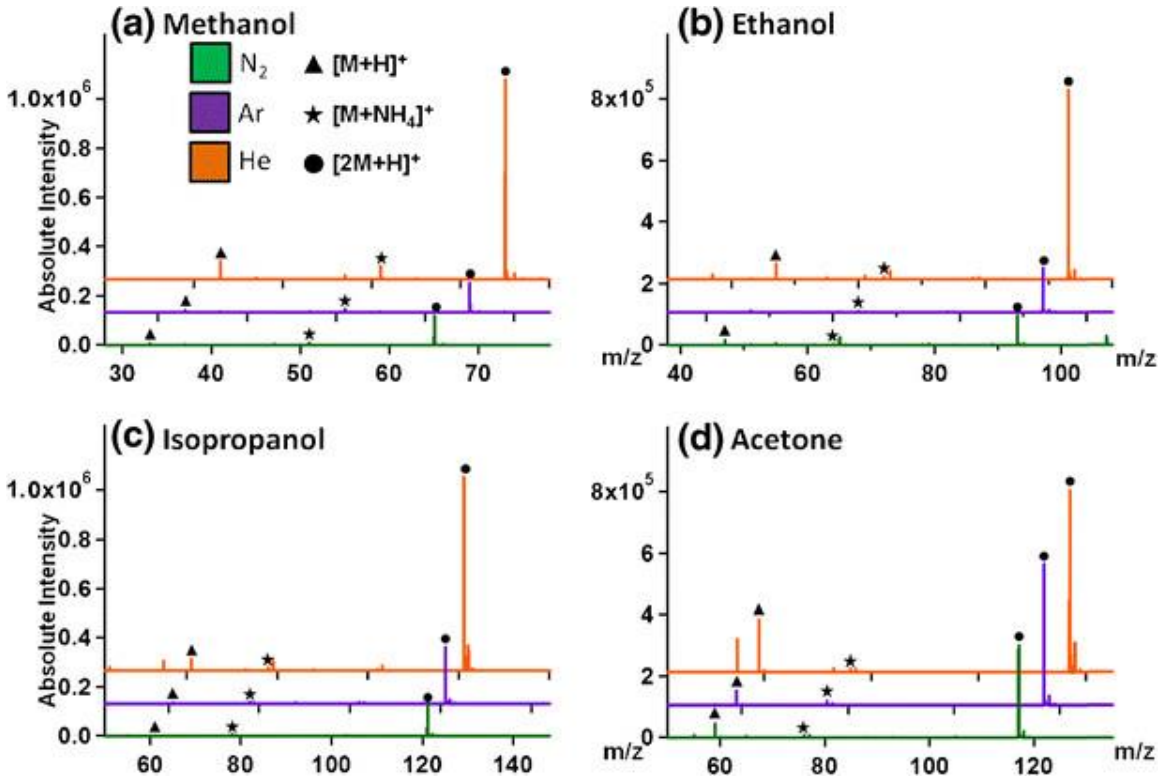

Figure A-3. Microplasma mass spectra for select target analytes acquired using N_2, Ar, and He as the plasma gases at optimized flow rates of 1.0, 0.3, and 0.5 L min–1, respectively and currents of 0.050 mA for all three. Compounds shown include (A) methanol, (B) ethanol, (C) isopropanol, and (D) acetone and show the positions and relative intensities of the $[M + H]^+$ (black triangles), $[M + NH_4]^+$ (black stars), and $[2 M + H]^+$ (black circles). Operation parameters set to same low-activation settings as in Figure A-2: orifice lens 1 at 10 V, ring lens at 6 V, orifice lens 2 at 2 V, bias at 29 V, pusher bias voltage at –0.28 V. Spectra are an average of three trials collected from one total ion chromatogram taken over multiple capillary introductions of the volatile sample.

Regardless of the plasma gas chosen, all microplasma spectra showed mainly $[2M + H]^+$ proton-bound dimers, as was the case in Figure A-2. It is clear for all test volatiles that the most intense $[M + H]^+$ and $[2M + H]^+$ signals were achieved with helium while sensitivity for argon and nitrogen remained essentially equal for each analyte. In the case of methanol (Figure A-3 A), ethanol (Figure A-3 B), and isopropanol (Figure A-3 C), the dimer intensity was about 3–5 times higher using helium than when using argon and nitrogen. For acetone, the signals for $[2M + H]^+$ with nitrogen and argon source gas were significantly greater, at approximately 50% and 75% of the dimer intensity detected using helium, respectively. Given the higher vapor pressure of acetone mentioned before, the higher acetone dimer ion abundances observed are reasonable. The much larger ion signal observed for helium was expected, since its higher thermal conductivity and metastable energy result in greater signal than is possible for either nitrogen or argon. Furthermore, it is of note that in order to achieve the highest intensity spectra for helium, an optimized flow rate of 1.0 L min^{-1} was used whereas for argon and nitrogen optimal signal was achieved at flow rates of 0.30 and 0.50 L min^{-1}, respectively. For higher density plasma gases such as Ar and N_2, higher flow rates appeared to destabilize the discharge, requiring the flow rates where maximum signal was achieved to be about 30%–50% of the optimized flow rates for helium.

We next considered the fundamental difference in flow rates needed for effective DART and MHCD operation and its effect on ionization efficiency. Figure A-4 compares the performance of the various plasma gases for both the MHCD and DART as a function of gas flow rate for the dimer $[2M + H]^+$ species. When operating the MHCD at helium flow rates of 0.05, 0.15, 0.30, and 0.50 L min^{-1}, analyte average peak areas were on par

with those seen for DART helium flow rates between 1.4 to 2.2 L min^{-1}. For nitrogen-based discharges, DART ion abundances appeared to generally increase across 1.0–2.3 L min^{-1}, with the exception of acetone. In this particular case, the nitrogen MHCD signal changed less across all flow rates tested, and dimer intensity remained 30% to 50% of the DART signal at flow rates above 1.4 L min^{-1}.

The formation of $[M + NH_4]^+$ adducts for each of the volatile analytes of interest was much more pronounced with DART than with the MHCD ion source at all flow rates tested, and with all plasma gases. Typically, MHCD $[M + NH4]^+$ ion signals averaged 0.1%–5.0% of those produced by helium DART. Given the lower ionization potential of ammonia (10.02 eV) versus that of water (12.62 eV), and the respective proton affinities of ~850 kJ mol^{-1} for ammonia and ~690 kJ mol^{-1} for water, the probability of ammonia protonation over water is greater, and ammonia adduction with an analyte may be preferred in instances where the analyte proton affinity is lower than that of ammonia [30, 31].

As seen in Figure A-4, regardless of the plasma gas used or analyte measured, the DART signals decreased drastically if gas flow rates fell below 1.0 L min^{-1}. Although decreasing the DART-inlet distance could improve ion transmission at lower flow rates, for gases such as helium the increased gas load on the mass spectrometer vacuum system could have short- and long-term detrimental effects. Additionally, it is suspected that for nitrogen plasma gas, the longer path length between the DART discharge chamber and sampling region may contribute to depletion (or relaxation) of metastable excited-state species in the plasma afterglow prior to interaction with the analyte, comparatively reducing ion signal intensity. Regardless, the nitrogen MHCD does perform well at a fraction of the flow rate needed for DART, as it also does with argon and helium. For this

reason, MHCD microplasmas are an attractive alternative when considering the limited resources aboard semi-autonomous space systems such as the ISS.

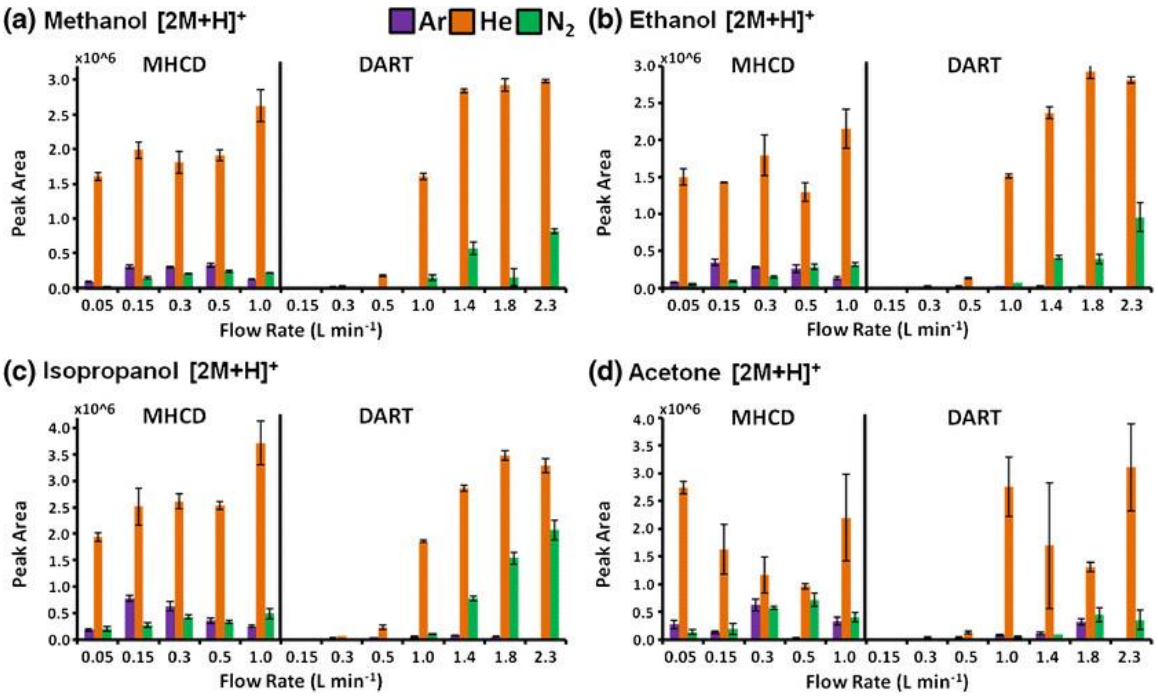

Figure A-4 Peak areas for the $[2M + H]^+$ species for (A) methanol, (B) ethanol, (C) isopropanol, and (D) acetone using argon gas (first - purple), helium gas (second - orange), and nitrogen gas (third - green) for microplasma (left) and DART (right) at a series flow rates (L min^{-1}). Flow rates for each gas were set to 0.05, 0.15, 0.3, 0.5, and 1.0 L min^{-1} for MHCD and 0.15, 0.3, 0.5, 1.0, 1.4, 1.8, and 2.2 L min^{-1} for DART. Error bars are derived from the standard deviation of three experiments.

A.4.3 Power and Lifetime Characterization

The durability of MCHD microplasmas is an important factor to evaluate prior to implementation for dependable routine use aboard ISS or any other space mission. A relevant consideration is device lifetime, as it was observed that the microplasma ion source elements could be prone to degradation and decrease in performance with continuous and prolonged use. Microplasma cavity durability is directly related to the sputtering rates induced by the specific plasma conditions chosen, largely determined by the choice of electrode material, plasma gas, and I/V regime. Figure A-5 describes the threshold plasma formation conditions for the MHCD and compares the power usage for the three plasma gases mentioned above.

The device power consumption depended on the discharge gas, as different applied voltages were required in each case to sustain an equivalent current. The power curves for each gas (Figure A-5) strongly indicate there is a clear difference in the power profile and the wattage used for nitrogen gas compared with argon and helium gases, as expected. In addition, it was observed that when using nitrogen and argon, the lifetime of the electrode at higher currents was significantly longer compared with helium. For this gas, lifetimes at powers above 0.120 mA were approximately 2–4 hours, with evident signs of electrode deterioration along the edges of the bored cavity, resulting in performance loss. Operation with nitrogen and argon was more robust and consistent even at these higher currents, with the ability to operate at over 24 h of constant use. Furthermore, operation at lower powers (<50 uA) increased lifetimes to over 100 h of operation for all plasma gas types examined. It is speculated that the rate of device degradation using helium is caused by the higher metastable energies [32] and higher plasma gas temperature because of the superior heat

capacity, thermal conductivity, and excited state distributions of helium versus nitrogen and argon. Driving MHCD devices with AC waveforms rather than a DC bias could further reduce electrode sputtering and prolong lifetime [33]. However, if operated with currents in the order of 0.050 mA, and equipped with molybdenum electrodes (E1 and E2, Figure A-1), we expect MHCDs could provide reliable operation for months if powered intermittently or upwards of several days when operating the discharge continuously.

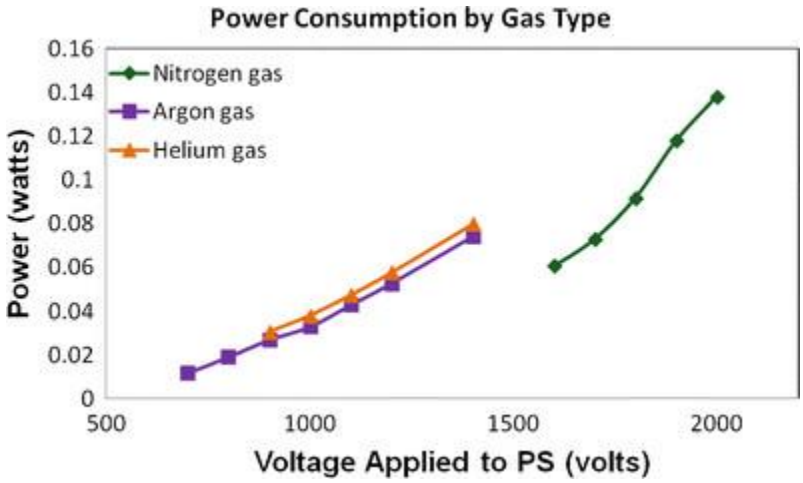

Figure A-5 Microplasma power consumption by plasma gas type at a constant flow rate of 0.100 L min^{-1} with nitrogen highlighted in green (diamonds), argon highlighted in purple (squares), and helium gas in orange (triangles).

MHCD operation using nitrogen provided an ideal balance of low power consumption and gas cost while affording adequate sensitivity and device longevity. As a possible alternative to nitrogen, argon microplasmas showed a lower onset discharge potential than helium (Figure A-5), and provided a similar sensitivity to nitrogen for volatile analysis at low gas flow rates (Figure A-3).

A.5 Conclusion

This study demonstrated the performance capabilities of a MHCD microplasma ion source for detection of organic volatiles important in environmental monitoring applications. The low power consumption and compact design make this type of plasma device a promising alternative ion source for miniature and field mass spectrometers. Both the DART and microplasma ion sources produced similar reactant ion populations and relative distributions of analyte ions, with higher-order ion clusters detected in abundance in both cases, given the relatively "soft" mass spectrometer transfer optics settings used. Analytes were observed as protonated neutrals and ammoniated adducts in most cases, with protonated dimers being the most common. Comparison experiments with various plasma gases provided significant evidence that the source of ammonia was ambient and that between nitrogen, argon, and helium at equivalent power use, there was a clear advantage for helium use in terms of sensitivity, but not power consumption or device durability.

In practice, nitrogen usage as the plasma gas would provide the most practical approach for implementing MHCD ionization aboard the ISS. It is available in large quantities and given the low flow rate required, should not make a significant impact on existing resources. It has been previously used for the volatile organic analyzer (VOA) [4]

and despite the power and signal performance observed for nitrogen operation, it would be a promising avenue for further development in designing a better water and air analysis platform. However, additional research is needed to enable the detection and quantitation of lower levels of analytes in these environments. Future studies will be aimed at improving ion transfer from the AP ionization region into the mass spectrometer. Other pursuits include device operation in AC versus DC power modes to assess device lifetime and sampling efficiency, and investigation of more complex molecular systems using flow-through sample introduction schemes for practical use aboard a manned space vessel, such as the ISS.

A.6 References

1. Limero, T.F., Nazarov, E.G., Menlyadiev, M., Eiceman, G.A.: Characterization of ion processes in a GC/DMS air quality monitor by integration of the instrument to a mass spectrometer. Analyst. 140, 922–930 (2015). https://doi.org/10.1039/c4an01800a

2. Rüdenauer, F.G.: Field emission devices for space applications. In: Surface and Interface Analysis. pp. 116–122 (2007)

3. Stuffler, T., Mosebach, H., Kampf, D., Honne, A., Tan, G.: The flight experiment ANITA - A high performance air analyser for manned space cabins. In: Acta Astronautica. pp. 573–579. Pergamon (2004)

4. Limero, T., Reese, E., Trowbridge, J., Hohmann, R., James, J.T.: Validation of the Volatile organic analyzer (VOA) aboard the International Space Station. In: SAE Technical Papers. SAE International (2003)

5. Ramanathan, R., James, J.T., McCoy, T.: Acceptable levels for ingestion of dimethylsilanediol in water on the international space station. Aviat. Sp. Environ. Med. 83, 598–603 (2012). https://doi.org/10.3357/ASEM.3198.2012

6. Gazda, D.B., Lipert, R.J., Fritz, J.S., Porter, M.D.: Investigation of the iodine-poly(vinylpyrrolidone) interaction employed in the determination of biocidal iodine by colorimetric solid-phase extraction. Anal. Chim. Acta. 510, 241–247 (2004). https://doi.org/10.1016/j.aca.2004.01.010

7. Dwivedi, P., Gazda, D.B., Keelor, J.D., Limero, T.F., Wallace, W.T., Macatangay,

A. V., Fernández, F.M.: Electro-thermal vaporization direct analysis in real time-mass spectrometry for water contaminant analysis during space missions. Anal. Chem. 85, 9898–9906 (2013). https://doi.org/10.1021/ac402365k

8. Yuan, X., Tang, J., Duan, Y.: Microplasma technology and its applications in analytical chemistry, (2011)

9. Bruggeman, P., Brandenburg, R.: Atmospheric pressure discharge filaments and microplasmas: Physics, chemistry and diagnostics. J. Phys. D. Appl. Phys. 46, 28 (2013). https://doi.org/10.1088/0022-3727/46/46/464001

10. Meyer, C., Heming, R., Gurevich, E.L., Marggraf, U., Okruss, M., Florek, S., Franzke, J.: Radiofrequency driven and low cost fabricated microhollow cathode discharge for gaseous atomic emission spectrometry. J. Anal. At. Spectrom. 26, 505–510 (2011). https://doi.org/10.1039/c0ja00216j

11. Kurunczi, P., Martus, K.E., Becker, K.: Neon excimer emission from pulsed high-pressure microhollow cathode discharge plasmas. Int. J. Mass Spectrom. 223–224, 37–43 (2003). https://doi.org/10.1016/S1387-3806(02)00778-9

12. Symond, J.M., Galhena, A.S., Fernández, F.M., Orlando, T.M.: Microplasma discharge ionization source for ambient mass spectrometry. Anal. Chem. 82, 621–627 (2010). https://doi.org/10.1021/ac901964m

13. Symonds, J.M., Gann, R.N., Fernández, F.M., Orlando, T.M.: Microplasma discharge vacuum ultraviolet photoionization source for atmospheric pressure ionization mass spectrometry. J. Am. Soc. Mass Spectrom. 25, 1557–1564 (2014). https://doi.org/10.1007/s13361-014-0937-5

14. Franzke, J.: The micro-discharge family (dark, corona, and glow-discharge) for analytical applications realized by dielectric barriers. Anal. Bioanal. Chem. 395, 549–557 (2009). https://doi.org/10.1007/s00216-009-2799-4

15. Karanassios, V.: Microplasmas for chemical analysis: Analytical tools or research toys?, (2004)

16. Gianchandani, Y.B., Wright, S.A., Eun, C.K., Wilson, C.G., Mitra, B.: Exploring microdischarges for portable sensing applications, (2009)

17. Mitra, B., Levey, B., Gianchandani, Y.B.: Hybrid arc/glow microdischarges at atmospheric pressure and their use in portable systems for liquid and gas sensing. IEEE Trans. Plasma Sci. 36, 1913–1924 (2008). https://doi.org/10.1109/TPS.2008.927135

18. Kumano, S., Sugiyama, M., Yamada, M., Nishimura, K., Hasegawa, H., Morokuma, H., Inoue, H., Hashimoto, Y.: Development of a portable mass spectrometer characterized by discontinuous sample gas introduction, a low-pressure dielectric barrier discharge ionization source, and a vacuumed headspace technique. Anal.

Chem. 85, 5033–5039 (2013). https://doi.org/10.1021/ac4002904

19. Wang, X., Zhou, X., Ouyang, Z.: Direct Analysis of Nonvolatile Chemical Compounds on Surfaces Using a Hand-Held Mass Spectrometer with Synchronized Discharge Ionization Function. Anal. Chem. 88, 826–831 (2016). https://doi.org/10.1021/acs.analchem.5b03356

20. Chen, T.C., Ouyang, Z.: Synchronized discharge ionization for analysis of volatile organic compounds using a hand-held ion trap mass spectrometer. Anal. Chem. 85, 1767–1772 (2013). https://doi.org/10.1021/ac303112d

21. Alberici, R.M., Simas, R.C., Sanvido, G.B., Romão, W., Lalli, P.M., Benassi, M., Cunha, I.B.S., Eberlin, M.N.: Ambient mass spectrometry: Bringing MS into the "real world," (2010)

22. Monge, M.E., Harris, G.A., Dwivedi, P., Fernández, F.M.: Mass spectrometry: Recent advances in direct open air surface sampling/ionization, (2013)

23. Zhou, M., McDonald, J.F., Fernández, F.M.: Optimization of a Direct Analysis in Real Time/Time-of-Flight Mass Spectrometry Method for Rapid Serum Metabolomic Fingerprinting. J. Am. Soc. Mass Spectrom. 21, 68–75 (2010). https://doi.org/10.1016/j.jasms.2009.09.004

24. Haynes, W.M.: Vapor pressures of organic compounds. In: CRC Handbook of Chemistry and Physics. p. 92. CRC Press/Taylor and Francis, Boca Raton, FL (2016)

25. Shelley, J.T., Wiley, J.S., Chan, G.C.Y., Schilling, G.D., Ray, S.J., Hieftje, G.M.: Characterization of Direct-Current Atmospheric-Pressure Discharges Useful for Ambient Desorption/Ionization Mass Spectrometry. J. Am. Soc. Mass Spectrom. 20, 837–844 (2009). https://doi.org/10.1016/j.jasms.2008.12.020

26. Shelley, J.T., Hieftje, G.M.: Ionization matrix effects in plasma-based ambient mass spectrometry sources. J. Anal. At. Spectrom. 25, 345–350 (2010). https://doi.org/10.1039/b923564g

27. Stark, R.H., Schoenbach, K.H.: Direct current high-pressure glow discharges. J. Appl. Phys. 85, 2075–2080 (1999). https://doi.org/10.1063/1.369505

28. Garcia, H.D.: Spacecraft water exposure guidelines for selected contaminants. In: National Research Council. p. 29. National Academy Press, Washington, DC (2007)

29. Garcia, H.D.: Spacecraft water exposure guidelines for selected contaminants. In: National Research Council. p. 139 and 160. National Academy Press, Washington, DC (2008)

30. Lias, S.G., Liebman, J.F., Levin, R.D.: Evaluated Gas Phase Basicities and Proton Affinities of Molecules; Heats of Formation of Protonated Molecules. J. Phys.

Chem. Ref. Data. 13, 695–808 (1984). https://doi.org/10.1063/1.555719

31. Wu, R., McMahon, T.B.: Stabilization of zwitterionic structures of amino acids (Gly, Ala, Val, Leu, Ile, Ser and Pro) by ammonium ions in the gas phase. J. Am. Chem. Soc. 130, 3065–3078 (2008). https://doi.org/10.1021/ja076685l

32. Noiri, Y., Kajita, S., Ohno, N.: Nanostructure growth by helium plasma irradiation to tungsten in sputtering regime. J. Nucl. Mater. 463, 285–288 (2015). https://doi.org/10.1016/j.jnucmat.2015.01.036

33. Hur, M., Kim, K.T., Song, Y.H.: Ac-driven plasma torch with a well-type cathode working in air and CO 2. J. Phys. D. Appl. Phys. 43, (2010). https://doi.org/10.1088/0022-3727/43/44/445201

APPENDIX B. A MULTI-PHASE EVALUATION OF PORTABLE SCREENING DEVICES TO ASSESS MEDICINES QUALITY FOR NATIONAL MEDICINES REGULATORY AUTHORITIES

B.1 Introduction

Adapted with permission from:

Caillet, C., Vickers, S., Zambrzycki, S., Luangasanatip, N., Vidhamaly, V., Boutsamay, K., Boupha, P., Lubell, Y., Fernández, F.M., Newton, P.N. "A multi-phase evaluation of portable screening devices to assess medicines quality for national Medicines Regulatory Authorities – Introduction" PLOS Negl. Trop. Dis. Accepted April 2021.

In this PLOS Collection, "A multiphase evaluation of portable screening devices to assess medicines quality for national Medicines Regulatory Authorities," we describe the results of the multiphase collaborative study conducted between 2016 and 2018 that was part of the Results for Malaria Elimination and Communicable Diseases Control (RECAP) under the Regional Malaria and Communicable Disease Trust Fund (RMTF) at the Asian Development Bank. The study aimed to evaluate the accuracy, utility, usability, and cost-effectiveness of different portable devices to identify SF medicines across a variety of essential anti-infective medicines commonly used in the Greater Mekong Sub-region (GMS) to treat malaria and bacterial infections.

As far as we are aware, this multiphase study is the first collaborative independent investigation listing the advantages and disadvantages from diverse chemical, economical,

and regulatory points of view. The overall study assesses and compares device accuracy, describes potential barriers, and evaluates the costs versus the benefits of the implementation of a wide diversity of portable medicine quality screening devices in a public health perspective. The series also highlights the difficulties and barriers to perform screening devices research and the important remaining gaps of scientific evidence.

B.2 Literature Review

Adapted with permission from:

Vickers, S., Bernier, M., Zambrzycki, S., Fernandez, F.M., Newton, P.N., Caillet, C.: Field detection devices for screening the quality of medicines: a systematic review. BMJ Glob. Heal. 3, e000725 (2018). https://doi.org/10.1136/bmjgh-2018-000725

B.2.1 Background

Poor quality medicines have devastating consequences. A plethora of innovative portable devices to screen for poor quality medicines has become available, leading to hope that they could empower medicine inspectors and enhance surveillance. However, information comparing these new technologies is woefully scarce.

B.2.2 Methods

We undertook a systematic review of Embase, PubMed, Web of Science and SciFinder databases up to 30 April 2018. Scientific studies evaluating the performances/abilities of portable devices to assess any aspect of the quality of pharmaceutical products were included.

B.2.3 Results

Forty-one devices, from small benchtop spectrometers to 'lab-on-a-chip' single-use devices, with prices ranging from <US$10 to >US$20 000, were included. Only six devices had been field-tested (GPHF-Minilab, CD3/CD3+, TruScan RM, lateral flow dipstick immunoassay, CBEx and Speedy Breedy). The median (range) number of active pharmaceutical ingredients (APIs) assessed per device was only 2 (1–20). The majority of devices showed promise to distinguish genuine from falsified medicines. Devices with the potential to assay API (semi)-quantitatively required consumables and were destructive (GPHF-Minilab, PharmaChk, PADs, lateral flow immunoassay dipsticks, paper-based microfluidic strip and capillary electrophoresis), except for spectroscopic devices. However, the 10 spectroscopic devices tested for their abilities to quantitate APIs required processing complex API-specific calibration models. Scientific evidence of the ability of the devices to accurately test liquid, capsule or topical formulations, or to distinguish between chiral molecules, was limited. There was no comment on cost-effectiveness and little information on where in the pharmaceutical supply chain these devices could be best deployed.

B.2.4 Conclusion

Although a diverse range of portable field detection devices for medicines quality screening is available, there is a vitally important lack of independent evaluation of the majority of devices, particularly in field settings. Intensive research is needed in order to inform national medicines regulatory authorities of the optimal choice of device(s) to combat poor quality medicines.

B.3 Field Evaluation

Adapted with permission from:

Caillet, C., Vickers, S., Zambrzycki, S., Fernandez, F.M., Vidhamaly, V., Boutsamay, K., Boupha, P., Mukaka,M., Newton, P.N. "A comparative field evaluation of six medicine quality screening devices in Laos." PLOS Negl. Trop. Dis. Compiling Revisions May 2021.

B.3.1 Background

Medicine quality screening devices hold great promise for post-market surveillance (PMS). However, there is little independent evidence on their field utility and usability to inform policy decisions. This pilot study in the Lao PDR tested six devices' utility and usability in detecting substandard and falsified medicines (SF).

B.3.2 Methodology/Principal findings

Observational time and motion studies of the inspections by 16 Lao medicine inspectors of 1) the stock of an Evaluation Pharmacy (EP), constructed to resemble a Lao pharmacy and 2) a sample set of medicines (SSM); were conducted without and with six devices: four handheld spectrometers (two infrared: MicroPHAZIR, NIR-S-G1 & two Raman: Progeny, Truscan); one portable infrared spectrometer (4500a), and single-use paper analytical devices (PAD). User experience was documented by interviews and focus group discussions.

Significantly more samples were wrongly categorized as pass/fail with the PAD compared to the other devices in EP inspections ($p<0.05$). The numbers of samples wrongly classified

in EP inspections were significantly lower than in initial visual inspections without devices for 3/6 devices (NIR-S-G1, MicroPHAZIR, 4500a). The NIR-S-G1 had the fastest time per sample (median 93.5 sec, $p<0.001$). The time spent on EP visual inspection was significantly shorter when using a device than for inspections without devices, except with the 4500a, risking missing visual clues of SF presence. The main user errors were the selection of wrong spectrometer reference libraries and wrong user interpretation of PAD results. Limitations included repeated inspections of the EP by the same inspectors with different devices and limited availability of SF medicines.

B.3.3 Conclusions/Significance

This pilot study suggests policy makers wishing to implement portable screening devices in PMS should be aware that overconfidence in devices may cause harm by reducing inspectors' investment in visual inspection. It also provides insight into the advantages/limitations of diverse screening devices in the hands of end-users.

B.4 Cost Effectiveness

Adapted with permission from:

Luangasanatip, N., Khonputsa, P., Caillet, C., Vickers, S., Zambrzycki, S., Fernandez, F.M., Newton, P.N., Lubell, Y. "Cost-effectiveness of six medicine quality screening devices in post-market surveillance of antimalarial treatments in Laos". PLOS Negl. Trop. Dis. Compiling Revisions May 2021.

B.4.1 Background

Substandard and falsified (SF) antimalarials have devastating consequences including increased morbidity, mortality and economic losses. Portable medicine quality screening devices are increasingly available, but whether their use for the detection of SF antimalarials is cost-effective is not known. We evaluated the cost-effectiveness of implementing such devices in medicine inspections in pharmacies in Laos PDR, conservatively focusing on their benefit in detecting SF artemisinin-based combination therapies (ACTs).

B.4.2 Methods and findings

We used a decision tree model to simulate the deployment of six portable screening devices: two handheld near-infrared [MicroPHAZIR RX, NIR-S-G1], two handheld Raman spectrometers [Progeny, TruScan RM]; one portable mid-infrared device [4500a FTIR], and single-use disposable paper analytical devices [PADs]. We considered two scenarios with varying prevalence of SF ACTs. In Scenario 1, 20% of ACTs were assumed to be substandard and 20% falsified. In Scenario 2, 10% were assumed to be substandard and 5% falsified. Different sampling strategies in which medicine inspectors would test 1, 2, or 3 sample(s) of each brand of ACT were evaluated. Incremental cost-effectiveness ratios were estimated for each device compared with a baseline of visual inspections alone. A multiway head-to-head comparison of all devices and sampling strategies was carried out by ranking the net monetary benefit of all options. In Scenario 1, all devices were cost-effective with a 1-sample strategy. In Scenario 2, only four devices (the MicroPHAZIR RX, 4500a FTIR, NIR-S-G1, and PADs) were cost-effective with a 1-sample strategy. In the multi-way comparative analysis, in both scenarios the NIR-S-G1 testing 2 samples was the most cost-effective option.

B.4.3 Conclusions:

Routine inspection of ACT quality using portable screening devices is likely to be cost-effective in the hypothetical Laos context. This work should encourage policy-makers or regulators to further investigate investment in portable screening devices to detect SF medicines and reduce their associated undesired health and economic burdens.

B.5 Recommendations and Next Steps

Adapted with permission from:

Caillet, C., Vickers, S., Vidhamaly, V., Boutsamay, K., Boupha, P., Zambrzycki, S., Luangasanatip, N., Fernandez, F.M., Lubell, Y., Newton, P.N. "Evaluation of portable devices for medicine quality screening: lessons learnt and next steps." PLOS Med. Compiling Revisions May 2021.

We assessed the performances, usability/utility and cost-effectiveness of implementation of devices that can assist in the detection of substandard and falsified medicines from different viewpoints. We conclude that, even if current technology does not enable one device to effectively monitor the quality of all medicines, there is great promise for portable devices to empower regulatory authorities in their key function to improve national and global public health. The devices assessed in our work have capabilities useful in specific contexts and needs. However, one should also be aware of their limits and difficulties that may arise for their implementation. With the current state of knowledge, for the devices to fully realize their promise, more than technological advances embedded in these devices will be required to ensure that their use has the

intended impact in mitigating the devastating effects of substandard and falsified medicines on global health. A strong regulatory framework, selecting the right device for the right job, cost & logistic considerations, standardized device protocols, and the need for more evidence is necessary for effective portable device implementation.

APPENDIX C. ATMOSPHERIC PRESSURE DRIFT TUBE ION MOBILITY–ORBITRAP MASS SPECTROMETRY: INITIAL PERFORMANCE CHARACTERIZATION.

Adapted with permission from:

Keelor, J.D., Zambrzycki, S., Li, A., Clowers, B.H., Fernández, F.M.: Atmospheric Pressure Drift Tube Ion Mobility–Orbitrap Mass Spectrometry: Initial Performance Characterization. Anal. Chem. 89, 11301–11309 (2017). https://doi.org/10.1021/acs.analchem.7b01866.

Keeler J.D. setup and optimized the drift tube. Zambrzycki S. performed replicated experiments, troubleshooting, and maintenance for the drift tube.

C.1 Abstract

Atmospheric pressure drift tube ion mobility spectrometry (AP-DTIMS) was coupled with Fourier transform Orbitrap mass spectrometry. The performance capabilities of this versatile new arrangement were demonstrated for different DTIMS ion gating operation modes and Orbitrap mass spectrometer parameters with regard to sensitivity and resolving power. Showcasing the optimized AP-DTIMS-Orbitrap MS system, isobaric peptide and sugar isomers were successfully resolved and the identities of separated species validated by high-energy collision dissociation experiments.

C.2 Introduction

Ion mobility (IM) spectrometry provides an additional analytical separation dimension when combined with mass spectrometry (MS) as well as the ability for ion selection and filtering based on size-to-charge ratios, ultimately enabling increases in instrument specificity, peak capacity, and dynamic range. By expanding spectral coverage across two or more dimensions (e.g., drift time and *m/z*), IM–MS analysis facilitates spectral interpretation by lessening spectral congestion [1] for different compounds with distinct structural motifs, e.g. lipids, carbohydrates, peptides, etc., mapping each to unique molecular trend lines [2]. Data extracted from this type of multidimensional space have immensely enriched chemical classification and molecular identification in various "omics" research fields. Further expansion of the IM–MS approach in time-nested liquid chromatography (LC)–IM–MS or IM–IM–MS systems further increases peak capacity, recovering more of the IM–MS dimensional space obscured by the pseudo-orthogonal dependence between ion mobility (K) and *m/z*, and also removing ambiguity in regions of CCS-*m/z* overlap [3, 4]. Such nested IM–MS platforms are capable of providing greater information density all the while reducing spectral complexity without a significant cost to analysis time.

Currently, the most successful commercial implementations of IMS paired with MS employ time-dispersive drift tube (DTIMS) or traveling wave (TWIMS) mobility techniques. These particular techniques, for which ion-neutral collision cross-section (CCS) determination is relatively straightforward, have proven exceptionally useful in the burgeoning fields of proteomics, metabolomics, and structural MS. The majority of traveling wave or drift tube IM–MS arrangements, best exemplified by the Waters Synapt G2-S or Agilent 6560 instruments, respectively, feature mobility cells embedded within

the MS system that are thereby restricted to operation at reduced pressures by the vacuum constraints of the mass analyzer [2, 5]. All IMS separations rely on ion/gas interactions that scale with pressure, and such reduced-pressure configurations inevitably limit the achievable mobility resolving power as levels of ion diffusion are more appreciable than at atmosphere. Ion trapping approaches, however, can partially or completely offset this limitation. Enhancements to resolution and sensitivity have also been made in reduced pressure systems by exploiting different gas polarizabilities [1, 6], or by applying additional electrodynamic RF field focusing to reduce diffusional broadening [7, 8], or electrostatic lens implementations that can restore IMS operation at atmospheric pressure [9]. In this pressure regime, the resolving power of DTIMS is maximized as diffusion is reduced, yielding peak capacities that may even surpass LC separation efficiencies [10, 11]. An additional benefit of atmospheric pressure operation is the assurance that the ion mobilities measured are from fully thermalized ions interacting with a neutral gas under the low field limit [12, 13]. However, very few implementations of atmospheric pressure (AP)-DTIMS–MS are commercially developed, with the TOFWERK IMS-TOF system recognized as the prime example [14].

Traditionally, time-dispersive ion mobility has been paired with quadrupole ion traps [15] and time-of-flight (TOF) analyzers [16], with modern TOF technology now providing mass resolutions and scan speeds ideally suited for time-nested analysis. Contemporary commercial IM-Q-TOF MS instruments are designed to maximize sensitivity and commonly incorporate ion trapping and transfer stages to alleviate the intrinsically low IM duty cycles [16–18]. Spatial and temporal DTIMS–MS multiplexing approaches, which encompass either arrays of mobility analyzers coupled to a single detector or time-

multiplexing of multiple ion injection pulses per IM acquisition, have also been used to improve IM duty cycle [19–21]. Hadamard transform and pseudorandom sequence multiplexing methods have enabled favorable increases in signal-to-noise ratios and sensitivity while also retaining the higher theoretical resolving powers, enhancing instrument efficiency for more practical applications of AP-DTIMS [22, 23]. Recent advances in coupling atmospheric pressure ion mobility with FT ion cyclotron resonance (ICR) mass spectrometry are pushing the boundaries of achievable peak capacity [24]. Initial cost, however, still prevents FT-ICR instrumentation from becoming mainstream.

Presented in this work is the combination of atmospheric pressure DTIMS with Orbitrap FT–MS, aimed at both increasing drift tube IMS separation power and providing higher mass accuracy and stability for better annotation of unknowns. One of the challenges with combining DTIMS with Orbitrap is that the analyzer scan times are rather long in comparison with those of TOF, with only a single report on a custom ion mobility drift cell paired with a modified Orbitrap MS currently in the literature [25]. In contrast, we here present the coupling of an unmodified Thermo Q-Exactive Orbitrap mass spectrometer to a commercially developed, fully modular EXCELLIMS MA3100 atmospheric pressure drift tube ion mobility spectrometer. The DTIMS module is equipped with dual ion gates, which not only serve to define the boundaries of the drift region but also enable several different modes of mobility selection and filtering, accommodating the Orbitrap scan speeds. Several key mobility parameters, including drift tube temperature, drift gas flow rate, and electric field strength in both positive and negative ion modes were optimized. The effect of DTIMS gate pulse width on IM–MS resolving power, together with the impact of fixed-gate versus scanned-gate acquisition modes on system sensitivity,

was also explored. Primary consideration was given to understanding Orbitrap variables that determine maximum detector scan rate such as injection time (IT) and automatic gain control (AGC) settings while investigating system limits of detection. Envisioned applications for this system include rapid screening of complex combinatorial libraries and rapid metabolomics phenotyping.

C.3 Experimental

C.3.1 Chemicals and Materials

Positive mode ion mobility calibration standards, including 2,6-ditertbutylpyridine (≥97%), nicotinamide (≥99.5%), trihexylamine (≥96%), and negative mode standard citric acid (≥99.5%), were purchased from Sigma-Aldrich (St. Louis, MO). Positive mode standards were mixed in a 1:1:1 ratio in 80:20 methanol:water at 25 ppm w/v (i.e., 130, 204, and 93 pmol μL^{-1} of 2,6-ditertbutylpyridine, nicotinamide, and trihexylamine, respectively). A concentration series of negative mode citric acid standard, ranging from 100 ppb to 100 ppm w/v (~0.52–520 pmol μL^{-1}), was prepared by serial dilution of a 1000 ppm w/v stock solution dissolved in 80:20 methanol:water. Solutions containing isomeric Gly-Asp-Gly-Arg-Ser and Ser-Arg-Gly-Asp-Gly peptide sequences were prepared in 50:50 acetonitrile:water with 0.1% formic acid to 1 mg mL^{-1} following the protocol provided with the Waters reverse peptide kit (P#700005089) obtained from Waters Corporation (Milford, MA) and then mixed and diluted to 100 ppm w/v (204 pmol μL–1). Sugar analytes d-(+)-raffinose pentahydrate (≥98%), d-(+)-melezitose hydrate (≥99%), and d-(+)-melibiose (≥98%) were also procured from Sigma-Aldrich and dissolved in 80:20 methanol:water as a 100 ppm w/v mixture (~168 pmol μL^{-1} for d-(+)-raffinose and d-(+)-

melezitose hydrates, and 292 pmol μL^{-1} for d-(+)-melebiose) with ≥2.5 molar excess of NaCl. HPLC grade methanol or acetonitrile organic solvents (Sigma-Aldrich) and ultrapure 18.2 MΩ cm deionized water (Barnstead Nanopure Diamond, Van Nuys, CA) were used for all analyte solutions. High-purity nitrogen (99.998%) and ultrazero grade compressed air (99.998%) were acquired from Airgas Inc. (Atlanta, GA) and used as DTIMS buffer gases.

C.3.2 Instrument and System Parameters

The EXCELLIMS MA3100 drift tube ion mobility spectrometer uses a traditional stacked-ring electrode construction with the cell body divided into a desolvation and a drift segment, 6.25 and 10.55 cm long, respectively. For reference, the electrodes are thin steel bands (width: ∼4.5 mm, spacing: ∼1 mm), all resistively coupled to one another via printed circuit board connections and secured to a rectangular ceramic support (50 × 25 mm). The insulated ceramic block is temperature-regulated (≤250 °C) using resistive heating elements positioned along the cell body and at the drift gas inlet. Operation potentials up to ±10 000 V were applied to the desolvation cell inlet, resulting in a maximum linear electric field gradient of ∼570 V cm^{-1} across the entire drift space.

Attached in front of the desolvation chamber is a source enclosure housing a sheathless (i.e., without nebulizing gas) electrospray tip (50 μm ID) adjustable to a maximum potential of ±5000 V relative to the IMS inlet bias. The MA3100 design features two Bradbury–Nielsen ion shutters situated at the entrance and the exit of the drift cell. The first and second ion gates are floated at ∼62.9 and ∼7.7% of the operation potential, respectively. The first ion gate is pulsed with a tunable symmetric potential of ±70 V during

conventional drift mode operation. At the end of the drift region and positioned directly behind the second ion gate/aperture grid is a Faraday anode disk with a 6.4 mm diameter opening allowing partial ion transmission to the entrance of the Orbitrap's ion transfer capillary. Compressed air or nitrogen drift gas ($\leq$3.0 L min^{-1}) is delivered through a heated input line at the drift cell terminus, passed as a symmetric sheath-flow across the anode and pumped out ($\leq$3.5 L min^{-1}) through an exhaust port located at the front of the desolvation cell via a diaphragm pump. Gas feed lines, high voltage electronics, and multifunction data acquisition DAQ hardware are contained in the MA3100 peripheral controller box connected to the DTIMS and Orbitrap computer system. Controller box commands were issued using the EXCELLIMS VisIon software (version 1.2.0.31). Known drift tube dimensions and experimentally determined optimal settings for key mobility parameters in positive and negative ion mode are outlined in Table 1.

Table C-1 Summary of key system parameters

MA3100 DTIMS	*Positive Mode* (+)	*Negative Mode* (-)
Electrospray Potential (kV) above IMS inlet	2400-2600	2200-2300
Spray Flow Rate (µL/min)	2-3	
Drift Length (cm)	~10.5	
Drift Tube/Gas Inlet Temperature (˚C)	200	
Ambient Pressure (Torr)	730-750	
Drift Gas Flow Rate (L/min)	2.0-3.0 (N2/air.)	2.0 (air)
Exhaust Pump Rate (L/min)	0.5-1.5 (N2/air)	1.0 (air)
DTIMS Operation Potential (kV)	8000-10000	7000-8000
Ion Gate Pulsing Potential (V)	±70	
GATE SCHEME PARAMETERS		
Scan Period (ms)	20.3	
Gate #1 Pulse Width (µs)	100	
Gate #2 Pulse Width (µs)	100	
Scan Step (µs)	25	
Dwell Time (ms)	1015 (50 scans)	
Q-Exactive MS		
Mass Range (Da)	50-500	
Resolution	17,500	
Scan Rate (Hz)	12	
Automatic Gain Control (AGC)	2E+04 counts & 5E+06 counts	
Microscans	1	
Maximum Injection Time (ms)	1000	
Inlet Capillary Temperature (˚C)	200	
S-Lens RF Level (V)	50	
HCD Normalized Collison Energy (V)	20-45	
AIF Range Center (m/z)	400	

The MA3100 module was mounted to the atmospheric pressure interface of a Thermo Fisher Q-Exactive Orbitrap mass spectrometer. A schematic of the system configuration is depicted in Figure C-1. Ion transport past the DTIMS Faraday detector was governed by the combined effect of the vacuum pull within the interface preceding the mass spectrometer inlet and the electrostatic fields applied. The Q-Exactive MS Tune source voltages and sheath gas flows were assigned "0" values (switched off), and the S-Lens RF level was held at 50 V. The ion transfer capillary temperature was set to match the drift tube temperature (60–240 °C). Parameter space experiments focused on the Orbitrap detector automatic gain control (AGC), injection time (IT), and resolution settings that influenced the effective analytical cycle time. Unless otherwise specified, the mass resolution was set at 17500 to afford the fastest possible analyzer scan rate (~12 Hz). During IM–MS analysis, AGC threshold was tuned to a minimum of 2.0×10^4 ion counts or a maximum of 5.0×10^6 ion counts, while IT was varied from 100 to 2000 ms. The number of microscans setting was left at 1, and the mass range was typically set between 50 and 500 Da. For fragmentation studies with peptides using the high-energy collision dissociation (HCD) cell, the normalized collision energy (NCE) was 20–45 V for an all ion fragmentation (AIF) range centered at m/z = 400 Da. Orbitrap analysis was conducted using Thermo Xcalibur 2.6 software. ProteinProspector software version 5.17.1 (University of California, San Francisco, CA) was used for assignment of peptide ion fragments. The most relevant MS settings are summarized in Table 1.

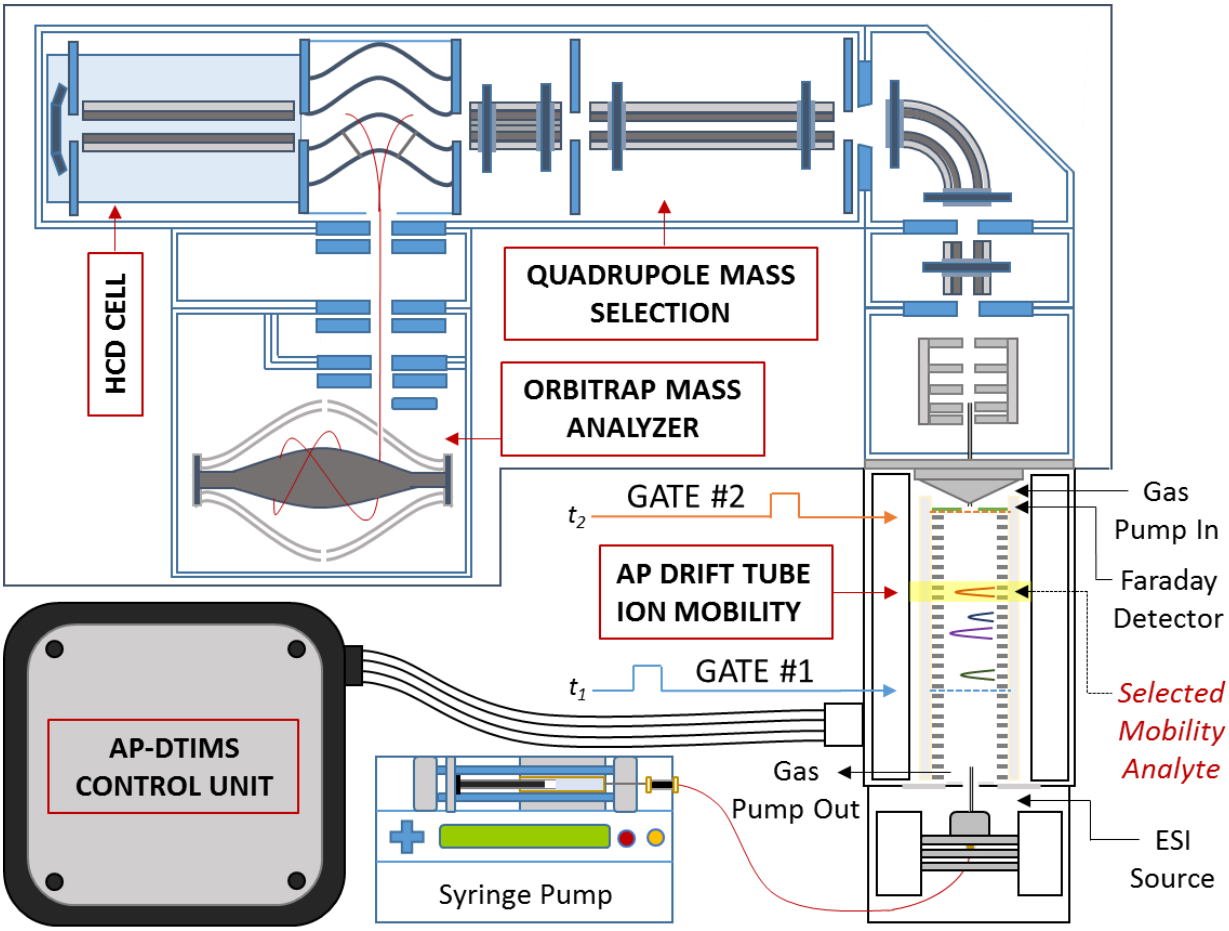

Figure C-1 Illustration of the AP-DTIMS-Orbitrap MS instrument configuration.

C.3.3 DTIMS Ion Gating Schemes

The MA3100 is equipped to perform several analysis modes based on various trigger configurations of the dual ion shutters. For Faraday mode acquisitions, the second ion gate was held open at a set potential, thereby serving as an open aperture grid, while the first ion gate was pulsed open/closed once per sweep scan, and signal current was recorded at the DTIMS anode. When operating with MS detection, the second ion gate was also utilized to select (or filter) target ions using several distinct modes (Figure C-2, Table C-1). In gated mode, the second ion gate was pulsed open following a delay after the first gate pulse, and signal for ions transmitted through the fixed-gate time window was measured by the Orbitrap MS detector. Using the alternative scan mode, the second gate pulse was scanned in sequential time bins across the defined drift period to generate a complete mobility-mass data set.

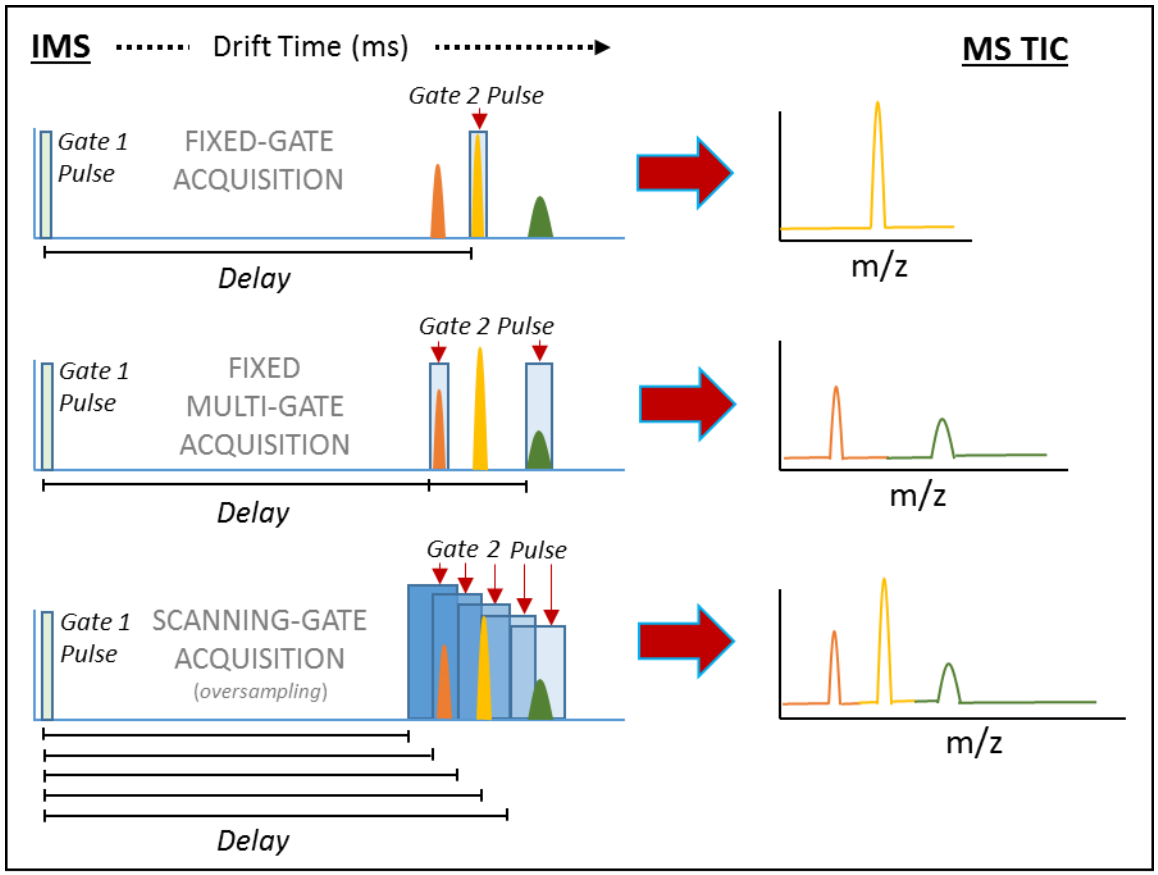

Figure C-2 Illustration of the DTIMS dual-gate modes of operation for ion selection and filtering. The corresponding MS TIC traces for gate #2 operations using gated mode and scan mode IM-MS acquisition schemes are shown.

The gate pulse widths for each ion shutter ranged from 30 μs to the full mobility acquisition period (≤50 ms). The first gate pulse width in all experiments was varied between 50 and 600 μs; larger pulse widths resulted in a total loss of spectral resolution. In gated mode, the second ion gate was typically pulsed open for a narrow 1–2 ms over the selected drift time interval or mobility peak of interest. Scan mode functions required definition of the drift time interval or scan duration, the second ion gate pulse width, and the step size of the scanned second gate. Unless otherwise specified, the scan time window was set within a range of 4–16 ms over the standard 20.3 ms mobility acquisition period, following a short delay (≤1 ms) from the first ion gate trigger pulse (the period was defined as an uneven value to reduce periodic anode noise). DTIMS dwell time was set to 1015 ms, which equated to 50 Faraday acquisitions per gate scan step for the set 20.3 ms scan period. Except during specific characterization experiments, the first and second gate pulse widths were set equal to one another. The second gate was stepped at time intervals 1/2 to 1/4 the pulse width over the defined scan window to effectively oversample, rendering scan-step-to-pulse-width ratios of 2:1 or 4:1. VisIon Faraday spectra were generated from 20 s summations of full-period mobility scans, and mass spectra were produced from total scan time averages of the Orbitrap TIC spectra. When ion mobility separations were not desired, the DTIMS unit functioned as a passive guide for ion transmission simply by floating both ion gates open at voltages defined by the drift cell potential gradient (e.g., open mode).

C.4 Results and Discussion

C.4.1 AP-DTIMS Basic Performance Optimization

Performance of the AP-DTIMS unit was first characterized for key physical parameters affecting ion mobility separation, namely drift electric field strength, drift gas temperature, and drift gas flow rate. A systematic exploration of these parameters on attributes such as sensitivity and resolution was conducted with optimum parameters presented in Table 1. In positive ion mode, the greatest resolving power ($Rp \geq 70$) and signal intensities were achieved using the highest programmable operating potentials (9000–10000 V). This resolving power is comparable to some existing low-pressure drift tube instruments (i.e., Agilent 6560) but with a short, compact drift tube. Maximum signal in negative mode was achieved at a slightly reduced DTIMS operating potential (−7000 to −8000 V) to avoid signal distortion from electron currents on the Faraday detector originating from ion source discharges. These distortions could also be mitigated by decreasing the electrospray potential (−2200 V) relative to the positive mode value (2600 V). Higher DTIMS temperatures (180–220 °C) assisted droplet desolvation while retaining resolving power, but temperatures in excess of 240 °C induced currents in the Faraday plate detector and an artificial elevation of the spectral baseline by ∼3 V. Drift gas flow rate, in combination with DTIMS temperature, had the most influence on drift gas uniformity and signal fidelity. Balancing a higher drift gas input (2.0–3.0 L min^{-1}) with a lower exhaust pumping rate (≤1.5 L min^{-1}) had an optimal effect on signal, facilitating ion declustering and stabilizing gas flow for ion transmission. High exhaust pump rates were prone to disrupt the electrospray stability.

C.4.2 DTIMS Gate Pulse Width Scan Step Functions

The contribution of various gate pulse widths on DTIMS-Orbitrap MS sensitivity and resolving power was investigated to better understand the effect of scanning gate

operation parameters. Analysis of a citric acid standard was performed in negative ion mode using different gate 1 and gate 2 pulse width ratios and different scan step increments to control over- or undersampling. Figure C-3 A shows the Faraday responses for 4 ppm w/v (~21 pmol μL^{-1}) citric acid with gradually increasing gate #1 pulse widths. The mobility peaks showed increasing abundances with near linearity until a gate #1 pulse width of approximately 300 μs. Beyond this value, the peaks plateaued and broadened, further diminishing mobility resolving power. In practice, increasing the gate #1 pulse width also extends the drift time by a commensurate amount on the falling edge of the widening peak so the peaks in Figure C-3 were aligned to a centroid by subtracting 1/2 pulse width from the drift time. For Faraday mode, gate #1 pulse widths of 75–150 μs were determined to provide the best balance between sensitivity and resolving power.

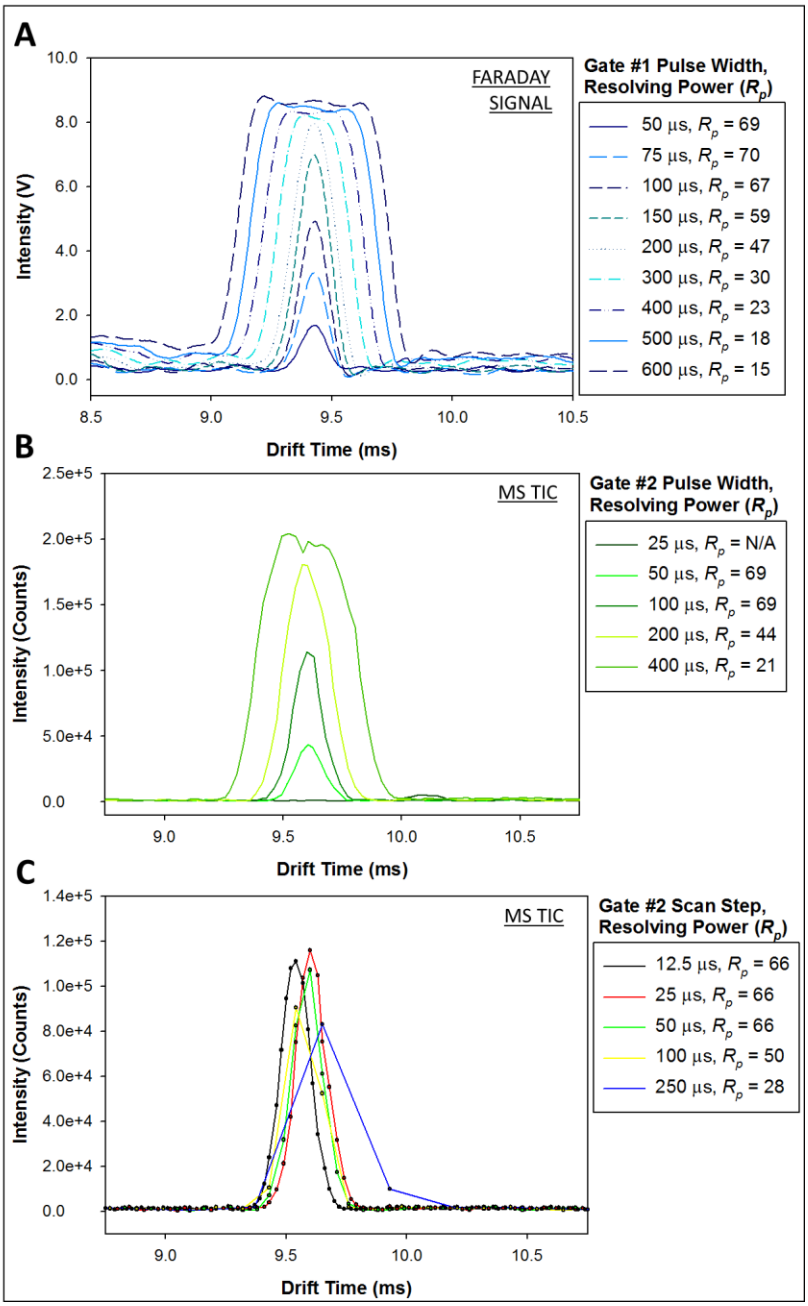

Figure C-3 (A) Faraday response for 4 ppm w/v citric acid in 80:20 methanol/water for increasing DTIMS gate #1 pulse widths. (B) MS signal for 10 ppm w/v citric acid for increasing DTIMS gate #2 pulse widths over a 2.5 ms scan window. The gate #1 pulse width was 100 µs and the scan step was 25 µs. (C) MS signal for 10 ppm w/v citric acid for increasing DTIMS gate #2 scan step ratios over a 2.5 ms scan window. Gate #1 and #2 pulse widths were set equal at 100 µs. The number of data points per peak is plotted with each curve trace. For (A-C), DTIMS operation potential was -7000 V, drift gas temperature was 200 ˚C, and drift gas flow rate and exhaust pump rate were 2.0 L min^{-1} and 0.5 L min^{-1}, respectively.

The effect of gate #2 pulse operations relative to that of gate #1 was evaluated in scan mode. Orbitrap parameters, further discussed in the next section, were set as follows: resolution = 17500 [12 Hz], AGC= 5.0×10^6, IT = 1000 ms. The gate #1 pulse width was set to 100 μs, while gate #2 pulse widths were varied from 25 to 400 μs over a drift time scan window of 2.5 ms centered on the citric acid drift time (Figure C-3 B). For the shortest gate #2 pulse width (25 μs), no signal was detected because the programmed pulse width was below the rated cutoff of the ion shutter. Peak area was observed to increase with gate #2 width, while resolution decreased for gates wider than 100 μs, but resolving powers remained comparable to those observed from the Faraday detector response (gate #1 and #2 at 100 μs: Rp ~ 60–70). For alignment, the citric acid peaks were corrected for gate pulse width by subtracting 1/2 of the first gate pulse width and adding 1/2 of the second gate pulse width. Improved timing correction for instances where the pulse width of gate #2 was larger than gate #1 required addition of an extra adjustment factor equal to (1/16) of gate#2, which is related to the scan step. As expected, shorter gate #2 pulse widths relative to gate #1 resulted in lower intensity MS signals due to gate shutter "clipping" of ion packets with modest or no improvement to resolving power.

The impact of the scan step duration on signal was investigated independently while setting gate #1 and gate #2 pulse widths equal (100 μs). Gate scan steps were varied from 12.5 μs up to 200 μs for an IMS dwell time of 1015 ms, equating to 50 DTIMS acquisitions per scan step over the 20.3 ms drift period. Orbitrap parameters were set as before (resolution: 17500 [12 Hz], AGC: 5.0×10^6, IT: 1000 ms). Figure C-3 C shows the citric acid MS signal using these various scan steps, which corresponded to oversampling ratios of 8:1 (12.5 μs), 4:1 (25 μs), and 2:1 (50 μs), a matched sampling ratio of 1:1 (100 μs), and

an undersampled ratio of 1:2.5 (250 μs). There was a minor drift time variance across peak apexes for the different scan steps, which may be correlated with minute fluctuations in measured ion intensity over the different mobility times. As expected, undersampling resulted in a dramatic loss of resolving power, with oversampling being critical to refine peak shape when using gate #1 widths of 100 μs or larger. An oversampling of 4:1 (25 μs) was observed to provide the best balance between adequate sampling and overall speed of analysis.

C.4.3 Effect of Orbitrap Automatic Gain Control and Injection Time

Apart from DTIMS gate pulsing schemes, the Orbitrap MS detector settings were the other principal determinants of performance, as they potentially had a substantial influence on sensitivity, resolution, and analytical cycle time. Analyzer resolution, injection time, and automatic gain control were examined while assessing DTIMS performance in both fixed-gate and scan modes. The lowest available analyzer resolution (17500) was chosen for all characterization experiments to permit the fastest allowable acquisition rate (~12 Hz) for the selected mass range (m/z = 50–500). The automatic gain control, which defined the threshold for the target ion number, was set initially to the highest available value (5.0×10^6) in order to fix injection time. The maximum injection time, or the nominal duration of ion accumulation and the rate-limiting cycle step governing sensitivity, was adjusted between 100 and 2000 ms, values that allowed for adequate analyte detection.

C.4.4 DTIMS-Orbitrap MS Applications

Several test analyte sets were investigated to explore system performance in applications involving isomer separation and identification. Figure C-4 A shows the Faraday response and associated mass spectrum for a 100 ppm w/v mixture of two reverse peptides (Ser-Asp-Gly-Arg-Gly and Gly-Arg-Gly-Asp-Ser) collected using optimized mobility parameters and scan mode acquisition (gate #1 and #2 pulse width: 150 μs, scan step: 50 μs, scan window: 5–15 ms). Three species were detected in the Faraday trace, representing the singly charged peptide monomers (*m/z* = 491.221) overlapping at td = 12.25 ms and the doubly protonated monomers (*m/z* = 246.114) of GRGDS and SDGRG at td = 7.12 and 7.45 ms, respectively. The $[M + 2H]^{2+}$ peptide species, having reported collision cross-section areas of $\Omega = 222.7$ Å^2 and $\Omega = 211.7$ Å^2 at 250 °C in N2 [26], were clearly resolved to baseline by AP-DTIMS (Rp ~ 72) with roughly double the resolving power possible for these ions using TWIMS (Rp > 36). Isomer identities were verified by drift time measurements for single-component peptide standards and further confirmed by high-energy collision dissociation (HCD) MS/MS experiments of the mobility-resolved sequence isomers. Figures C-4 B&C shows the characteristic HCD MS/MS spectra for the peptide sequences with their unique fragment assignments.

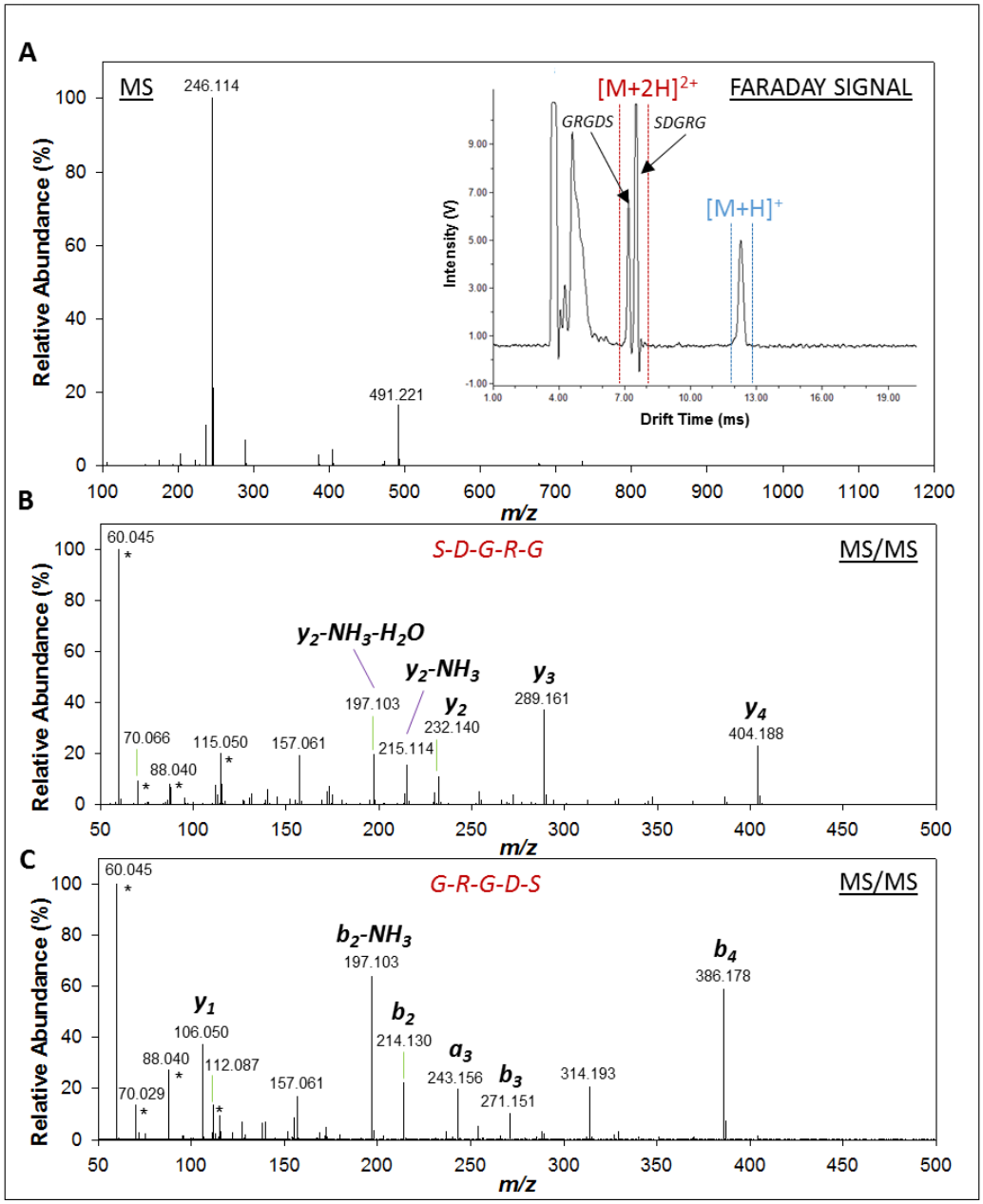

Figure C-4 Scan mode averaged mass spectrum and Faraday response (inset) for 100 ppm w/v of mixture of [Ser-Asp-Gly-Arg-Gly] and [Gly-Arg-Gly-Asp-Ser] peptide sequence isomers in 50:50 acetonitrile/water with 0.1% formic acid (A). All ion fragmentation HCD of the separated peptide isomers using a normalized collision energy of 20 V, where individual $[M+2H]^+$ species were isolated by ion mobility before fragmentation (B and C). Asterisks (*) denote identified sidechain fragments of serine, aspartic acid, and arginine. (DTIMS operation potential: 10,000 V, drift gas temperature: 220 ˚C, drift gas flow rate: 3.0 L min^{-1}, exhaust pump rate: 1.5 L min^{-1}; gate #1 and #2 pulse width: 150 µs; scan step: 50 µs).

In addition to the reverse peptide sequences, a simple carbohydrate mixture of sugar isomers and structural homologues was examined. Analyte solutions were concentrated at 100 ppm w/v with a 2.5× excess of NaCl salt to facilitate positive mode ionization via sodium adduct formation. Figures C-5 A–D depict VisIon spectral data for both Faraday and MS detectors obtained using a DTIMS scan mode over a 4 ms scan acquisition window. The 200 μs gate pulse widths used resulted in a small reduction in Rp to benefit sensitivity and a large solvent signal recorded in the Faraday channel. Within the drift time zone of 9–13 ms, four distinct signals were observed. In order of increasing td, the carbohydrate peaks were assigned to $[M + Na]^+$ for the disaccharide d-(+)-melibiose (*m/z* = 365.105) at td = 9.94 ms, and the trisaccharide isomers d-(+)-melezitose (*m/z* = 527.158) and d-(+)-raffinose (*m/z* = 527.158) at td = 11.70 ms and td = 12.19 ms, respectively. The peak order was consistent with mobility distribution reports from the literature [15, 27] and was verified by injecting single-component solutions of the standards. The one peak not assigned to a sugar at td = 10.70 ms is a suspected contaminant tentatively identified as the sodiated adduct of decamethylcyclopentasiloxane (*m/z* = 393.082), a common ESI background ion. The *m/z* vs drift time plot conveyed an additional approach to visualize the data, portraying the nested IM–MS distribution and precursor ion trendlines. The ellipses drawn on the plot mark peaks for the carbohydrates and contaminant ion while filtering any other background signal overlapping in the same mass/mobility region. This data show the power of AP-DTIMS-Orbitrap MS for discriminating isobaric analytes in complex chemical systems.

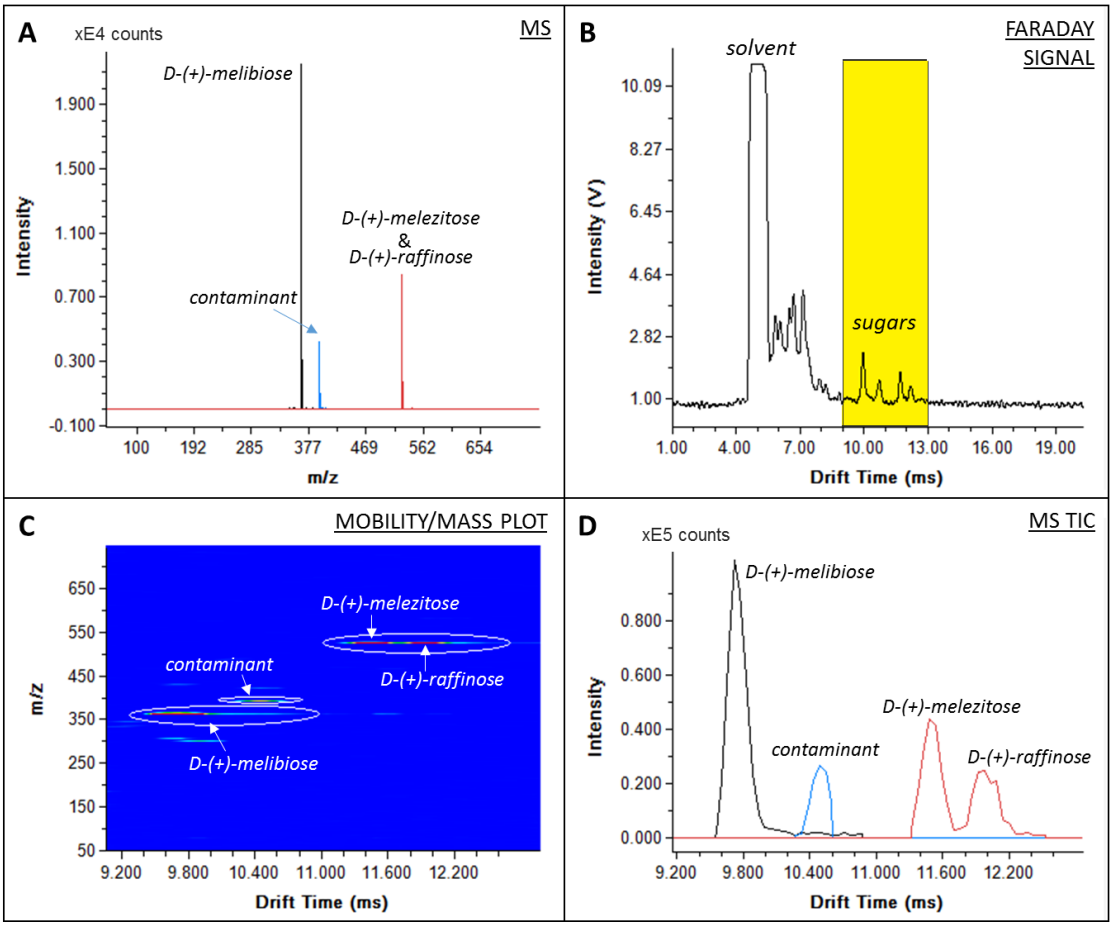

Figure C-5 AP-DTIMS-Orbitrap MS analysis for 100 ppm solution (w/v in 50:50 methanol/water) of 3 saccharides: D-(+)-melibiose, D-(+)-melezitose, and D-(+)-raffinose. Panels show the extracted mass spectra for each mixture component (A), the corresponding Faraday response (B), a map of the chemical space with *m/z* plotted as a function of drift time (C), and the extracted MS total ion chronograms (D). (gate #1 & #2: 200 µs, scan step: 50 µs; AGC: 5.0E+06, IT: 1000 ms, Resolution: 35,000).

C.5 Conclusion

This work involved characterization of a dual-gate AP-DTIMS-Orbitrap system, showcasing its performance capabilities to date. The DTIMS unit afforded the greatest separation efficiency near the maximum operation potential of 10000 V while using gas temperatures ≥200 °C and high drift gas flow rates of 2.0–3.0 L min^{-1} balanced with lower exhaust pump rates of 0.5–1.5 L min^{-1}. The effects of different ion mobility gating schemes on sensitivity and resolving power were thoroughly investigated. It was found that resolving power ($Rp \leq 70$) was mostly determined by the initial DTIMS gate pulse width (50–150 μs), and during scan mode analysis, the scan step bin width for the second ion gate if pulse width was set equal to the first gate. Likewise, sensitivity and throughput were primarily dictated by DTIMS gate pulse width, while Orbitrap parameters governing analytical cycle had a subtler and more complex influence. Orbitrap variable injection times did not appear to significantly alter intensity levels at high gain settings but had a more pronounced impact on average signal intensity at the lowest gain settings and higher analyte concentrations. The optimized AP-DTIMS-Orbitrap MS parameter settings were used to successfully resolve simple mixtures of peptide and sugar isomers, and HCD MS/MS was performed to further confirm peptide identities based on characteristic fragmentation spectra. Future experiments will include collision cross section measurements and peak capacity estimations for the IM–MS platform, with the ultimate outlook for this system involving implementation of multiplexed sampling approaches. Further improvements in resolving power through the use of longer drift tubes, more effective ion gating, and higher drift voltages are also envisioned.

C.6 References

1. Ruotolo, B.T., McLean, J.A., Gillig, K.J., Russell, D.H.: Peak capacity of ion mobility mass spectrometry: the utility of varying drift gas polarizability for the separation of tryptic peptides. J. Mass Spectrom. 39, 361–367 (2004). https://doi.org/10.1002/jms.592

2. C. May, J., R. Goodwin, C., M. Lareau, N., L. Leaptrot, K., B. Morris, C., T. Kurulugama, R., Mordehai, A., Klein, C., Barry, W., Darland, E., Overney, G., Imatani, K., C. Stafford, G., C. Fjeldsted, J., A. McLean, J.: Conformational Ordering of Biomolecules in the Gas Phase: Nitrogen Collision Cross Sections Measured on a Prototype High Resolution Drift Tube Ion Mobility-Mass Spectrometer. Anal. Chem. 86, 2107–2116 (2014). https://doi.org/10.1021/ac4038448

3. Valentine, S.J., Kulchania, M., Barnes, C.A.S., Clemmer, D.E.: Multidimensional separations of complex peptide mixtures: A combined high-performance liquid chromatography/ion mobility/time-of-flight mass spectrometry approach. Int. J. Mass Spectrom. 212, 97–109 (2001). https://doi.org/10.1016/S1387-3806(01)00511-5

4. Valentine, S.J., Kurulugama, R.T., Bohrer, B.C., Merenbloom, S.I., Sowell, R.A., Mechref, Y., Clemmer, D.E.: Developing IMS-IMS-MS for rapid characterization of abundant proteins in human plasma. Int. J. Mass Spectrom. 283, 149–160 (2009). https://doi.org/10.1016/j.ijms.2009.02.030

5. Pringle, S.D., Giles, K., Wildgoose, J.L., Williams, J.P., Slade, S.E., Thalassinos, K., Bateman, R.H., Bowers, M.T., Scrivens, J.H.: An investigation of the mobility separation of some peptide and protein ions using a new hybrid quadrupole/travelling wave IMS/oa-TOF instrument. Int. J. Mass Spectrom. 261, 1–12 (2007). https://doi.org/10.1016/j.ijms.2006.07.021

6. Matz, L.M., Hill, H.H., Beegle, L.W., Kanik, I.: Investigation of drift gas selectivity in high resolution ion mobility spectrometry with mass spectrometry detection. J. Am. Soc. Mass Spectrom. 13, 300–307 (2002). https://doi.org/10.1016/S1044-0305(01)00366-X

7. Allen, S.J., Giles, K., Gilbert, T., Bush, M.F.: Ion mobility mass spectrometry of peptide, protein, and protein complex ions using a radio-frequency confining drift cell. Analyst. 141, 884–891 (2016). https://doi.org/10.1039/c5an02107c

8. Gillig, K.J., Chen, C.-H.: Increasing the Performance of Portable Ion Mobility Analyzers: Development of the Periodic Focusing Differential Mobility Analyzer (PFDMA). Mass Spectrom. 3, S0032–S0032 (2014). https://doi.org/10.5702/massspectrometry.s0032

9. Gillig, K.J., Ruotolo, B.T., Stone, E.G., Russell, D.H.: An electrostatic focusing ion guide for ion mobility-mass spectrometry. Int. J. Mass Spectrom. 239, 43–49 (2004). https://doi.org/10.1016/j.ijms.2004.09.005

10. Hill, H.H., Siems, W.F., Louis, R.H.S., McMinn, D.G.: Ion Mobility Spectrometry. Anal. Chem. 62, 1201–1209 (1990). https://doi.org/10.1021/ac00222a001

11. Kanu, A.B., Gribb, M.M., Hill, H.H.: Predicting optimal resolving power for ambient pressure ion mobility spectrometry. Anal. Chem. 80, 6610–6619 (2008). https://doi.org/10.1021/ac8008143

12. Revercomb, H.E., Mason, E.A.: Theory of Plasma Chromatography/Gaseous Electrophoresis. A Review. Anal. Chem. 47, 970–983 (1975). https://doi.org/10.1021/ac60357a043

13. Siems, W.F., Wu, C., Tarver, E.E., Hill, H.H., Larsen, P.R., McMinn, D.G.: Measuring the Resolving Power of Ion Mobility Spectrometers. Anal. Chem. 66, 4195–4201 (1994). https://doi.org/10.1021/ac00095a014

14. Kaplan, K., Graf, S., Tanner, C., Gonin, M., Fuhrer, K., Knochenmuss, R., Dwivedi, P., Hill, H.H.: Resistive glass IM-TOFMS. Anal. Chem. 82, 9336–9343 (2010). https://doi.org/10.1021/ac1017259

15. Clowers, B.H., Hill, H.H.: Mass analysis of mobility-selected ion populations using dual gate, ion mobility, quadrupole ion trap mass spectrometry. Anal. Chem. 77, 5877–5885 (2005). https://doi.org/10.1021/ac050700s

16. Henderson, S.C., Valentine, S.J., Counterman, A.E., Clemmer, D.E.: ESI/ion trap/ion mobility/time-of-flight mass spectrometry for rapid and sensitive analysis of biomolecular mixtures. Anal. Chem. 71, 291–301 (1999). https://doi.org/10.1021/ac9809175

17. Clowers, B.H., Ibrahim, Y.M., Prior, D.C., Danielson, W.F., Belov, M.E., Smith, R.D.: Enhanced ion utilization efficiency using an electrodynamic ion funnel trap as an injection mechanism for ion mobility spectrometry. Anal. Chem. 80, 612–623 (2008). https://doi.org/10.1021/ac701648p

18. Ibrahim, Y.M., Baker, E.S., Danielson, W.F., Norheim, R. V., Prior, D.C., Anderson, G.A., Belov, M.E., Smith, R.D.: Development of a new ion mobility (quadrupole) time-of-flight mass spectrometer. Int. J. Mass Spectrom. 377, 655–662 (2015). https://doi.org/10.1016/j.ijms.2014.07.034

19. May, J.C., McLean, J.A.: Ion mobility-mass spectrometry: Time-dispersive instrumentation, (2015)

20. Belov, M.E., Clowers, B.H., Prior, D.C., Danielson, W.F., Liyu, A. V., Petritis, B.O., Smith, R.D.: Dynamically multiplexed ion mobility time-of-flight mass spectrometry. Anal. Chem. 80, 5873–5883 (2008). https://doi.org/10.1021/ac8003665

21. Kwasnik, M., Caramore, J., Fernández, F.M.: Digitally-multiplexed nanoelectrospray ionization atmospheric pressure drift tube ion mobility

spectrometry. Anal. Chem. 81, 1587–1594 (2009). https://doi.org/10.1021/ac802383k

22. Clowers, B.H., Belov, M.E., Prior, D.C., Danielson, W.F., Ibrahim, Y., Smith, R.D.: Pseudorandom sequence modifications for ion mobility orthogonal time-of-flight mass spectrometry. Anal. Chem. 80, 2464–2473 (2008). https://doi.org/10.1021/ac7022712

23. Zhang, X., Knochenmuss, R., Siems, W.F., Liu, W., Graf, S., Hill, H.H.: Evaluation of Hadamard transform atmospheric pressure ion mobility time-of-flight mass spectrometry for complex mixture analysis. Anal. Chem. 86, 1661–1670 (2014). https://doi.org/10.1021/ac403435p

24. Tang, X., Bruce, J.E., Hill, H.H.: Design and performance of an atmospheric pressure ion mobility Fourier transform ion cyclotron resonance mass spectrometer. Rapid Commun. Mass Spectrom. 21, 1115–1122 (2007). https://doi.org/10.1002/rcm.2928

25. Ibrahim, Y.M., Garimella, S.V.B., Prost, S.A., Wojcik, R., Norheim, R. V., Baker, E.S., Rusyn, I., Smith, R.D.: Development of an ion mobility spectrometry-Orbitrap mass spectrometer platform. Anal. Chem. 88, 12152–12160 (2016). https://doi.org/10.1021/acs.analchem.6b03027

26. Wu, C., Siems, W.F., Klasmeier, J., Hill, H.H.: Separation of isomeric peptides using electrospray ionization/high- resolution ion mobility spectrometry. Anal. Chem. 72, 391–395 (2000). https://doi.org/10.1021/ac990601c

27. Huang, Y., Dodds, E.D.: Ion mobility studies of carbohydrates as group i adducts: Isomer specific collisional cross section dependence on metal ion radius. Anal. Chem. 85, 9728–9735 (2013). https://doi.org/10.1021/ac402133f

APPENDIX D. ROBOTIC SURFACE ANALYSIS MASS SPECTROMETRY (ROSA-MS) OF THREE-DIMENSIONAL OBJECTS.

Adapted with permission from:

Li, A., Paine, M.R.L., Zambrzycki, S., Stryffeler, R.B., Wu, J., Bouza, M., Huckaby, J., Chang, C.-Y., Kumar, M., Mukhija, P., Fernández, F.M.: Robotic Surface Analysis Mass Spectrometry (RoSA-MS) of Three-Dimensional Objects. Anal. Chem. 90, 3981–3986 (2018). https://doi.org/10.1021/acs.analchem.7b04980

Li, A. and Paine, M.R.L. engineered the initial robot and performed experiments. Zambrzycki, S. assisted in construction of the robot, evaluation or robotic arm precision, and screening of falsified medicines.

D.1 Abstract

Many technologies currently exist that are capable of analyzing the surface of solid samples under ambient or vacuum conditions, but they are typically limited to smooth, planar surfaces. Those few that can be applied to nonplanar surfaces, however, require manual sampling and a high degree of human intervention. Herein, we describe a new platform, Robotic Surface Analysis Mass Spectrometry (RoSA-MS), for direct surface sampling of three-dimensional (3D) objects. In RoSA-MS, a sampling probe is attached to a robotic arm that has 360° rotation through 6 individual joints. A 3D laser scanner, also attached to the robotic arm, generates a digital map of the sample surface that is used to direct a probe to specific (x, y, z) locations. The sampling probe consists of a spring-

loaded needle that briefly contacts the object surface, collecting trace amounts of material. The probe is then directed at an open port liquid sampling interface coupled to the electrospray ion source of a mass spectrometer. Material on the probe tip is dissolved by the solvent flow in the liquid interface and mass analyzed with high mass resolution and accuracy. The surface of bulky, nonplanar objects can thus be probed to produce chemical maps at the molecular level. Applications demonstrated herein include the examination of food sample surfaces, lifestyle chemistry, and chemical reactions on curved substrates. The modular design of this system also allows for modifications to the sampling probe and the ionization source, thereby expanding the potential of RoSA-MS for a great diversity of applications.

D.2 Introduction

Over past decades, tools for surface analysis by mass spectrometry (MS) have rapidly progressed [1]. The ability to probe solid samples by MS directly has enabled correlation of analyte abundances with their spatial distribution. This is most notably exemplified by MS imaging (MSI) of biological tissues, where mapping of analytes across different features has revealed biological information that would otherwise be lost if only analyzing the corresponding sample homogenate [2, 3].

Matrix-assisted laser desorption/ionization (MALDI) [4] and secondary ion mass spectrometry (SIMS) [5] are two of the first methods developed for MSI of solid surfaces in vacuum. Ambient ionization methods, such as desorption electrospray ionization (DESI), [6] liquid microjunction surface sampling probe (LMJ-SSP), [7] liquid extraction surface analysis (LESA), [8] nanospray desorption electrospray ionization, [9] matrix-

assisted laser desorption electrospray ionization (MALDESI), [10] and laser ablation-electrospray ionization (LAESI) [11] have also been used for MSI, but with the additional advantage of keeping samples in a state closer to their native form. Despite their usefulness, however, these ambient techniques were not necessarily conceived for probing large, bulky, curved, three-dimensional (3D) objects. For this purpose, other approaches such as probe electrospray ionization, [12, 13] and swab procedures [14–16] have been used with success, but still requiring a high-degree of human intervention.

Robotic arms coupled with various techniques, such as laser-induced breakdown spectroscopy, have been previously implemented for the analysis of 3D surfaces with success [17, 18]. In previous work, we combined remote sampling and plasma ionization with a 3-dimensional (3D) IR camera [19]. This proof-of-principle work demonstrated that point cloud output data from that 3D camera could be used to direct a robotic arm to the samples' surface for ambient MS analysis. However, the range of analytes amenable to plasma ionization was limited to those of significant volatility due to the use of the heated desorption gas plume of a direct analysis in real time (DART) ion source, and resolution was limited to 3 mm spots due to imprecisions in surface digitization. Moreover, the industrial robotic arm employed required very specific measures for its safe operation in the laboratory environment.

Here, we report on a new generation of instrument and methods for 3D surface chemical analysis, named robotic surface analysis mass spectrometry (RoSA-MS). In RoSA-MS, surface topography digitization is accomplished at higher accuracy by a custom-built laser scanner mounted on a safe, force-sensing robotic arm via a 3D-printed adapter. The point cloud data generated by the scanner is used by scripts in a custom

graphical user interface (GUI) to direct a spring-loaded semiblunt needle probe that is also mounted on the arm. This probe is used to touch points of interest in the surface of irregularly shaped, nonplanar objects. Following surface sampling, the robot control scripts direct the arm to place the needle probe into an open port sampling interface (OPSI) [20, 21] feeding into an electrospray ion for MS and MS/MS analysis. MS data acquisition is performed in parallel with robot motion and probe insertion. Molecular cartography [15] plots for a wide range of object types and target analytes are then generated by combining peak-picked MS data, the coordinates for the sampled points of interest, and the mesh surface created from the laser scan.

D.3 Experimental

D.3.1 RoSA System

A UR5-Cb2 (gen 2) robotic arm (Universal Robots, Odense, Denmark) with 360° rotation and force-sensing capabilities through six individual joints was used for all experiments. A control framework, "Actin-MS", was coded in the Actin software environment (Energid, Cambridge, MA) and used to control the robot as well as other system components. A 3D line laser scanner was attached to the robotic arm's "wrist" with a custom 3D-printed mount. The Actin GUI guided the robot movement so that the probe can approach the digitized (x, y, z) coordinates selected by the user. The major objects (bench, mass spectrometer, etc.) in the laboratory environment were built into the GUI (Figure D-1 A) so that collision avoidance boundaries could be incorporated into the Actin framework to appropriately constrain robot motion trajectory calculations.

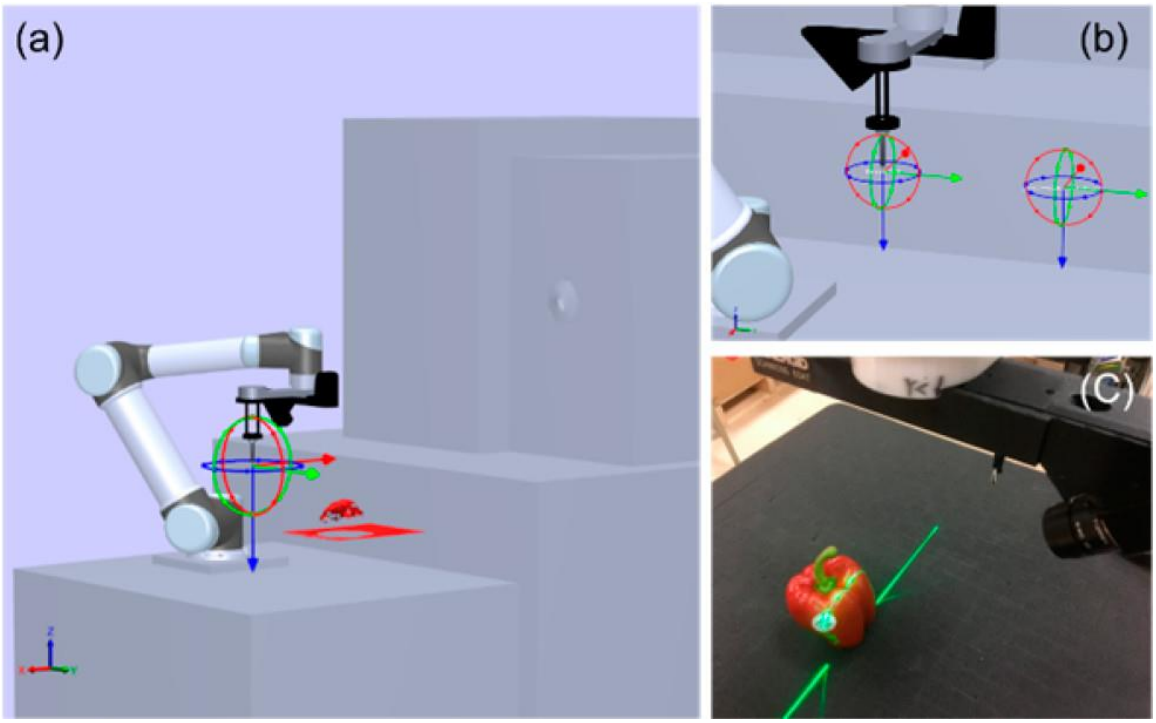

Figure D-1 (A) The robot and laboratory environment integrated into the Actin GUI. The digitized object surface contour following the laser scan was also included (shown in red). (B) Laser scan start and end waypoints being programmed in Actin-MS to define the length of the scan. (C) A bell pepper being scanned by the laser. A block of foam was placed on the actual workbench to define a safety buffer zone. The scanned object contour appears to be "floating" in GUI space because it was placed on this foam piece, which was not digitized.

A line laser (532 nm, 50 mW, class I, BES532-L, Apinex, Montreal, Canada) and a Ximea camera (MQ013CG-E2, Ximea Corp. Lakewood, CO) were used to build the laser scanner and were attached to the robot's end-effector. The laser scanner control and data collection were integrated in the Actin-MS GUI, allowing to set parameters such as scan waypoints and direction, scan speed, exposure, and height threshold (Figure D-1 B). To digitize an object's topography, a laser line was projected across such object, and moved by the robotic arm in a direction perpendicular to the laser line along the *y*-direction, while maintaining the x and z coordinates identical at a speed of 3 cm s^{-1}. The laser line reflection on the object was captured by the camera at a rate of 30 frames per second (Figure D-1 C). Using computer vision techniques, the video frames captured with laser projections were used to construct the point cloud data that formed the object's surface contours in 3D. This data showed a resolution of 0.2 mm in the *x*-direction, 1.0 mm in the *y*-direction, and 0.6 mm in the *z*-direction. The Actin-MS GUI created a mesh file with this data, representing the surface of the sample object. The laser scanner/camera system worked well for most types of surfaces, except those highly reflective (e.g., mirrors) that did not produce sufficient diffuse radiation.

By clicking on the mesh surface displayed in the GUI, the coordinates of the clicked point were immediately obtained, designating the sampling point for the probe to be directed at. The RoSA-MS probe was guided by Actin-MS to contact the surface at this set of coordinates. The needle probe was constructed by securing a round stainless-steel tip (0.2 mm diameter) on a compression spring (1/8 in. OD × 0.093 ID × 0.75 in. length, 5.27 lbs in^{-1}, McMaster Carr). This spring provided extra travel for the needle following contact with the surface, avoiding any possible damage by the probe. To ensure adequate pressure

for analyte transfer during probe-surface contact, the *z*-axis of the robot was offset in the control software by −1 mm.

D.3.2 Mass Spectrometric Analysis

A sampling interface was used to couple RoSA with the atmospheric pressure inlet of mass spectrometers without modifying existing source parameters. Both a Thermo Q Exactive Plus Orbitrap and a Waters Synapt G2-S quadrupole-time-of-flight were tested. This interface featured a flow system similar to the OPSI reported by Van Berkel [20] with the difference that it was sealed by the needle probe when the robot-arm docked. As shown in Figure D-2 A, a coaxial tubing configuration was adopted to enable solvent delivery to the OPSI through the annulus, and solvent delivery to the ESI ion source via a center capillary. A PTFE outer tube (1/16 in. OD × 0.03 in. ID × 20 mm length; IDEX, Oak Harbor, WA) and a fused silica center capillary (361 μm OD × 254 μm ID × ∼300 mm length; Polymicro Technologies, Phoenix, AZ) were used for constructing the interface. The inner capillary had a dead volume of 15 μL. A PEEK tee (IDEX, Oak Harbor, WA) was used to secure the OPSI assembly. Solvent delivery to the OPSI was controlled by a syringe pump, while a continuous solvent flow to the ESI ion source was ensured by sealing the annulus tubing with the needle probe (Figure D-2 B). A methanol–water solvent mixture (1:1) was used in all experiments. Flow rates ranging from 5 to 50 μL min^{-1} could be chosen on demand by controlling the syringe pump and were independent from the ion source settings. At flow rates lower than 5 μL min^{-1}, stable ion signals were difficult to maintain and leaking was observed at flow rates higher than 50 μL min^{-1}. In the majority of cases, a flow rate of 20 μL min^{-1} was used, resulting in a 45 s wash-through time. The OSPI assembly was tilted 45° from vertical for easier access by the robotic arm. Using this

setup, typical times for RoSA-MS operations were as follows: 10 s for the laser scan, 8 s for sampling one surface point starting from the robot's home position, and 42 s for orienting and introducing the needle probe into the OPSI. Following these events, the needle probe stayed in the OPSI for 180 s and returned to the home position in 42 s.

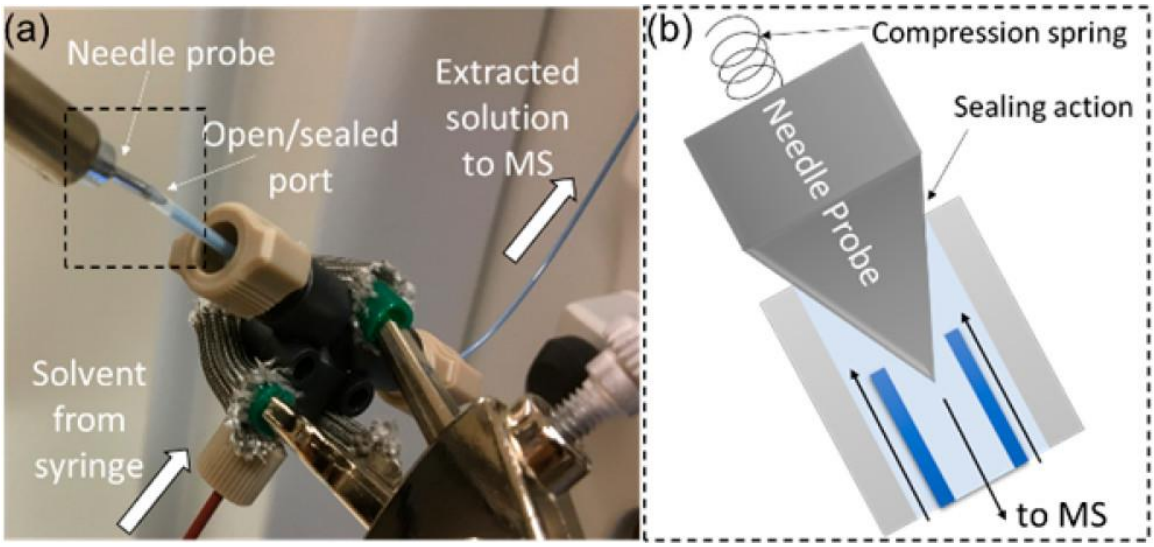

Figure D-2 (A) During RoSA-MS analysis, the robot docks the needle probe into an open port sampling interface (OPSI). (B) Schematic of the needle probe docked in the OPSI. Pressure from the spring-loaded probe against the annulus tubing maintains a sealed junction. The solvent flow between the annulus and the center capillary dissolves the material on the needle tip. The sealed fluidics system delivers the solubilized sample to the mass spectrometer.

The Orbitrap mass spectrometer was used to conduct most experiments. A heated electrospray ionization (HESI) ion source attached to the Ion Max housing was used without modification. Ion source parameters were as follows: sheath gas flow rate 15–25 arb. units, aux. gas flow rate 2 arb. units; sweep gas flow rate 0 arb. units, heater (aux.) temperature 80 °C, spray voltage: ± 2.5 kV, capillary voltage 0 V, capillary temperature 200 °C; S-lens RF level 50 arb. units. Unless noted otherwise, the Orbitrap was operated in either positive- or negative-ion modes at a mass resolution of 17 500 at *m*/*z* 200. The automatic gain control target was set to 1×10^6 ions, and the maximum ion injection time was set to 65 ms. The Xcalibur software was used to process and export MS data into a.csv format file.

A Waters Synapt G2-S HDMS mass spectrometer was also easily coupled with the RoSA robot. MS data was obtained using its built-in ESI ion source operated with the following parameters: capillary voltage ±2.5 kV, sampling cone 12 V, source offset 30 V; source temperature 200 °C, desolvation temperature 100 °C; cone gas flow 2 L h^{-1}, desolvation gas flow 300 L h^{-1}, nebulizer gas pressure 5.8–6.2 bar. Unless noted otherwise, this mass spectrometer was operated in positive- or negative-ion, time-of-flight resolution mode.

D.3.3 RoSA Data Processing and Fusion

Meshlab (version 2016.12) [22], an open source software, was used to process the raw point cloud data from the laser scan. Poisson parameters (12, 1.5, 4) were used to achieve a good balance between smoothing noise and preserving surface details in the mesh generation process [23]. Topological artifacts in the generated mesh were manually

removed, if needed. The curated 3D surface mesh data was converted to a .stl file format for fusion with MS data. Integrated abundance areas were listed in a .csv file together with the sampled 3D coordinates and the peaks' m/z values [15, 24]. Spot sizes of 1–5 mm were used for visualizing sampled spots on objects of different sizes.

Visualization was achieved by loading the .stl surface mesh file and the .csv file into the ili software [24–26]. Unless indicated otherwise, the following ili visualization parameters were used: spot opacity 1, border opacity 0.1, size factor 1, mapping: scale linear or logarithmic, color map jet; hotspot quantile 1. All molecular cartography data is available at the following link: https://ww2.chemistry.gatech.edu/fernandez/supplementary-material

D.4 Results and Discussion

D.4.1 Sampling Precision and Resolution

The UR-5 robot controls its position coordinates with an accuracy of 0.01 mm, and the Actin GUI reserves position accuracy of 0.0001 mm for robot simulation and control. However, due to control system integration and the added custom-built probe, the precision of the system was expected to be lower. For this reason, the sampling precision was evaluated by repeatedly piercing a paper sheet using a 0.125 mm-diameter solid needle at the same nominal location following random arm movement through various waypoints (Figure D-3). As shown in Figure D-3 A&B, the Actin-UR-5 system was observed to achieve a precision estimated to be in the order of 40 μm under optimum conditions.

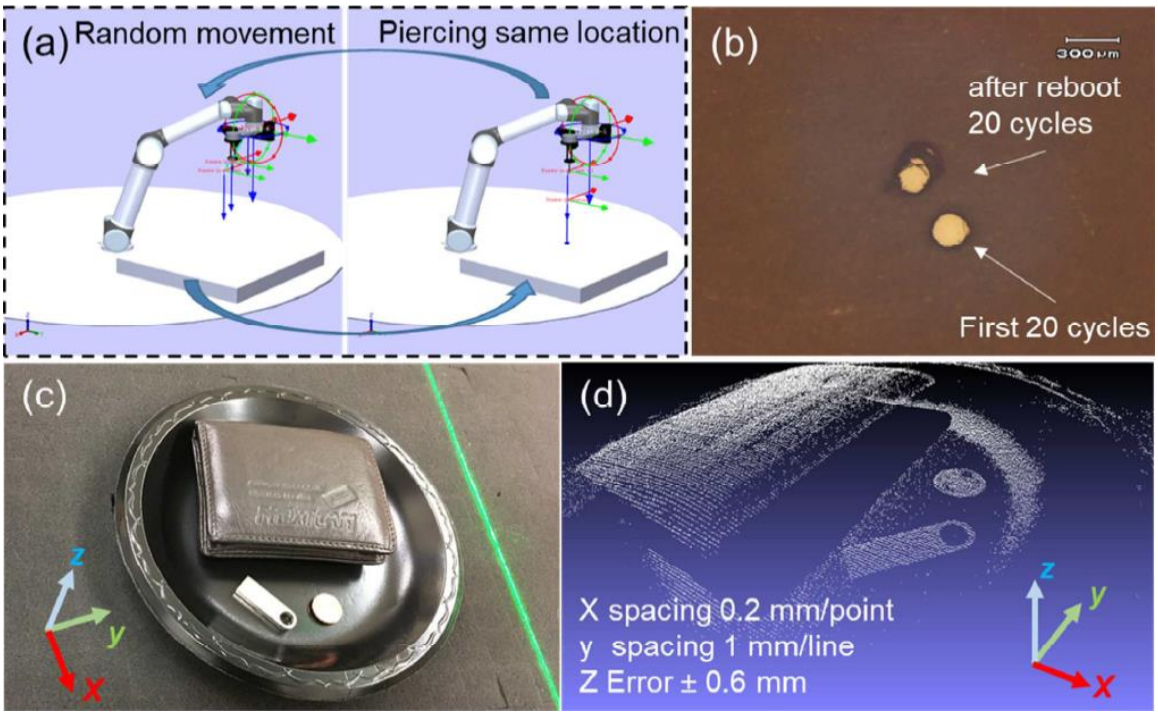

Figure D-3 (A) To evaluate the precision of the robot controlled by Actin, a 0.125 mm OD needle was programed to pierce the same location on a piece of paper after a random 3-waypoint arm movement. (B) For the first twenty cycles of piercing, the needle went through the paper creating a single hole 200 µm in diameter. From these measurements, the estimated deviation was calculated to be in the order of 200 µm -125 µm =75 µm, for an overall precision of 75 µm/2=37.5 µm (~40 µm). Following this experiment, the RoSA system was restarted to test experiment-to-experiment positioning robustness. The system was programmed to pierce the same location as in the previous experiment for an additional 20 cycles. In this case, it was observed that the system showed a offset that created a new hole ~300 µm away from the original location. (C) Several objects scanned by the laser scanner, (D) the obtained point cloud data revealing the laser scanner's precision in the x, y, z directions.

The laser scanner's contribution to sampling precision was also investigated. Point cloud data for a series of objects placed on a flat surface were collected (Figure D-3 C&D). Investigation of the generated point cloud data showed a spacing of 0.2 mm in the x-direction and 1.0 mm in the y-direction. Standard deviations in the z-values of 100 identical points scanned from a flat surface revealed a precision of ±0.6 mm along that coordinate. Considering the observed z-direction precision, a sampling position tolerance of 1.0 mm was built-in the probe design by means of a compression spring, and a 1 mm z-direction offset in the robotic sampling GUI operation. In all performed experiments, the sampling probe always came into contact with the selected surface points, suggesting an overall spatial resolution of approximately 1 mm, an improvement over the ~3 mm obtained in previous work [19]. The spring loaded tip had the additional advantage of providing a softer touch that did not pierce surfaces of more delicate samples.

D.4.2 Characterization of OPSI Performance

Prior to examining 3D objects, the operation of the OSP interface was tested by analyzing model analytes on relatively flat surfaces. First, the RoSA probe was directed to contact for 1 s an area where 1 μL of a 100 μM neat caffeine solution had been allowed to dry on a cotton swab. Following sampling, the robot docked the tip of the needle probe into the OPSI while the mass spectrometer was being operated continuously in positive-ion mode. A signal at m/z 217 corresponding to the $[M + Na]^+$ ion of caffeine was readily observed in the real-time mass spectrum, ~45 s after the probe docking event, at a solvent flow rate of 20 μL min–1. The extracted ion chronogram (EIC) showed a peak of approximately 18 s FWHM. Although shorter wash through times and sharper peaks could be obtained by using a shorter center capillary [20], the OPSI configuration chosen in these

experiments provided the extra clearance needed between the robotic arm and the mass spectrometer. The signal at m/z 217 returned to background levels ~45 s after it was first detected, with negligible carryover.

The detection limit and dynamic range achievable with the RoSA-MS system were evaluated by pipetting neat cocaine samples of increasing concentrations directly onto the probe needle. The samples were applied in the form of 1 μL solution and allowed to dry. The lowest detectable level of cocaine with the current system using parallel reaction monitoring (PRM) mode of the m/z 182.12 fragment ion was 1 pg (1 ppb). A dynamic range of 4 orders of magnitude was achieved until the EIC started to broaden at a concentration level of 10 ng (10 ppm). These experiments indicated the potential of this system for direct, automated, surface semiquantitative experiments.

D.4.3 Molecular Cartography RoSA-MS Applications

One driver for implementing robotics for MS sampling purposes is to replace error-prone, labor-intensive human operations. Both commercial systems such as LESA [27] and laboratory-built systems [28] can perform automated sample screening either on flat surfaces, or after appropriate sample preparation. With RoSA-MS, sample objects can be directly scanned in their native form and shape, coregistering the chemical analysis data, the 3D contour of the sample object, and the sample collection coordinates. We therefore tested RoSA on several model samples, obtaining both full survey and tandem mass spectra for each point sampled.

In the first test, a plastic coffee cup cover with a dried coffee stain was probed by RoSA-MS, as a simulation of a sample of potential forensic interest. Mesh coordinates

were selected so as to guide the probe to touch the stain on the cup (Figure D-4 A&B). The needle probe was then docked in the OPSI to subject the detached material to ESI-MS analysis. As expected, the MS data confirmed the presence of caffeine on this spot at m/z 217 (Figure D-4 C).

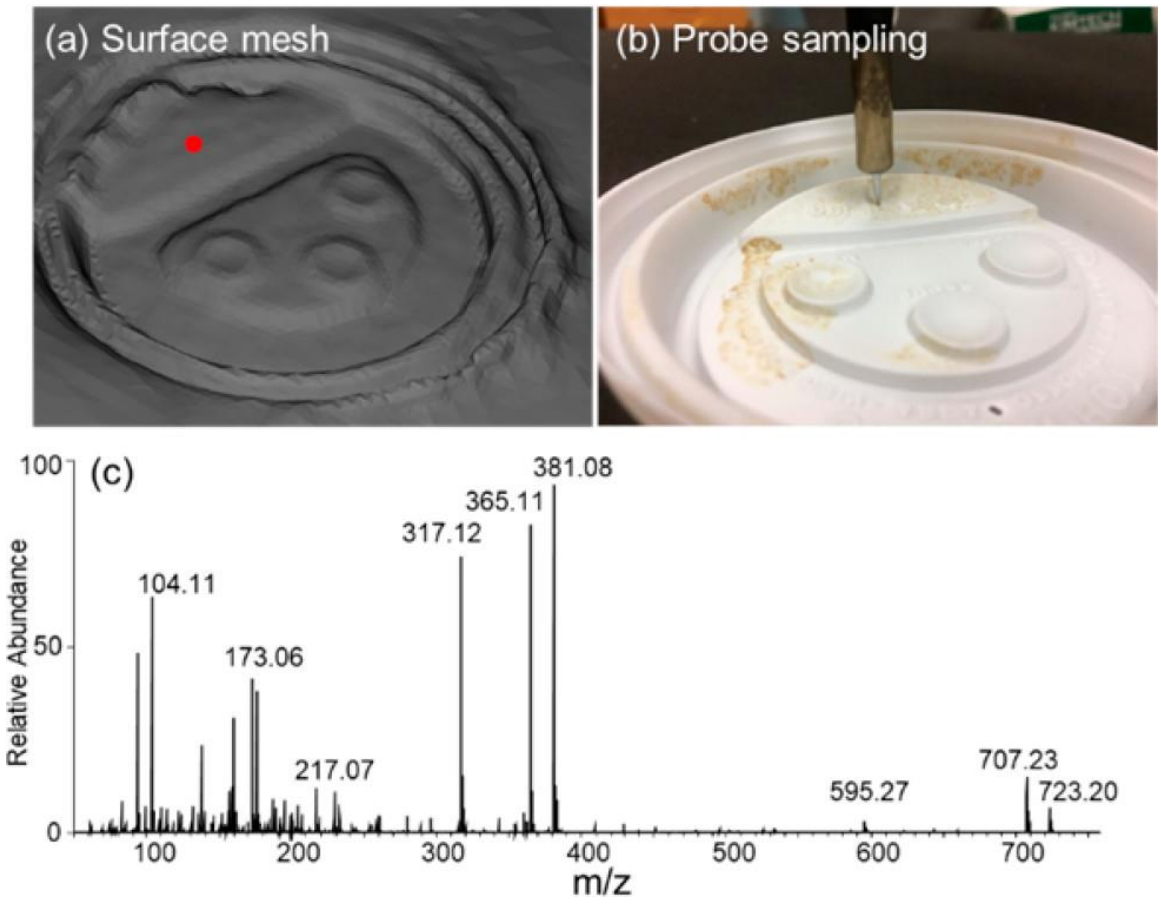

Figure D-4 (A) Digitized surface mesh for a coffee cup. The red dot indicates the selected sampling point. (B) Photo showing the needle probe contacting the sample surface. (C) Mass spectrum obtained for the material detached by the probe and injected into the OPSI.

The rapid screening of medicine quality is another potential application of RoSA-MS. Falsified medicines (in particular anti-infectives and antimalarials) have become a significant worldwide problem, requiring constant surveillance [29]. Genuine and falsified artemether/lumefantrine antimalarial tablets [30] in their original blister packs, were screened by RoSA-MS (Figure D-5). The needle probe was used to pierce through the aluminum foil seal, touching the tablet surface. For a genuine tablet, intense peaks at *m*/*z* 321 and 619, corresponding to the $[M + Na]^+$ and $[2M+Na]^+$ ions of artemether were observed. For a fake tablet, peaks at *m*/*z* 203, 205, and 365, corresponding to the $[M + Na]^+$ ions of glucose, mannitol, and sucrose, respectively, were detected (Figure D-5), rapidly distinguishing the falsified sample from the genuine product.

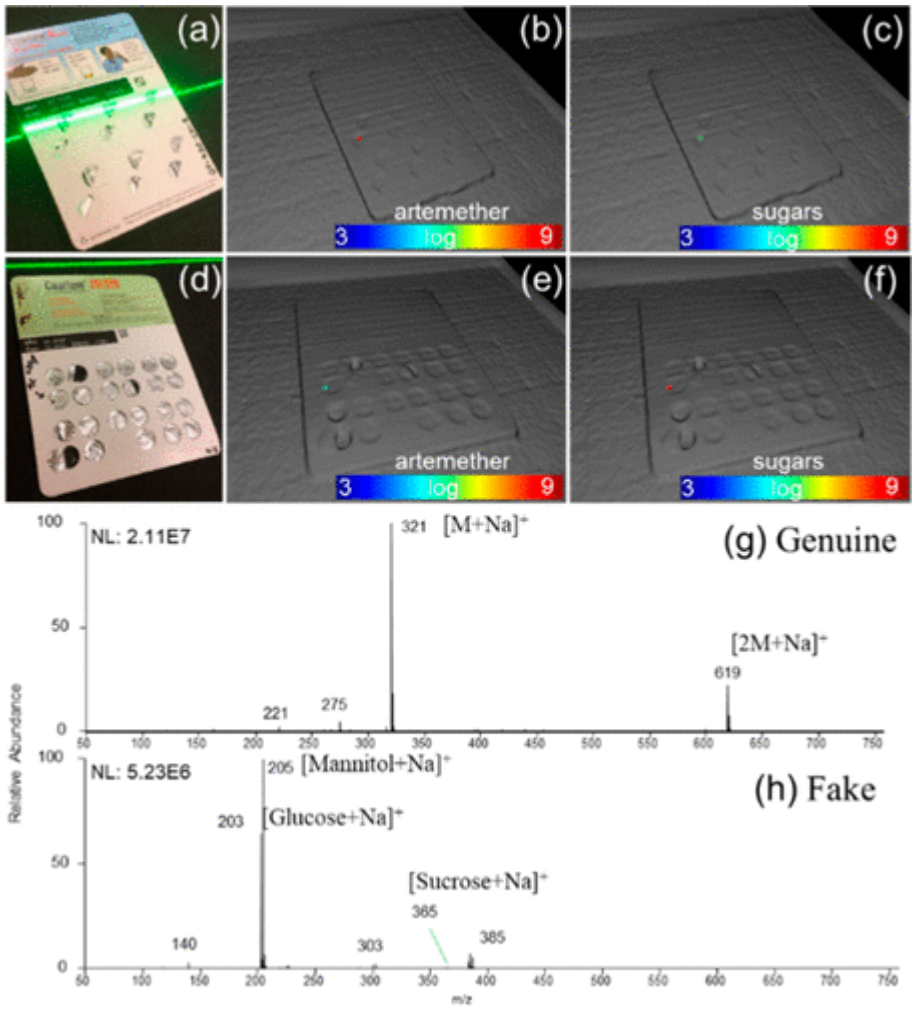

Figure D-5 (A) Genuine artemether/lumefantrine antimalarial combination medicine blister pack being laser scanned. The relative abundances for artemether (m/z = 321, 619) (B) and various sugar-like compounds (m/z = 203, 205, and 365) (C) are plotted on the mesh surface. (D) Falsified antimalarial combination medicine blister pack being laser scanned, (E) and (F) show intensities for artemether (m/z = 321, 619) and various sugar ions (m/z = 203, 205, and 365) ions. The corresponding survey mass spectra are shown in (G) and (H).

In another example, a rubber football which had been touched by a person who used *N*,*N*-diethyl-meta-toluamide (DEET) to fight off mosquitoes was subjected to RoSA-MS. Spots in the area that had been touched by the hand showed significantly higher abundances for ions at *m*/*z* 192 and 214, corresponding to the $[M + H]^+$ and $[M + Na]^+$ species of DEET (Figure D-6). Most of the other regions, however, did not produce DEET signals much higher than the background level, agreeing with the fact that this football had only been touched by the DEET-exposed hand once, and in specific places.

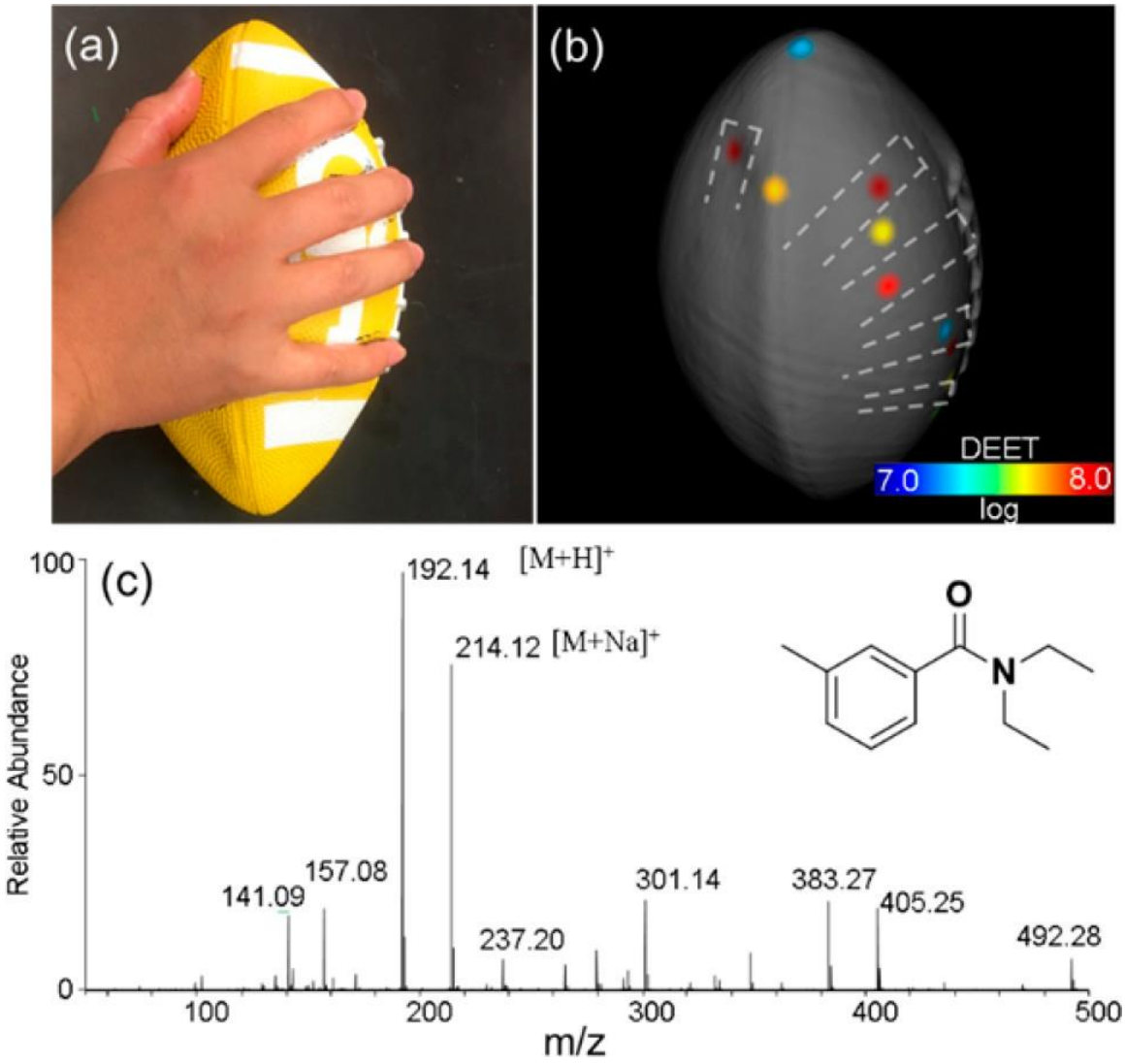

Figure D-6 (A) A hand that was sprayed with DEET holding a football. (B) Several locations on this football were analyzed by RoSA-MS. The summed peak area (m/z 192 + 214) for DEET ions was converted to a pseudo color scale for the specific coordinates sampled. The dashed lines indicate the approximate boundary of the fingers when touching the football surface. (C) Full scan mass spectrum obtained from the coordinates where the thumb contacted the surface.

A useful application of RoSA-MS is that of monitoring products of chemical reactions on 3D surfaces as a means of understanding the role that these surfaces play in facilitating (or hampering) chemical reactivity. As an example, we studied the condensation polymerization reaction of amino acids and alpha hydroxy acids, following an ester–amide exchange mechanism leading to depsipeptides—a plausible prebiotic route to modern peptides [31–33]. Thus, far, these reactions have been carried out in bulk with the role of heterogeneous surfaces still yet to be determined. To test the applicability of using RoSA-MS for studying this system, a simulated condensation experiment was performed on a laboratory spot plate. A roughened 6-well spot plate (Figure D-7 A) was used to carry out a dry down reaction with 600 μL of an aqueous solution of glycolic acid (120 mM, "g′"), alanine (40 mM, "A"), glycine (40 mM, "G"), and leucine (40 mM, "L"), at 80 °C. The spotted solution initially occupied approximately half the volume of each of the wells. After an overnight dry down in the oven to favor condensation polymerization followed by cooling of the plate at room temperature, a darker region at half the well height was observed due to the "coffee ring effect". The solid residue was found to have climbed up the well wall toward the rim, and against gravity during the drying process. RoSA-MS was then used to visualize the distribution of reagents and products along the wall. After generating the corresponding mesh surface by a laser scan, seven points located at places ranging from the bottom of the well to the rim were probed. The full scan MS intensities were normalized against the leucine abundance to eliminate any variability in sample collection amount. Figure D-7 B shows the distribution of the g′GAg′ depsipeptide reaction product. Its observed abundance changed over 2 orders of magnitude across the well wall, with a maximum at the center of the scanned transect line, corresponding to the darker

“coffee ring” regions in the photo. In comparison, leucine only showed a difference of 1 order of magnitude in abundance.

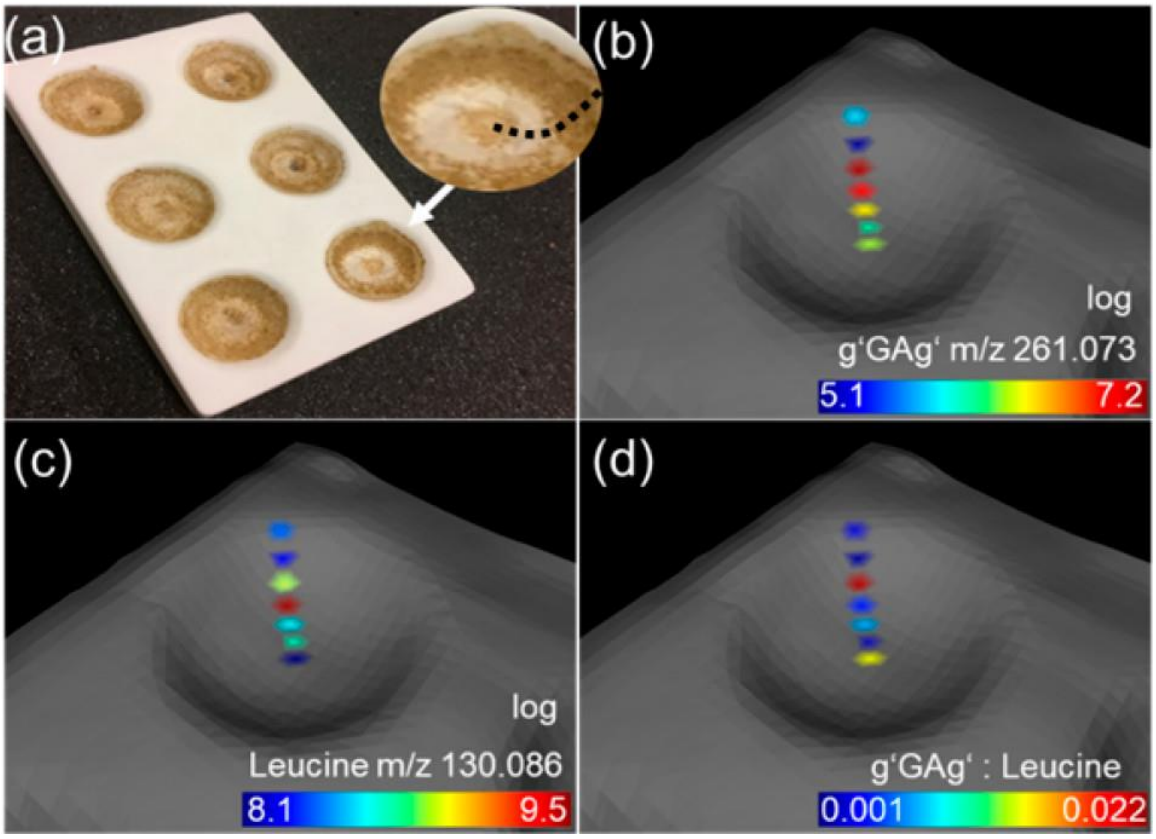

Figure D-7 (A) A spot plate following a dry down condensation reaction involving amino acids and hydroxy acids to form mixed amide/ester-linked oligomers, known as depsipeptides. The surface of the wells was analyzed by RoSA-MS to detect product formation. The dashed line in the inset indicates the sampled transect. (B) Seven independent surface points were probed, and the abundances of the g′GAg′ depsipeptide, one of the reaction products, mapped on the mesh representation of the surface. (g′, glycolic acid; G, glycine; A, alanine.) (C) Surface abundance for leucine, one of the starting reagents. (D) Surface abundance ratio between the g′GAg′ depsipeptide and leucine.

D.5 Conclusion

A new platform for robotic surface analysis coupled with 3D surface sampling that incorporates surface contour digitization, robotic sampling, and 3D surface molecular cartography has been developed. With a 1 mm spatial resolution afforded by the line laser scanning technique, RoSA-MS is well suited to discrete sampling analyses for a variety of applications within the food industry, forensics, chemical reaction monitoring, and many others yet to be explored. In the present configuration, a spring-loaded semiblunt needle was used to collect sample from various surfaces. However, due to the modular nature of the system, the sampling probe could be easily tailored to different applications. For example, replacing the metal needle with a cotton swab would allow for more delicate sample-probe interactions. A sealed open sampling port interface effectively extracted analytes from the tip of the probe and was easily coupled to high resolution mass spectrometers. It is expected that the open and modular nature of RoSA-MS will enable further developments in automated, 3D computer vision-based MS analysis, further harnessing ongoing advances in robotics.

D.6 References

1. Monge, M.E., Harris, G.A., Dwivedi, P., Fernández, F.M.: Mass spectrometry: Recent advances in direct open air surface sampling/ionization, (2013)
2. Norris, J.L., Caprioli, R.M.: Analysis of tissue specimens by matrix-assisted laser desorption/ionization imaging mass spectrometry in biological and clinical research, (2013)
3. Wu, C., Dill, A.L., Eberlin, L.S., Cooks, R.G., Ifa, D.R.: Mass spectrometry imaging under ambient conditions, (2013)
4. Caprioli, R.M., Farmer, T.B., Gile, J.: Molecular Imaging of Biological Samples: Localization of Peptides and Proteins Using MALDI-TOF MS. Anal. Chem. 69,

4751–4760 (1997). https://doi.org/10.1021/ac970888i

5. Pacholski, M.L., Winograd, N.: Imaging with Mass Spectrometry. Chem. Rev. 99, 2977–3005 (1999). https://doi.org/10.1021/cr980137w

6. Takáts, Z., Wiseman, J.M., Gologan, B., Cooks, R.G.: Mass spectrometry sampling under ambient conditions with desorption electrospray ionization. Science (80-.). 306, 471–473 (2004). https://doi.org/10.1126/science.1104404

7. Van Berkel, G.J., Kertesz, V., Koeplinger, K.A., Vavrek, M., Kong, A.N.T.: Liquid microjunction surface sampling probe electrospray mass spectrometry for detection of drugs and metabolites in thin tissue sections. J. Mass Spectrom. 43, 500–508 (2008). https://doi.org/10.1002/jms.1340

8. Eikel, D., Vavrek, M., Smith, S., Bason, C., Yeh, S., Korfmacher, W.A., Henion, J.D.: Liquid extraction surface analysis mass spectrometry (LESA-MS) as a novel profiling tool for drug distribution and metabolism analysis: The terfenadine example. Rapid Commun. Mass Spectrom. 25, 3587–3596 (2011). https://doi.org/10.1002/rcm.5274

9. Lanekoff, I., Heath, B.S., Liyu, A., Thomas, M., Carson, J.P., Laskin, J.: Automated platform for high-resolution tissue imaging using nanospray desorption electrospray ionization mass spectrometry. Anal. Chem. 84, 8351–8356 (2012). https://doi.org/10.1021/ac301909a

10. Sampson, J.S., Hawkridge, A.M., Muddiman, D.C.: Generation and Detection of Multiply-Charged Peptides and Proteins by Matrix-Assisted Laser Desorption Electrospray Ionization (MALDESI) Fourier Transform Ion Cyclotron Resonance Mass Spectrometry. J. Am. Soc. Mass Spectrom. 17, 1712–1716 (2006). https://doi.org/10.1016/j.jasms.2006.08.003

11. Nemes, P., Barton, A.A., Li, Y., Vertes, A.: Ambient molecular imaging and depth profiling of live tissue by infrared laser ablation electrospray ionization mass spectrometry. Anal. Chem. 80, 4575–4582 (2008). https://doi.org/10.1021/ac8004082

12. Hiraoka, K., Nishidate, K., Mori, K., Asakawa, D., Suzuki, S.: Development of probe electrospray using a solid needle. Rapid Commun. Mass Spectrom. 21, 3139–3144 (2007). https://doi.org/10.1002/rcm.3201

13. Lee, C.C., Yoshimura, K., Yu, Z., Iwata, R., Ito, H., Suzuki, H., Mori, K., Ariyada, O., Takeda, S., Kubota, T., Hiraoka, K.: Ambient imaging mass spectrometry by electrospray ionization using solid needle as sampling probe. J. Mass Spectrom. 44, 1469–1477 (2009). https://doi.org/10.1002/jms.1632

14. Edison, S.E., Lin, L.A., Gamble, B.M., Wong, J., Zhang, K.: Surface swabbing technique for the rapid screening for pesticides using ambient pressure desorption ionization with high-resolution mass spectrometry. Rapid Commun. Mass

Spectrom. 25, 127–139 (2011). https://doi.org/10.1002/rcm.4831

15. Bouslimani, A., Porto, C., Rath, C.M., Wang, M., Guo, Y., Gonzalez, A., Berg-Lyon, D., Ackermann, G., Christensen, G.J.M., Nakatsuji, T., Zhang, L., Borkowski, A.W., Meehan, M.J., Dorrestein, K., Gallo, R.L., Bandeira, N., Knight, R., Alexandrov, T., Dorrestein, P.C.: Molecular cartography of the human skin surface in 3D. Proc. Natl. Acad. Sci. U. S. A. 112, E2120–E2129 (2015). https://doi.org/10.1073/pnas.1424409112

16. Jarmusch, A.K., Pirro, V., Kerian, K.S., Cooks, R.G.: Detection of strep throat causing bacterium directly from medical swabs by touch spray-mass spectrometry. Analyst. 139, 4785–4789 (2014). https://doi.org/10.1039/c4an00959b

17. Palanco, S., Laserna, J.J.: Full automation of a laser-induced breakdown spectrometer for quality assessment in the steel industry with sample handling, surface preparation and quantitative analysis capabilities. J. Anal. At. Spectrom. 15, 1321–1327 (2000). https://doi.org/10.1039/b003632n

18. Nicolas, G., Mateo, M.P., Piñon, V.: 3D chemical maps of non-flat surfaces by laser-induced breakdown spectroscopy. J. Anal. At. Spectrom. 22, 1244–1249 (2007). https://doi.org/10.1039/b704682k

19. Bennett, R. V., Morzan, E.M., Huckaby, J.O., Monge, M.E., Christensen, H.I., Fernández, F.M.: Robotic plasma probe ionization mass spectrometry (RoPPI-MS) of non-planar surfaces. Analyst. 139, 2658–2662 (2014). https://doi.org/10.1039/c4an00277f

20. Van Berkel, G.J., Kertesz, V.: An open port sampling interface for liquid introduction atmospheric pressure ionization mass spectrometry. Rapid Commun. Mass Spectrom. 29, 1749–1756 (2015). https://doi.org/10.1002/rcm.7274

21. Gómez-Ríos, G.A., Liu, C., Tascon, M., Reyes-Garcés, N., Arnold, D.W., Covey, T.R., Pawliszyn, J.: Open Port Probe Sampling Interface for the Direct Coupling of Biocompatible Solid-Phase Microextraction to Atmospheric Pressure Ionization Mass Spectrometry, (2017)

22. Cignoni, P., Callieri, M., Corsini, M., Dellepiane, M., Ganovelli, F., Ranzuglia, G.: MeshLab: an Open-Source Mesh Processing Tool.

23. Kazhdan, M., Hoppe, H.: Screened poisson surface reconstruction. ACM Trans. Graph. 32, (2013). https://doi.org/10.1145/2487228.2487237

24. Bouslimani, A., Melnik, A. V., Xu, Z., Amir, A., Da Silva, R.R., Wang, M., Bandeira, N., Alexandrov, T., Knight, R., Dorrestein, P.C.: Lifestyle chemistries from phones for individual profiling. Proc. Natl. Acad. Sci. U. S. A. 113, E7645–E7654 (2016). https://doi.org/10.1073/pnas.1610019113

25. Petras, D., Nothias, L.F., Quinn, R.A., Alexandrov, T., Bandeira, N., Bouslimani,

A., Castro-Falcón, G., Chen, L., Dang, T., Floros, D.J., Hook, V., Garg, N., Hoffner, N., Jiang, Y., Kapono, C.A., Koester, I., Knight, R., Leber, C.A., Ling, T.J., Luzzatto-Knaan, T., McCall, L.I., McGrath, A.P., Meehan, M.J., Merritt, J.K., Mills, R.H., Morton, J., Podvin, S., Protsyuk, I., Purdy, T., Satterfield, K., Searles, S., Shah, S., Shires, S., Steffen, D., White, M., Todoric, J., Tuttle, R., Wojnicz, A., Sapp, V., Vargas, F., Yang, J., Zhang, C., Dorrestein, P.C.: Mass spectrometry-based visualization of molecules associated with human habitats, (2016)

26. Protsyuk, I., Melnik, A. V., Nothias, L.F., Rappez, L., Phapale, P., Aksenov, A.A., Bouslimani, A., Ryazanov, S., Dorrestein, P.C., Alexandrov, T.: 3D molecular cartography using LC-MS facilitated by Optimus and 'ili software. Nat. Protoc. 13, 134–154 (2018). https://doi.org/10.1038/nprot.2017.122

27. Eikel, D., Henion, J.: Liquid extraction surface analysis (LESA) of food surfaces employing chip-based nano-electrospray mass spectrometry. Rapid Commun. Mass Spectrom. 25, 2345–2354 (2011). https://doi.org/10.1002/rcm.5107

28. Chen, C.L., Chen, T.R., Chiu, S.H., Urban, P.L.: Dual robotic arm "production line" mass spectrometry assay guided by multiple Arduino-type microcontrollers. Sensors Actuators, B Chem. 239, 608–616 (2017). https://doi.org/10.1016/j.snb.2016.08.031

29. Nayyar, G.M.L., Attaran, A., Clark, J.P., Culzoni, M.J., Fernandez, F.M., Herrington, J.E., Kendall, M., Newton, P.N., Breman, J.G.: Responding to the pandemic of falsified medicines. Am. J. Trop. Med. Hyg. 92, 113–8 (2015). https://doi.org/10.4269/ajtmh.14-0393

30. Bernier, M.C., Li, F., Musselman, B., Newton, P.N., Fernández, F.M.: Fingerprinting of falsified artemisinin combination therapies via direct analysis in real time coupled to a compact single quadrupole mass spectrometer. Anal. Methods. 8, 6616–6624 (2016). https://doi.org/10.1039/C6AY01418F

31. Forsythe, J.G., Yu, S.-S., Mamajanov, I., Grover, M.A., Krishnamurthy, R., Fernández, F.M., Hud, N. V.: Ester-Mediated Amide Bond Formation Driven by Wet-Dry Cycles: A Possible Path to Polypeptides on the Prebiotic Earth. Angew. Chemie Int. Ed. 54, 9871–9875 (2015). https://doi.org/10.1002/anie.201503792

32. Yu, S.S., Krishnamurthy, R., Fernández, F.M., Hud, N. V., Schork, F.J., Grover, M.A.: Kinetics of prebiotic depsipeptide formation from the ester-amide exchange reaction. Phys. Chem. Chem. Phys. 18, 28441–28450 (2016). https://doi.org/10.1039/c6cp05527c

33. Forsythe, J.G., Petrov, A.S., Millar, W.C., Yu, S.S., Krishnamurthy, R., Grover, M.A., Hud, N. V., Fernández, F.M.: Surveying the sequence diversity of model prebiotic peptides by mass spectrometry. Proc. Natl. Acad. Sci. U. S. A. 114, E7652–E7659 (2017). https://doi.org/10.1073/pnas.1711631114